EVALUATION OF INTERNAL DAMAGE IN REINFORCED CONCRETE ELEMENTS USING ULTRASONIC TOMOGRAPHY

BY

HAJIN CHOI

DISSERTATION

Submitted in partial fulfillment of the requirements
for the degree of Doctor of Philosophy in Civil Engineering
in the Graduate College of the
University of Illinois at Urbana-Champaign, 2016

Urbana, Illinois

Doctoral Committee:

Professor John S. Popovics, Chair
Professor Minh N. Do
Associate Professor Mani Golparvar-Fard
Associate Professor Shih-Ho Chao, University of Texas at Arlington

ABSTRACT

Quality control and quality assurance (QC/QA) of the concrete infrastructure has become an important national issue, especially because construction inaccuracies and invisible internal defects can result in unexpected structural response and failure. In order to evaluate the condition of an existing concrete structure, non-destructive testing (NDT) has been widely used as an assessment tool. Ultrasonic pulse velocity (UPV) is an efficient method to characterize the condition of concrete elements, and tomographic imaging is a powerful tool for visually identifying internal damage. However, the implementation of UPV data within a tomographic imaging scheme for application to full-scale concrete (RC) structures has not been realized to date because of practical and technological restrictions.

In this dissertation, some of those barriers are overcome by using contactless air-coupled ultrasonic sensors in a scanning test configuration to acquire large amounts of ultrasonic data to create ultrasonic tomograms of large-scale concrete structures. The development of the testing system is described. The measurements are carried out using an automated robotic scanning frame using new sensing technology. Image reconstruction algorithms, including synthetic aperture focusing technique (SAFT) and algebraic reconstruction technique (ART), are reviewed and evaluated for application to imaging of full-scale RC columns. The performance of the data collection system and selected optimal imaging approach are verified through tests on a RC column test sample containing embedded artificial defects. The obtained tomographic images are compared with those from a commercially available ultrasonic imaging device. A comprehensive visualization scheme to characterize the column test sample, based on fusion of integrated ultrasonic tomography and 3-D computer vision, is presented. Such integrated visualization provides holistic characterization of the test sample. Next, the utility of attenuation tomography for enhanced damage detection is evaluated, both through numerical simulation and experimental studies.

Finally, the developed ultrasonic tomographic testing system is applied to full-scale RC columns and slab-beam-column sub-assemblages subjected to simulated earthquake loads. Different concrete types, including

normal reinforced concrete and high performance fiber-reinforced concrete, and seismic different loading schemes are considered. Comparisons of ultrasonic tomograms and strain gauge data illustrate the potential for velocity and attenuation tomography to monitor internal damage progression of structural RC elements both at global and local levels.

ACKNOWLEDGEMENTS

It is with my sweet memories that I look back on years I spent for this research at the University of Illinois at Urbana-Champaign and recall the people who have helped and encouraged me. First of all, I would like to express my special thanks to Dr. John S. Popovics. I am truly lucky in that I was able to work with him. His open-minded attitude toward various strands of scholarship and unflagging insights will be a model which I will pursue in my scholarly life. I should like to thank the members of my dissertation committee. Their cutting-edge research; image processing from Dr. Mihn N. Do, computer vision sensing from Dr. Mani Golparvar-Fard, and full-scale structural experiment from Dr. Shih-Ho Chao, motivates me and forms the foundation of this dissertation. I appreciate for their suggestion and constructive feedback.

My deepest thanks should go to my teachers in Korea as well: Dr. Oan Chul Choi, Dr. Jong-Rak Kim, Dr. Yoon-Ki Choi, Dr. Kyung-Kyu Choi, Dr. Sumin Kim, and Dr. Thomas Kang. Their lectures and instruction during my master period set the firm ground for my understanding of research in architectural and civil engineering. I have also benefitted greatly from many scholars: Dr. Daryl Tweeton, Dr. Teakuen Oh, Dr. Thomas Schumacher, Dr. Daniel King, Dr. Kerry Hall, Dr. Jiyoung Min, Dr. Youngjib Ham, Mr. Ralf Moller, Mr. Timothy Prunkard, Mr. Guillermo Palacios, and Mr. Young-Jae Choi. I appreciate for their valuable discussion and providing materials.

I was fortunate to be supported by research grant during my Ph.D.; The work reported here was made possible by support from the National Science Foundation's George E. Brown Jr. Network for Earthquake Engineering Simulation (NEES) program under award number CMMI-1041633. The SAFT imaging work was supported from the Illinois Department of Transportation through grant ICT R27-146.

A great deal of my sweet memories entails the time I have spent with many friends and colleagues. I would like to thank my NDT lab mates: James Bittner, Agustin Spalvier, Homin Song, Chi-Luen Huang, Sai Evani, Vincent Wenzel, and Yubing Liang. I would also like to thank my friends: Donghyuk Jung, Soonpil Kang,

Deuck Hang Lee, Seunggu Kang, Dongkook Woo, Eun Hyun Park, Gunho Kim, Andy Hur, Xu Chen, Ranjani Vijayakumar, Quang Tran.

Last but not least, I deeply thank my family; parents Byunghyun Choi and Sung-ok So, my sister Sun-Ah Choi for their wholehearted support, and my love, Hana for her sacrifice and encouragement. I dedicate this dissertation to them.

TABLE OF CONTENTS

CHAPTER 1 INTRODUCTION 1
1.1 Problem statement 1
1.2 Research objective 1
CHAPTER 2 BACKGROUND INFORMATION 2
2.1 Mechanical waves 2
2.1.1 Wave propagation in solids 2
2.1.2 Mathematics 3
2.1.3 Ray tracing methods 4
2.2 Non-destructive tests using mechanical waves 5
2.2.1 Ultrasonic pulse velocity (UPV) 6
2.2.2 Seismic tests: SASW, MASW and Impact-echo 6
2.2.3 Air-coupled ultrasonics 6
2.3 Signal processing 7
2.3.1 Basic signal processing 7
2.3.2 Automated arrival picking algorithms 7
2.4 Ultrasonic image reconstruction algorithms 8
2.4.1 Synthetic aperture focusing technique (SAFT) 9
2.4.2 Reverse time migration (RTM) 9
2.4.3 Filtered back-projection (FBP) 10
2.4.4 Algebraic reconstruction technique (ART) 10
2.5 Digital image reconstruction methods 12
2.5.1 Digital image correlation (DIC) 12
2.5.2 Structure from motion (SfM) 12
CHAPTER 3 EVALUATION OF TOMOGRAPHY ALGORITHMS 13
3.1 Evaluation with synthetic data 13
3.1.1 Linear equations for velocity tomography and iterative solvers 13
3.1.2 Synthetic data analysis 16
3.2 Evaluation with numerical data 18
3.2.1 Finite element model development 18
3.2.2 Evaluation of auto-picking algorithms 22
3.2.3 Velocity tomography 25
3.2.4 Differential velocity tomography 28

CHAPTER 4 DEVELOPMENT OF A HYBRID AIR-COUPLED ULTRASONIC SYSTEM 29
4.1 Development of the ultrasonic scanning system 29
4.1.1 Air-coupled electrostatic ultrasonic transducer 30
4.1.2 Hybrid air-coupled ultrasonic testing configuration 32
4.2 Application to a full-scale reinforced concrete element 34
4.2.1 Description of full-scale RC column sample 34
4.2.2 Data collection and signal quality 35
4.2.3 Auto-picking algorithms 41
4.2.4 Stacked A-scan representations 42
4.3 Velocity tomography 43
4.3.1 Evaluation of cross-sectional velocity reconstructions 44
4.3.2 Comparison to commercial tomographic software (GeoTomCG) 45
CHAPTER 5 COMPARISON OF ULTRASONIC IMAGING METHODS 47
5.1 Introduction of one-sided imaging method 47
5.1.1 Dry-coupled ultrasonic pulse echo unit 49
5.1.2 Data measurement from full-scale RC column mock-up 49
5.1.3 Synthetic aperture focusing technique 50
5.2 Data processing for velocity tomography 52
5.3 Analysis of two imaging methods 53
CHAPTER 6 INTEGRATED VISUALIZATION 56
6.1 Reconstruction of external surface condition 56
6.1.1 Structure from motion and multi-view stereo 56
6.1.2 Data measurement and processing 57
6.2 Integrated visualization 60
6.2.1 Registration of images in 3-D 60
6.2.2 Analysis of integrated visualization 61
CHAPTER 7 VELOCITY TOMOGRAPHY APPLIED TO RC COLUMNS SUBJECTED TO SEISMIC LOADING 63
7.1 Application of velocity tomography to RC columns 63
7.1.1 Description of full-scale RC columns 63
7.1.2 Ultrasonic data measurement 68
7.1.3 Development of velocity tomography 70
7.2 Damage evaluation of RC columns 70

7.2.1 Ultrasonic velocity tomography 76
7.2.2 Global compliance of the columns across drift levels 81
7.2.3 Cross-sectional imaging at fixed drift levels 81
CHAPTER 8 ATTENUATION TOMOGRAPHY 83
8.1 Attenuation 83
8.1.1 Finite element model analysis 84
8.1.2 Linear equations for attenuation tomography 89
8.1.3 Differential attenuation tomography 92
8.2 Application to full-scale RC column 96
8.2.1 Data analysis 96
8.2.2 Differential attenuation tomography from experimental data 99
CHAPTER 9 DIFFERENTIAL VELOCITY AND ATTENUATION TOMOGRAPHY APPLIED TO BEAM AND COLUMN CONNECTIONS SUBJECTED TO SEISMIC LOADING 101
9.1 Application of velocity and attenuation tomography 101
9.1.1 Description of full-scale RC slab-beam-column sub-assemblages 101
9.1.2 Ultrasonic data measurement 104
9.1.3 Development of differential ultrasonic tomography 110
9.2 Damage evaluation of RC beam and column connections 110
9.2.1 Stacked A-scan representations 115
9.2.2 Differential velocity and attenuation tomograms 120
CHAPTER 10 CONCLUSIONS 126
10.1 Evaluation of velocity and attenuation tomographic algorithms 126
10.2 Development of hybrid air-coupled ultrasonic scanning system 127
10.3 Comparison of ultrasonic imaging methods 127
10.4 Application of integrated visualization 128
10.5 Tomography applied to full-scale RC structural elements subjected to seismic loading 128
10.5.1 Columns 129
10.5.2 Beam and column connections 129
10.6 Future work 130
10.6.1 Deployment of a configurable robotic scanning platform 130
10.6.2 Fusion with external imaging technologies 131
10.6.3 Consideration of other ultrasonic analysis and imaging techniques 131
REFERENCES 133

APPENDIX A: Tomographic inversion code and auto-picking algorithms 139
APPENDIX B: NEEShub databases 148

LIST OF FIGURES

Figure 2.1 Schematic illustration of ART (adopted from Kak 1988). 11

Figure 3.1 Example of ray contribution to pixels. 14

Figure 3.2 Synthetic data model showing P-wave velocity profiles. 16

Figure 3.3 Error percentage of reconstructed slowness profiles from each iterative solver: (a) 900 pixels, (b) 1,600 pixels, and (c) 2,500 pixels. 17

Figure 3.4 Cross-sectional models showing input (pink arrow) and receiver (yellow points) positions: (a) plain concrete, (b) concrete and steel, (c) concrete, steel and defect case 1, and (d) concrete, steel and defect case 2. 19

Figure 3.5 Input force representing ultrasonic wave pulse with center frequency 50 kHz. 20

Figure 3.6 Wave propagation at 204 μs after excitation: (a) plain concrete, (b) concrete and steel, (c) concrete, steel and defect case 1, and (d) concrete, steel and defect case 2; the colors represent the von Mises stress. 21

Figure 3.7 Stacked A-scan images: (a) plain concrete, (b) concrete and steel, (c) concrete, steel and defect case 1, and (d) concrete, steel and defect case 2. 22

Figure 3.8 Illustration of the arrival picking algorithms: (a) Signal with AIC, HIC, and noise-threshold indicated (b) enlargement of the dash-lined box from (a) 23

Figure 3.9 P-wave velocity profiles obtained from plain concrete model: (a) velocity defined by AIC, (b) velocity defined by HIC, and (c) velocity defined by the noise-threshold method 24

Figure 3.10 Velocity tomograms (Kaczmarz's method): (a) plain concrete, (b) concrete and steel, (c) concrete, steel and defect case 1, and (d) concrete, steel and defect case 2. 26

Figure 3.11 Velocity tomograms (Randomized Kaczmarz method): (a) plain concrete, (b) concrete and steel, (c) concrete, steel and defect case 1, and (d) concrete, steel and defect case 2. 26

Figure 3.12 Velocity tomograms (least square method): (a) plain concrete, (b) concrete and steel, (c) concrete, steel and defect case 1, and (d) concrete, steel and defect case 2. 27

Figure 3.13 Example of color scale adjustment of tomogram in fig 3.11(d): (a) tomogram with a minimum color scale of 3800 m/s, and (b) tomogram with a maximum color scale of 5000 m/s. 27

Figure 3.14 Differential tomograms: (a) tomogram based on the arrival time differentials between CSD1-CS, (b) tomogram based on the arrival time differentials between CSD2-CS. 28

Figure 4.1 Electrostatic ultrasonic transducer (SensComp 600). 32

Figure 4.2 Schematic illustration of sensor configurations for through-thickness ultrasonic methods. 33

Figure 4.3 The experimental testing set-up showing automated scanning frame, air-coupled sending transducers (top inset), and array of receiving accelerometers (bottom inset). 34

Figure 4.4 Test specimen detail with dimensions shown in units of mm: (a) Cross section A-A; (b) Design of the concrete column with embedded steel bars and artificial defects indicated (Red dotted lines represent scanning sections;) (c) Photo before casting concrete; (d) Photo after casting concrete. 35

Figure 4.5 Illustration of air-gap adjustment from measured signal data (green line is a trigger signal from air-coupled transducer, blue line is a pulse for air-gap measurement, and red curves are ultrasonic signals measured by the accelerometer). 36

Figure 4.6 Schematic illustration of hybrid air-coupled ultrasonic test configuration. 37

Figure 4.7 Time signals measured through the thickness of the concrete column: (a) Single shot (red line) and time averaged (black line) signals; (b) Time averaged (black line) and low pass filtered (blue line) signals. 39

Figure 4.8 Examples of time averaged signals measured through the thickness of the specimen: (a) Raw signal, (b) 5 time-averaged signal, (c) 10 time-averaged signal, (d) 20 time-averaged signal, (e) 30 time-averaged signal, (f) 40 time-averaged signal. 40

Figure 4.9 Calculated SNR for time-averaged signals presented in Fig 4.8: (a) the entire signal case (b) the first cycle of signal case. 40

Figure 4.10 Stacked A-scan images with P-wave arrivals defined by the noise-threshold (yellow), AIC (red), and HIC (blue) criteria: (a) Receiver 1, (b) Receiver 2, (c) Receiver 3, and (d) Receiver 4. 41

Figure 4.11 Illustration of auto-picking algorithm based on statistical threshold using multiple time signals. 42

Figure 4.12 Stacked A-scan images from different receiver positions (a) to (h) through section A-A of the column specimen; image brightness is related to time signal amplitude. 43

Figure 4.13 Developed P-wave velocity tomograms: (a) 50 mm above section A-A (b) Section A-A (c) 50 mm below section A-A; in the drawing the green box indicates the position of the void defect and the blue box that of the cracked concrete defect. 45

Figure 4.14 Comparison of developed P-wave velocity tomograms: cross-section at 18 in. from the top of the RC mock-up; (a) using Matlab; (b) using GEOTOMCG assuming straight ray paths (c) using GEOTOMCG assuming bent ray paths, and cross-section at 28 in. from the top of the RC mock-up; (b) using Matlab; (d) using GEOTOMCG assuming straight ray paths (f) using GEOTOMCG assuming bent ray paths. 46

Figure 5.1 Schematic illustration of sensor configurations for ultrasonic methods 48

Figure 5.2 Bottom view of ultrasonic multi-element shear wave dry point contact array test unit. 49

Figure 5.3 Application of dry-coupled ultrasonic pulse echo test unit. 50

Figure 5.4 Graphical sequential illustration of the SAFT process: (a) A-Scan signals after signal processing, (b) single A-Scan integrated about region of interest, (c) apodization factor for one transducer pair, (d) integration of scan data and apodization factor, (e) summation of all transducer pairs, and (f) final B-scan after Hilbert transform (Distance units in mm). 51

Figure 5.5 Stacked P-wave velocity tomograms: (a) horizontal images around section A-A (b) stacked tomograms through the height of the concrete column (c) vertical section images around the center of the column specimen. 53

Figure 5.6 Sectional images representing the full height of the column specimen along a plane at the center that includes artificial defects: (a) vertical section tomogram built up from two-sided velocity data, and (b) vertical section SAFT image built up from s-wave array data..... 54

Figure 5.7 Sectional images representing the height of the concrete column specimen along a plane near a free surface including rebar: (a) vertical section velocity tomogram built up from two-sided ultrasonic data, and (b) vertical section SAFT image built up from s-wave array data. 55

Figure 6.1 Flowchart describing the 3-D computer vision technique. 57

Figure 6.2 Illustration of image-based 3-D reconstruction from unordered photographs collected around a concrete column. 58

Figure 6.3 Comparison between photograph and 3-D point cloud model: (a) single photograph of the concrete column and (b) 3-D dense point cloud model of the concrete column, where insets show surface texture and coloring detail 59

Figure 6.4 Comparison between the column as designed and 3-D point cloud model: (a) box frame representing originally designed shape; (b) 3-D point cloud model where insets show dimension details (1cm error in width); (c) 3-D point cloud model overlaid with the box frame, where insets reveal geometric construction error. 59

Figure 6.5 Graphical illustration of the integrated visualization scheme. 60

Figure 6.6 Integrated visualization of tomograms and image-based 3-D reconstruction: (a) Photograph of sample before casting concrete, (b) 3-D dense point cloud model of the concrete column where position of defects (green box: Styrofoam, blue box: pre-cracked) are also indicated, and (c) integrated interior and exterior images showing relative position of internal defects. 62

Figure 6.7 Integrated visualization fields from different perspectives; (a) side views and (b) top views. . 62

Figure 7.1 Detail of columns and embedded strain gauges (a) RC1 and RC2 (b) RC3 and UHP-FRC. 64

Figure 7.2 Illustration of embedded concrete strain gauges. 65

Figure 7.3 Experimental set-up to test full-scale columns at the Multi-Axial Subassemblage Testing (MAST) laboratory. 66

Figure 7.4 Applied loading protocols, where dotted circles indicate instance of ultrasonic scanning tests in terms of applied drift level for columns (a) RC1 and (b) RC2, RC3, and UHP-FRC. The bi-axial nature of the loading protocol for column RC2 is illustrated in (c). 67

Figure 7.5 Detail of ultrasonic scanning tests: (a) ultrasonic testing configuration, (b) application of ultrasonic scan to column. 69

Figure 7.6 Example of stiffness slope behavior for column RC1, where calculated numbers of stiffness slope from each subsequent drift cycle are indicated. Units of presented stiffness slope values are applied lateral force in the Y' direction in kN per percentage column drift in that direction. 71

Figure 7.7 Example of residual strain behavior from stain gauge CTRH for column RC1 where calculated numbers of residual strain from each subsequent drift cycle are indicated. Presented strain values are expressed in units of microstrain. 72

Figure 7.8 Stiffness slope as a function of applied drift level for (a) columns RC1 and RC2 and (b) columns RC3 and UHP-FRC. Units of presented stiffness slope values are applied lateral force in the Y' direction in kN per percentage column drift in that direction. 73

Figure 7.9 Cumulative residual strain as a function of applied drift level for columns RC1 and RC2: (a) CTRB gauges from RC1, (b) CTRH gauges from RC1, (c) CTRB gauges from RC2, and (d) CTRH gauges from RC2; Presented strain values are expressed in units of microstrain. 74

Figure 7.10 Cumulative residual strain as a function of applied drift level for columns RC3 and UHP-FRC: (a) CTRB gauges from RC3, (b) CTRH gauges from RC3, (c) CTRB gauges from UHP-FRC, and (d) CTRH gauges from UHP-FRC; Presented strain values are expressed in units of microstrain. 74

Figure 7.11 Photographs from columns RC1 and RC2 at indicated drift levels: (a) photo from RC1 at 1% drift level (Front side), (b) photo from RC1 at 1% drift level (Back side), (c) photo from RC2 at 0.75% drift level (Front side), and (d) photo from RC2 at 0.75% drift level (Back side). 75

Figure 7.12 Photographs from columns RC3 and UHP-FRC at 1% drift level: (a) photo from RC3 at 1% drift level (Front side), (b) photo from RC3 at 1% drift level (Back side), (c) photo from UHP-FRC at 1% drift level (Front side), and (d) photo from UHP-FRC at 1% drift level (Back side). 76

Figure 7.13 Example of through thickness ultrasonic time signals from column RC1 measured at drift levels indicated. 77

Figure 7.14 Normalized P-wave velocity distribution, expressed in box plot form, as a function of applied drift level: (a) RC1, (b) RC2, and (c) UHP-FRC. 78

Figure 7.15 Stacked ultrasonic tomograms showing normalized P-wave velocity across test cross-section at different applied drift levels for columns: (a) RC1 (0%, 0.5%, 1% drift levels), (b) RC2 (0%, 0.75% drift levels), and (c) UHP-FRC (0%, 0.25%, 0.5%, 1% drift levels) 79

Figure 7.16 Comparison of cross-sectional normalized P-wave velocity tomogram and photographs of column RC1 at 1% applied drift level: (a) tomogram from RC1 at 1% drift level, (b) photo from RC1 at 1% drift level (side-A), and (c) photo from RC1 at 1% drift level (side-B). 80

Figure 7.17 Global behavior of tested columns showing relation between normalized P-wave velocity and normalized stiffness slope. 81

Figure 7.18 Local behavior of tested columns showing relation between normalized P-wave velocity and residual strain at specific strain gauge locations. 82

Figure 7.19 Local behavior of column RC2 at applied drift level of 0.75%, comparing computed P-wave velocity obtained from tomogram to stain values measured at locations of specific gauges indicated: (a) tomogram from RC2 at 0.75% drift level, (b) comparison between normalized P-wave velocity and CL gauges, (c) comparison between normalized P-wave velocity and CTRB gauges, and (d) comparison between normalized P-wave velocity and CTRH gauges. 82

Figure 8.1 Finite element model cross-sections: (a) plain concrete, (b) concrete and steel, (c) concrete and defect case 1, and (d) concrete, steel and defect case 1. Input (pink arrow) and receiver (yellow points) positions are indicated..... 85

Figure 8.2 Finite element model cross-sections s showing the location of receiver 1 and ray coverage above and corresponding stacked A-scans below: (a) plain concrete model, (b) concrete, steel and defect case 1, (c) stacked A-scans from receiver 1, and (d) stacked A-scans from receiver 1. 85

Figure 8.3 Comparison of FEM signal data: (a) model cross-sections showing ray path, (b) the obtained signals from the ray path defined in (a), and (c) the enlargement of dashed line box in (b)..... 86

Figure 8.4 The calculation of signal energy from the digitized signal: (a) the defined area under the signal curve, and (b) enlargement of blue dashed line box in (a) presenting peak amplitudes and digitizing errors (dashed line box)..... 88

Figure 8.5 Computed signal energy across all rays (the integral area) for each model: (a) Receiver 1, (b) Receiver 2, (c) Receiver 3, and (d) Receiver 4 (see fig 8.1). 88

Figure 8.6 Computed signal amplitude across all rays for each model: (a) Receiver 1, (b) Receiver 2, (c) Receiver 3, and (d) Receiver 4. 89

Figure 8.7 Illustration of the calculation of the geometric spreading factor: (a) plain concrete model showing input position (pink arrow) and output positions (yellow dots), (b) peak amplitudes from the output data (points) with best fit power curve (line, the inset presents the function of the power line). 90

Figure 8.8 Computed attenuation coefficient across all rays for each model: (a) Receiver 1, (b) Receiver 2, (c) Receiver 3, and (d) Receiver 4. 91

Figure 8.9 Constructed attenuation tomograms: (a) plain concrete, (b) concrete and steel, (c) concrete and defect case 1, and (d) concrete, steel and defect case 1. 92

Figure 8.10 Computed differential attenuation coefficient across all rays for defect and defect-free cases: (a) Receiver 1, (b) Receiver 2, (c) Receiver 3, and (d) Receiver 4. 94

Figure 8.11 Computed differential attenuation coefficient across all rays for rebar and rebar-free cases: (a) Receiver 1, (b) Receiver 2, (c) Receiver 3, and (d) Receiver 4. 95

Figure 8.12 Computed normalized differential tomograms: (a) attenuation difference between CSD1 and CS, (b) velocity difference between CSD1 and CS, (c) attenuation difference between CS and C, (b) velocity difference between CS and C. 95

Figure 8.13 Five selected cross-sections for the concrete column sample including descriptions of the cross-sections. 96

Figure 8.14 Illustration of peak amplitude picking process: (a) stacked A-scans with picked arrivals and peak amplitude, (b) 3-D visualization of the stacked A-scan. 97

Figure 8.15 Computed peak amplitude across all rays from cross-sections 1 to 5: (a) Receiver 1, (b) Receiver 2, (c) Receiver 3, (d) Receiver 4, (e) Receiver 5, (f) Receiver 6, (g) Receiver 7, and (f) Receiver 8. 97

Figure 8.16 Comparison of normalized peak amplitude results among experimental and FEM simulation data for different paths through the concrete column: (a) Receiver 1, (b) Receiver 2, (c) Receiver 3, (d) Receiver 4, (e) Receiver 5, (f) Receiver 6, (g) Receiver 7, and (f) Receiver 8. 98

Figure 8.17 Comparison of the peak amplitude results among non-defect (blue) and defect (red) sections from: (a) Receiver 1, (b) Receiver 2, (c) Receiver 3, (d) Receiver 4, (e) Receiver 5, (f) Receiver 6, (g) Receiver 7, and (f) Receiver 8. 99

Figure 8.18 Differential tomograms using experimental data from the concrete column: (a) tomogram based on the attenuation differentials between sections 1 and 5, (b) tomogram based on the attenuation differentials between sections 1 and 2, (c) tomogram based on the attenuation differentials between section 1 and 3, and (d) tomogram based on the attenuation differentials between section 1 and 4. 100

Figure 9.1 Experimental set-up to test full-scale beam and column connections at the Multi-Axial Subassemblage Testing (MAST) laboratory: (a) illustration of test plan indicating the direction of the cyclic loading, (b) photograph of the experimental set-up. 102

Figure 9.2 Detail of the beam and column connections indicating embedded strain gauges: (a) RC connection, (b) cross-section A-A presented in (a), (c) HP-FRC connection, and (d) cross-section B-B presented in (c). 103

Figure 9.3 Comparison of seismic RC structural design: (a) conventional RC in California and (b) an example of that for HP-FRC (Parra-Montesinos et al. 2005). 103

Figure 9.4 Applied loading protocol where dotted circles indicate instance of ultrasonic scanning tests expressed in terms of applied drift level. 104

Figure 9.5 Detail of ultrasonic scanning tests: (a) grid lines (red lines) indicate e the four lines A through D where ultrasonic scanning tests were performed and (b) the shaded blue box indicates approximate scanned volume position and relative of moving transmitter and eight receivers. The cross-sections for ultrasonic scanning test are identical for both RC and HP-FRC structures..... 105

Figure 9.6 Schematic illustration of ultrasonic scanning test set-up: (a) the front side where receivers were attached and (b) the back side where robotic scanning frame was set up. 106

Figure 9.7 Example photographs from ultrasonic scanning tests: (a) attached receiving sensors on the surface of the connection, (b) robotic scanning frame set-up, (c) air-coupled ultrasonic scanning process, and (d) through-thickness ultrasonic signal data collection. 107

Figure 9.8 Example time signal data from repeated ultrasonic scans on the HP-FRC connection collected from the same position and drift level. 108

Figure 9.9 Stacked A-scan images measured by receiver positions (a) to (h) through section B of the HP-FRC connection at 1% drift level; trial 2. Data are collected under the same conditions as those in Fig. 9.9. Brightness is related to time signal amplitude. 109

Figure 9.10 Stacked A-scan images from different receiver positions (a) to (h) through section B of the HP-FRC connection at 1% drift level; brightness is related to time signal amplitude. Data are collected under the same conditions as those in Fig. 9.9. 109

Figure 9.11 Photographs from the beam and column connections at 0.5% drift level: (a) the front side of RC connection, (b) the back side of RC connection, (c) the front side of HP-FRC connection, and (d) the back side of HP-FRC connection. 111

Figure 9.12 Photographs from the beam and column connections at 1% drift level: (a) the front side of RC connection, (b) the back side of RC connection, (c) the front side of HP-FRC connection, and (d) the back side of HP-FRC connection. 111

Figure 9.13 Photographs from the beam and column connections at 1.75% drift level: (a) the front side of RC connection, (b) the back side of RC connection, (c) the front side of HP-FRC connection, and (d) the back side of HP-FRC connection. 112

Figure 9.14 Digital image correlation images indicating the magnitude of surface strain in the direction of loading on the back side of the connection: (a) RC at 0.5% drift level, (b) HP-FRC connection at 0.5% drift level, (c) RC at 1% drift level, and (d) HP-FRC at 1% drift level; the color scale represents the magnitude of strain in the Y' direction with units of strain percentage. 113

Figure 9.15 Mechanical behavior curves under cyclic loadings up to 1.75% drift level: (a) RC and (b) HP-FRC. 114

Figure 9.16 Stiffness slope as a function of applied drift level. Units of presented stiffness slope values are applied lateral force in the Y' direction in kN per percentage column drift in that direction. 114

Figure 9.17 Residual strain (microstrain) from internal embedded strain gauges as a function of applied drift level: (a) gauges in column at 0.5% drift level, (b) gauges in beam at 0.5% drift level, (c)

gauges in column at 1% drift level, and (d) gauges in beam at 1% drift level. Position of strain gauges shown in Fig. 9.2 115

Figure 9.18 Stacked A-scan images from RC connection obtained by accelerometer 4 at 0% drift level: (a) cross-section A, (b) cross-section B, (c) cross section C, and (d) cross-section D; brightness is related to time signal relative amplitude. Cross-section locations shown in Fig. 9.5. 117

Figure 9.19 Stacked A-scan images from RC connection obtained by accelerometer 4 at 0.5% drift level: (a) cross-section A, (b) cross-section B, (c) cross section C, and (d) cross-section D; brightness is related to time signal relative amplitude. Cross-section locations shown in Fig. 9.5. 117

Figure 9.20 Stacked A-scan images from HP-FRC connection obtained by accelerometer 4 at 0% drift level: (a) cross-section A, (b) cross-section B, (c) cross section C, and (d) cross-section D; brightness is related to time signal relative amplitude. Cross-section locations shown in Fig. 9.5..... 118

Figure 9.21 Stacked A-scan images from HP-FRC connection obtained by accelerometer 4 at 0.5% drift level: (a) cross-section A, (b) cross-section B, (c) cross section C, and (d) cross-section D; brightness is related to time signal relative amplitude. Cross-section locations shown in Fig. 9.5..... 118

Figure 9.22 Stacked A-scan images from HP-FRC connection obtained by accelerometer 4 at 1% drift level: (a) cross-section A, (b) cross-section B, (c) cross section C, and (d) cross-section D; brightness is related to time signal relative amplitude. Cross-section locations shown in Fig. 9.5..... 119

Figure 9.23 Normalized P-wave velocity distribution, expressed in box plot form, as a function of applied drift level: (a) RC and (b) HP-FRC. 120

Figure 9.24 Differential velocity tomograms for RC connections computed from responses at 0% and 5% drift levels: (a) cross-section A, (b) cross-section B, (c) cross-section C, and (d) cross-section D. Yellow dotted line in each image represents the location of beam and column joint interface. 122

Figure 9.25 Differential attenuation tomograms for RC connections computed from responses at 0% and 5% drift levels: (a) cross-section A, (b) cross-section B, (c) cross-section C, and (d) cross-section D. Yellow dotted line in each image represents the location of beam and column joint interface. 123

Figure 9.26 Differential velocity tomograms for HP-FRC connections computed from responses at 0% and 5% drift levels: (a) cross-section A, (b) cross-section B, (c) cross-section C, and (d) cross-section D. Yellow dotted line in each image represents the location of beam and column joint interface. .. 124

Figure 9.27 Differential attenuation tomograms for HP-FRC connections computed from responses at 0% and 5% drift levels: (a) cross-section A, (b) cross-section B, (c) cross-section C, and (d) cross-section D. Yellow dotted line in each image represents the location of beam and column joint interface. .. 125

LIST OF TABLES

Table 3.1 List of tomographic reconstruction algorithms 15

Table 3.2 Material properties applied in the numerical analysis 19

Table 4.1 Acoustic properties for concrete, air, and piezoelectric material 31

Table 4.2 Material properties of concrete mixtures 35

Table 4.3 Practical and technical characteristics of ultrasonic testing configurations 38

Table 7.1 Details of the test specimens and procedures 64

Table 7.2 Information about tomography set-up and maximum computation time 70

Table 8.1 Comparison of arrival times and peak amplitudes for the defined rays. 87

Table 9.1 Details of the test specimens. 102

CHAPTER 1 INTRODUCTION

1.1 Problem statement

The construction of civil infrastructure requires both long periods of time and intensive labor and finance. Therefore, long life cycles are needed, obtained through accurate management with social requirements. Quality control and quality assurance (QC/QA) of infrastructure have become important issues in the construction field. The American Society of Civil Engineers' report card gave America's infrastructure a *D*+ overall in 2013, which represented a total expenditure of 3.6 trillion dollars to improve its quality (ASCE 2013). Because structural inaccuracies and internal defects cause unexpected secondary damage in structures, engineering judgment based on suitable measurements is required. In order to evaluate the condition of a structure, non-destructive testing (NDT) is widely used as an indispensable part of assessments (Naik 2004, ACI 2013). While destructive tests provide direct information with high accuracy, their use on existing structures may damage the aesthetics of the external appearance and also the structural stability, which causes limit number of data acquisition. Therefore, a statistical approach cannot be applied to destructive methods, which limits the ability of engineers to evaluate structures in situ. On the other hand, NDT offers large amount of data measurements and corresponding broad information such as localized internal defects and the overall condition of elements without causing severe damage. Concrete is the most popular material in civil infrastructure, and it is usually used with embedded steel rebar as reinforcement. Although concrete has several benefits such as strength and cost, the material has intrinsic problems such as its durability due to corrosion and alkali-silica reaction (Mindess 2002, Metha 2005). Those chemical reactions induce internal cracking and create further safety issues. On top of that, construction errors such as voiding and honeycombing in concrete may lead to structural instability (ACI 2001). Because deterioration of reinforced concrete (RC) structures may give rise to an unexpected brittle failure, frequent inspections and accurate management are required, preferably without destructive test methods.

1.2 Research objective

The objective of this research is to develop a system for damage evaluation of full-scale steel-reinforced concrete elements using a contactless ultrasonic approach. To achieve this objective, the following tasks were proposed:

1) Development of an effective ultrasonic system for the inspection of full-scale reinforced concrete elements and verification of the system through structural experiments;
2) Investigation of ultrasonic tomography and other wave characteristics associated with internal damage characterization for reinforced concrete structures; and
3) Design of holistic visualization of NDT results for smart structure management/inspection

CHAPTER 2 BACKGROUND INFORMATION

2.1 Mechanical waves

Mechanical waves propagate a physical disturbance through a medium. Unlike electromagnetic waves, mechanical waves transmit through media which possess elasticity and inertia, and transfer its energy to the media. Therefore, the mechanical waves cannot be produced in vacuum. Because the characteristics of the waves are controlled by mechanical properties, wave phenomena have been applied to non-destructive evaluation/tests (NDE/T). Ultrasound is a subset of mechanical waves, which have higher frequencies than the audible limit of human hearing.

2.1.1 Wave propagation in solids

The energy of mechanical waves within the body of a solid is divided into compression (longitudinal or primary wave, P-wave), shear (transverse and secondary wave, S-wave) modes of propagation. The wave mode is defined by the direction of particle motion. While the travel direction of P-wave is the same as the direction of particle motion, S-wave has perpendicular particle motion to the travel direction. P-wave velocity is directly related to Young's modulus in the medium while S-wave velocity to the shear modulus. S-waves are only produced in solid media. In addition, the waves can be guided by the geometrical boundary in solids, and different modes of propagation are defined, such as surface-guided waves (Rayleigh wave, R-wave) and plate waves (Lamb wave).

Acoustic impedance plays an important role in wave propagation through multi-phased media. The ultrasonic wave is reflected and transmitted at the interface between two different materials. Each material has an acoustic impedance Z, which is calculated in the case of P-wave propagation by

$$Z = \rho V_P \tag{2.1}$$

where V_P is P-wave velocity and ρ is density of the material. Based on the relationship of the acoustic impedance between two different materials, amplitude transmission and reflection coefficients, in the case of waves that are normally incident on the interface, are defined by

$$T = \frac{A_T}{A_i} = 1 + \frac{Z_2 - Z_1}{Z_2 + Z_1} \tag{2.2}$$

$$R = \frac{A_R}{A_i} = \frac{Z_2 - Z_1}{Z_2 + Z_1} \tag{2.3}$$

where Z_1 and Z_2 are the acoustic impedances of the material on the near and far side of the interfaces respectively, and A_T, A_R and A_i are the amplitude of the transmitted, reflected and incident waves,

respectively.

If waves propagate across an interface between two different media at a certain angle, more complicated angular reflection and refraction are set up. The phenomenon is described by Snell's law,

$$\frac{\sin\theta_1}{V_1} = \frac{\sin\theta_2}{V_2} = constant \tag{2.4}$$

where θ_1 and θ_2 are incident and refracted angles measured from the normal to the boundary, and $V_1$and $V_2$are velocity of waves in each medium. This equation quantifies the direction of transmitted waves in medium.

2.1.2 Mathematics

The propagation behavior of waves are well represented by the wave equation, which is a hyperbolic partial differential equation. In the case of one-dimensional wave propagation, the wave equation is expressed by

$$\frac{\partial^2\varphi}{\partial x^2} = \frac{1}{c(x)^2}\frac{\partial^2\varphi}{\partial t^2} \tag{2.5}$$

where t is time, φ is a scalar potential that is a function of x and t, and c represents wave speed at position x. In homogeneous media, wave speed is constant. The wave equation has a remarkable general solution called the D'Alembert solution

$$\varphi(x,t) = f(x-ct) + g(x+ct) \tag{2.6}$$

where f and g are arbitrary, twice-differentiable functions. The signs of the arbitrary functions indicate that two modes of wave propagate in opposites direction with velocity c. Solutions to the wave equation become complicated when the influence of both nonhomogeneous boundary conditions and forcing terms are considered. For example, wave propagation in elastic solids is mathematically derived based on constitutive laws and boundary conditions. Generally, solutions at certain spatial position are needed that are set up by a known forcing function. Among many mathematical solution methods for the wave equation, such as the method of separation of variables, the Green's function method is a powerful technique because the solution is directly derived from the constructed wave equation using spatial and time Fourier transforms and the complex residue theorem. The solution is represented in the form of convolution

$$\varphi(x,t) = \iint G(x,t;x_0,t_0)F(x_0,t_0)dx_0dt_0 \tag{2.7}$$

where x_0 and t_0 are position and time the source acts and G and F are the Green's function and forcing function, respectively.

2.1.3 Ray tracing methods

In heterogeneous media the direction of wave propagation is affected by variable velocity among the various solid phases, and thus the wave may not propagate along a straight ray path line. Generally, the actual ray path of a wave should be defined in order to image the medium through which the wave travels. Generally, two famous principles, Fermat's principle and Huygens' principle, are used to trace the ray path. Fermat's principle states that the ray path between any two points A and B is the one defined by the lowest composite travel time of the wave, and the first variation of the travel time along the path between two fixed points A and B vanishes

$$\delta \int_A^B \frac{1}{v} ds = 0 \tag{2.8}$$

where v is the wave velocity at the corresponding point in the medium, δ is the functional derivative and ds is an infinitesimal displacement along the ray. Huygens' principle states that any point reached by a wave front is considered, from that instant, as a point source of another wave. Although the principles originate from different bases, it is demonstrated that the two statements are mathematically equivalent in the case of ray path estimation (De Witte 1959).

In geophysical imaging, ray tracing is applied to enhance the accuracy of a reconstructed image. The two principles, Fermat's principle and Huygens' principle, form the basis of conventional ray tracing methods in tomography. During tomographic computation, the ray tracing methods repeat the calculation of the time residual between two points to be set to zero (Fermat's principle) or iterate the new position of wave front from a given velocity field (Huygens' principle). Therefore, the methods are computationally intensive, especially for large data sets (Joulian and Gubbins 1977).

More recently, the Eikonal equation has been applied to estimate the arrival time in a given velocity field without concerns about computation effort (Sethian and Vladimirsky 2000, Zhao et al. 2006, Hassouna and Farag 2007). From the asymptotic expansion (WKB approximation) of the wave equation (Eqn. 2.5), the first order term represents the Eikonal equation

$$\left(\frac{\partial T}{\partial x}\right)^2 = \frac{1}{c(x)^2} \tag{2.9}$$

where T is wave front or arrival time of wave. The Eikonal equation represents the relation between the direction of the wave and the velocity field in medium. The physical implication of the equation implies

that the gradient of wave front specifies the ray path in the medium. The Finite Difference method has been used for the solution of the Eikonal equation T, and the estimated ray path is adopted in tomographic imaging.

Ray tracing methods give the correction of ray path inside the object during tomographic imaging; however, overall procedure of tomography can be computationally expensive. Furthermore, the given velocity model is needed for some of the methods, which may not be practical in the field. In tomographic reconstruction, the straight ray-path approximation is generally acceptable under the condition of less than 10 percent of wave velocity contrast among material phases within in the object (Jackson and Tweeton 1994). In the case of heterogeneous materials that have velocity contrast from 10 to 50 percent, the straight ray path may be acceptable, depending on the requirement of the user (Tweeton et al. 1992). If the velocity difference between two media is more than 50 percent, the straight ray approximation becomes inaccurate and the tracing methods are required to compute the correct the curved ray path.

2.2 Non-destructive tests using mechanical waves

Various NDE/T methods such as X-ray, infrared thermography, and ground penetration radar (GPR) have been applied to the civil infrastructure. Each method is based on different underlying phenomena, such as penetrating radiation, heat flow, and electromagnetic wave propagation, respectively. Although the methods provide internal information of the object, each method has limits: 1) X-ray is dangerous and difficult to apply to field infrastructure in use, 2) Infrared thermography is affected by the weather and daylight exposure, and 3) GPR is affected by di-electric and electrical properties of material, and not mechanical properties. The significant drawbacks of the methods sometimes make them unpractical or ineffective for providing information about full-scale infrastructure (Naik et al. 2004). Mechanical wave-based methods, such as ultrasound or seismic wave propagation, are directly related to the mechanical properties of the material, and the energy source is not a harmful to humans. Therefore, mechanical waves show great potential for evaluating the properties of civil infrastructures in situ.

Concrete is the most broadly used building material in the world. Because concrete is a highly heterogeneous material that includes complex microstructures and different sizes of aggregate, mechanical waves with high frequency are attenuated and scattered inside the medium. For concrete NDE/T, the wavelength of mechanical waves should be large enough to avoid wave scattering. Less than 100 kHz is usually recommended to avoid the scattering with the assumption of maximum aggregate size as 1 in. (Popovics et al. 2000).

2.2.1 Ultrasonic pulse velocity (UPV)

Ultrasonic pulse velocity (UPV) is one of the most widely applied NDT/E techniques to concrete structures. The travel time of a P-wave pulse is measured through the thickness of a concrete specimen, and the velocity of the ultrasound is computed from the measurement, which is typically 3700 to 4200 m/s for ordinary concrete (Naik et al. 2004). Since the velocity of ultrasound in air is 343m/s, which is much lower than that in solid concrete, low-strength or damaged concrete usually exhibits lower ultrasound velocity. By theory, the velocity is determined by material properties such as density and the elastic modulus, so that a relationship between strength and velocity can be only indirectly estimated (Krautkramer and Krautkramer 1990, Kewalramani and Gupta 2006). Although UPV is a simple and effective operation for finding cracks and voids inside concrete, it has several limitations regarding its use in the field. UPV cannot provide information on the depth of a flaw nor detect cracks parallel to the wave path. Furthermore, data acquisition of UPV requires two-sided access on the structure and a coupling process between transducers and the surface of the concrete. Surface preparation such as grinding is sometimes required when the surface of concrete is rough, and a gel-type couplant is needed to reduce the acoustic impedance mismatch between sensor and material. This coupling process is time-consuming and labor intensive, thus the application on full-scale concrete structure is limited (Long 2010, Hall 2011).

2.2.2 Seismic tests: SASW, MASW and Impact-echo

Spectral analysis of surface waves (SASW) method was originally designed to determine the thickness and elastic stiffness of pavements and other layered structures (Jones 1955). An R-wave is generated by an impactor or a vibrator, and then measured by two aligned receivers. A dispersion curve with respect to phase velocity and the wavelength is calculated based on each travel time of various frequency components between the two sensors (Jones 1962). The dispersion curve shows information about the thickness and elastic constants of layered structures, estimated by an inversion process (Nazarian and Stokoe 1986). Multichannel analysis of surface waves (MASW) method was developed to increase the speed and the accuracy of SASW, using automatic data acquisition and analysis with linearly placed receivers (Gabriels et al. 1987). Impact-echo (IE) is a vibration based method applied to concrete structures for slab depth or delamination defect detection (Pratt and Sansalone 1992, Lu et al. 2007). The IE technique has been effectively deployed using an air-coupled receiver and recent research demonstrate the accuracy of the method for evaluating internal flaws in concrete slabs (Oh 2012).

2.2.3 Air-coupled ultrasonics

More recently, contactless ultrasonic methods have been applied for the evaluation of concrete elements. Air-coupled transducers and laser interferometers have been used to measure leaky R-waves in concrete without physical contact on the surface (Chekroun et al. 2009, Abraham et al. 2012). Contactless ultrasonic systems provide faster data acquisition from large concrete structures. The fully contactless ultrasonic

surface wave method requires access to only one side of the tested object, which is a significant advantage for the application to concrete structures in situ. The air-coupled test configurations were applied to concrete structures in various forms. The test set-up of the impact-echo was improved using contactless receivers so that fast data measurements can be performed (Zhu 2005, Oh 2012). Micro-electro-mechanical systems (MEMs) are applied to multiple receiver arrays for identifying internal defects of concrete slab or rail ties (Ham and Popovics 2015). The air-coupled test configuration is also applied for monitoring setting and hardening process in fresh concrete (Choi et al. 2016).

2.3 Signal processing

Data acquisition in experiments can face a challenge of obtaining high-quality signals. Especially in inhomogeneous media, it can be difficult to measure low-noise signals. Signal processing is an effective way to improve the quality of data during or after the measurement, minimizing the distortion of the original signal.

2.3.1 Basic signal processing

The time averaging process can dramatically increase the signal to noise ratio (SNR) without complicated procedures (Centrangolo and Popovics 2010). The technique assumes the noise content is a random fluctuation. The time signals are measured at the same position during certain period and averaged over the period. The procedure erases the random noise components from the obtained signal. Generally, the time-averaging over longer time period improves SNR of the signal. However, the set-up of the time period totally depends on the testing environment because the noise contents from the signals are variable in every experiment. Therefore, an ideal period (or number) of time averaging can be decided by the experimental efforts. Based on experimental data, the details of SNR and the number of time averaging are discussed in Chapter 4.

After signal data are collected, digital signal processing (finite impulse response filtering, FIR filtering) is helpful to attenuate a noise level of signals or otherwise improve signals. The digital filtering attenuates selected frequency components from the signals. The function, *filtfilt*, in Matlab performs zero-phase filtering without signal phase distortion in time domain. The start, end, and stop frequencies and the level of attenuation are options. It is noted that signal processing techniques significantly improve the quality of the original signal; however, inappropriate filtering distorts the original signals and makes false results.

2.3.2 Automated arrival picking algorithms

The very first wave arrivals (P-waves) in time signals should be identified to determine P-wave velocity. Even if good quality signal data are acquired, however, it may be difficult to define that first arrival in the

digitized signal because the amplitude of the first peak of the waves can be low, similar to noise levels. On top of that, the large amount of data makes the arrival-picking procedure tedious. Several auto-picking algorithms, such as the Akaike information criterion (AIC), Hinkley criterion (HIC), and noise-threshold criterion have been established to define the wave front arrival (Carpinteri et al. 2012, Hu et al. 2013, King 2012). The AIC method is based on iterative statistical analysis of a waveform and is given by

$$\mathrm{AIC}(t_w) = t_w \log(var(Sig_w[1, t_w])) + (N - t_w - 1)\log(var(Sig_w[1 + t_w, N])) \qquad (2.10)$$

where t_w is range through all time of the portion of the time signal Sig_w, and N is the last index of the windowed time series. The minimum of calculated AIC values indicates the first arrival in the signal. The HIC method is based on the processed partial energy of the signal as presented by

$$S_i' = S_i - i\frac{S_N}{\alpha N} = \sum_{k=1}^{i} x_k^2 - i\sum_{k=1}^{N}\frac{x_k^2}{\alpha N} \qquad (2.11)$$

where S_i' is the processed partial energy, S_i is the partial energy, S_N is the total energy of the signal, x_k is the amplitude of the signal at k-th sample, and α is the trend parameter that ranges in value between 5 to 20. Similar to the AIC method, the minimum of the processed partial energy indicates the first arrival in the signal. Both methods work efficiently in the case of signals with high SNR. However, the results are not stable if the amplitude of the first arrival is similar to that of noise content. In that case, the two methods incorrectly define the first arrival as the second cycle of the signal, even if the arrivals of the signal are visually distinguished.

Recently, a statistically defined threshold method has been proposed and applied to wave analysis (King 2012). The amplitude of the noise content is assumed to have a Gaussian distribution and the standard deviations from the mean of that distribution can be assigned, which corresponds a level of the threshold. With a selected level of the threshold from the entire data set, the first arrival time in the signal is defined if the amplitude of the signal is beyond the threshold. Because the algorithm statistically selects a threshold value based on an amplitude level of noise content from the entire measurements, the arrival picking procedures are more stable than individual-signal-based AIC and HIC.

2.4 Ultrasonic image reconstruction algorithms

Several image reconstruction techniques have been applied for NDE/T of concrete structures based on ultrasonic wave data. The imaging techniques are mainly divided by the measurement set-up. The synthetic aperture focusing technique (SAFT) and reverse time migration (RTM) use one-sided measurements, while

filtered back-projection (FBP) and the algebraic reconstruction technique (ART) use two-sided measurements.

2.4.1 Synthetic aperture focusing technique (SAFT)

Recently developed dry-point contact transducers improve the physical coupling process between ultrasonic transducers and concrete surface. The tip of the dry-coupled transducers vibrates horizontally onto the concrete surface and generates shear-horizontal waves. This technique is commercially available as called, *Mira*, which uses the transducer array and increases lateral resolution of measurements. The system can be effectively applied to full-scale concrete structures and it identifies the location of grouting faults and internal air void using Synthetic aperture focusing technique (SAFT) (Shevaldykin et al. 2003, De La Haza et al. 2013).

The synthetic aperture focusing technique (SAFT) was developed to improve the insufficient lateral resolution of reflected ultrasonic pulse-echo data. Because concrete is heterogeneous at the large scale, ultrasound is scattered and promotes structural noise in the signal. Thus it may be difficult to present meaningful results using conventional time signals (A-scan) or laterally or vertically stacked time signals (B-scan or C-scan). SAFT provides numerical superposition of reflected signals through the concept of synthetic focus. Measured signals are focused, through signal post-processing to every pixel in a reconstructed image. As a result, the SNR of the image increases because of spatial superposition (Schickert et al. 2003). However, SAFT is known to have insensitivity to the presence of boundaries or objects far away from the tested surface, and also to steeply dipping interfaces because the energy of the waves is attenuated by the geometry and the reflections do not travel back to the sensor at the surface (Muller et al. 2012). More detail on imaging procedures is discussed in Chapter 5.

2.4.2 Reverse time migration (RTM)

Reverse time migration (RTM) originates from the seismic imaging community. RTM has a similar data measurement procedure as SAFT' only one-sided data are needed. However, RTM overcomes some drawbacks of SAFT. RTM uses the superposition between an analytically produced wave field and measured experimental data. Because the algorithm considers the entire wave field with multiple reflections, as opposed to SAFT which considers the intensity of the first reflection, it is possible to detect deeply embedded defects and complicated geometry such as deeply dipping surfaces (Wang and Yuan 2005, Muller et al. 2012). However, the measurements of multiple reflections from full-scale concrete structures are time-consuming. Also, the required pre-processing needed for analytical wave field generation is computationally intensive, especially for large-scale structures in the field.

2.4.3 Filtered back-projection (FBP)

Tomography is an imaging technique that produces a cross-sectional image of an object using the information from penetrating waves through the object. Since Johann Radon suggested the mathematical solution to reconstruct the internal images from projections in 1917, efficient tomographic algorithms have been developed (Kak and Slaney 1988). Radon transform assumes that projections are formed by stacked line integrals, and the object can be reconstructed by projections measured from multiple angles P_θ,

$$P_\theta = \int_{-\infty}^{\infty}\int_{-\infty}^{\infty} f(x,y)\delta(x\cos\theta + y\sin\theta - k)dxdy \tag{2.12}$$

where $f(x,y)$ is an image of the object in the space domain, θ is an angle of projection, δ is the Dirac delta function, and k is a line parameter that represents a projection axis. Based on the theory, an image is reconstructed by an explicit form of inverse Radon transform. Although the inverse Radon transform illustrates a mathematical solution for reconstruction of the object, the inversion process also produces noise based on the quality of measurement data. The relationship between the Radon transform and the Fourier transform is investigated (Fourier slice theorem), and the connection makes a better use of reconstruction theory. In Fourier domain, the two-dimensional function, P_θ is projected onto a one-dimensional line, and the set of lines (or projections) can be inversely transformed to the image. The algorithm is known as filtered back-projection (FBP), and is defined by

$$f(x,y) = \int_{-\infty}^{\infty}\int_{-\infty}^{\infty} F(u,v)e^{i2\pi(ux+vy)}dudv \tag{2.13}$$

where $F(u,v)$ is a combination of projections in frequency domain. Since the algorithm is based on a mathematically stable transform, the computational process is very effective, and commercial software like Matlab supports the function, for example through the *iradon* subroutine. Therefore, it has been widely used in computed tomography (CT) and magnetic resonance imaging (MRI) medical imaging (Shepp and Logan 1974). However, the concept of a line integral assumes a straight ray path from a source to receivers, and thus it may not be appropriate for a diffracted wave, such as those encountered with ultrasound in heterogeneous material (Kak and Slaney 1988). Furthermore, the algorithm requires multiple projections through the object across continuously varying angles. In the case of civil infrastructure, it is difficult to collect the multiple projections across continuous angles.

2.4.4 Algebraic reconstruction technique (ART)

The algebraic reconstruction technique (ART), which was introduced in 1937, is one of the most popular algorithms for tomography (Kaczmarz 1937). The method is also known as Kaczmarz's method, which has been applied to computer tomography and medical imaging (Hounsfield 1973, Herman 2009, Natterer

2001). The algorithm is based on the linear equations

$$\mathrm{Ax} = \mathrm{b} \tag{2.14}$$

where x represents pixel values of a tomographic image, A is the matrix of weight factors of the penetrating ray at pixel x, and b is the ray-sum measured from the experiment. It is noted that the matrix A may be sparse because only a small number of pixels is affected by the given ray-sum.

In the hyperplane, the concept of the iterative method is illustrated in fig 2.1, where two variables x_1 and x_2 satisfies Eqn. 2.14. First, ART starts from an initial estimation of pixel values. Then, a normal vector, $\overrightarrow{dx}$ can be defined based on given information. The vector represents a residual between initial estimation and the nearest ray, and it can be re-defined in the next iteration. ART iterates the sum of the residuals until the residual becomes less than the assigned threshold level closed to zero. The first estimation affects overall duration of the computation. Also, the design of the linear equation is flexible because any measurement variable can be defined as the intensity of pixels based on wave phenomenon. Unlike FBP, where the Fourier transform generates undefined intensities as a result of the imaging, we can define the physical meaning of pixels using ART. However, the algorithm is computationally intensive compared to FBP (Guan and Gordon 1994).

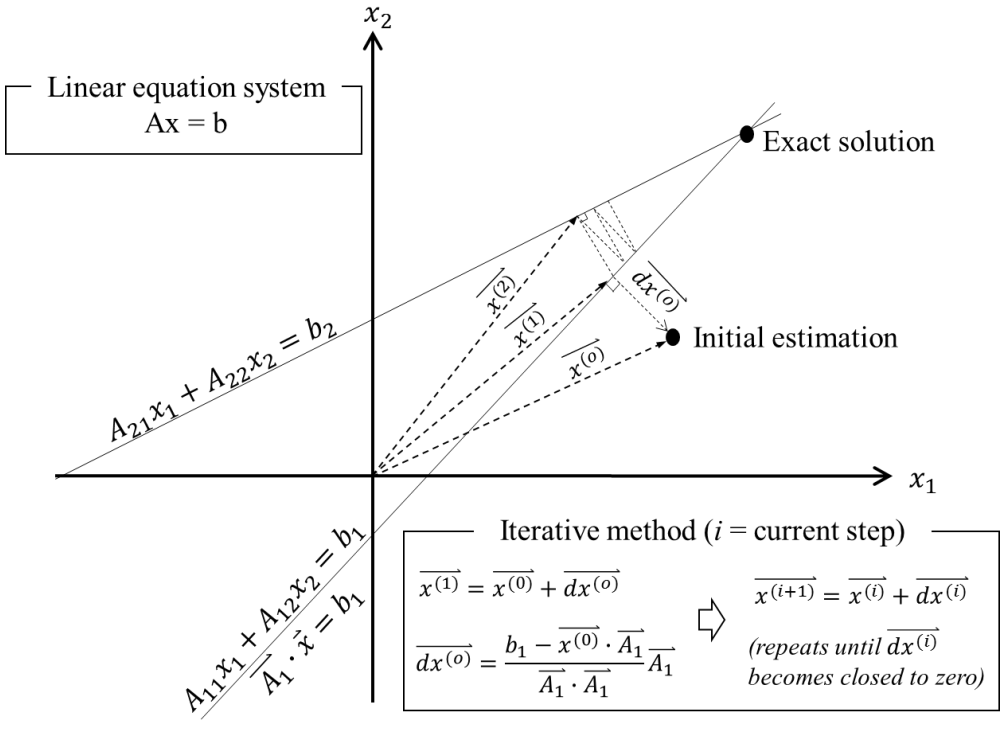

Figure 2.1 Schematic illustration of ART (adopted from Kak 1988).

Recently, the algebraic reconstruction technique has been applied to concrete structures (Chai et al. 2011, Aggelis 2013). Those research efforts show that the ART method can be used to reconstruct cross-sectional images from concrete specimens and embedded defects are visually detected. However, the applications are restricted to small-sized concrete elements without rebar, which is not realistic of structures in the field. The application of velocity and attenuation tomography using ART to full-scale RC structures are discussed in Chapter 3 and Chapter 9, respectively.

2.5 Digital image reconstruction methods

With the development of digital camera technology, digital images have been applied to various research fields including the civil engineering. Digital images benefit from several aspects of application to full-scale civil infrastructure such as contactless data measurement procedure and a visual-aid output.

2.5.1 Digital image correlation (DIC)

Digital image correlation (DIC) exploits changes among a set of digital images to determine external deformation and strain. Using the concept of cross-correlation, the DIC tracks the features in the image and performs deformation mapping. The DIC significantly improves data acquisition procedure compared to conventional sensor-based measurement systems. Furthermore, the advantage of the DIC is to capture the realistic motion of the object under loading. The method has been applied to concrete structures to analyze the deformation structural elements and failure pattern during a loading test (Dutton et al. 2014).

2.5.2 Structure from motion (SfM)

Structure from motion (SfM) is an effective way to reconstruct three-dimensional structures from two-dimensional images. The SfM provides the three-dimensional perspectives of the object in virtual environment. First, scale-invariant feature transform (SIFT) automatically detects and tracks overlapped points from several digital images, and matches the features among the set of images. Then, a strong initial pair of images are picked (two-frame SfM) and the pose of the camera is estimated. More images are added onto the procedure and three-dimensional point clouds are created in the virtual environment (bundle adjustment). Because the procedure is totally automated and uses only conventional digital images, the method is highly efficient to monitor the large-scale structure in the field. Recently, the technique has been applied to construction management (CM) and building information modeling (BIM) (Golparvar-Fard et al. 2011). This automated vision-based method is also used to evaluate the energy performance of buildings in three-dimensional viewpoint (Ham and Golparvar-Fard 2013, Ham and Golparvar-Fard 2013).

CHAPTER 3 EVALUATION OF TOMOGRAPHY ALGORITHMS

In this chapter, the algebraic reconstruction technique (ART) is evaluated for tomographic reconstruction using synthetically and numerically simulated data. A total of nine iterative solvers and three auto-picking algorithms are tested and the details of tomographic procedure for full-scale RC elements are described. The selected optimal tomographic procedure is applied to experimental data presented in the following chapters. Based on the evaluation, Kaczmarz's method and randomized Kaczmarz method show minimum error among the iterative solvers, and the noise-threshold method offers the most stable auto-picking procedure for digitized signals. Results shown in this chapter also demonstrate the potential for internal defect (or damage) detection in concrete using ultrasonic velocity tomography.

3.1 Evaluation with synthetic data

Several iterative solvers for tomography were first evaluated with synthetic data. With tomography it is possible to reconstruct an internal slice from an object with a full set of projections; however, full-scale reinforced concrete (RC) structures offer limited access for data acquisition. Mechanical waves (e.g., ultrasound) also suffer from high levels of scattering and attenuation in concrete. Therefore, the excitation and sensing of the waves are limited and a sufficiently complete set of projections is extremely difficult to obtain. The application of tomography to RC structures thus often begins with an insufficient data set and as such the results may have significant errors compared to the original object. In order to verify and minimize possible errors, a synthetic data set that simulates an RC cross-section was generated and each iterative solver was evaluated.

3.1.1 Linear equations for velocity tomography and iterative solvers

Linear equations for velocity tomography are constructed from the arrival time of waves travelling along a ray that cross pixels within the medium. The arrival time set $t_i$is given by

$$t_i = \sum_{j=1}^{M} d_{ij} p_j \ \ (\mathrm{i} = 1 \sim \mathrm{N}) \tag{3.1}$$

where d_{ij} is the distance traveled by ray i in pixel j, p is slowness or inverse velocity, t_i is arrival time of wave by ray i, and N and M are the number of measurements and pixels, respectively. In matrix form, equation 3.1 is presented by

$$\mathbf{T} = \mathbf{DP} \tag{3.2}$$

where the bold faced font symbol represents a matrix. The resulting velocity tomogram is the solution to the slowness matrix **P** using known information from the measured arrival time matrix **T** along path length

matrix **D**. We see that path length matrix **D** has many singularities, as each index of the matrix only represents ray path length in one pixel corresponding to the assigned ray, as illustrated by Fig 3.1. For example, consider a ray that transmits from the 12th pixel to 121th pixel, as illustrated in Fig 3.1. The path length matrix indices corresponding to that ray, $\boldsymbol{D_{1j}}$ have only a few non-zero values (indicated by shadowed color) among the entire image domain. Therefore, **D** is sparse and it may not be possible to solve the set of linear equations with conventional matrix inversion.

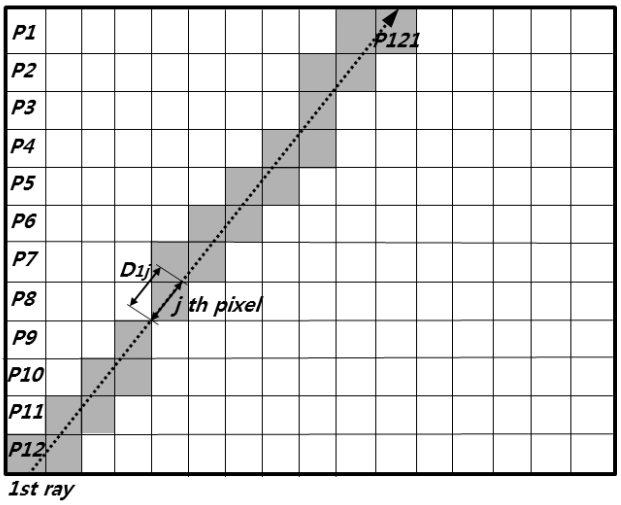

Figure 3.1 Example of ray contribution to pixels.

Iterative matrix inversion solution, known as the algebraic reconstruction technique (Kaczmarz 1937), can be applied when conventional matrix solution procedures are not sufficient. The iterative solver updates the residual of time, and the iteration continues until the calculated slowness vector, which represents the values of all pixels, converges to a solution with minimal error. The iterative reconstruction starts from an initial estimate of slowness, $\mathbf{P'}$. The temporary predicted time of flight, T′, is calculated by

$$\mathbf{T'} = \mathbf{D}\boldsymbol{P'}. \tag{3.3}$$

The calculated residual error from the measurements, dT′, is computed by

$$\mathbf{dT'} = \boldsymbol{T} - \mathbf{T'}. \tag{3.4}$$

The calculated time residual is substituted into a back-projection equation

$$\boldsymbol{dP'} = \boldsymbol{dT'}\frac{\boldsymbol{D}}{row(\boldsymbol{D})^2} \tag{3.5}$$

where $\boldsymbol{dP'}$ is a slowness residual and the function *row(**D**)* represents each row of matrix **D** corresponding

to a particular ray path. The name "back-projection" originates from the representation of the linear equations in the hyperplane, indicating that **dP′** is a normal vector to the measurement line (Kak and Slaney 1988). The concept of the normal vector in the hyperplane is illustrated in Chapter 2 (Fig 2.1). Among several measurement lines in the hyperplane, **dP′** is projected onto the lines and becomes smaller as it approaches the solution. The iterative solver updates the back-projection for the next step by

$$\boldsymbol{P''} = \boldsymbol{P'} + \boldsymbol{dP'} \tag{3.6}$$

where **P′′** is the next iterative estimation of the slowness field. The process is repeated until **dP′** converges with the assigned threshold error. In the iterative process, the initial estimation of slowness is an important factor in controlling total computation time and accuracy. The average of slowness across all pixels from the measurements is typically used for the initial estimation in velocity tomography.

Iterative solution methods can be divided into two technique types, based on the updating procedure of the back-projection used: algebraic reconstruction techniques (ART) and simultaneous iterative reconstruction techniques (SIRT). While ART updates the back-projection to a new measurement for each iteration, SIRT updates the residual after considering all corrections of N measurements. Many studies have been carried out to analyze iterative solvers. AIR tools (algebraic iterative reconstruction) is an open package of several tomographic algorithms, including ART and SIRT, coded in the Matlab platform (Hansen and Saxild-HansenM 2012). In this work, several inversion techniques were evaluated using synthetic model arrival time data that simulates and RC cross-section: the studied methods include Kaczmarz's method coded by the author, algorithms from AIR tools, and least square functions from Matlab. All inversion methods considered in this work are listed in Table 3.1.

Table 3.1 List of tomographic reconstruction algorithms.

Method	Type (provider)
Kaczmarz's method	ART (coded by the author)
Randomized Kaczmarz (rKaczmarz) method	ART (AIR tools)
Symmetric Kaczmarz (sKaczmarz) method	ART (AIR tools)
Component averaging (CAV) method	SIRT (AIR tools)
Cimmino's method	SIRT (AIR tools)
Diagonally relaxed orthogonal projection (DROP) method	SIRT (AIR tools)
Landweber's method	SIRT (AIR tools)
Simultaneous algebraic reconstruction technique (SART)	ART and SIRT (AIR tools)
Least square method (LSQR)	Pseudoinverse (Matlab)

3.1.2 Synthetic data analysis

In order to evaluate each iterative algorithm, synthetic data (**Ps**) are generated. **Ps** is a set of slowness profiles from an ideal simulated model shown in Fig 3.2. The model simulates a cross-section of reinforced concrete column, including embedded reinforcing bar, concrete, and defects. Each medium has different wave velocity (or slowness) values ranging from 343 m/s to 5000 m/s. The N by M matrix, **D**, is generated based on the hybrid/air-coupled ultrasonic test configuration and the number of pixels. The number of measurements, N, is set to 2,560 based on all possible positions of 320 sources and 8 receivers, while the number of pixels in the image, M, varies to include 900, 1,600 and 2,500. The two known matrices, **Ps** and **D**, are substituted in equation 3.2 and a matrix, **T** is calculated. Then, the iterative algorithms are applied to **T** and **D** for reconstruction of **Ps′**. Since the matrix, **T**, includes a limited set of measurements, the reconstructed **Ps′** may have errors compared to the original known data, **Ps**.

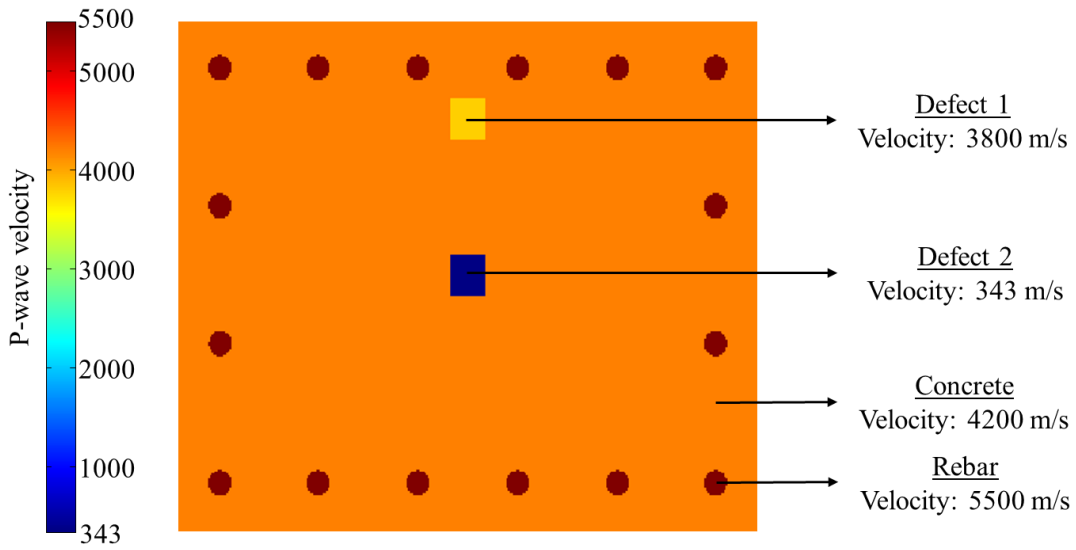

Figure 3.2 Synthetic data model showing P-wave velocity profiles.

The iterative algorithms were evaluated based on the error percentage of predicted slowness values with respect to the original synthetic data

$$\text{error } (\%) = \frac{\boldsymbol{P_s} - \boldsymbol{P'_s}}{\boldsymbol{P_s}} \times 100. \tag{3.7}$$

Figure 3.3 presents the error percentage per each iterative algorithm. The maximum iteration of each algorithm was set to 10,000 and the solution was identified when the back-projection, **dP′**, is the smallest among the iterations. The initial estimation was the average of slowness from the synthetic data across all pixel values.

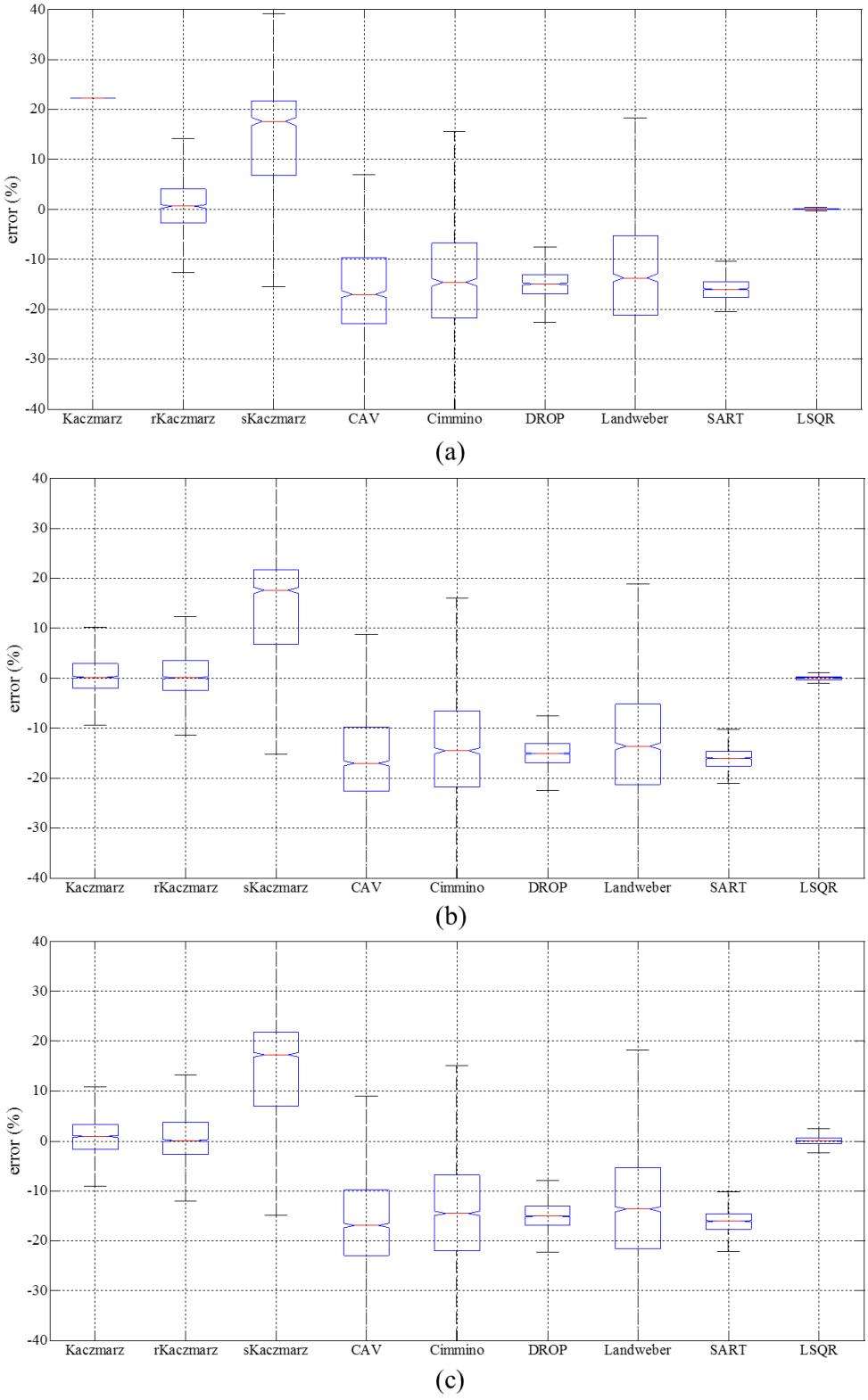

Figure 3.3 Error percentage of reconstructed slowness profiles from each iterative solver: (a) 900 pixels, (b) 1,600 pixels, and (c) 2,500 pixels.

The results show that the least square method shows the minimum error in all cases. However, the method can be disrupted by noise content, which will be addressed in next section. Among the iterative solvers excluding the least square method, ART methods generally overestimated the solution, while SIRT methods underestimated the solution and with higher variance. Kaczmarz's method and Randomized Kaczmarz's method yielded the best results, within ± 10 percentage error. It should also be noted that Randomized Kaczmarz's method was stable even with limited numbers of assigned pixels, while Kaczmarz's method overestimated the solution when pixel density is limited.

3.2 Evaluation with numerical data

Wave propagation behavior in typical RC cross-sections was simulated numerically. The simulation results were used to simulate the experimental test configuration and also to evaluate the tomographic procedure, to evaluate ancillary processes associated with the test procedure, such as signal auto-picking algorithms, and to understand mechanical wave propagation behavior in reinforced concrete elements more deeply. In this numerical simulation, HYPERMESH was used for modeling, meshing, and analysis while ABAQUS was used as the numerical solver.

3.2.1 Finite element model development

Four different simulated cross-sections are presented in Fig 3.4. The simulated models include plain concrete (C); concrete and steel (CS); and concrete, steel and defects (CSD1 and CSD2). In the models, all media were assumed to be homogeneous within a single phase, including concrete, steel, and defects. A triangular mesh was applied to the model with 2.5 mm size, which is about 32 times smaller than the applied P-wave wavelength which is 81.2 mm in concrete. The input force was a 16-cycle damped pulse with a center frequency of 50 kHz as shown in Fig 3.5. The assumed material properties are presented in Table 3.2. To simulate the hybrid/air-coupled ultrasonic test configuration, individual input point sources were applied sequentially to 327 individual locations along the top surface of the simulation; source position 1 and 327 are located at 48.45 mm apart from the corner with a spacing of 2.5 mm between intermediate source point positions. On the opposite surface of the simulation model, the accelerations (Y2-direction) from 8 receiver positions, shown by yellow points in Fig. 3.4(a), were obtained. The sampling rate for output signals was 1 MS/s.

Table 3.2 Material properties applied in the numerical analysis.

Materials (color presented in Fig 3.4)	Density (kg/m^3)	Young's modulus (MPa)	Poisson ratio	P-wave velocity (m/s)	50 kHz wavelength (mm)
Concrete (gray)	2,400	35,570	0.2	4,058	81.2
Steel (green)	8,000	200,000	0.3	5,875	117.5
Defect1 (blue)	0.001	0.142	0	377	7.5
Defect2 (red)	2,400	28,456	0.2	3630	72.6

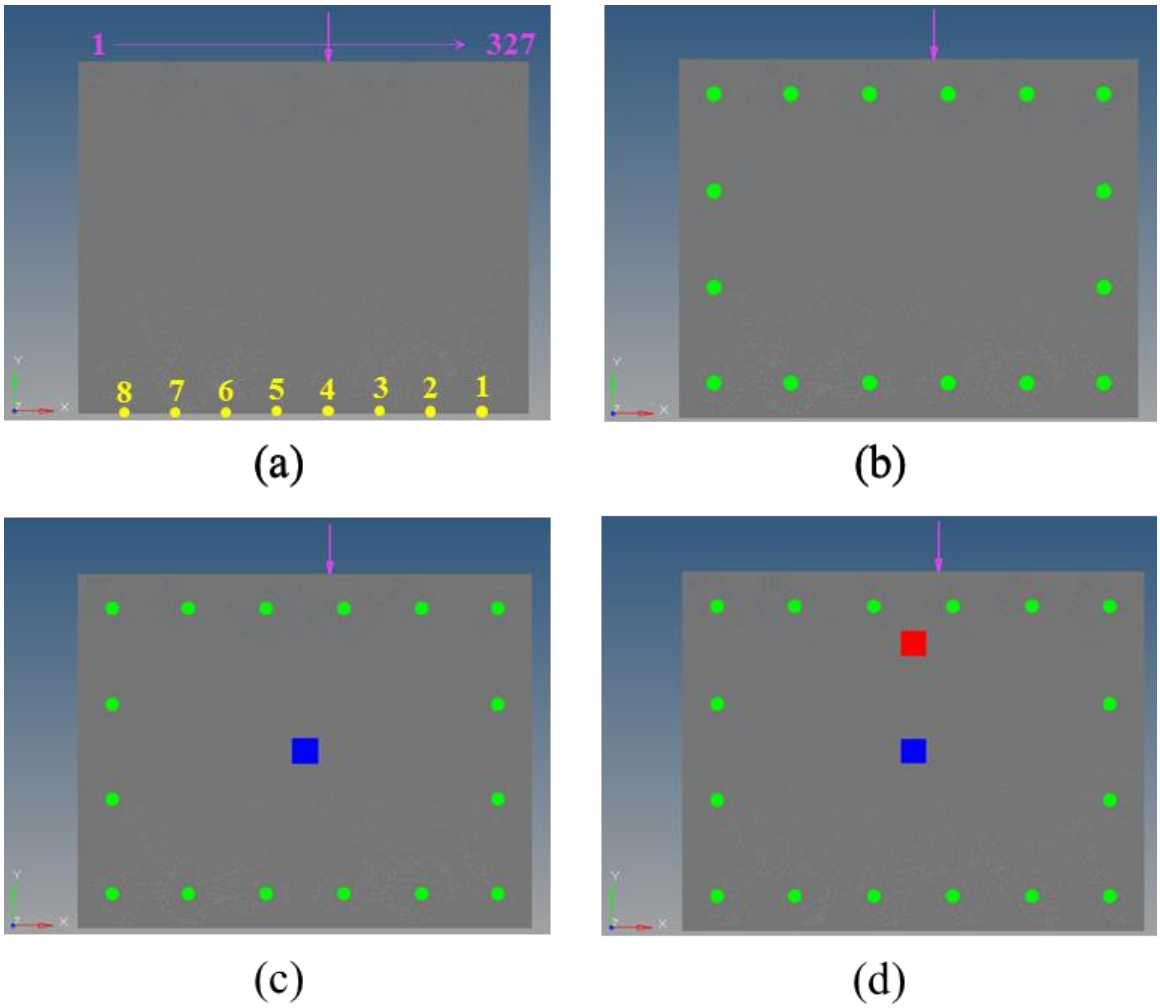

Figure 3.4 Cross-sectional models showing input (pink arrow) and receiver (yellow points) positions: (a) plain concrete, (b) concrete and steel, (c) concrete, steel and defect case 1, and (d) concrete, steel and defect case 2.

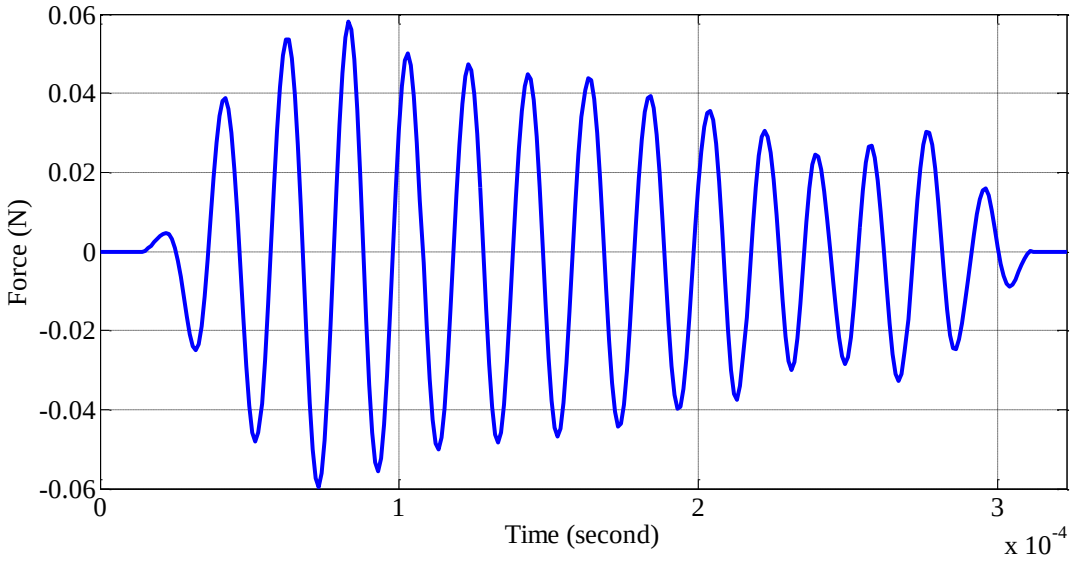

Figure 3.5 Input force representing ultrasonic wave pulse with center frequency 50 kHz.

Figure 3.6 represents a snapshot of wave propagation 204 micro-seconds after applying one input source, the location of which is shown as a pink arrow in Fig 3.4. In the plain concrete case, it is clear that the initial P-wave front propagates through the entire section, and then several reflections and mode conversions occur at the geometric boundaries of the section. Also it can be seen that the amplitude of the initial P-wave front is relatively small. Following the initial P-wave front, and S-wave front is observed with a maximum amplitude along a ray at 45 degrees from the surface. The large amplitude R-wave propagates along the surface. The wave propagation becomes more complicated if the model has a higher degree of heterogeneity. Embedded rebar in concrete disturbed the wave propagation, and irregularly shaped wave fronts and uneven distribution of S-wave energy can be observed. The disruption is caused by the difference of the acoustic impedance between concrete and inclusions. For example, the acoustic impedance mismatch between concrete and defect 1 is significantly large, such that almost all waves are not transmitted but reflected, and the first arrival of P-waves through thickness is delayed at the receiver position.

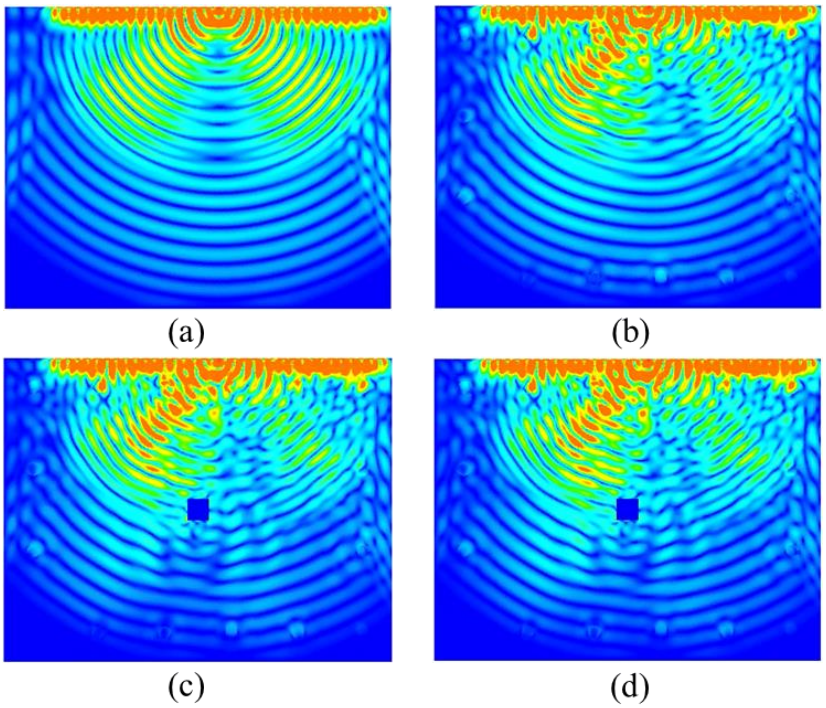

Figure 3.6 Wave field at 204 μs after excitation: (a) plain concrete, (b) concrete and steel, (c) concrete, steel and defect case 1, and (d) concrete, steel and defect case 2; the plot colors represent von Mises stress amplitude where warm colors indicate high stress magnitude.

The stacked A-scan images in Fig 3.7 are obtained from a signal set from one reviver attached in the center of the cross-section as the input source moves along the surface. The x- and y-axes represent time in micro-seconds and ray number based on the movement of the input source, respectively. The color scale of the image indicates the amplitude of the signal set where bright color indicates high acceleration amplitude. The image shows wave propagation behavior from the receiver's point of view. In the case of the plain concrete model, the image shows a smooth rounded shape of the initial P-wave front and following reflections from side walls. The smooth wave front profile is disrupted as non-homogeneity of the model increases. The stacked A-scan images clearly show that wave propagation is affected by inclusions in RC cross-sections, and this disruption is indicated to some degree by the shape of initial P-wave front. Thus, wave information obtained at the initial P-wave arrival front can be used in tomographic reconstruction to indicate the presence of internal inclusions.

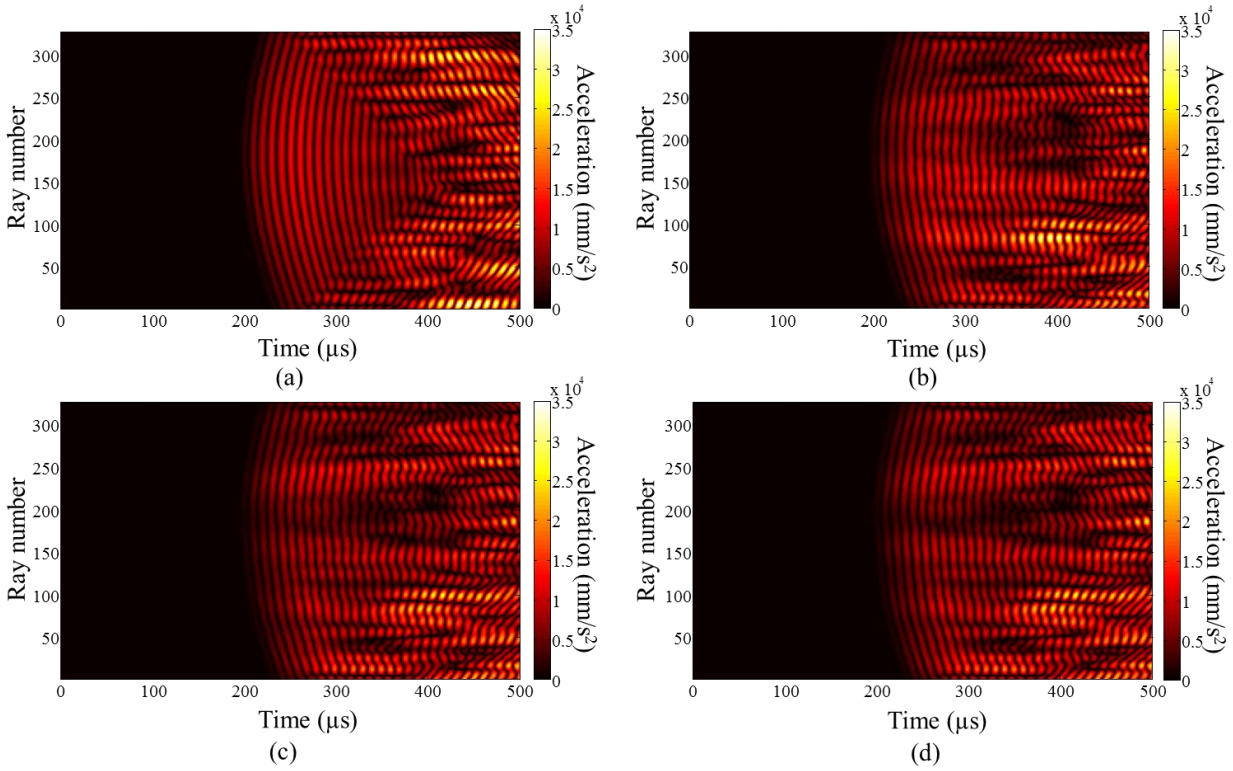

Figure 3.7 Stacked A-scan images: (a) plain concrete, (b) concrete and steel, (c) concrete, steel and defect case 1, and (d) concrete, steel and defect case 2.

3.2.2 Evaluation of auto-picking algorithms

Auto-picking algorithms including Akaike information criterion (AIC), Hinkley criterion (HIC), and noise-threshold method are evaluated using the obtained signal data-set from the numerical simulation. The first arrivals of P-waves in the time signal through the simulated plain concrete section are defined using the three different algorithms. Figure 3.8 represents an example of arrival picking using the three algorithms from the same signal. Since the data are simulated, the signal contains a section of zeroes before the waves arrive instead of any system noise. AIC defined the arrival of the P-wave as the first non-zero point in the time signal, which is not the actual wave arrival but residual error from the simulation. The HIC and noise-threshold method picked slightly different arrivals in the signal.

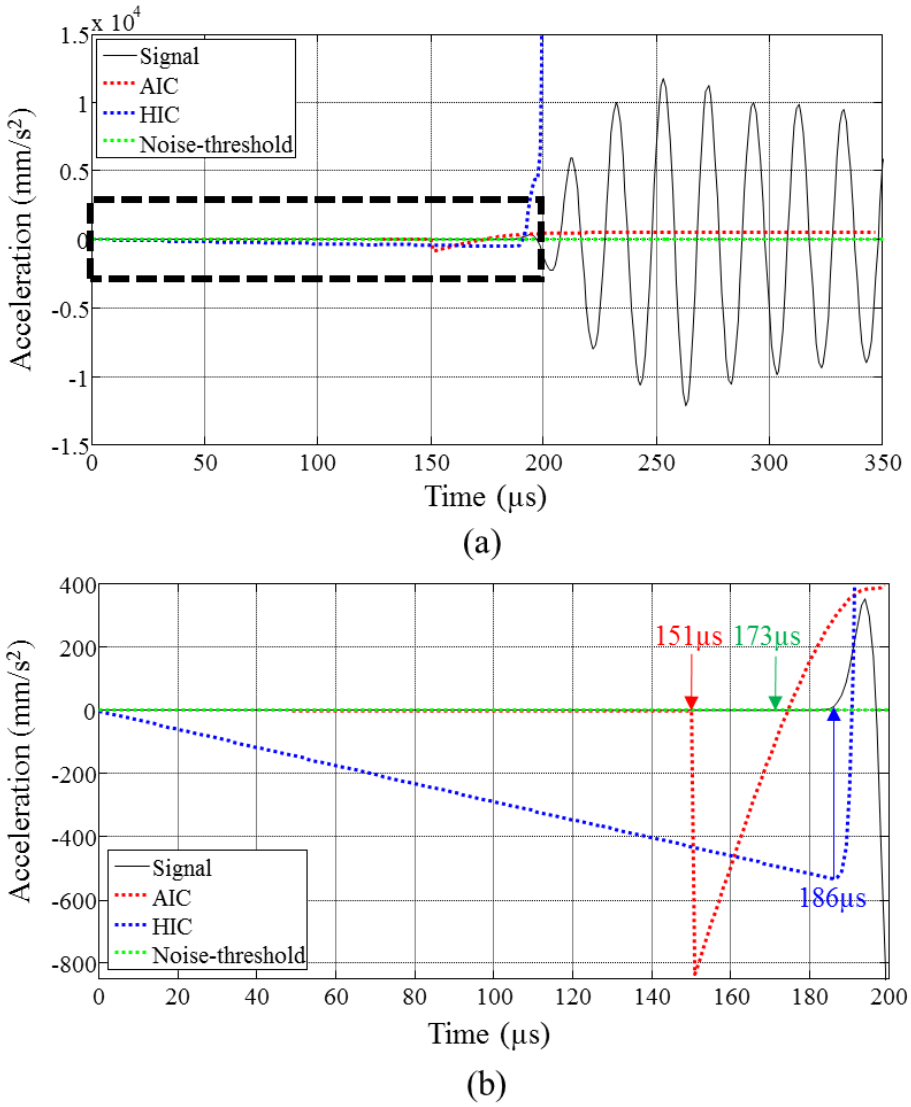

Figure 3.8 Illustration of the arrival picking algorithms: (a) Signal with AIC, HIC, and noise-threshold indicated (b) enlargement of the dash-lined box from (a).

Using the obtained arrival times from all signals across the cross-section in plain concrete model, the velocity is calculated with the assumption of straight ray path from sender to receiver; the results are shown in fig 3.9. Because the time signals are discrete, a perfectly uniform velocity cannot be obtained, even from the plain concrete case. Some variance in the velocity data should be expected. To evaluate the efficacy of the different procedures, the difference between velocity maximum and minimum is calculated. The range of the y-axis in the graphs are set to 400 m/s for all cases in fig 3.9. Among the applied algorithms, the noise-threshold results in a minimum difference of 64 m/s. The maximum velocity differences from AIC and HIC are 244 m/s and 90 m/s, respectively.

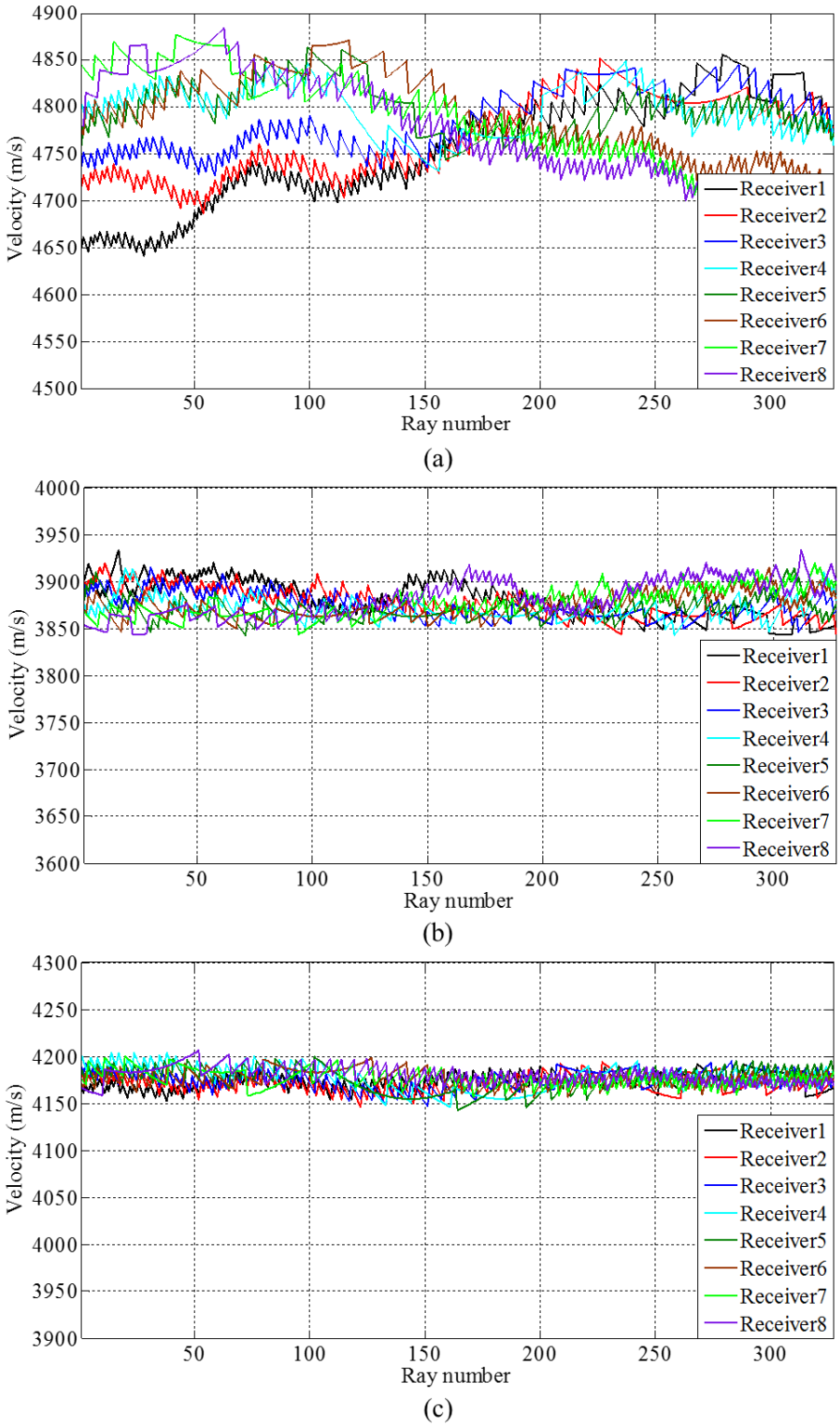

Figure 3.9 P-wave velocity profiles obtained from plain concrete model: (a) velocity defined by AIC, (b) velocity defined by HIC, and (c) velocity defined by the noise-threshold method.

The absolute velocity values provided by each algorithm are different. The assigned P-wave velocity in concrete is 4058 m/s, so velocity profiles from the noise-threshold method are closest to the assigned velocity. Furthermore, the noise-threshold method shows relatively better results compared to AIC and HIC in terms of velocity consistency shown in fig 3.9. This is because the thresholding process is based on the amplitude distribution of the first part of the signals from the entire dataset, which represent stable criteria from a large experimental sample size. In the cases of AIC and HIC, the algorithms are applied to individual signals and the criteria are not stable for the entire dataset, which may lead to inaccurate velocity estimates in the case of low amplitude or highly noisy signals.

3.2.3 Velocity tomography

Tomograms from the numerical simulation are built up based on P-wave arrival time, $\mathbf{T_n}$, as defined by the noise-threshold method. The number of pixels in the tomograms was assigned to be 2,500, and the path length matrix, **D** was constructed. Based on the constructed matrices, the linear equations for velocity tomography are

$$\boldsymbol{T} + e^* = \boldsymbol{T_n} = \boldsymbol{DP} \tag{3.8}$$

where T is the correct arrival time of P-waves without any system noise, e^*. In the numerical simulation, the system noise includes errors from the arrival picking procedure. In the case of the experimental data, the level of the system noise would be higher owing to low signal to noise ratio in the obtained signals.

Three algorithms were applied to carry out the iteration: Kaczmarz's method, Randomized Kaczmarz's method, and the least square method. The developed tomograms from each iterative solver are shown in Figs. 3.10 to 3.12. The jet color-map is applied using the Matlab platform to plot the images, and the color scale of the image is set to the maximum and minimum of the velocity solution from each iterative solver. It is noted that the slowness values from the iteration are converted to velocity with units of m/s in the image. In the case of the least square method shown in Fig 3.12, the solutions presented in the images did not converge to a correct value and are far out of range. This is because the system noise e^* disturbed the entire system, unlike synthetic data analysis presented in section 3.1.2, and the iteration procedure falsely converges to unrealistic values. The images from Kaczmarz's method and Randomized Kaczmarz method provide more stable behavior and show the location of defects as regions of low velocity.

The images in Fig 3.11 show the developed tomograms from the four different models, using Randomized Kaczmarz method. While the plain concrete model has all pixel values within the range of 100 m/s, the CS model shows a higher velocity region (red color) near the location of applied input sources, which represents rebar. Because the top part of the image, where the input sources were applied, has significantly higher ray density, the locations of rebar are only presented in one side of the image. The tomograms in figs 3.11(c)

and (d) clearly show the defects as lower velocity; i.e., blue color. Besides the locations of rebar and defects, artifacts (unexpected dark blue zones) can also be found. This is a result of low ray density in receiver part of the image and also the selected color scale of the image.

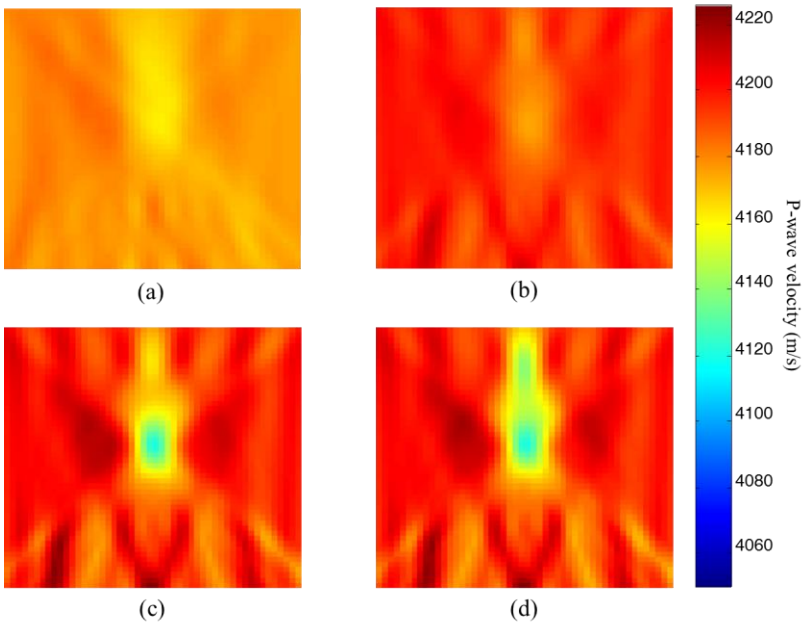

Figure 3.10 Velocity tomograms (Kaczmarz's method): (a) plain concrete, (b) concrete and steel, (c) concrete, steel and defect case 1, and (d) concrete, steel and defect case 2.

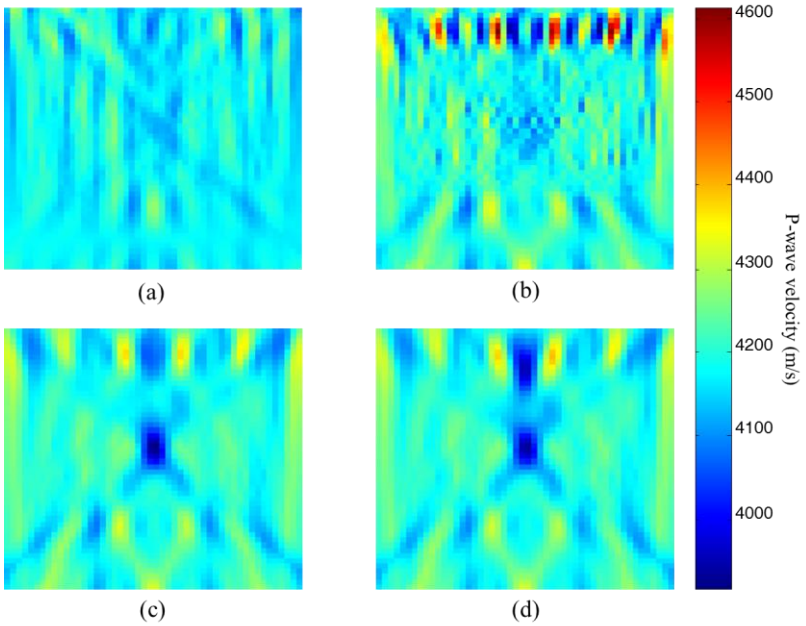

Figure 3.11 Velocity tomograms (Randomized Kaczmarz method): (a) plain concrete, (b) concrete and steel, (c) concrete, steel and defect case 1, and (d) concrete, steel and defect case 2.

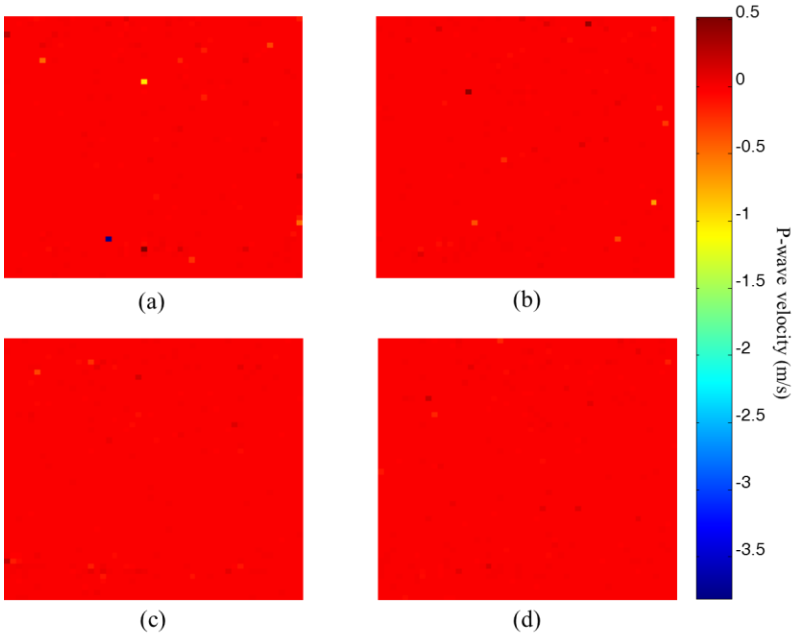

Figure 3.12 Velocity tomograms (least square method): (a) plain concrete, (b) concrete and steel, (c) concrete, steel and defect case 1, and (d) concrete, steel and defect case 2.

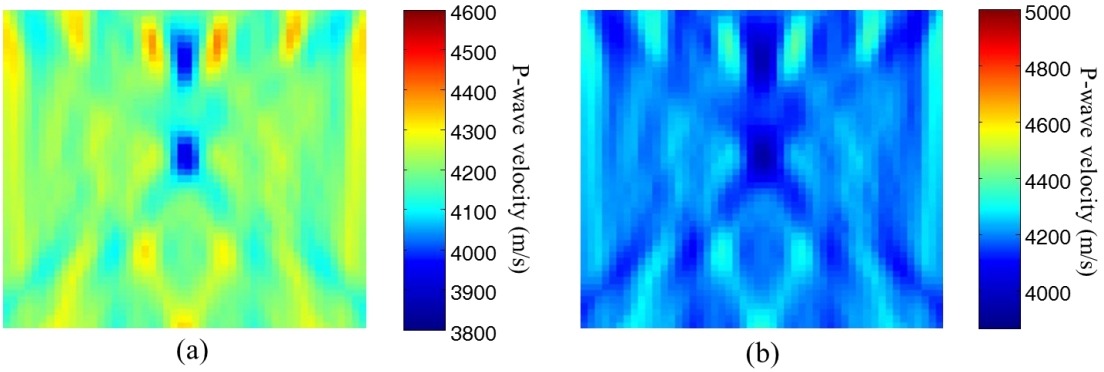

Figure 3.13 Example of color scale adjustments tomogram in fig 3.11(d): (a) tomogram with a minimum color scale of 3800 m/s, and (b) tomogram with a maximum color scale of 5000 m/s.

Improvements to the tomographic reconstruction and analysis procedures are needed in order to better detect and characterize the defects in a quantitative manner. However, quantitative analyses procedures may lead to misleading or incorrect images—for example, setting an arbitrary P-wave velocity threshold value to define a defect region. The color scale in Fig 3.11 is set based on the maximum and minimum of P-wave velocity pixel values. Then, the color scale of the tomogram in Fig 3.11(d) is adjusted in two different ways, and the results are shown in Fig 3.13, where the two images are same velocity profiles but presented in different color scales: Figure 3.14 (a) shows the minimum value around 200 m/s lower than the original image, and Figure 3.14(b) the maximum value around 400 m/s higher than the original image.

The tomogram in Fig 3.13(a) clearly identifies the location of defects without false indications while the image in Fig 3.13(b) shows the entire section in dark blue colors. These results confirm that quantitative analyses procedure based on visualized results should be carefully performed and evaluated.

3.2.4 Differential velocity tomography

Relative comparisons of tomographic images from defected and non-damaged areas can provide deeper understanding of the inspected structure. For example, differentials of velocity profiles between two areas can better define the presence of defects than individual tomograms from each area. The differentials of the arrival time, Δt_n from CS to CSD1 and CSD2 cross-section models were obtained and substituted in the equation (3.7) instead of Tn. The randomized Kaczmarz method was applied to solve the differential velocity (slowness) equations. Because differential velocity has an arbitrary scale, the results are normalized as shown in Fig 3.14. The red color represents the maximum differentials of velocity profiles between two different simulations. From the images, the defects are clearly and accurately identified with minimal artifacts. In Fig 3.14(b), the defect near the surface of the model (presented by red color in CSD2) has less intensity compared to the center defect, which matches the simulation model. Thus, differential tomography can minimize false interpretation of images, and has great potential to monitor damage in the RC structures if a reference image is available.

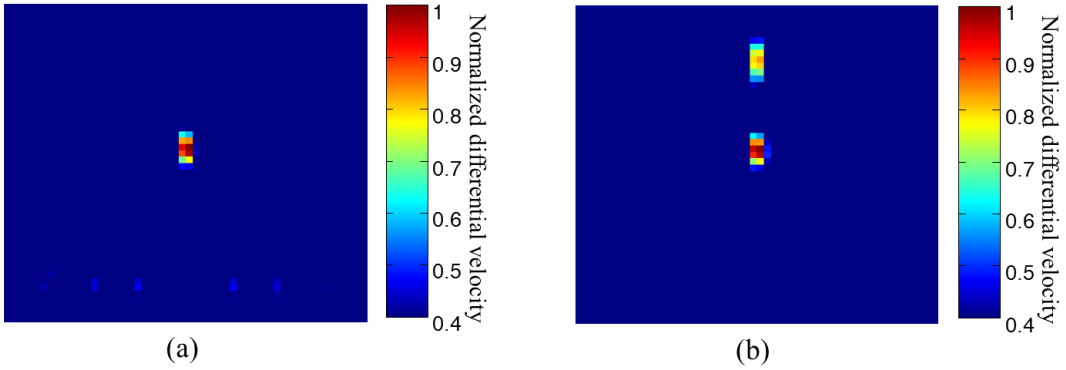

Figure 3.14 Differential velocity tomograms: (a) tomogram based on the arrival time differentials between CSD1-CS, (b) tomogram based on the arrival time differentials between CSD2-CS.

CHAPTER 4 DEVELOPMENT OF A HYBRID AIR-COUPLED ULTRASONIC SYSTEM

In this chapter, a hybrid air-coupled ultrasonic testing system is described and applied to collect large amounts of data from a full-scale RC column that includes artificial defects. The evaluated tomographic procedure presented in Chapter 3 is applied using the experimentally obtained data. The ultrasonic system and tomographic procedure demonstrate that large amounts of high quality data can be collected from full-scale RC cross-sections, and that internal defects can be located using the developed images. A portion of the work described in this chapter was published in a journal paper titled "NDE application of ultrasonic tomography to a full-scale concrete structure" published in *IEEE Transactions on Ultrasonics, Ferroelectrics, and Frequency Control* (Choi and Popovics 2015).

4.1 Development of the ultrasonic scanning system

Ultrasonic NDT methods in general are well-suited to characterizing cracks and void defects in concrete. However, the application of ultrasonic tests to large-sized concrete structures has practical limitations because of the physical coupling required between the transducer and test object. Furthermore, surface preparation, such as grinding, is sometimes needed to ensure good transducer contact with the surface of rough concrete. These problems limit the amount of data that can be acquired in a reasonable amount of time with conventional ultrasonic transducer hardware. In addition, insufficient amounts of measurement data limit tomographic and other imaging methods that are deployed using the data, leading to inaccurate images (Guan and Gordon 1994). Therefore, the application of through-thickness ultrasonic tomography to defect detection in concrete has thus far been limited to small-sized specimens (Chai et al. 2011, Aggelis 2013)

Contactless, air-coupled, through-thickness, ultrasonic measurements offer the potential to advance the state of practical infrastructure assessment. This is because they enable more rapid and consistent data collection regardless of material surface condition and provide coverage of the full volume of an element (Chimenti 2014). The application of air-coupled, though-thickness, ultrasonic data to create images in concrete has been recently reported (Centrangolo and Popovics 2010). Although these previous research efforts illustrate the potential of air-coupled ultrasound to concrete, the size of the specimens in those studies were much smaller than actual concrete structures in the field. However, ultrasonic through-thickness tomography that fully investigates large concrete structures with the necessary sensitivity, accuracy, and efficiency to detect and characterize important internal defects has not yet been reported.

In this work, a hybrid air-coupled/contact transducer system is deployed on a full-sized, realistic, steel-reinforced concrete column specimen using an automated measurement system. Electrostatic air-coupled

transducers are used to generate ultrasonic energy; contact accelerometers that are attached on the opposing side of the concrete element detect the ultrasonic pulses. It is exceedingly difficult to obtain high-quality, coherent pulse signals through a full-scale concrete element with a fully air-coupled ultrasonic test configuration because of the significant signal attenuation as a result of the material and the large acoustic impedance mismatch in both the transmitting and receiving sides. This hybrid testing configuration is one solution to this dilemma for large concrete samples, providing high volumes of usable signal data obtained across the entire cross-section of the structure. Through-thickness ultrasonic data are used to reconstruct velocity tomograms that represent internal defects within the specimen. The large amount of data provided by air-coupled transmission scanning significantly increases sectional ray coverage, enabling the creation of accurate internal images. This work reports a new diagnostic capability over and above what is provided by existing technology: full-thickness internal imaging of large concrete structures. This research aims to broaden and to optimize the application of ultrasonic tomography techniques to the civil infrastructure, especially for large steel reinforced concrete structures.

4.1.1 Air-coupled electrostatic ultrasonic transducer

Table 4.1 provides acoustic impedance and reflection coefficient data of air, concrete, and active materials in conventionally used contact ultrasonic transducers; the data are based on computations using equations (2.2) and (2.3). The large difference in acoustic impedances between air and the solid materials gives rise to reflection coefficients that are nearly one in value. This result shows that very little wave energy generated by the transducer and propagating through air is transmitted into the object (concrete). Note that these reflection losses would occur at both sides of an investigated object (ingoing and outgoing ultrasonic waves) in the case of through-thickness air-coupled measurements. Thus we need to maximize the energy of the ultrasonic wave that is launched into the air from the generating transducer, and then process the received signal to extract the small amplitude characteristics of interest from the detected signal.

Table 4.1 Acoustic properties for concrete, air, and piezoelectric material.

Acoustic properties	Transducer crystal (PZT-4)	Air (at 25 °C)	Concrete
Acoustic impedance (MRayl)	36.15	0.00042	8.36 to 11.3
Transmission coefficient (transmits from left to right in fig. 4.2)	0.00000232 (PZT to air)		1.999 (~ 2) (air to concrete)
Reflection coefficient (transmits from left to right in fig. 4.2)	-0.999(~ -1) (PZT to air)		0.999 (~ 1) (air to concrete)

Specially designed air-coupled transducers maximize the wave energy launched into the air. Conventional contact ultrasonic transducers are generally made of piezoelectric solid materials, such as PZT-4. Although the performance of conventional contact transducers can be improved for air-coupled applications—e.g., by employing impedance matching layers (Centrangolo and Popovics 2010) the huge impedance mismatch between PZT and air limits the amount of wave energy that can be launched. Electrostatic-type transducers, on the other hand, can generate much larger amounts of wave energy into the air. The work reported here uses commercially available electrostatic transducers manufactured by SensComp (Livonia, MI, USA) (Siciliano and Khatib 2008). The transducer is composed of a gold-foil-coated plastic membrane that lies next to an aluminum back plate, as shown in Fig 4.1. The conductive foil membrane is charged with a bias voltage with respect to the back plate, and the membrane stretches and separates from this plate. When an excitation signal is applied to the biased membrane, an electrostatic attraction force between the foil membrane and the back plate arises, and the membrane vibrates and launches an ultrasonic (acoustic) pulse into the air. The frequency content of the ultrasound is mostly defined by the shape and boundary of the membrane. Electrostatic transducers can also detect acoustic waves propagating in the air, where the voltage is inversely generated proportional to varying capacitance of the vibrating membrane. The design of electrostatic transducers is tolerant to high excitation amplitudes and furthermore requires relatively simple electronic circuitry to operate. Thus, additional hardware, such as arbitrary pulse generators, are not needed.

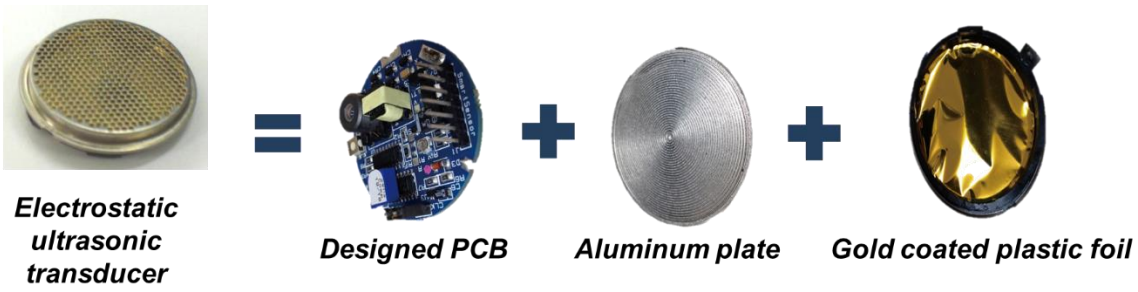

Figure 4.1 Electrostatic ultrasonic transducer (SensComp 600).

In this work, a SensComp 600 transducer was used to launch ultrasonic waves into the air. The standard driving and control circuitry associated with the sensor was used, which generates a 50-kHz ultrasonic pulse with a narrow band of frequencies at a repetition rate of 5 Hz. The selection of this relatively low frequency arises from the natural large-scale inhomogeneity of concrete material and the large sample size. Concrete is composed of hydrated cement paste and mineral aggregates with wide ranges of size (maximum aggregate size is 20 mm for the concreted tested here) and porosity. As such, high-frequency ultrasound is intensively scattered by this material structure. To obtain meaningful coherent wave pulses for propagation distances greater than several centimeters, ultrasonic frequencies less than 100 kHz must be used for concrete NDT (Landis and Shah 1995). Considering the large sample thickness in of the work reported here, a 50-kHz ultrasonic pulse was selected. This frequency has been successfully used for ultrasonic NDE of concrete (Ismail et al 2001, ACI Committee 228).

4.1.2 Hybrid air-coupled ultrasonic testing configuration

Although electrostatic transducers generate high-amplitude wave energy into the air, the reflection losses at the front (ingoing ultrasonic pulse) and back (outgoing ultrasonic pulse) are significant. As a result, fully air-coupled ultrasonic configurations, that is using both air-coupled sending and receiving transducers, provide through-thickness signals with very low amplitude. To overcome this problem, while at the same time making use of the advantages provided by air-coupled scanning, a hybrid testing configuration was used in this work. A schematic illustration of the test configuration is shown in Fig. 4.2.

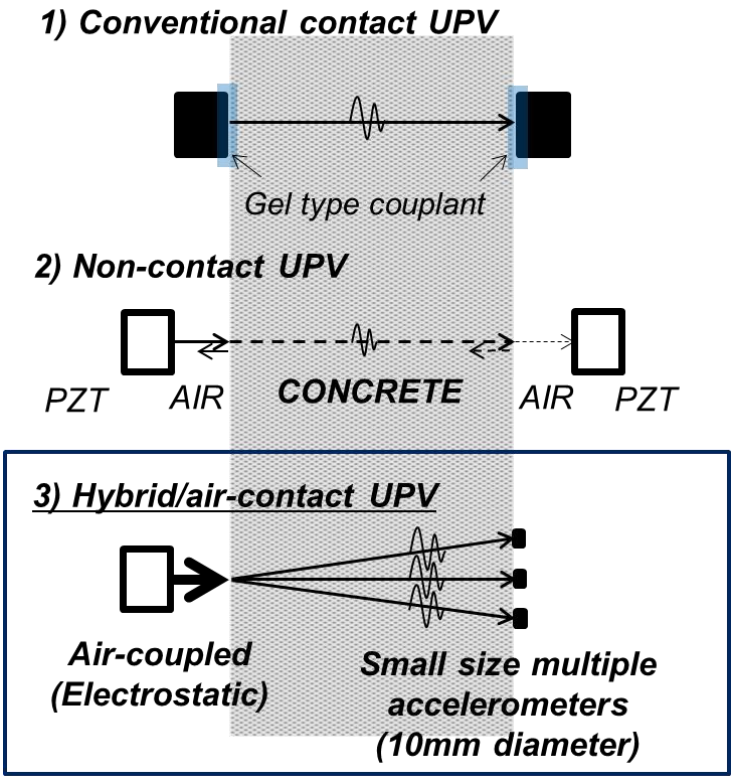

Figure 4.2 Schematic illustration of sensor configurations for through-thickness ultrasonic methods.

An array of contact accelerometers (PCB 352c15) attached on the opposing surface was used to detect the waves generated by the air-coupled transducer. The accelerometers have high sensitivity in the frequency range of interest and are small in size, so mounting quality is largely unaffected by the surface condition of the concrete. A commercially available glue (Loctite, Super Glue ultra gel control) was used to mount the accelerometers at fixed positions. The glue was carefully applied to the mounting base of the accelerometers, and the accelerometer directly attached to the surface of the concrete. The mounting process took only a few seconds for each sensor and the sensors remained affixed to the surface throughout the tests.

A robotic scanning frame system was developed to control the position and movement of the air-coupled transmitting transducer with an accuracy of 0.1 mm. The automated scanning frame was controlled by programmed microcontroller and step motors. The frame moved the position of the transducers horizontally and vertically while maintaining a constant air gap distance between the air-coupled transducer and the concrete surface, ensuring the accurate spatial position of the transducer. The developed test setup including air-coupled transmitter, array of accelerometers, and automated scanning frame is shown in Fig. 4.3.

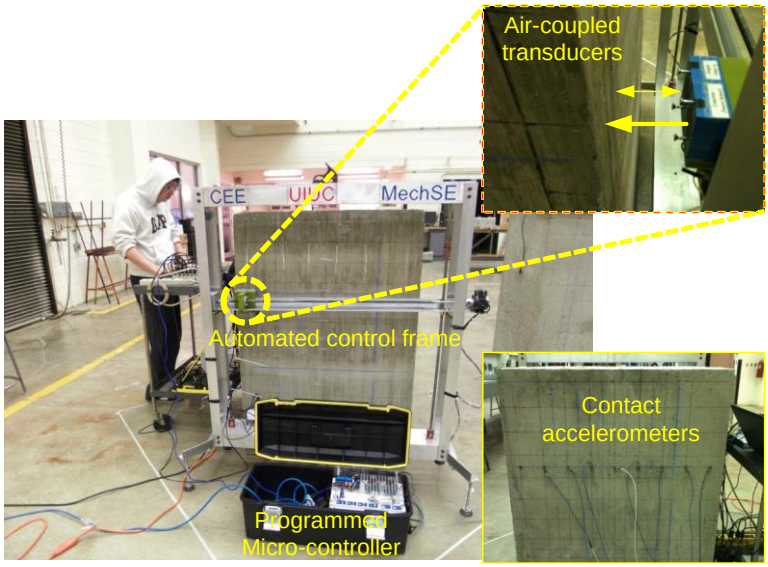

Figure 4.3 The experimental testing set-up showing automated scanning frame, air-coupled sending transducers (top inset), and array of receiving accelerometers (bottom inset).

4.2 Application to a full-scale reinforced concrete element

The ultrasonic testing approach was tested on a full-scale reinforced concrete column that contains artificial defects. The test specimen simulates a realistic design of a concrete column in a large building.

4.2.1 Description of full-scale RC column sample

The test specimen was a steel reinforced concrete column with a nominal rectangular cross-section of 36 inches (914 mm) by 28 inches (711 mm), as shown in Fig. 4.4. Before casting the concrete, several artificial defects were embedded into the steel reinforcing bar framework. Concrete voids, which can be caused by construction error, are simulated with Styrofoam prisms. Internal cracking damage, which can be caused by freezing and thawing action or alkali silica reactivity, is simulated with pre-cracked concrete prisms. The dimensions of the embedded defects are 3 × 3 × 9 in. (76.2 × 76.2 × 228.6 mm) in width, length, and height, respectively. To make the pre-cracked concrete prisms, controlled compressive loads were applied to precast mature concrete prisms. After a certain level of compressive loading, visible aligned cracks were distributed throughout the prism. The column sample was cast using conventional structural concrete with target 28-day compressive strength of 5000 psi (34.4 MPa). The material properties of concrete in the column were similar to those of the pre-cracked prisms. The Styrofoam had much lower elastic constants and density than the concrete. The material properties of concrete mixtures used for this test sample are presented in Table 4.2.

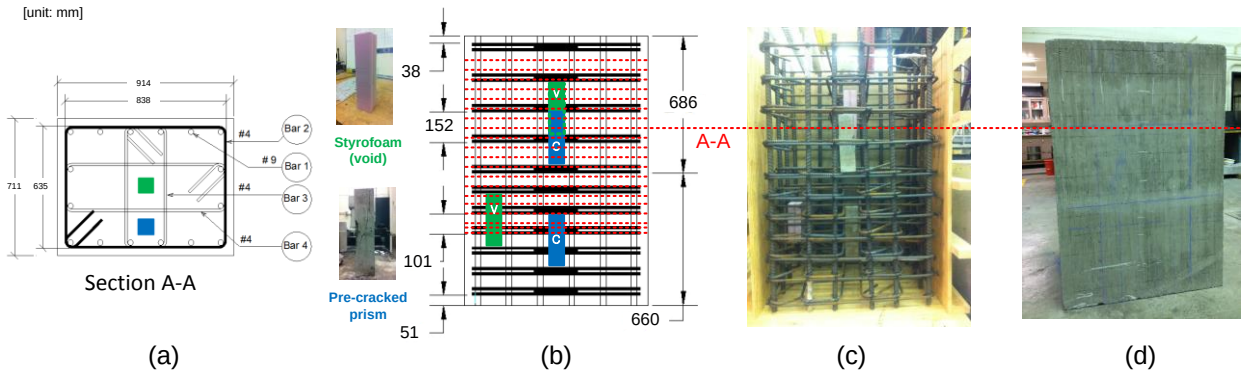

Figure 4.4 Test specimen detail with dimensions shown in units of mm: (a) Cross section A-A; (b) Design of the concrete column with embedded steel bars and artificial defects indicated (Red dotted lines represent scanning sections;) (c) Photo before casting concrete; (d) Photo after casting concrete.

The column was also designed to have different transverse steel bar spacing: high volume dense reinforcement, with 4 in. (101.6 mm) bar spacing, is positioned at the bottom part of the column, and more conventional 6 in. (152.4 mm) bar spacing at the top part of the column. The test column was designed to evaluate the validity of the proposed ultrasonic scheme and to check the effect of closely spaced steel bars on the results.

Table 4.2 Material properties of concrete mixtures.

Properties	Measured data	
	Ready mixed concrete	Pre-cracked defect
Air content (%)	2	1.7
Slump (in., cm)	5, 12.5	8, 20.0
28-day compressive strength (psi, MPa)	6090, 42.0	5750, 39.6

4.2.2 Data collection and signal quality

The through-thickness ultrasonic signal data were collected using the specially designed testing equipment described above. An example of signal data measured by the system is shown in Fig 4.5, where the trigger of the signal (green) from the electrostatic transducer, air-gap measurement (blue) from another transducer, and the received through-thickness signals (red) from the accelerometers are illustrated. The sending

transducer emitted an ultrasonic pulse that was directed normally on the concrete surface, initiating a P-wave that propagated into the volume of the specimen. The trigger signal (green) is generated when the air-coupled transducer starts to operate, and the initiation of the trigger is set to the time zero at first. A second electrostatic transducer positioned next to the sending transducer sent and received a separate ultrasonic pulse in the air. The pulse from the second transducer is recorded as a transistor–transistor logic (TTL) format, indicating the rising and falling of the pulse as an initiation and arrival of the reflection respectively. The reflection includes twice travel distance of the air-gap between the transducer and the surface of the specimen. Therefore, the half-length of the TTL signal represents the portion of the air-gap for through-thickness measurements. The rising of the TTL pulse (blue) is aligned with the trigger signal in time and the half-length of the pulse is omitted from the through-thickness measurements. In other words, the time at the half-length of the pulse is newly set to time zero. It is noted that all signals were digitized using a 32-bit digitizer at a sampling rate of 2 MS/s. This measurement was used to accurately determine the air gap distance between transmitting sensor and the surface. Accurate information about the air gap distance was needed to compute the complete travel time of the through-thickness wave that propagated in the concrete. The transmitted P-wave pulses that travel through the thickness of the specimen were detected by an array of eight accelerometers, directly mounted on the opposing surface of the specimen.

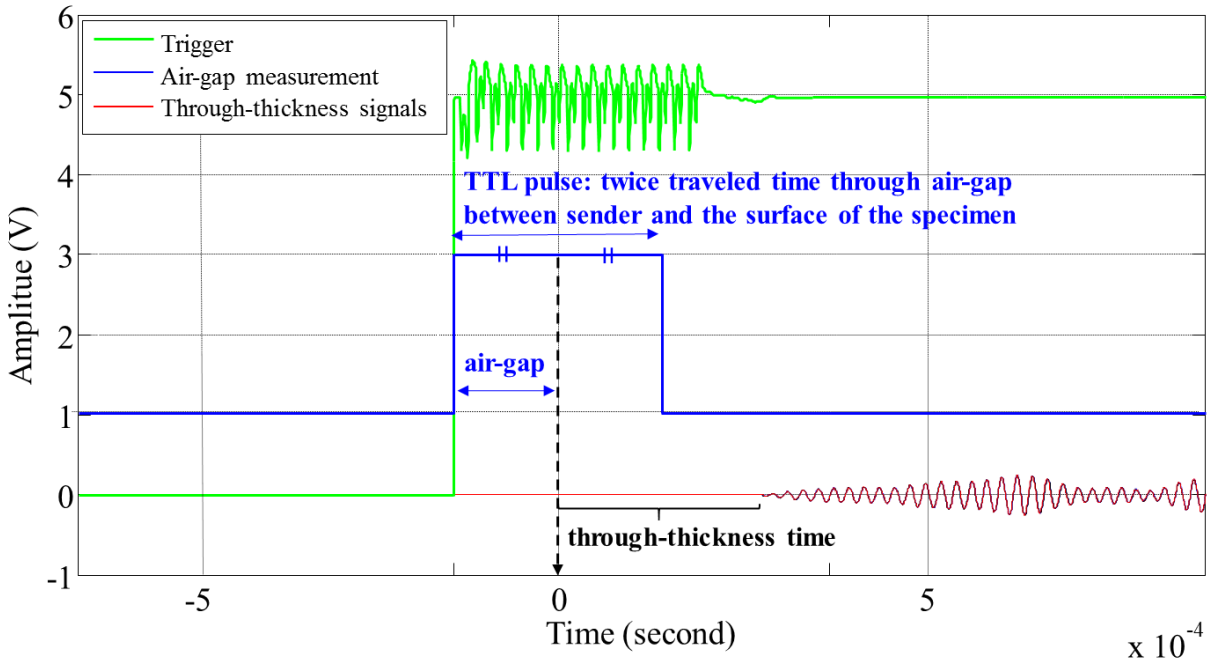

Figure 4.5 Illustration of air-gap adjustment from measured signal data (green line is a trigger signal from air-coupled transducer, blue line is a pulse for air-gap measurement, and red curves are ultrasonic signals measured by the accelerometer).

The accelerometers had a nominal sensitivity of 10 mV/g with a height and width of 10.9 and 7.6 mm, respectively. The accelerometers were positioned along parallel rows with 4 in. (101.6 mm) spacing between sensors within a row. A schematic drawing of the test configuration is provided in Fig 4.6. The entire data acquisition procedure of the hybrid ultrasonic system was fully controlled by a personal computer, including the automated position movement of the air-coupled transducer. A quantitative comparison between a conventional contact ultrasonic system and the developed hybrid system is represented in Table 4.3. One cross-section of the column mock-up was scanned within maximum one hour using the two methods. The data in the table show that the automated system significantly improves the speed of the measurement, provides high accuracy, and enables a dense volume of data to be collected from a cross-section thus enabling higher resolution internal images.

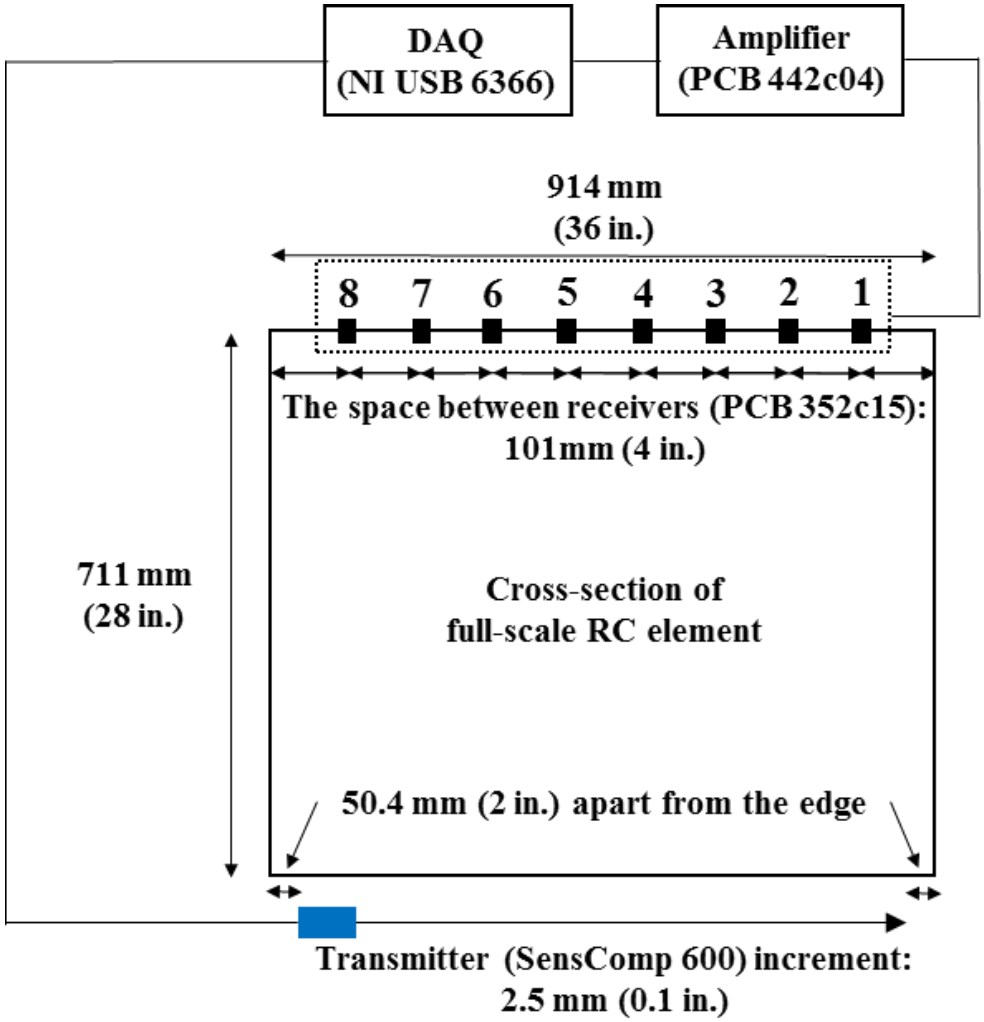

Figure 4.6 Schematic illustration of hybrid air-coupled ultrasonic test configuration.

Table 4.3 Practical and technical characteristics of ultrasonic testing configurations.

	Surface Preparation	Couplant	Measurement mode	Position accuracy	Data acquisition duration (based on a single 1m linear scan)	Ray coverage
Contact UPV	Possibly required	gel-type	Manual (two people)	plus or minus 5mm	1 hour, 64 signal set	Sparse, every 11 cm
Hybrid ultrasonic system	N/A	N/A (transmitter) Adhesive (receivers)	automated	plus or minus 0.1mm	Less than 6 min, 2,720 signal set	Dense, every 0.25 cm

The received signals from each accelerometer were time-averaged 5 times. The signals were digitized using a 32-bit digitizer at a sampling rate of 2 MS/s. The digitized data were saved and processed on a personal computer. The ultrasonic transmitter moved horizontally in 0.1 in. (2.54 mm) increments across the front face of the sample in twenty separate horizontal line scans with 2 in. (50.8 mm) vertical spacing scan lines as shown in Fig. 4.4 (marked as red lines). It took less than 10 min. to collect data for each horizontal scan line across the column width, and the total scanning time for the entire column specimen was 200 min., including the time needed to re-attach the accelerometer sets between scanning lines. Two sides of the column were scanned with a 1-inch offset from both edges, resulting in a total of 4,800 collected time signals for one cross-section. High-frequency noise was removed from each signal using FIR equi-ripple low-pass filtering, carried out using the Matlab platform. The assigned frequencies at the start of the pass band and the end of the stop band were 90 and 100 kHz, respectively. The pass band ripple was 1 dB, and the stop band attenuation was 20 dB. It should be noted that only basic signal processing techniques were applied here because the input energy emitted by the electrostatic transducer was sufficiently high to transmit through the concrete element. Example time signals affected by processing procedures are illustrated in Fig. 4.7.

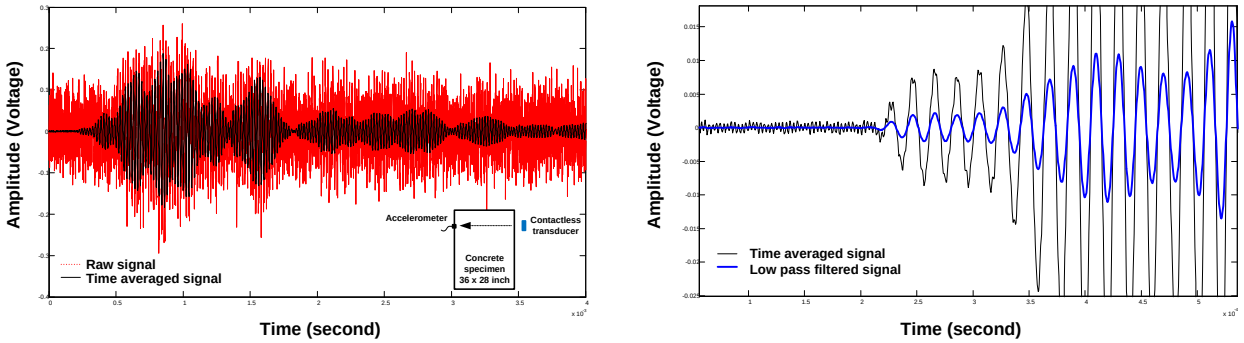

Figure 4.7 Time signals measured through the thickness of the concrete column: (a) Single shot (red line) and time averaged (black line) signals; (b) Time averaged (black line) and low pass filtered (blue line) signals.

Additionally, signal to noise ratio (SNR) from obtained signals is investigated to evaluate signal quality and establish an optimum number of time averages. Time averaging significantly increases SNR of signal data; however, the processing can extend the time required for measurements. SNR is defined using a statistical basis

$$\text{SNR (dB)} = 10\log(\sigma_s^2/\sigma_n^2) \tag{4.1}$$

where σ_s^2 and σ_n^2 are the statistical variances of the time signal that contains the wave content of interest and noise and that which contains only noise, respectively. Figure 4.8 shows examples of obtained signals across the longest ray path through the column mock-up. The computed SNR data for each signal are shown in Fig 4.9. From Fig 4.9a, the time averaging process increases SNR about 2 times higher than SNR of raw signal. For this research, arrival time of the P-wave is mainly considered so that SNR should be high enough to distinguish the first arrivals from the preceding noise content. In Fig 4.9b, the first cycle of signal is used in σ_s^2 instead of the entire time signal and SNR is re-calculated, showing that SNR is significantly increased about 7 to 10 times higher compared to the raw signal. The 5 times time-averaging process took less than 1 second and SNR is high enough to distinguish the first wave arrival among noise contents.

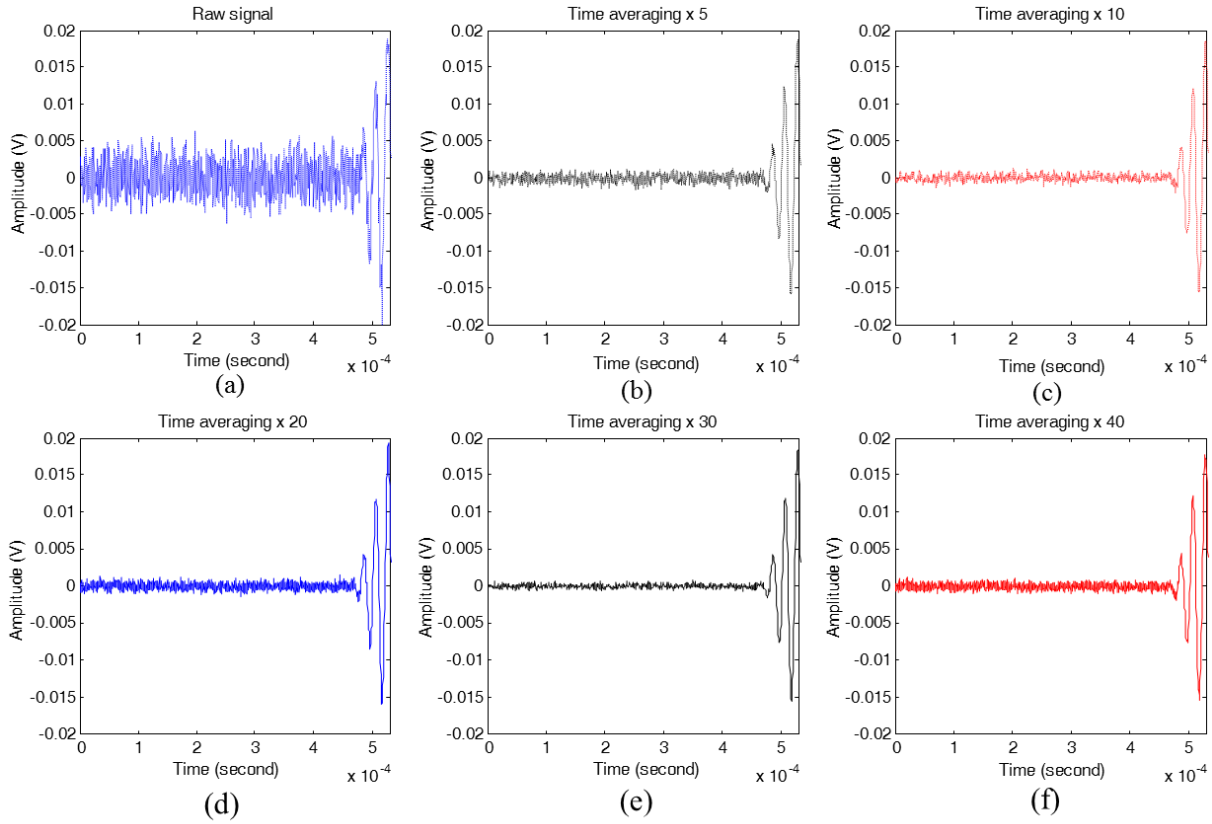

Figure 4.8 Examples of time averaged signals measured through the thickness of the specimen: (a) Raw signal, (b) 5 time-averaged signal, (c) 10 time-averaged signal, (d) 20 time-averaged signal, (e) 30 time-averaged signal, (f) 40 time-averaged signal.

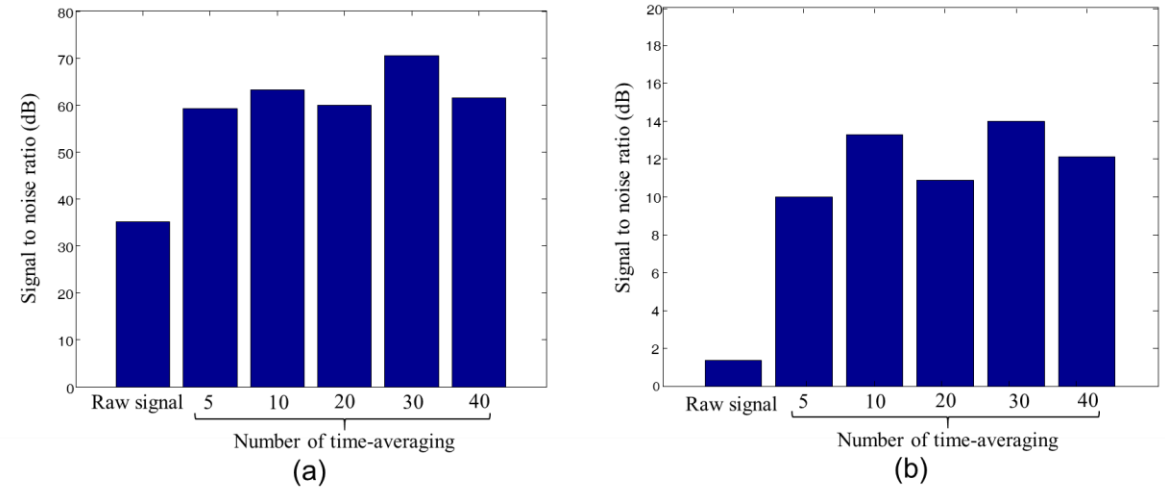

Figure 4.9 Calculated SNR for time-averaged signals presented in Fig 4.8: (a) the entire signal case (b) the first cycle of signal case.

4.2.3 Auto-picking algorithms

The large amount of collected data requires an autonomous procedure to determine the P-wave arrival time in each signal. The time arrival picking procedure should be robust considering the high levels of thermal and structural (scattering) noise expected in the signal, thus the wave arrival must be determined using reliable criteria. Several auto-picking algorithms have been established by others, such as the Akaike criteria (AIC), Hinkley criteria (HIC), and the noise-threshold method (Carpinteri et al. 2012, Hu et al. 2013). Figure 4.10 shows the stacked A-scan images from the column mock-up using four accelerometers (see the order of the receiver in Fig 4.6). The predicted arrivals are overlaid on the image for the three criteria: yellow lines from the noise-threshold, red lines from AIC, and blue lines from HIC. While AIC and HIC falsely picked the arrivals of the wave fronts, the noise-threshold method provided the most stable and consistent performance for the data. In the beginning part of ray number in the first accelerometer (Fig 4.10a), the ACI and HIC algorithms missed the wave fronts arrivals more than the other signal set. This is because the wave front of the signals through long ray paths has a lower amplitude and the AIC and HIC criteria falsely picked the arrivals. The noise-threshold method statistically calculates the amplitude of the noise contents from the measured signal set so that thresholding process is consistent from the experimental data.

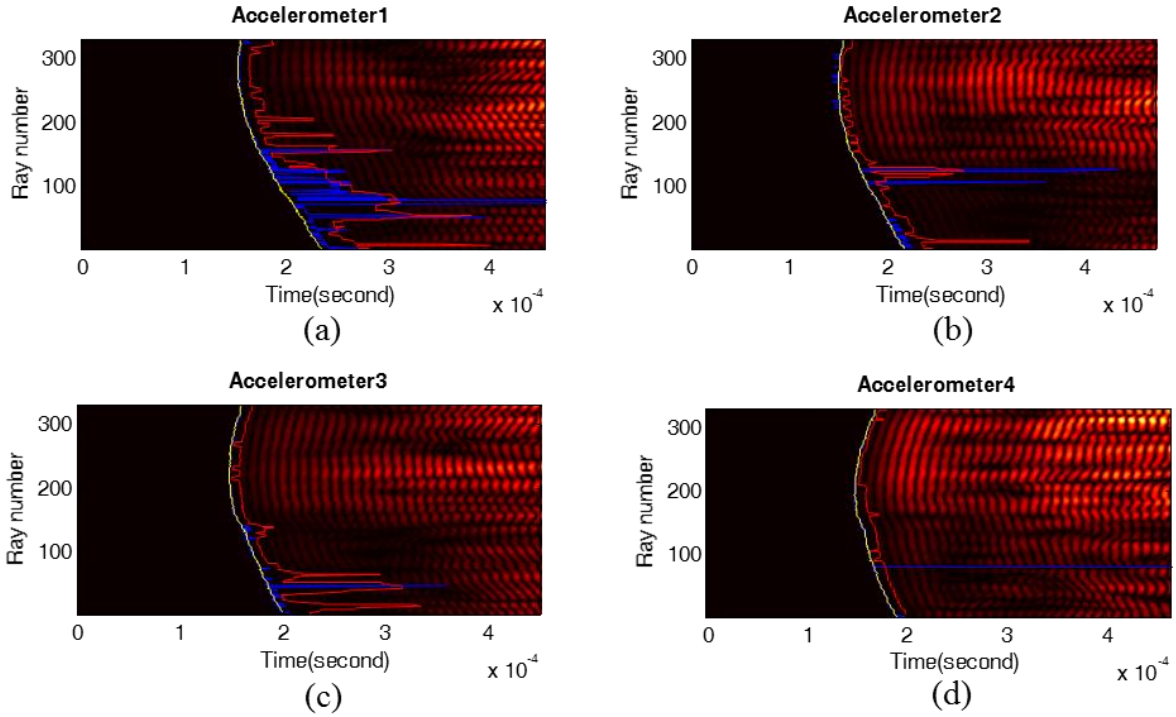

Figure 4.10 Stacked A-scan images with P-wave arrivals defined by the noise-threshold (yellow), AIC (red), and HIC (blue) criteria: (a) Receiver 1, (b) Receiver 2, (c) Receiver 3, and (d) Receiver 4.

Based on the good performance of the statistically based threshold method, that approach was used to pick P-wave arrivals in the remained for this work. The statistical distribution of amplitude in the noise was assumed to follow a Gaussian behavior. The threshold value was set greater than 3.3 standard deviations from the mean of noise amplitude (King, 2012) for each individual signal. This assigned threshold value is equivalent to the 99.9 percentile. An illustration of the procedure is shown in Fig. 4.11. Because the various accelerometers exhibit distinct noise levels because of individual sensitivity values and coupling conditions, distinct amplitude threshold values were determined for a signal set for each receiver at each mounting position.

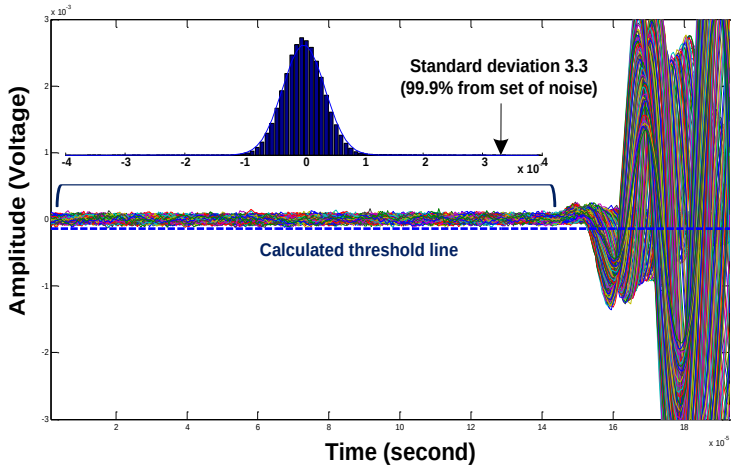

Figure 4.11 Illustration of auto-picking algorithm based on statistical threshold using multiple time signals.

4.2.4 Stacked A-scan representations

Stacked time signal sets obtained with the moving air-coupled transmitter across column section A-A from eight different receivers are shown in Fig. 4.12. The images illustrate the dense signal data set collected from the concrete sample. The wave front arrival determined by the statistical threshold method is indicated by a yellow line on the stacked A-scan images.

The arrival wave fronts of the P-waves are curved due to the relative positions of sending and receiving sensors. The wave fronts show additional indentations at the center in every image because section A-A contains an artificial void defect (Styrofoam prism) placed in the center of the column. Thus the apparent P-wave velocity along a path through the defect is reduced owing to the low elastic constants and density of the embedded Styrofoam. The average P-wave velocity in sound concrete is approximately 4600 m/s, whereas that through the defected path decreased to approximately 4000 m/s.

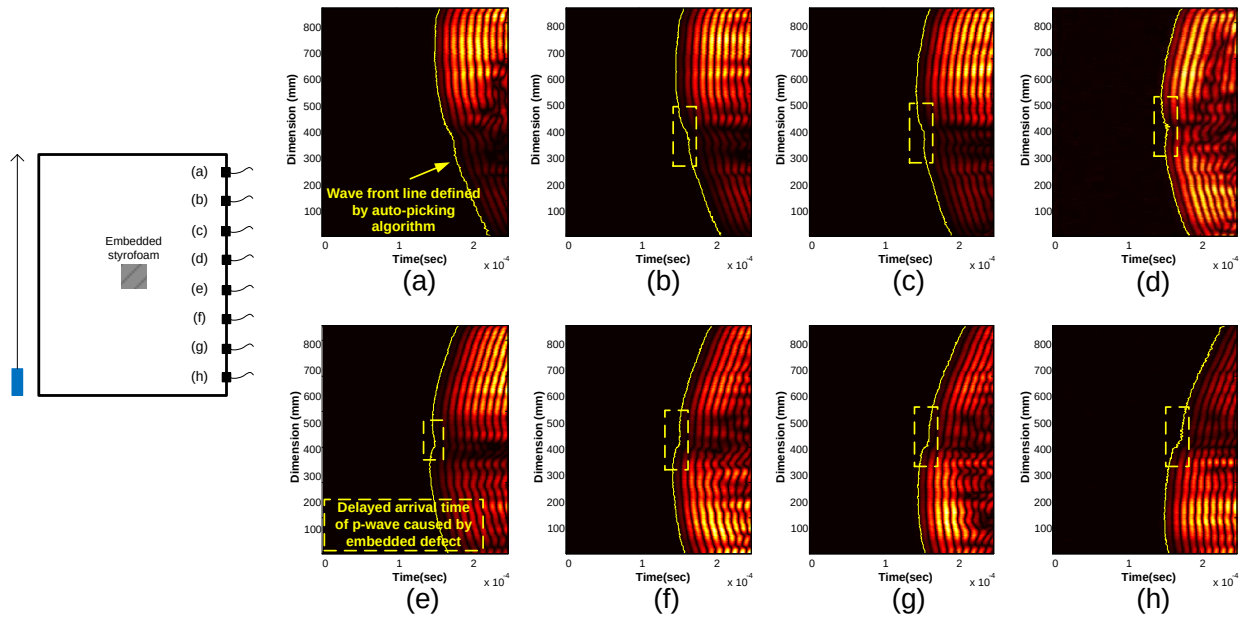

Figure 4.12 Stacked A-scan images from different receiver positions (a) to (h) through section A-A of the column specimen; image brightness is related to time signal amplitude.

4.3 Velocity tomography

Travel time tomograms were generated using the algebraic reconstruction technique (back-projection algorithm). It is known that the P-wave speed in elastic solids is directly related to elastic material constants. Because the elastic properties of solid concrete, cracked concrete, and Styrofoam are significantly different from each other, it should be possible to characterize internal damage or defects using P-wave velocity differences.

To minimize the effect of scattering from the concrete material itself, ultrasonic signals with a relatively low center frequency of 50 kHz were used. The rays of the first arriving P-wave pulses are assumed to travel along a straight line from sending surface point to receiving surface point. This assumption is justified because the relative velocity difference between concrete and steel is modest (approximately 20%) and also because the wavelengths of the signals are relatively large compared with the aggregate pieces within the concrete (Jackson and Tweeton 1994). Thus, ray tracing procedures were not included in the ART tomographic reconstruction process.

The iterative solver starts with an initial estimation of the P-wave velocity using the averaged velocity from the experimental data. The straight ray path between source and receiver is assumed. The size of image matrix was set to 50 by 50. The image reconstruction process from one section took 3 min. using Matlab to

run the computations. The calculated slowness values were transformed to P-wave velocity to indicate velocity differences between defected and sound regions within the concrete. All tomograms are presented in the jet-color scale, where red colors represent higher velocity, and blue colors lower velocity regions.

4.3.1 Evaluation of cross-sectional velocity reconstructions

The reconstructed velocity tomogram sections along parallel slices through and nearby section A-A are shown in Fig. 4.13. All three presented tomogram planes include the void defect (at the center) and cracking defect (at bottom edge). All the tomograms accurately indicate the location and size of the central void as a lower velocity (blue) region. However, the position of cracking defect is not readily identified: the pre-cracked defect exhibits as a lower velocity region in only one of the shown tomograms (Fig. 4.13c). Internal cracking in concrete was difficult to detect using P-wave velocity as an indicator.

Note that the embedded steel bars are not indicated in the tomograms, likely because of coupled effects of large wavelength compared with the bar diameter, and the relatively modest wave velocity difference between concrete and steel. The latter effect is significant for through-thickness measurements because the velocity difference between concrete and steel back-calculated by the tomographic algorithm is not significant enough to affect the intensity in the image. Several false indications are also found in the tomograms, especially near the structure boundaries. These artificial indications are a result of ray path aliasing caused by insufficient ray density near the fixed receiver positions. These indications are readily identified as distinct lines emanating from the receiver positions. The artificial effect appears in areas that are not traversed by ray paths because of the limited number of receivers. Thus the pixels within that image area remain at the initial estimate value throughout the tomographic iteration procedure. More receivers and denser internal ray distributions overcome this issue.

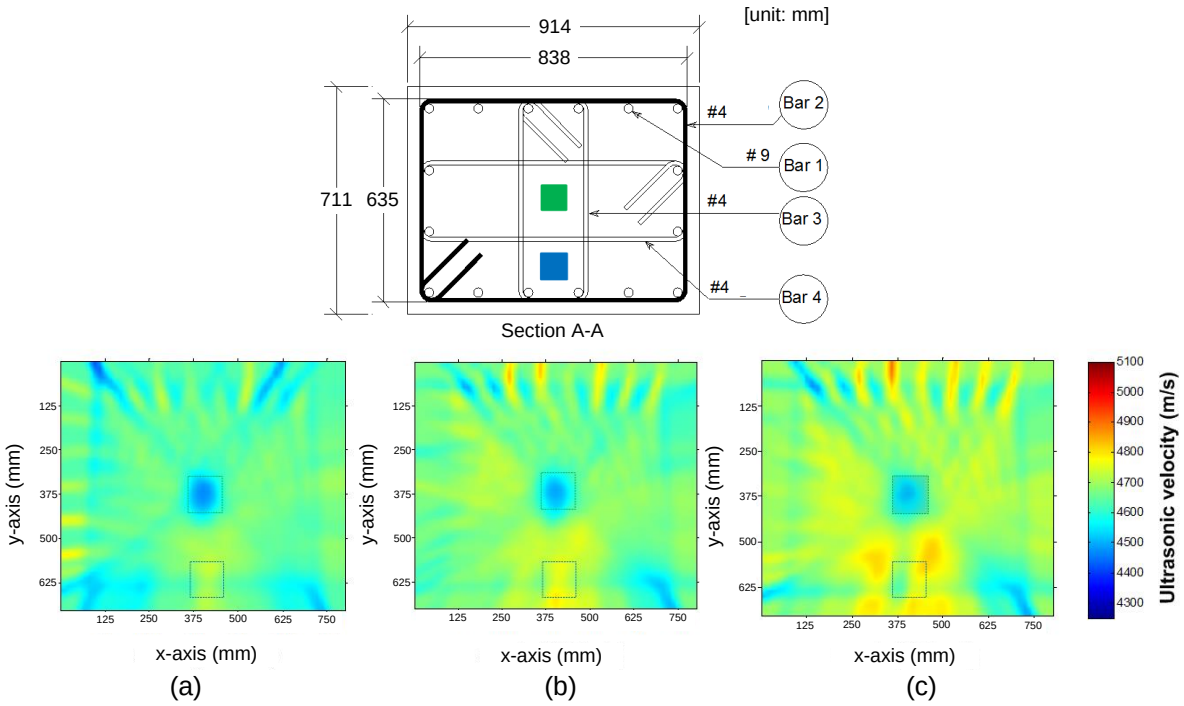

Figure 4.13 Developed P-wave velocity tomograms: (a) 50 mm above section A-A (b) Section A-A (c) 50 mm below section A-A; in the drawing the green box indicates the position of the void defect and the blue box that of the cracked concrete defect.

4.3.2 Comparison to commercial tomographic software (GeoTomCG)

The developed tomograms using the Matlab platform were compared with those reconstructed by commercial tomographic software using the same data set. GeoTomCG performs tomographic analyses using source-to-receiver travel times. This software provides a ray tracing method with its iterative solver. The program recommends the bent ray path option for materials that contain strong velocity contrasts. The bent ray path algorithm re-calculates the subdivision of an initial solution from a straight ray path and increases the numbers of segments. The subdividing process is performed until a stable minimum time is attained. This bent ray path slows overall tomographic computation; however, it has been demonstrated to greatly improves the reliability of results in the case of strong velocity contrast (Um and Thurber 1987).

The comparison study was performed with same arrival time profile. Two cross-sections from the column mock-up were selected: 1) a cross-section at 18 in. (457.2 mm) from the top of the RC mock-up including artificial defects (50 mm below section A-A in Fig 4.12), and 2) a cross-section at 28 in. (711.2 mm) from the top of the RC mock-up having no defect (cross-section A-A without defects). Figure 4.14 shows the developed tomograms from the two cross-sections in the same color scale. It should be noted that the commercial software has a limited access in terms of the spatial resolution of the image. The computation times were 4 and 50 seconds for straight ray path and bending ray path simulations, respectively.

In general, GeoTomCG reconstructed similar images with tomograms generated by Matlab. The embedded Styrofoam is detected as the region of relatively low velocity in the center of the cross-section from the images presented in Figs 4.14a and c while there are no damaged regions from the tomograms in Figs 4.14b and d. Due to the limited pixel resolution, tomograms from the commercial software minimize to show the artificial ray path near the receiver positions. However, tomography from GeoTomCG reconstructs the velocity profiles of the defect around 4600 m/s, which is difficult to distinguish from the soundness in the image (less size representation). The tomographic reconstructions with straight (Figs 4.14c and e) and bent ray path (Figs 4.14d and f) methods have a difference of computation time; however, tomograms are not significantly improved. This is because the cross-section has modest relative velocity difference between concrete and steel. This result suggests that ray tracing processes can be possibly omitted in application to reinforced concrete elements.

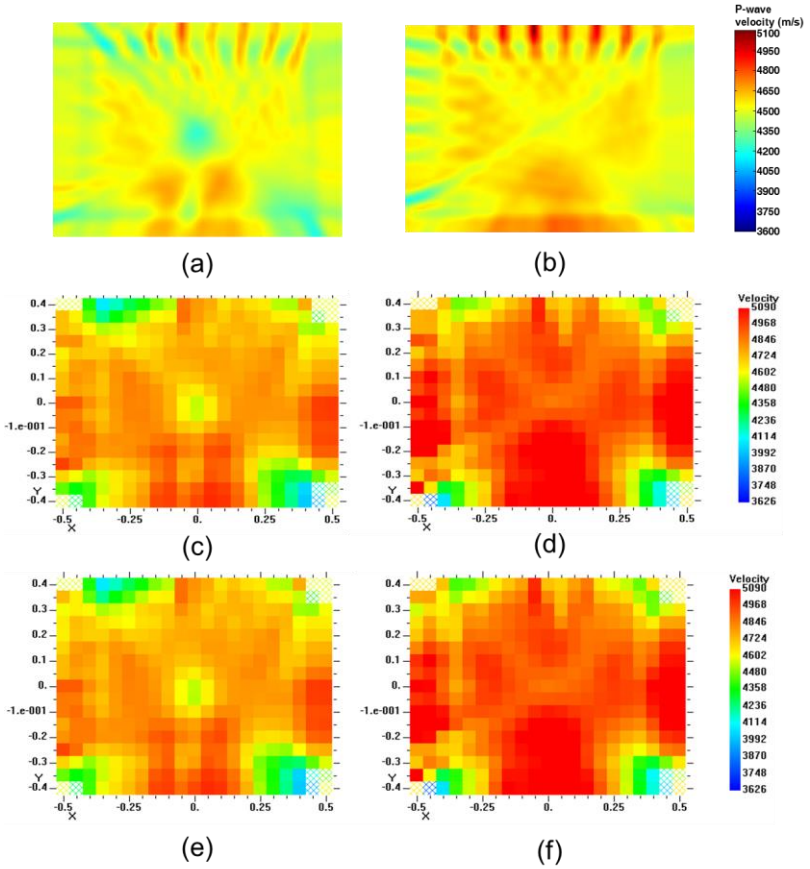

Figure 4.14 Comparison of developed P-wave velocity tomograms: cross-section at 18 in. from the top of the RC mock-up; (a) using Matlab; (b) using GEOTOMCG assuming straight ray paths (c) using GEOTOMCG assuming bent ray paths, and cross-section at 28 in. from the top of the RC mock-up; (b) using Matlab; (d) using GEOTOMCG assuming straight ray paths (f) using GEOTOMCG assuming bent ray paths.

CHAPTER 5 COMPARISON OF ULTRASONIC IMAGING METHODS

In this chapter, two different ultrasonic imaging schemes are compared for defect detection in full-scale RC elements: tomographic imaging based on algebraic reconstruction technique (ART) of through thickness data, presented in prior chapters and synthetic aperture focusing technique (SAFT) of one-sided data. The work described in this chapter aims to broaden and to optimize the application of ultrasonic imaging techniques to steel reinforced concrete structures. The comparison provides new understanding the relative strengths and limitations of each technique. A portion of the work described in this chapter was published in a journal paper titled "Comparison of ultrasonic imaging techniques for full-scale reinforced concrete" published in *Transportation Research Record* (Choi et al. 2016).

5.1 Introduction of one-sided imaging method

One-sided ultrasonic array technology has been recently simplified to enable the detection of defects in concrete on the order of wavelength size. The dry-coupled transducer array unit is a commercially available dry-coupled transducer array system that collects shear wave signals reflected from internal reflectors. The synthetic aperture focusing technique (SAFT) reconstructs an internal image. The image is generated from the ensemble of reflected signals, identifying internal reflectors such as voids and steel bars (Hoegh and Khazanovich 2011, Shevaldykin et al. 2003, De La Haza et al. 2013, Maierhofer et al. 2010, Shokouhi et al. 2011). SAFT numerically superposes the reflected signals within the ensemble, and corrects for the expected beam spread of the transducer. The measured signals are focused to every pixel in the process, such that scattering noise significantly decreases with increased spatial superposition (Schickert et al. 2003). The approach offers the benefit of providing internal information about concrete using a relatively straightforward, one-sided testing procedure with an array of transducers.

Although one-sided s-wave array technology offers practical benefits, it also suffers from some limitations. For example, the array requires physical contact with the concrete surface for a short period of time, such that the data collection process may be slower and more labor-intensive than is acceptable for tests on large structures. Also, information throughout the full cross-section of deep structures may be incomplete because of insufficient wave energy penetration or shadowing behind layers of densely placed steel reinforcement bars. Finally, SAFT images built up of data from one-sided arrays are known to be insensitive to near-surface reflectors and vertical interfaces because of the inherent nature of the sensor's surface-based configuration and imaging process (Muller et al. 2012). Thus a "blind zone" is created, which extends to a depth of approximately 1.5 in. (38 mm).

Schematic illustrations of test configurations are presented in Fig 5.1, including conventional contact ultrasonic testing (top), hybrid/air-coupled ultrasonic pulse velocity (middle), and dry-coupled ultrasonic

pulse echo. The conventional ultrasonic test configuration for concrete requires a gel-type couplant to reduce acoustic impedance mismatch between sensor and concrete. This coupling process can restrict practical application of the ultrasonic methods to full-scale concrete structures. In order to overcome this limitation, hybrid air-coupled and dry-coupled ultrasonic transducers have been introduced, which do not require the use of couplant.

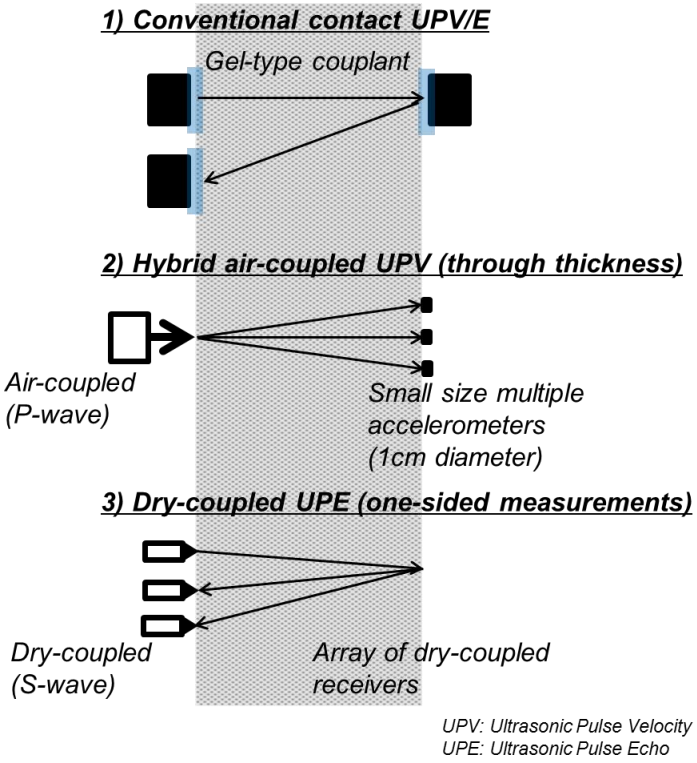

Figure 5.1 Schematic illustration of sensor configurations for ultrasonic methods.

In this work, hybrid/air-coupled and dry-coupled transducers are deployed to the full-scale RC column mock-up described in Chapter 4. Through-thickness ultrasonic data are used to reconstruct velocity tomograms that represent internal defects within the specimen as presented in Chapter 4. One-sided ultrasonic signals are used with SAFT imaging to reconstruct the same sectional images. This work reports a comparison of full thickness internal imaging for large concrete structures with the aim of broadening and optimizing the application of ultrasonic tomography techniques to the civil infrastructure, especially for steel reinforced concrete structures. Furthermore, understanding the relative strengths and limitations of each technique contributes to the development of improved sensors, test setups, and experimental configurations.

5.1.1 Dry-coupled ultrasonic pulse echo unit

A commercially available dry-coupled transducer array (the "MIRA" unit produced by Acsys) is used to collect data for all SAFT data presented here. The device consists of twelve columns of a four dry-point coupled transducer set. The transducers are designed to transmit and receive 30-80 kHz shear-horizontal (SH) waves polarized perpendicular to the long axis of the array. Each column of four transducers transmits and receives simultaneously as a uniform sensor set. The data acquisition hardware operates at a 1 MHz sampling rate. The transducer firing sequence is configured to transmit with Set 0 and listen with Set 1, Set 2, etc. as illustrated in Fig 5.2. Then Set 1 transmits and sequentially detected by Set 2, Set3, etc.This process repeats until all array combinations are captured. The measured signals by the dry-coupled transducer array are extracted and analyzed with various commercial (Ideals by Acsys) and public (OpenSAFT) software packages (Bittner 2015).

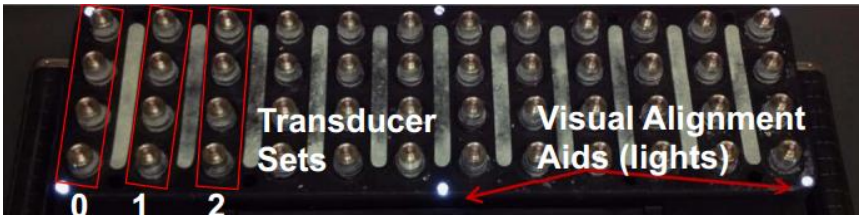

Figure 5.2 Bottom view of ultrasonic multi-element shear wave dry point contact array test unit.

5.1.2 Data measurement from full-scale RC column mock-up

The dry-coupled ultrasonic test equipment was applied to the full-scale RC column mock-up that includes pre-embedded artificial defects described in Chapter 4. A commercially available ultrasonic shear wave array testing unit was applied to one outer vertical surface of the column as shown in Fig 5.3. The spacing of dry-contact transducers within the 12 x 4 sensor array is 1.2 in. and 1 in. (30.5 mm and 25.4 mm) in the horizontal and vertical directions within the array, respectively. A total of 1600 signals were collected, obtained with overlapping footprint placements of the array unit across the tested surface. The array was moved in segments of 2 in. (50.8 mm) along its axial direction such that 11 array footprints were needed to achieve a complete footprint overlap. The s-wave pulse frequency was 50 kHz. All data measurements across the face of the column took one hour to complete. The collected data set was used to make multiple sectional images for defect detection. The data acquisition device used in the experiments provided a sampling rate of 1 MHz.



Figure 5.3 Application of dry-coupled ultrasonic pulse echo test unit.

5.1.3 Synthetic aperture focusing technique

The SAFT procedure consists of preprocessing signals, indexing the correct portion of each signal to each pixel, and applying scaling factors, as illustrated in Fig 5.4. The first step in the SAFT algorithm is to apply signal processing algorithms to increase the signal to noise ratio of the individual time signals. The signal data were band-pass filtered using the Matlab platform. The selected frequencies for the pass band and the end band were 20 kHz and 80 kHz, respectively. The pass band ripple was 1 dB, and the filtered band attenuation was 50 dB. The processed A-scan signals are presented in Fig 5.4a. It is noted that the arrival of the surface-guided shear wave mode needs to be identified in the time signals obtained between transducer arrays in order to determine the shear wave velocity at that test location. Subsequently, the surface-guided shear wave pulse in the time signals is windowed out because these wave components do not reflect from internal defects, and thus cause disruption to the SAFT reconstruction algorithm. The removal of the surface-guided shear wave component thus creates a near-surface "blind zone" wherein information within several centimeters beneath the surface is not obtained.

The second step is to apply a directional apodization factor to average the received array signals based the transducer locations along the surface (Fig 5.4b). The apodization factor accounts for the beam radiation pattern of the transmitter, which is a weighting parameter in a function of the pixel and transducer locations (Clayton et al. 2013). A typical apodization factor (Fig 5.4c) for a unique transmitter/receiver pair at point (Xs, Zs) is

$$A = \frac{Z_s}{\sqrt{X_{Reciever}^2 + Z_s^2}} \times \frac{Z_s}{\sqrt{X_{Transmitter}^2 + Z_s^2}} . \quad (5.1)$$

where Z_s is the distance from the point to the inspection surface, $X_{Receiver}$ and $X_{Transmitter}$ are the distances between the point and the transmitter or receiver along the surface.

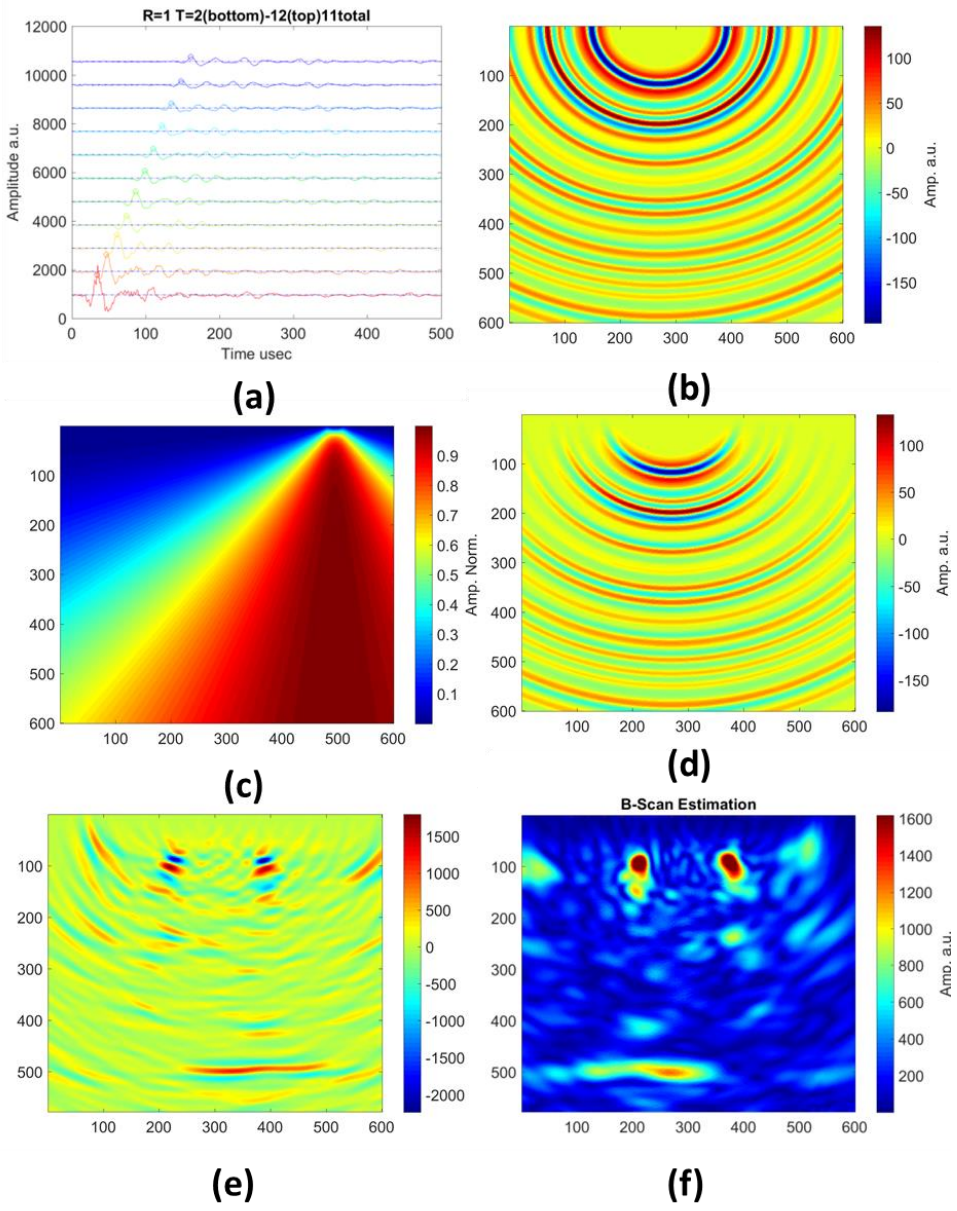

Figure 5.4 Graphical sequential illustration of the SAFT process: (a) A-Scan signals after signal processing, (b) single A-Scan integrated about region of interest, (c) apodization factor for one transducer pair, (d) integration of scan data and apodization factor, (e) summation of all transducer pairs, and (f) final B-scan after Hilbert transform (Distance units in mm).

The third step presented in Fig 5.4d is performed through application of a general synthetic aperture to the collected signal data

$$f(x,z) = \sum_{N_{Pairs}} \int_{t_0}^{t_1} A \times Signals(t, X_{Transmitter}, X_{Receiver}) dt \tag{5.2}$$

where t_0 and t_1 are an absolute time of initial and final points that encompasses the representative signal duration for the pixel size and $Signals$ are the recorded signal contents as a function of the pixel and transducer locations and (Clayton et al. 2013). The solution requires a defined region of interest in two-dimensional spatial terms (x, z) to be resolved. For every point in the region, the shortest distance between the emitter transducer and the receiver transducer must be calculated. With an obtained or assumed shear wave speed, the estimated time of flight for a potential echo from this reflector pixel is defined. These calculations result in an array of estimated time of flights for each unique sender and receiver pair to each pixel.

Next, every pixel is summed across all sender receiver pairs (Fig 5.4e). This computation results in a single pixel within the composite SAFT image. This summation is repeated for every pixel in the B-scan region of interest. The final step of the SAFT algorithm is to obtain the magnitude of the Hilbert transform operated over the columns of the resulting B-scan image (Fig 5.4f). The Hilbert transform provides an amplitude scale of the reflection rather than a direct sinusoidal plot (Langenberg et al. 2012).

The computations for this work are carried out using the Matlab platform and the public SAFT processing code OpenSAFT (Bittner 2015). The quality of the processed SAFT image by Matlab was observed to match or exceed the images calculated by supplied commercial software for the ultrasonic device. The shear wave velocity was approximated based on the arrival of a wave packet along the surface of the column. The total time for computation for SAFT processing was recorded as approximately 3-5 seconds per ultrasonic inspection location, resulting in a total processing time of a few minutes. Each individual B-Scan image was combined into a panorama, based upon the global position of each pixel. The maximum signal amplitude at each pixel was stored for the resulting panorama image (De La Haza et al. 2013, Clayton et al. 2013).

5.2 Data processing for velocity tomography

Velocity tomograms indicate the locations of embedded defects using variation in color. Interpretation of a single cross-sectional image, however, may not be sufficient to accurately assess the condition of the whole structure. Although true 3-D tomography provides many benefits, the required tests and analysis are

computationally expensive. In this work, we generate 3-D tomographic reconstructions of an object using a set of stacked 2-D tomogram slices (Lee et al. 2013). Multiple stacked tomograms provide enhanced visual interpretation over that provided by one image slice. Twenty different velocity tomograms reconstructed using data collected from the column were stacked with 2 in. (50.8 mm) vertical spacing along a 3-D axis; the individual image slices are linearly interpolated to produce a 3-D volumetric data set. An example of stacked images is shown in Fig 5.5, where several image sections are extracted and displayed. The vertical velocity map accurately identifies the positions and sizes of both void defects and one of the cracking defects as low P-wave velocity regions, in good agreement with the original specimen design.

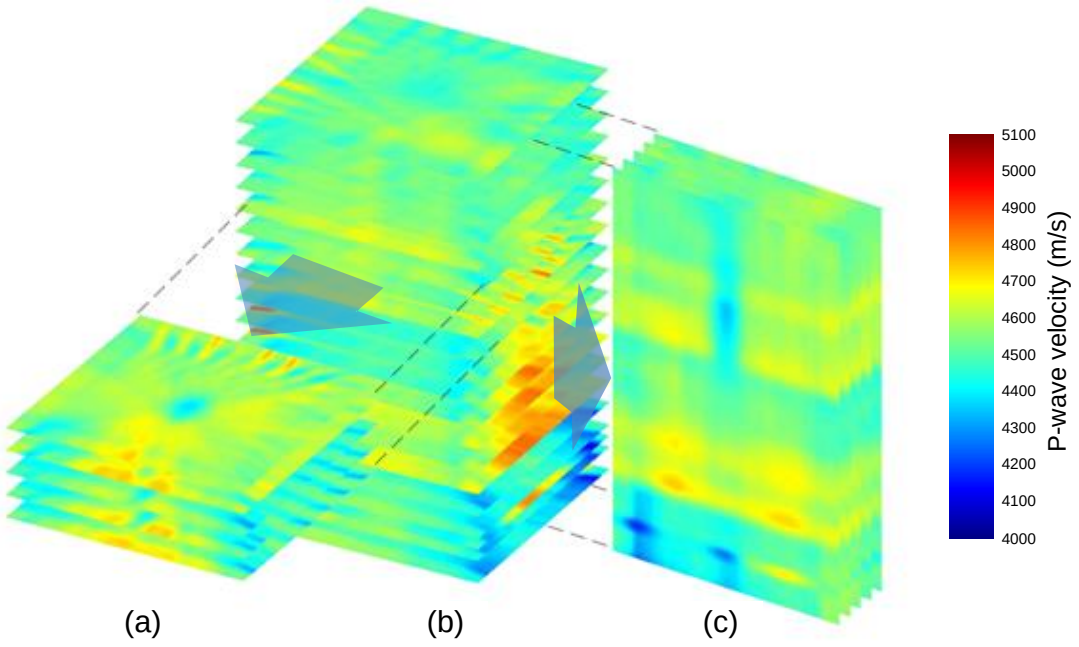

Figure 5.5 Stacked P-wave velocity tomograms: (a) horizontal images around section A-A (b) stacked tomograms through the height of the concrete column (c) vertical section images around the center of the column specimen.

5.3 Analysis of two imaging methods

The vertical section images generated by the developed tomography and by the SAFT algorithms from the same concrete column are compared in Figs 5.6 and 7. Because SAFT images are reconstructed based on reflected amplitude and the beam spreading factor of transducers, the units within the images represent

arbitrary reflection intensity. The images show a distinct red color (high reflection intensity) where inclusions are most likely located.

The images shown in Fig 5.6 represent the central vertical section of the column that contains Styrofoam toward the top and another Styrofoam pre-cracked prism toward the bottom. Both velocity tomogram and SAFT image accurately indicate the location of the central void defect on top part of the column. However, the SAFT image provides no information about internal defects within the bottom portion of the column, where the higher volume of steel bars is located. This is likely caused by the intense ultrasonic reflection from the mat of bars, which creates a shadow zone in the column volume behind the bars. The inability to image behind densely placed reinforcing bars poses difficulty for one-sided ultrasonic imaging methods such as SAFT, especially for heavily reinforced seismically-critical concrete structures.

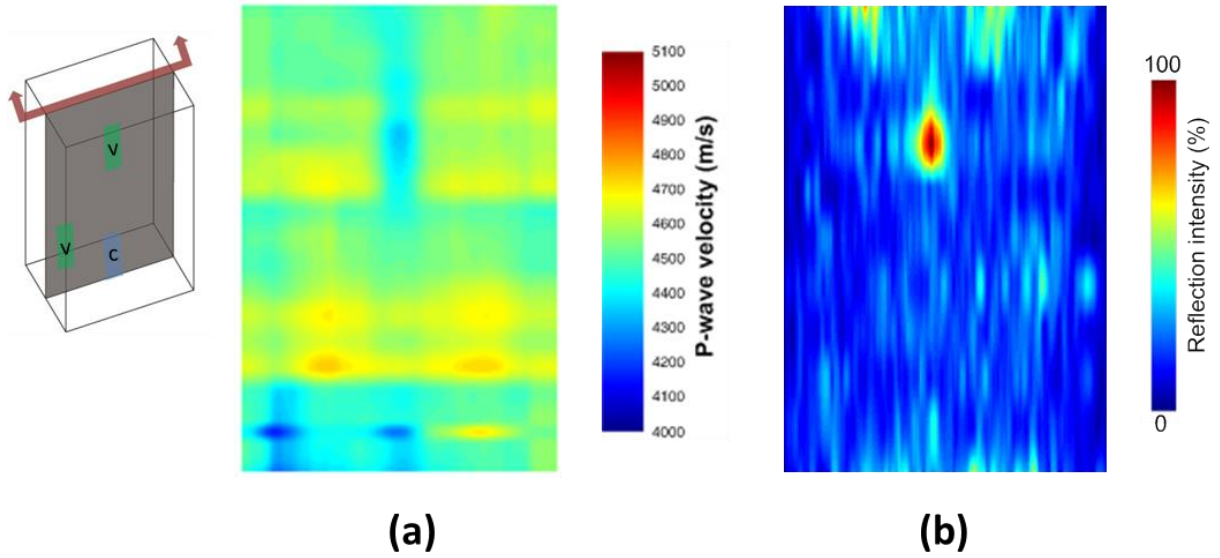

Figure 5.6 Sectional images representing the full height of the column specimen along a plane at the center that includes artificial defects: (a) vertical section tomogram built up from two-sided velocity data, and (b) vertical section SAFT image built up from s-wave array data.

The vertical tomogram provides no specific information about embedded rebar as seen in Fig 5.7a, while the SAFT image clearly shows vertical bars embedded in concrete column in Fig 5.7b. This difference may occur because transmitted P-wave velocity is less affected by embedded rebar in concrete. In the case of one-sided S-wave measurement, however, a relatively large amount of reflection would likely occur at the interface between concrete and steel. It is noted that steel reinforcing bars does not significantly perturb the wave arrival across RC cross-section, while they do affect reflection due to the acoustic impedance mismatch and close proximity to one-sided transducers. Therefore, SAFT image presents the location of embedded rebar with same frequency component, while velocity tomogram does not.

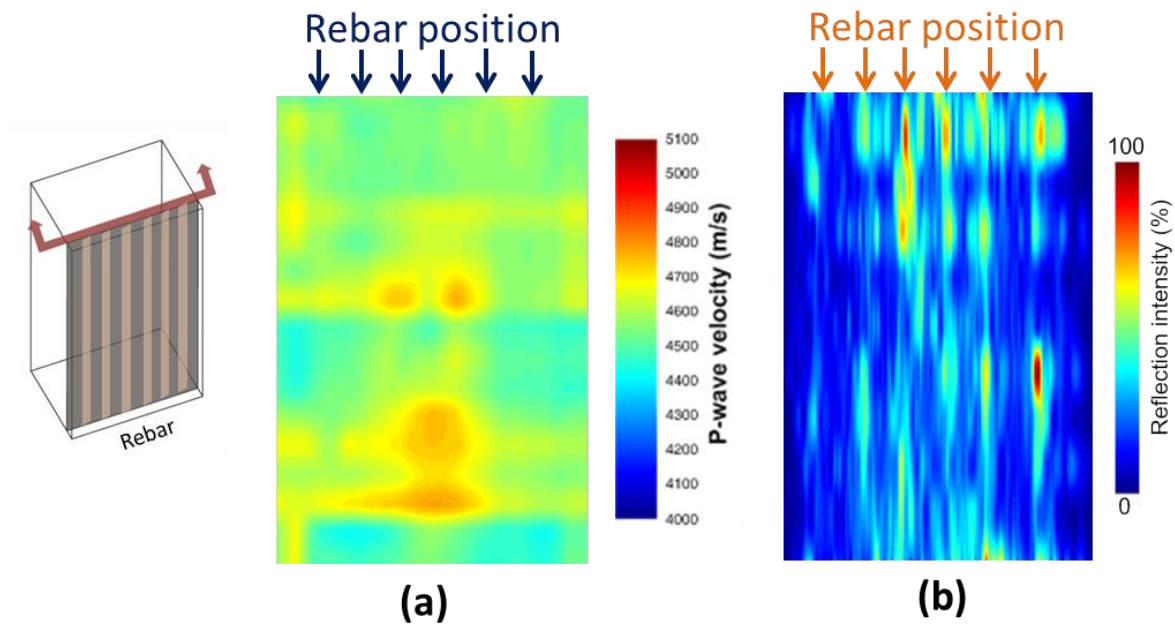

Figure 5.7 Sectional images representing the height of the concrete column specimen along a plane near a free surface including rebar: (a) vertical section velocity tomogram built up from two-sided ultrasonic data, and (b) vertical section SAFT image built up from s-wave array data.

Overall, the vertical velocity map of the developed tomography method accurately identifies the positions and sizes of both void defects and one of the cracking defects. These results are in good agreement with the original specimen design, and are not adversely affected by the presence of rebar. The SAFT image identifies where artificial defects are embedded at the upper part of the column; however, no information about defect presence is provided for the lower half of the column, which has more densely placed rebar.

For the inspection of reinforced concrete structures, we need to understand and exploit these differences between the two ultrasonic imaging techniques and apply the most suitable method for given applications in the field. Optimal application of each depends on the type of structure tested and the image target of interest. For example, velocity tomograms constructed from through-thickness data show superior performance for isolated critical concrete elements that contain high volumes of steel reinforcement. On the other hand, SAFT imaging techniques show superior performance for detecting volumetric inclusions like rebars or voids.

CHAPTER 6 INTEGRATED VISUALIZATION

In this chapter, a new comprehensive visualization scheme that characterizes reinforced concrete structures using a fusion of ultrasonic tomograms and 3-D computer vision images, is investigated. An automated image-based 3-D reconstruction technique is applied to the full-scale RC column described in Chapter 4 to visualize external condition. The work described in this chapter broadens visualization capability for the civil infrastructure, especially reinforced concrete structures. The fused images expand the capability to evaluate structures in a new way. The experimental results demonstrate that such integrated visualization provides holistic characterization of the interior and exterior of concrete, thus providing potential for improved inspection capability for existing structures in the field. A portion of the work described in this chapter was published in a journal paper titled "Integrated visualization for reinforced concrete using ultrasonic tomography and image-based 3-D reconstruction" published in *Construction and Building Materials* (Choi et al. 2016).

6.1 Reconstruction of external surface condition

Prior efforts to apply image-based 3-D reconstruction for concrete structural condition assessment were limited to exterior evaluations, such as surface crack detection (Jahanshahi and Masri 2012, Torok et al. 2013). The integrated graphical representation of ultrasonic tomograms and point cloud models can provide infrastructure inspectors an intuitive and cost effective approach to assess structural condition powered by a 3-D virtual environment. An external 3-D reconstruction in the form of a point cloud is built up from individual digital photographs using Structure-from-Motion (SfM) (Snavely et al. 2008) and Multi-View Stereo (MVS) algorithms (Furukawa and Ponce 2008). This approach automatically generates 3-D geometrical models of an object from unordered collections of digital photographs of that object.

6.1.1 Structure from motion and multi-view stereo

The data collection and image processing associated with image-based 3-D reconstruction are illustrated in Fig 6.1. A consumer-level digital camera is used to collect a set of photographic images of the object under inspection. The SfM process automatically computes the intrinsic (e.g., focal length and radial distortion parameters) and extrinsic (e.g., rotation and translation) camera parameters from a given set of images. In order to reduce the computational cost, a Graphic Processing Unit (GPU)-based SfM implementation is used, (Wu 2011) which consists of following steps: 1) detecting distinct visual features that are invariant to changes in illumination, rotation, and scale for all images; 2) matching their descriptors across each image pair using a nearest neighborhood matching algorithm; and 3) forming the Epipolar geometry between each image pair by estimating the Fundamental matrix within a RANdom SAmple Consensus (RANSAC) loop and fitting the Fundamental matrix in the RANSAC loop (Hartley and Zisserman 2004). By forcing the corresponding features to have consistent transformation, this process minimizes false

matches, which typically occur due to similar visual features, that are inconsistent by the general transformation from one camera to another; 4) selecting a pair of images for initializing 3-D reconstruction process based on the selection heuristics (Snavely et al. 2008) and deriving the relative translation and rotation between the initial image pair; 5) incrementally computing the camera parameters and the location of the 3-D feature points starting from an initial triangulation; and 6) optimizing the estimated camera parameters and the locations of the 3-D points using the GPU-based library (Wu et al. 2011) of the bundle adjustment algorithm (Triggs et al. 1999) to cut the computation time. Then, the resulting intrinsic and extrinsic camera parameters are fed into the MVS algorithm. In this process, distinct visual features detected by Harris and Difference-of-Gaussians (DoG) operators are first matched across all images, yielding a set of sparse patches (possibly including false positives). Then, expansion and filtering steps are iteratively implemented to make the patches denser and remove the false matches. Because the underlying reconstruction process generates a 3-D point cloud until image projections of the feature points cover all the registered images, an increase in the number of target images brings about denser 3-D reconstruction. The final outcome is a dense 3-D point cloud which represents the geometrical base of the given object.

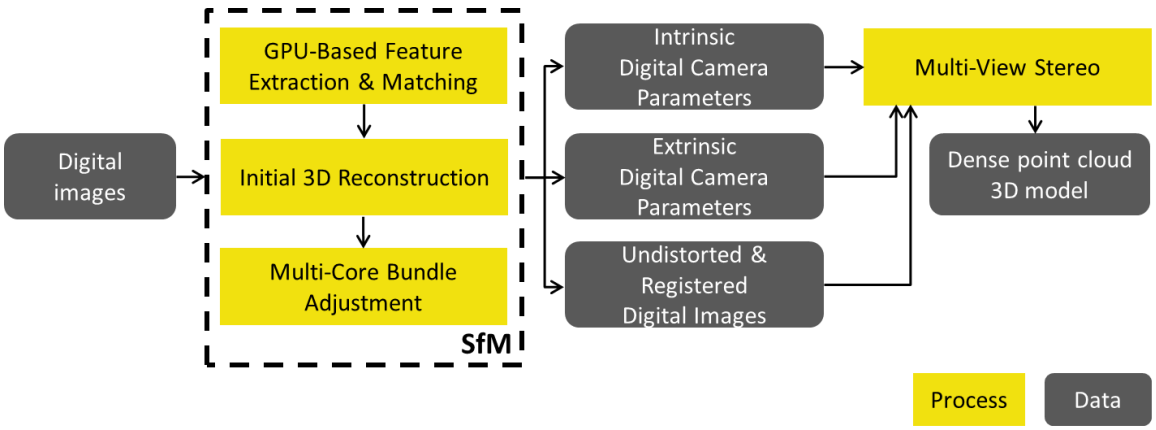

Figure 6.1 Flowchart describing the 3-D computer vision technique.

6.1.2 Data measurement and processing

A consumer-level digital camera (Canon EOS 60D) was used to collect 110 digital photos around the concrete column. Each photograph from the camera has a spatial resolution of 3264 × 2448 pixels. All vertical surfaces of the column were photographed from multiple perspectives. The photographs were collected from unordered positions of interest without strict regulation of the camera position, and the total procedure took less than 10 minutes. Figure 6.2 shows all camera positions for the photographs. Finally, the photographs were combined to generate a point cloud reconstruction of the surface of the specimen in simulated stereoscopic vision.



Figure 6.2 Illustration of image-based 3-D reconstruction from unordered photographs collected around a concrete column.

The external geometry reconstructed using the 3-D computer vision technique illustrates detailed geometric and surface properties of the test column. The 3-D point cloud model and a single photograph of the concrete column from the same viewpoint are compared in Fig 6.3. The surface characteristics, grid lines and marked numbers are indicated in both. However, the 3-D point cloud model offers benefits over the single photograph. For example, detailed dimensional information from the 3-D point cloud image provides geo-spatial references in virtual 3-D space. Furthermore, detail of concrete texture is provided. The 3-D image offers qualitative surface texture information such as color differences and level of roughness (flatness), as shown Fig 6.3b. The as-designed column is compared to the reconstructed model in terms of geometrical accuracy in Fig 6.4. The red box in the figure indicates the intended design shape of the column (Fig 6.4a), over which the 3-D point cloud model is overlaid (Fig 6.4c). The photo insets (Fig 6.4b) show the width of the column measured at a horizontal edge, where there is approximately 10 mm expansion at the bottom that is attributed to form construction error. Figure 6.4c illustrates the mismatch between the original shape of the column and reconstructed 3-D model, showing the construction error on the bottom part of the column. The 3-D model demonstrates high resolution surface visualization and geometric measurement and interpretation not provided by individual photographs.

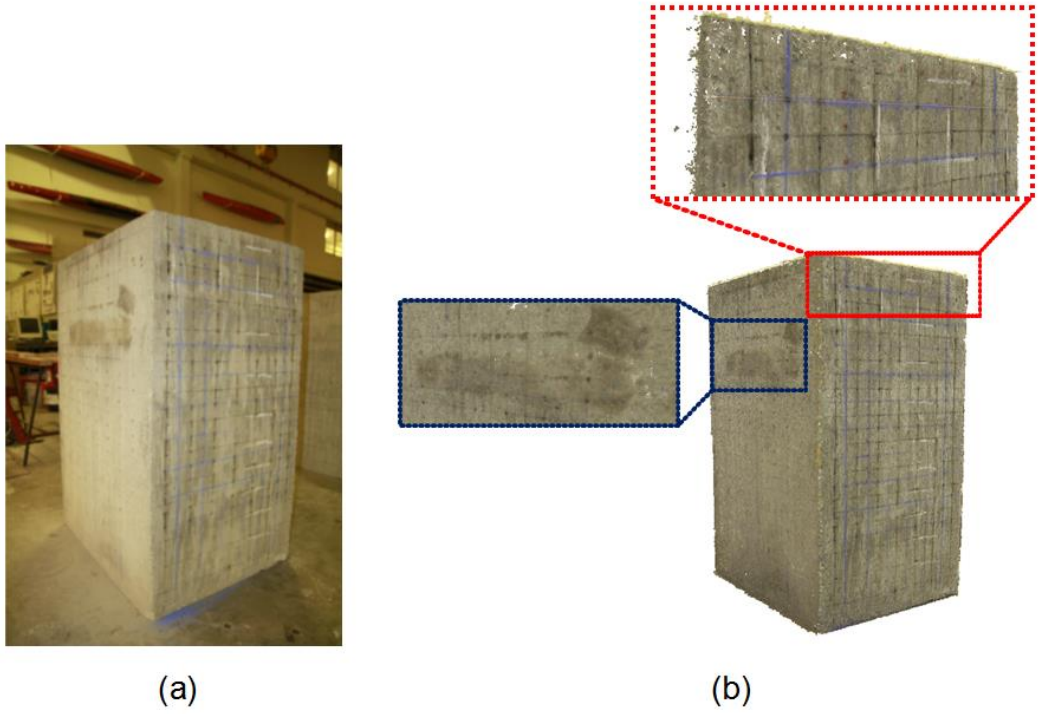

Figure 6.3 Comparison between photograph and 3-D point cloud model: (a) single photograph of the concrete column and (b) 3-D dense point cloud model of the concrete column, where insets show surface texture and coloring detail.

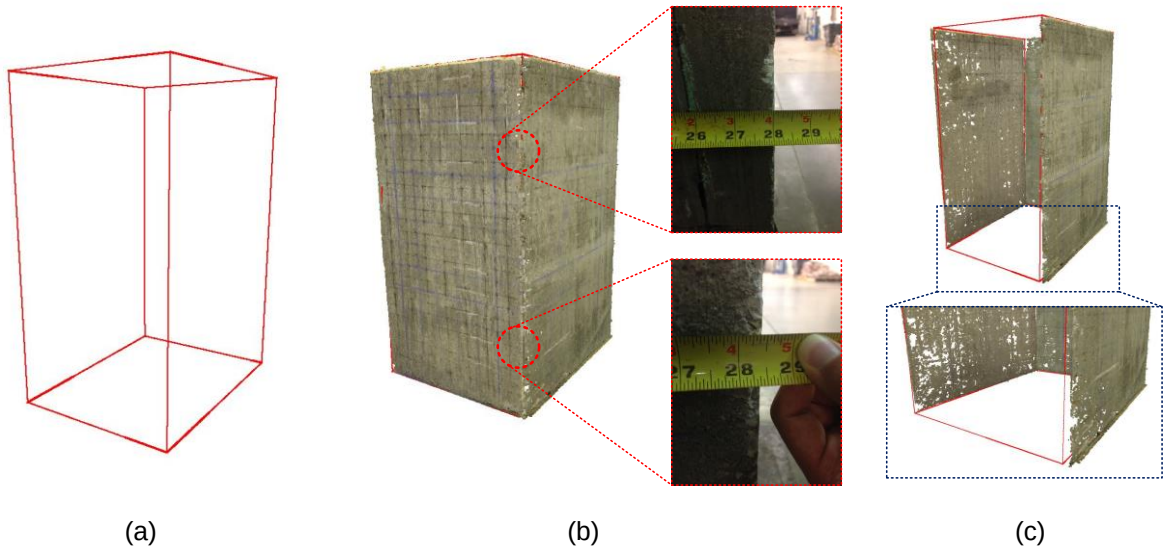

Figure 6.4 Comparison between the column as designed and 3-D point cloud model: (a) box frame representing originally designed shape; (b) 3-D point cloud model where insets show dimension details (1cm error in width); (c) 3-D point cloud model overlaid with the box frame, where insets reveal geometric construction error.

6.2 Integrated visualization

Figure 6.5 illustrates the process of 3-D visualization by integrating internal (e.g. tomogram) and external (3-D visualization) data. Cross-sectional ultrasonic P-wave velocity tomograms of the column were developed using the algebraic reconstruction technique described in Chapter 4. The individual image slices were linearly interpolated to produce a 3-D volumetric data set presented in Chapter 5. The external surface of concrete column was reconstructed in a virtual 3-D environment using the SfM-based computer vision technique. Then, multi-view stereo generated a dense point cloud model of the exterior of the concrete specimen. The resulting 3-D reconstruction was transformed into a real-world coordinate system by using the grid lines marked on the column as reference. Finally, the velocity tomograms and the reconstructed 3-D concrete column were integrated into a single 3-D environment and coordinate system. The tomograms were geo-registered with respect to the underlying reconstructed concrete column in 3-D axes.

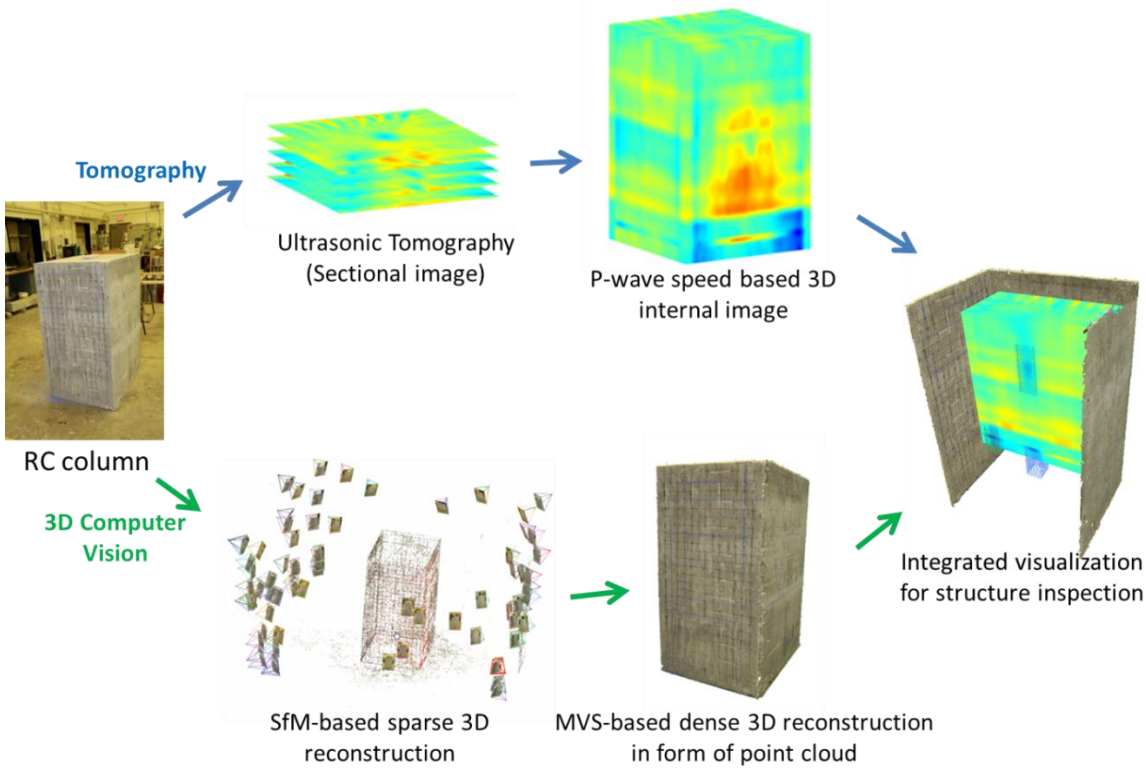

Figure 6.5 Graphical illustration of the integrated visualization scheme.

6.2.1 Registration of images in 3-D

Integrated visualization requires scaling, rotation and translation of 3-D external images to enable transformation into a new coordinate system with actual physical dimensions. The geo-registration in 3-D was performed using the closed-form solution of absolute orientation using unit quaternions (Horn 1987). The method assumes the transformation results from rigid body motion and assuming seven unknowns;

three from rotation, three from translation, and one from scaling, are needed to be solved. In the process, at least three voxel points were selected from the 3-D point cloud. Three points provide a total of nine constraints, which are enough to determine the seven unknowns. In this work, the eight corners and another eight mid points of the image were chosen as up-to-scale reference. Then actual coordinate values corresponding the selected points were generated based on direct measurement of the column. Using the closed solution, the values of scaling, rotation, and translation were calculated. Finally, every voxel point was transformed into new coordinate system with an actual dimension. The registration process and 3-D imaging analysis were performed using Matlab and Meshlab platforms, respectively.

6.2.2 Analysis of integrated visualization

In Fig 6.6, the integrated ultrasonic tomogram and 3-D point cloud image is illustrated for the column. The photo in Fig 6.6a shows the placement of artificial defects before casting concrete. Figure 6.6b shows the 3-D point cloud image of the cast column with the location of internal defects indicated by green and blue boxes for voids and pre-cracked concrete prisms, respectively. The integrated image is shown in fig 6.6c where blue colored zones, representing lower P-wave velocity, match well with the boundaries of internal defects marked by boxes. Figure 6.7 illustrates that the integrated visualization can be manipulated for improved utility, for example by viewing from different perspectives or by extracting portions of the image for detailed analysis. Figure 6.7a indicates the location of all embedded defects within the column, including the two pre-cracked prisms. In fig 6.7b, a partial cut-away perspective composed of integrated tomogram slides reveals that a part of the embedded cracked region is observed within the marked box, which is not clearly identified in any individual tomogram slice.

Integrated ultrasonic tomography and image-based 3-D reconstruction visualization provides more information beyond that from the individual visualizations alone. An integrated visualization provides intuitive understanding of positions of internal defects with respect to the external 3-D point cloud. Furthermore, integrated visualization enhances understanding of the nature of internal damage through the use of multiple perspectives or splice cuts. The 3-D virtual space enables users to analyze more data collectively across multiple cross-sections and perspectives, providing benefit over individual 2-D based cross-sectional tomograms.

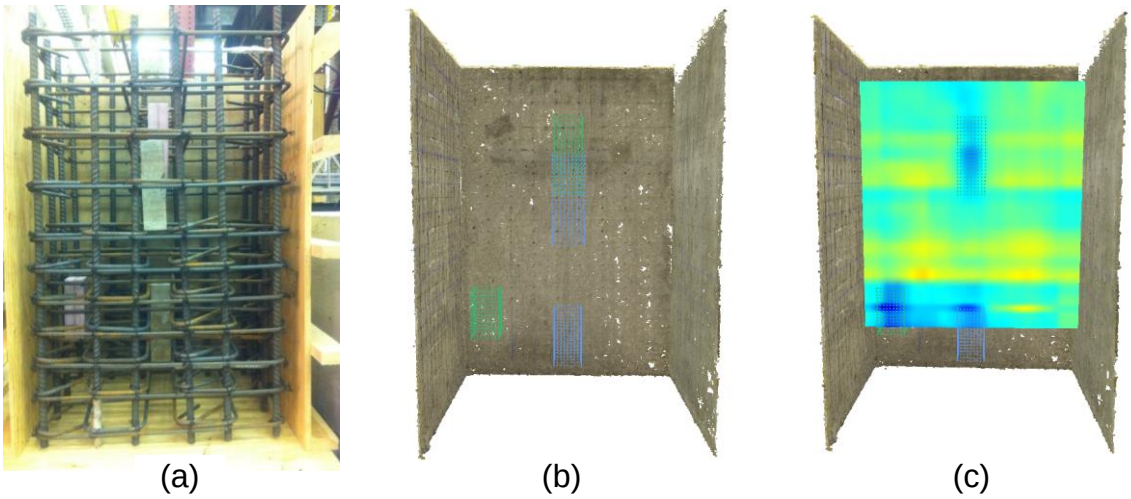

Figure 6.6 Integrated visualization of tomograms and image-based 3-D reconstruction: (a) Photograph of sample before casting concrete, (b) 3-D dense point cloud model of the concrete column where position of defects (green box: Styrofoam, blue box: pre-cracked) are also indicated, and (c) integrated interior and exterior images showing relative position of internal defects.

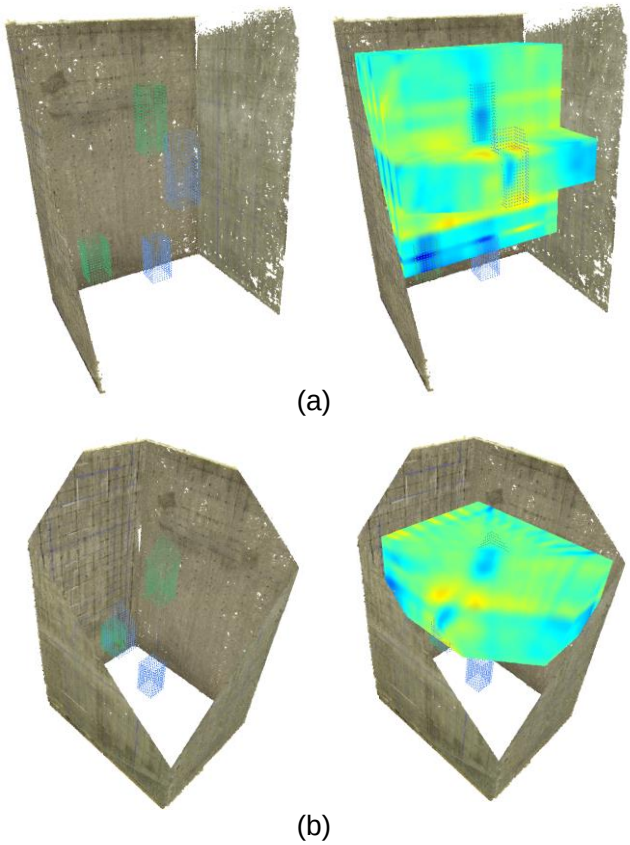

Figure 6.7 Integrated visualization fields from different perspectives; (a) side views and (b) top views.

CHAPTER 7 VELOCITY TOMOGRAPHY APPLIED TO RC COLUMNS SUBJECTED TO SEISMIC LOADING

In this chapter, the developed hybrid air-coupled ultrasonic testing system and ultrasonic velocity tomographic schemes are applied for the first time to full-scale reinforced concrete (RC) columns subjected to simulated earthquake loading, demonstrating that large amounts of high quality ultrasonic data can be obtained from concrete structures under test and transformed into useful images. The developed ultrasonic tomograms demonstrate that decreases in global P-wave velocity within a cross-section correlate well with global damage from applied simulated seismic loads, as characterized by column-stiffness slope. Also, localized decreases in velocity from tomograms correlate well with increases in residual strains from transversely and axially embedded strain gauges. The UHP-FRC column shows distinct responses to simulated seismic loading as compared with conventional RC columns; UHP-FRC column exhibits relatively low residual strain and slow rate of P-wave velocity loss with loading.

7.1 Application of velocity tomography to RC columns

The seismic performance of reinforced concrete columns is normally characterized by monitoring cracking, rebar debonding, yielding of rebars, and crushing damage that develops during the earthquake loading. External images (e.g. photographs) cannot fully assess damage that occurs below the visible surface, and embedded internal strain gauges provide information within the interior at only a few points where they are located and thus cannot give comprehensive information across the internal volume. Non-destructive imaging can overcome these restrictions, providing more complete and useful information about internal damage state after an event. The developed hybrid air-coupled ultrasonic methods enable large amounts of ultrasonic data to be collected, providing new and powerful potential for structural evaluation. Seismic performance of three different full-scale RC columns and one UHP-FRC column is investigated in this section.

7.1.1 Description of full-scale RC columns

The dynamic response of three different full-scale RC columns and one UHP-FRC column subjected to simulated seismic loading is investigated. Table 7.1 shows detail about the geometry and material make-up of the columns. Two columns, including one composed of UFP-FRC, have a square cross-section of 28 by 28 inches (711.2 by 711.2 mm) and represent the interior column of a building. The other two columns have a larger rectangular 36 by 28 inch (914.4 by 711.2 mm) cross-section and represent an exterior column of a building. Figure 7.1 shows the column details including location of installed strain gauges and the cross-section where ultrasonic scanning performs. At the cross-section, the three set of gauges are embedded in the direction of X' (CTRH), Y' (CTRB), and axial (CL) of the column as shown in Fig 7.2,

respectively. The cross-sections where the ultrasonic tests were carried out are expected to have relatively large amount of cracking damage, where the plastic hinge can be made under the earthquake loads.

Table 7.1 Details of the test specimens and procedures.

Specimen	$b \times h$ in. ×in. (mm× mm)	f'_c, ksi (MPa)	Loading protocols	Ultrasonic scanning test (drift levels when the tests were performed)
RC1	36×28 (914×711)	4.61 (31.78)	Near Collapse	Yes (0%, 0.5%, 1%)
RC2	36×28 (914×711)	4.90 (33.78)	Bi-Axial	Yes (0%, 0.75%)
RC3	28×28 (711×711)	5.27 (36.34)	Symmetric Cyclic (ACI 374-05)	No
UHP-FRC	28×28 (711×711)	22.9 (157.89)	Symmetric Cyclic (ACI 374-05)	Yes (0%, 0.25%, 0.5%, 1%)

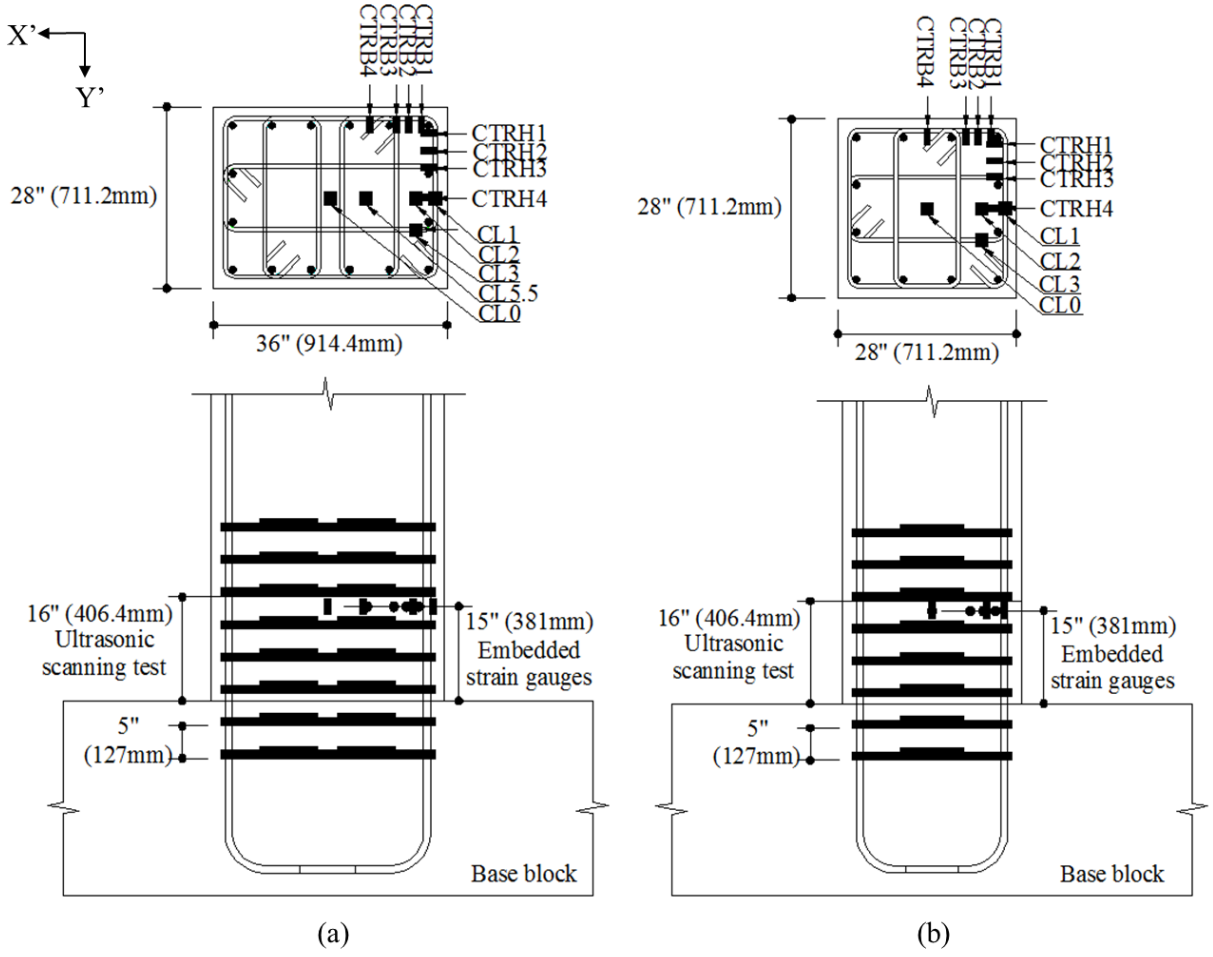

Figure 7.1 Detail of columns and embedded strain gauges (a) RC1 and RC2 (b) RC3 and UHP-FRC.

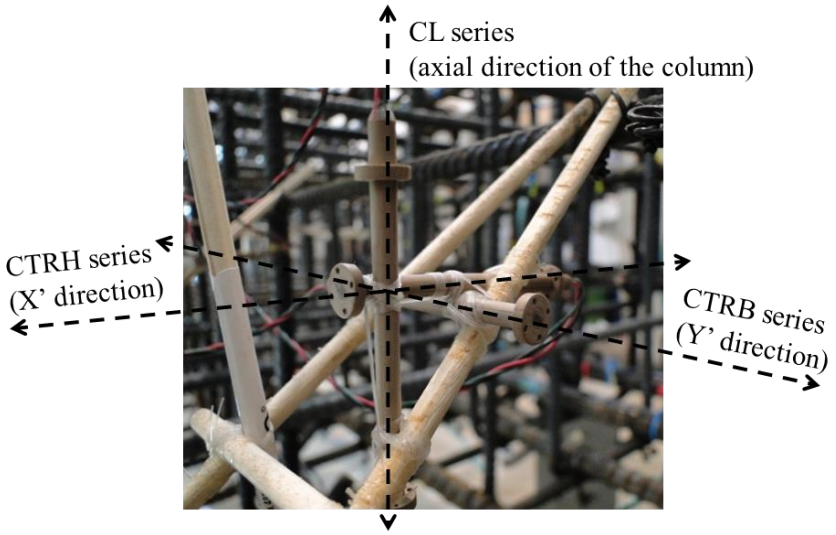

Figure 7.2 Illustration of embedded concrete strain gauges.

Figure 7.3 shows the experimental column testing configuration, where the X' and Y' directions are defined. These tests are a part of a research project funded by Network for Earthquake Engineering Simulation (NEES) of the National Science Foundation (NSF) (Appendix B). The columns were tested at Multi-Axial Sub-Assemblage Testing (MAST) Laboratory at the University of Minnesota. Figure 7.4 describes the loading protocol applied to each column. The drift level is the ratio between the height of specimen and lateral displacement under the seismic loading. Column RC1 column was subjected to bi-axial loading protocol while columns RC2, RC3 and UHPFRC were subjected to only transverse loading in the Y' direction as indicated in Fig 7.4.

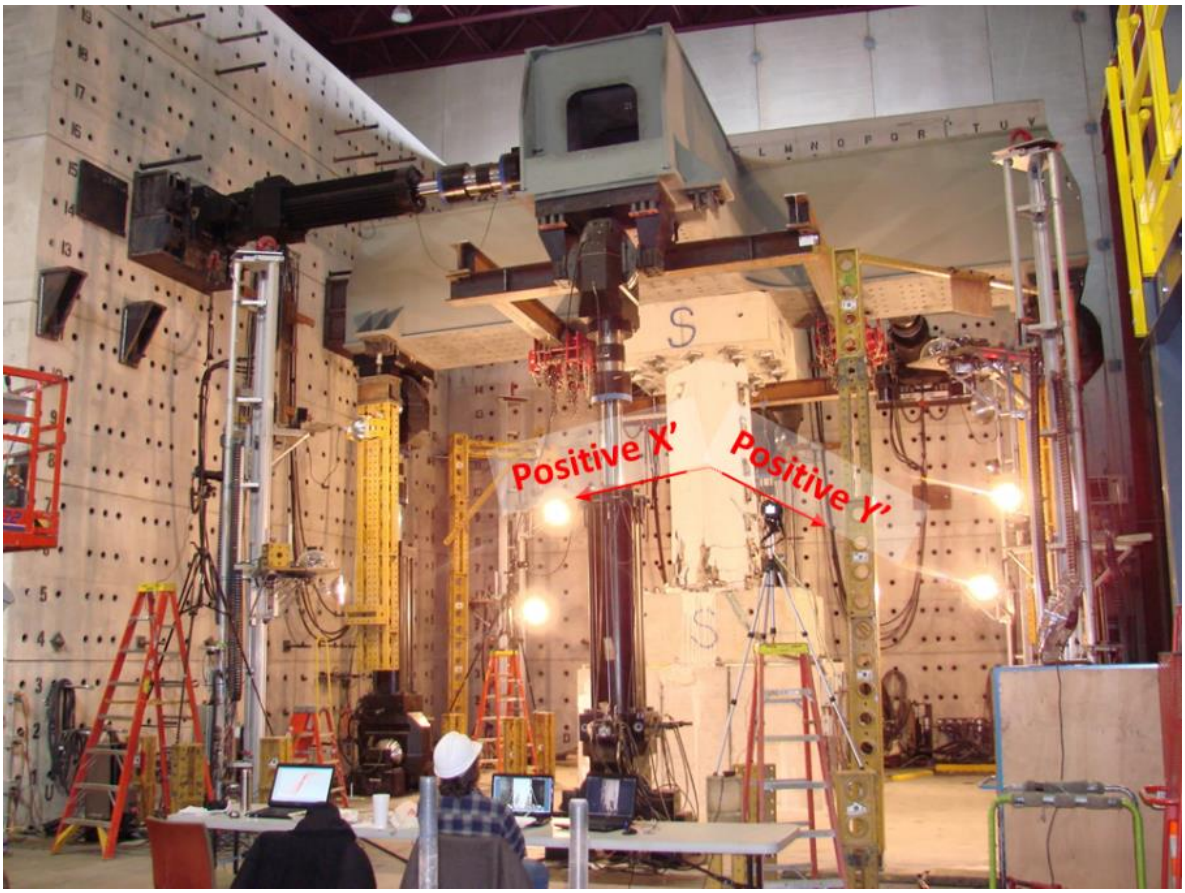

Figure 7.3 Experimental set-up to test full-scale columns at the Multi-Axial Subassemblage Testing (MAST) laboratory.

Ultra-high-performance fiber-reinforced concrete (UHP-FRC) is an innovative material which offers high compressive strength (172~207 MPa) and shear strength with high performance of ductility and excellent confinement characteristics (Aghdasi et al. 2015, Palacios, 2015). The beneficial properties of UHP-FRC can be exploited to reduce excessive transverse reinforcement needed for seismic design in a column. The UHP-FRC mixture used in this research was specially designed to maximize the dense particle packing concept, and showed self-consolidating properties at the time of placement.

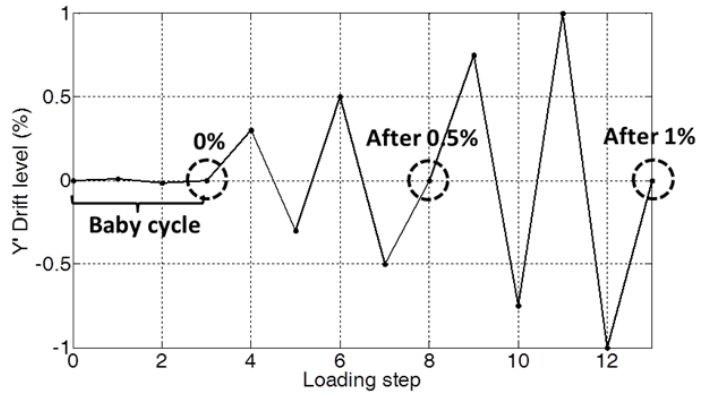

(a)

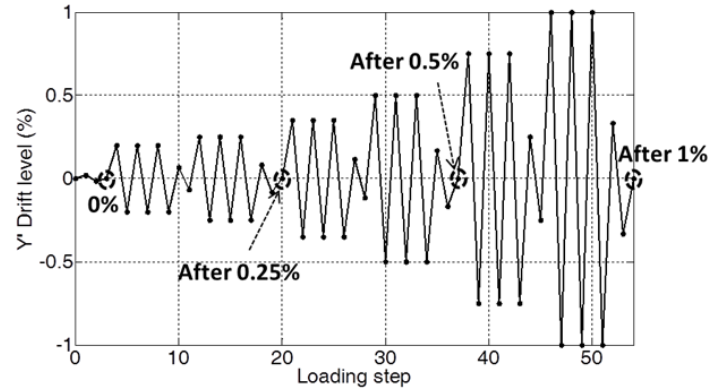

(b)

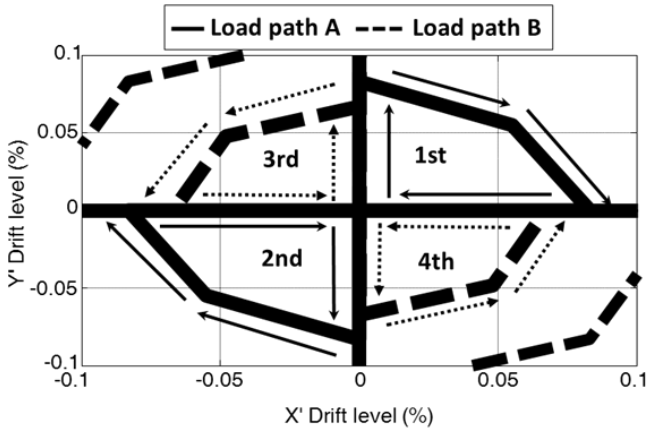

(c)

Figure 7.4 Applied loading protocols, where dotted circles indicate instance of ultrasonic scanning tests in terms of applied drift level for columns (a) RC1 and (b) RC2, RC3, and UHP-FRC. The bi-axial nature of the loading protocol for column RC2 is illustrated in (c).

7.1.2 Ultrasonic data measurement

The RC columns including RC1, RC2 and the UHP-FRC were tested with ultrasonic scans along the indicated cross-section height. Column RC3 was not tested with ultrasonic scanning, but mechanical response results are included here for comparison purposes. The ultrasonic waves were generated by an air-coupled transducer (SensComp 600) that was positioned approximately 3 in. (76.2 mm) above the surface of the column. The air-coupled transducer was fixed in a motorized testing fame that precisely controlled horizontal position of the sensor at a set height above the surface. The ultrasonic generating system and transducer produced 16-cycle 50 kHz pulses, where the ultrasonic pulses were projected normally on the surface of the concrete column. The test configuration is illustrated in Fig 7.5a. The ultrasonic transducer was moved horizontally at 0.5 in. (12.7 mm) or 1 in. (25.4 mm) increments along the horizontal scan line, and ultrasonic pulse was generated at each position increment. On the opposite side of the column, multiple accelerometers (PCB 352c15) were physically attached on the surface and placed along a line that was parallel to the scan line followed by the air-coupled transducer; these lines define the scanned cross-sectional of the column. An array of eight accelerometers were mounted with 4 in. (101.6 mm) spacing between sensors for columns RC1 and RC2. An array of ten accelerometers were mounted with 3 in. spacing (76.2 mm) between sensors for column UHP-FRC. At each position increment of the ultrasonic transducer, individual time signal was time-averaged ten times. The time signals sensed by the accelerometers were sent through a signal conditioner (PCB 442c04) for 100 times signal amplification and then collected by a digitizing acquisition unit (NI USB-6366) at a 2 MS/s sampling rate.

The responses from all attached accelerometers were collected for each transducer sending position, and the propagation time required for the P-wave pulse to travel from the sending transducer to each accelerometer was measured from the time signal. Because P-wave velocity in air (around 340 m/s) is much lower than that in normal concrete (around 4500 m/s), small variations in the air-gap between the air-coupled transducer and the column surface affect the total measured propagation time. To correct for this, the gap at every sending transducer position was measured using ultrasonic wave reflection through the air gap by companion ultrasonic transducer placed next to the sending transducer before performing the through-thickness measurements. The reflected time signal was used to measure the travel time of the P-wave propagating through the air gap and then that value was subtracted from the total through-thickness propagation time measurement to obtain the estimate of propagation time through the wave path in concrete.

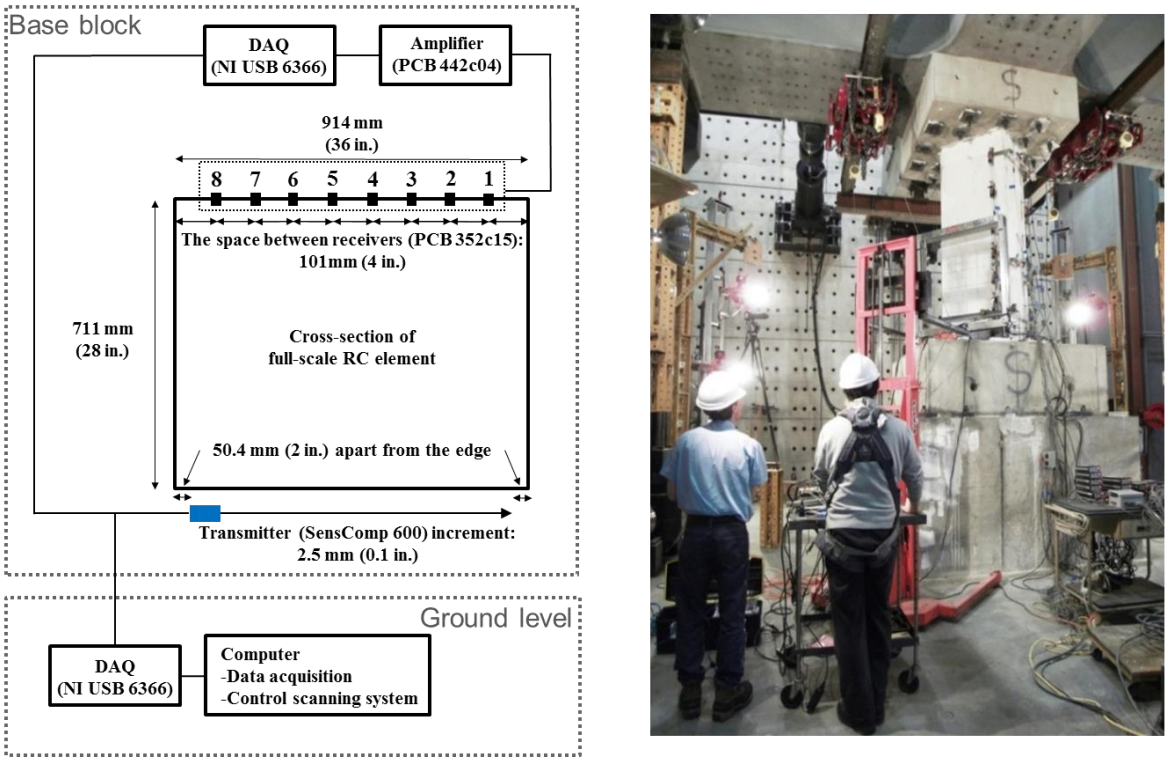

Figure 7.5 Detail of ultrasonic scanning tests: (a) ultrasonic testing configuration, (b) application of ultrasonic scan to column.

The P-wave pulse was assumed to travel along a straight line through the column from the surface point on which the ultrasound was projected to the location of each receiving accelerometer, so a path distance could be computed for each sending and receiver position. By collecting such data sets for each sending transducer position, a cross-cutting nexus of ray paths, each with a measured P-wave propagation time and computed path length, is formed across the scanned column cross-section. Figure 7.5b shows a photo of the ultrasonic test scanning configuration applied during a column load test and a schematic illustration of the sensor positions. A total 288 and 440 signals were obtained across the cross-sections of columns RC1 and RC2, respectively, while 550 signals were obtained from column UHP-FRC. Complete ultrasonic cross-sectional scans were conducted after a certain level of loading cycles as defined by the column drift. For each scan set, the column was returned to the neutral position (0% drift) after loading and maintained in that position during the ultrasonic scanning procedure. Before each ultrasonic scan, the controlled scanning frame was installed near the test specimen, as seen in Fig 7.5b, where the scanning process of was controlled remotely from the test floor.

7.1.3 Development of velocity tomography

Each measured ultrasonic signal was processed to remove noise content. Using the Matlab platform, low-pass filter was applied with a stop band value of 100 kHz. P-wave arrivals from each signal were automatically picked by a statistically based threshold method (King 2012), which assumes the statistical distribution of signal noise amplitude shows Gaussian behavior. A threshold signal amplitude value of 3.3 standard deviations from the mean of noise amplitude is assigned. The statistically calculated threshold method provided the most stable performance to determine pulse arrival times in low-amplitude signals compared to the other auto-picking algorithms such as the Akaike and Hinkley criteria (Carpinteri et al. 2012, Hu et al. 2013).

The data set for one complete cross-sectional scan contains P-wave propagation time and computed path length for each of the ray paths. Using this data set, the linear equation (Eq 3.1 in Chapter 3) is used to invoke the tomographic algorithm. First, two matrices were created; the P-wave arrival time matrix, t_i from the obtained ultrasonic signals and the ray travel distance matrix, d_{ij}. The size of the matrices is N (number of measurements) by 1 and N by M (assigned number of the pixels in the image) for ti and d_{ij}, respectively. The assigned numbers of N and M in each experiment are explained in Table 7.2. Then, the randomized Kaczmarz algebraic reconstruction algorithm was employed as an iterative solver for the linear equations (Hansen, and Saxild-Hansen 2012). The iteration solver starts with initial guess, which is the average slowness value from the experimental data. Velocity was then computed by inverting slowness, and that value was plotted at each pixel in the cross-section representation to provide a P-wave velocity tomogram. All computations were performed using the Matlab platform.

Table 7.2 Information about tomography set-up and maximum computation time.

Specimen	Number of obtained ultrasonic signals, N	Number of assigned pixels in image, M	Maximum computation time (seconds)
RC1	288	256 (16 by 16)	34
RC2	440	400 (20 by 20)	57
UHP-FRC	550	529 (20 by 20)	62

7.2 Damage evaluation of RC columns

The mechanical responses of the columns were monitored with stiffness slope and embedded concrete strain gauge data. Figure 7.6 shows the column drift from the applied force for column RC1. From the graph, the slope is a line across the maximum and minimum forces from each loading cycle. As drift percentage of the column increases, the slope of the line decreases, indicating a global behavior of the column during the loading cycles. Column RC2 has two different values of stiffness slopes, one for each direction of load in

the bi-axial loading protocol. Here, the slope stiffness value associated with the Y' direction is used for the equivalent comparison with the other columns. Figure 7.7 presents a strain behavior of CTRH1 from RC1 by 1% drift level, indicating the calculation of residual strain. After applying cyclic loads, the degradation of internal materials causes a permanent displacement (or strain). For the qualitative analysis of the strain, the residual strain at each loading cycle is calculated based on the difference between the strains at the neutral position.

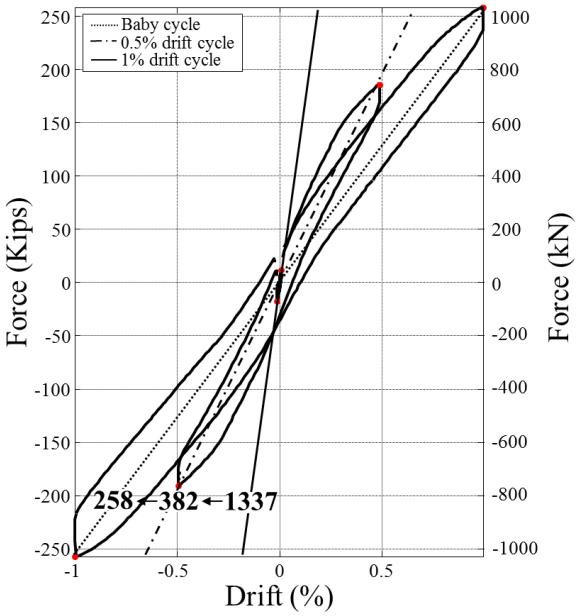

Figure 7.6 Example of stiffness slope behavior for column RC1, where calculated numbers of stiffness slope from each subsequent drift cycle are indicated. Units of presented stiffness slope values are applied lateral force in the Y' direction in kN per percentage column drift in that direction.

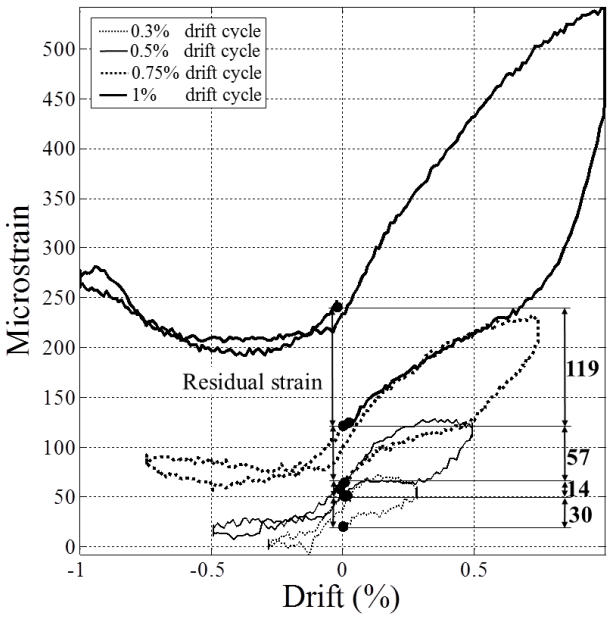

Figure 7.7 Example of residual strain behavior from stain gauge CTRH for column RC1 where calculated numbers of residual strain from each subsequent drift cycle are indicated. Presented strain values are expressed in units of microstrain.

The obtained stiffness slope data are presented in Fig 7.8., representing a behavior of entire column under the action of applied loads. Under repeated cyclic loading, stiffness slope decreases as the drift level increases. The obtained residual strain is cumulated as the drift percentage increases in order to quantify material degradation at the location where the gauge is embedded. The cumulative residual strains measured by gauges CTRB and CTRH are presented in Figs 7.9 and 10. Because RC2 was loaded bi-axially, the faster material degradation progress is expected and corresponding residual strains from both gauge sets are much higher than those in column RC1. Comparison between RC3 and UHP-FRC shows much difference in CTRH gauge set, which was embedded at same direction with cyclic loading. From the results, it is expected that composite materials in UHP-FRC significantly release internal stress compared to normal concrete.

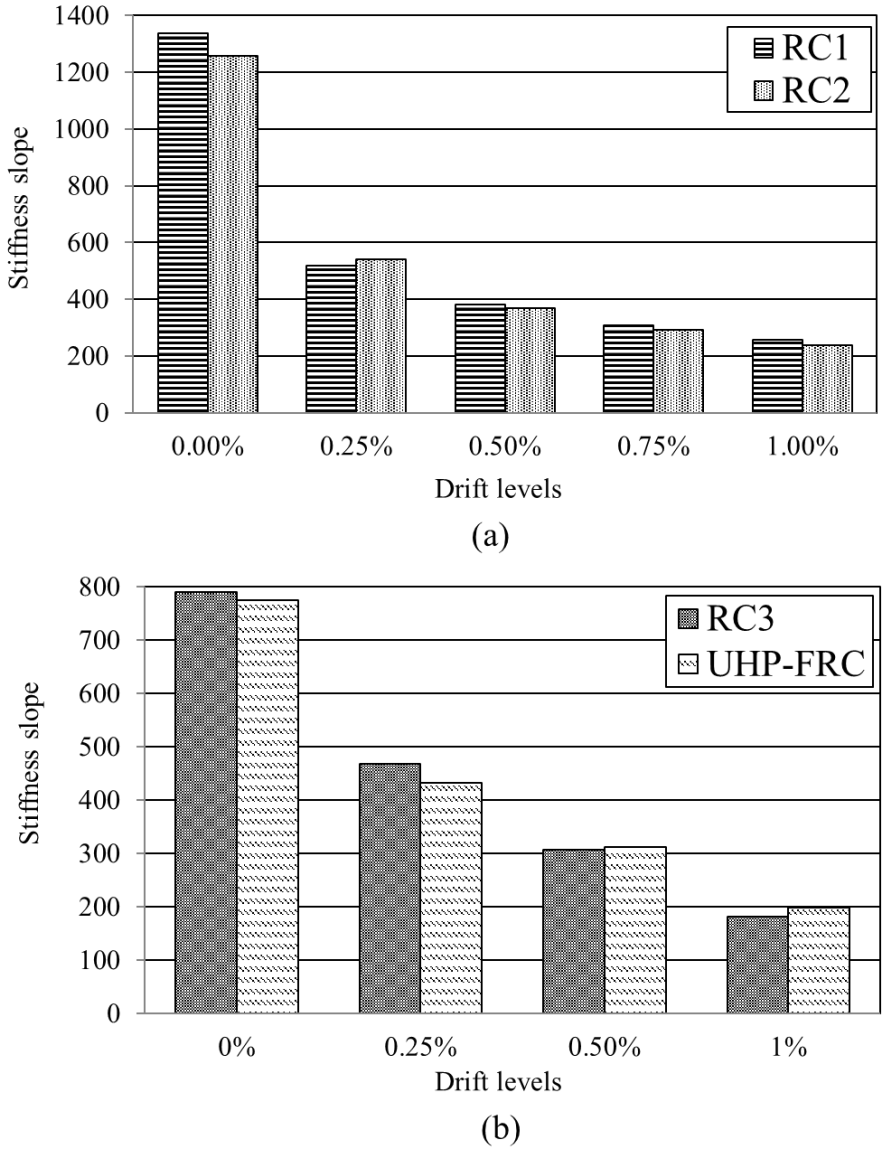

Figure 7.8 Stiffness slope as a function of applied drift level for (a) columns RC1 and RC2 and (b) columns RC3 and UHP-FRC. Units of presented stiffness slope values are applied lateral force in the Y' direction in kN per percentage column drift in that direction.

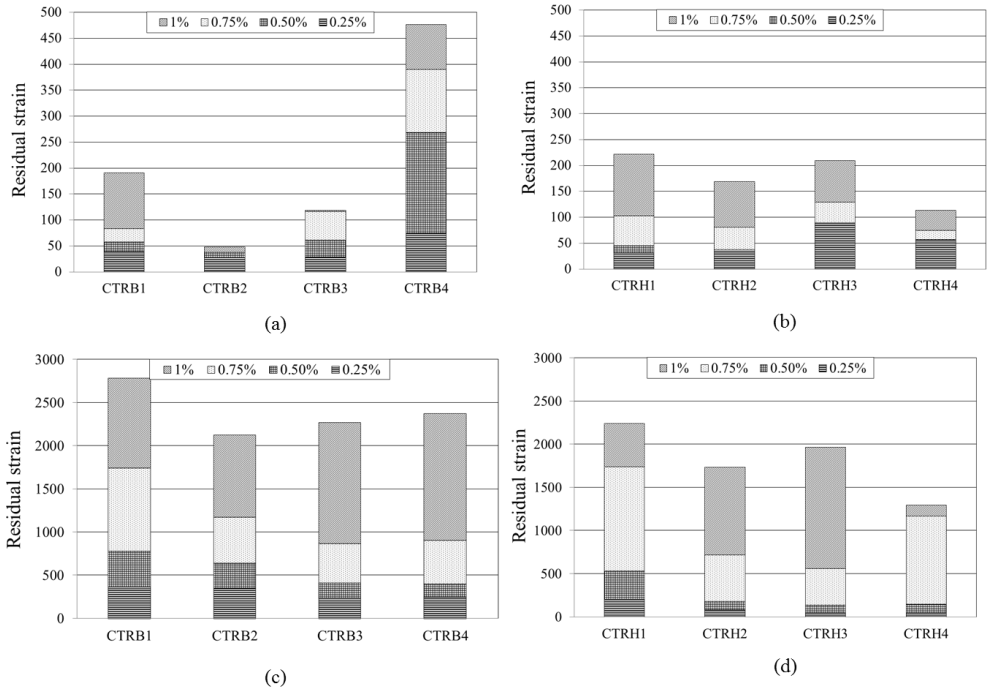

Figure 7.9 Cumulative residual strain as a function of applied drift level for columns RC1 and RC2: (a) CTRB gauges from RC1, (b) CTRH gauges from RC1, (c) CTRB gauges from RC2, and (d) CTRH gauges from RC2; Presented strain values are expressed in units of microstrain.

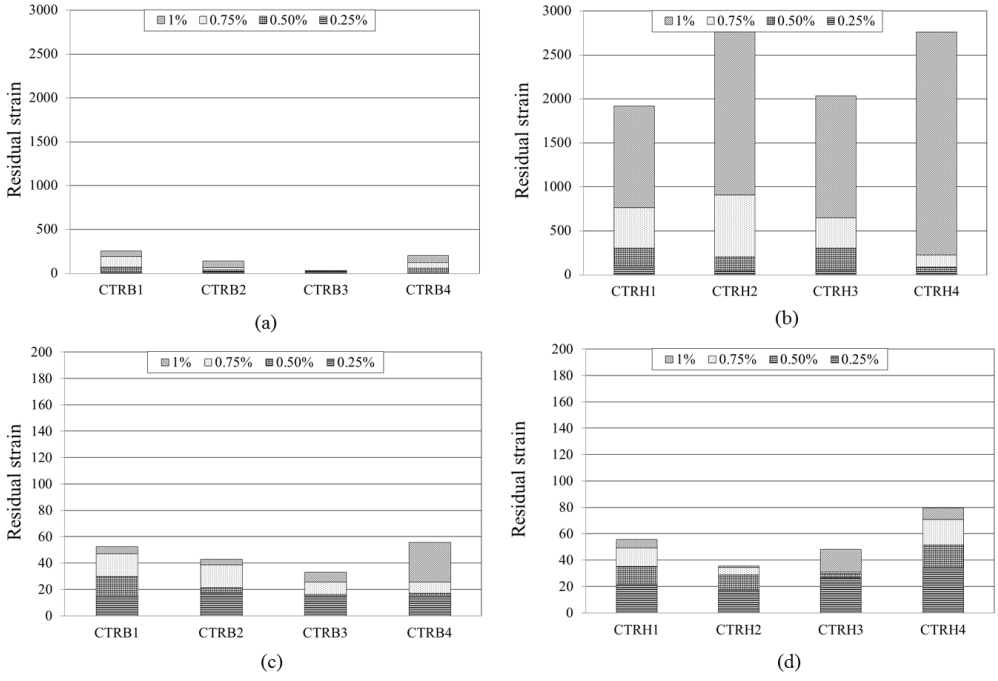

Figure 7.10 Cumulative residual strain as a function of applied drift level for columns RC3 and UHP-FRC: (a) CTRB gauges from RC3, (b) CTRH gauges from RC3, (c) CTRB gauges from UHP-FRC, and (d) CTRH gauges from UHP-FRC; Presented strain values are expressed in units of microstrain.

Photographs of the columns' exterior were taken from different perspectives at each drift level. Figure 7.11 shows photographs of columns RC1 and RC2 at selected drift levels when ultrasonic scanning tests were performed. Column RC1 at 1% drift level shows vertical cracks originating from the bottom and surface spalling damage on the left side of the column. Column RC2 at the 0.75% drift level shows initiation of tensile cracks across a large portion of the surface. The difference in external damage patterns between columns RC1 and RC2 is a result of differing loading protocols. Figure 7.12 presents the surfaces of RC3 and UHP-FRC. From the photographs, UHP-FRC column shows no external damage up to 1% drift level while RC3 has horizontal cracks and surface spalling damage on the left side of the column.

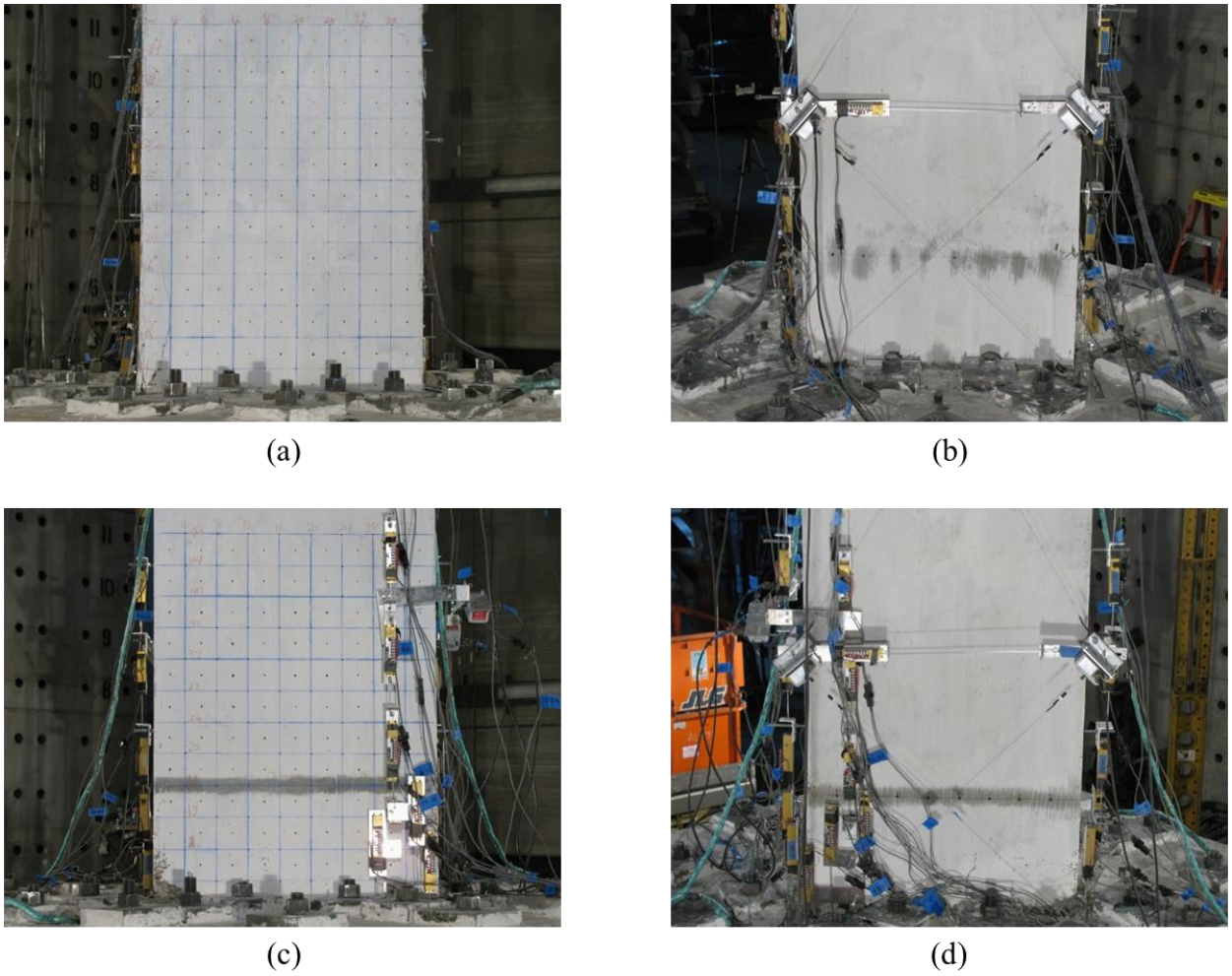

Figure 7.11 Photographs from columns RC1 and RC2 at indicated drift levels: (a) photo from RC1 at 1% drift level (Front side), (b) photo from RC1 at 1% drift level (Back side), (c) photo from RC2 at 0.75% drift level (Front side), and (d) photo from RC2 at 0.75% drift level (Back side).

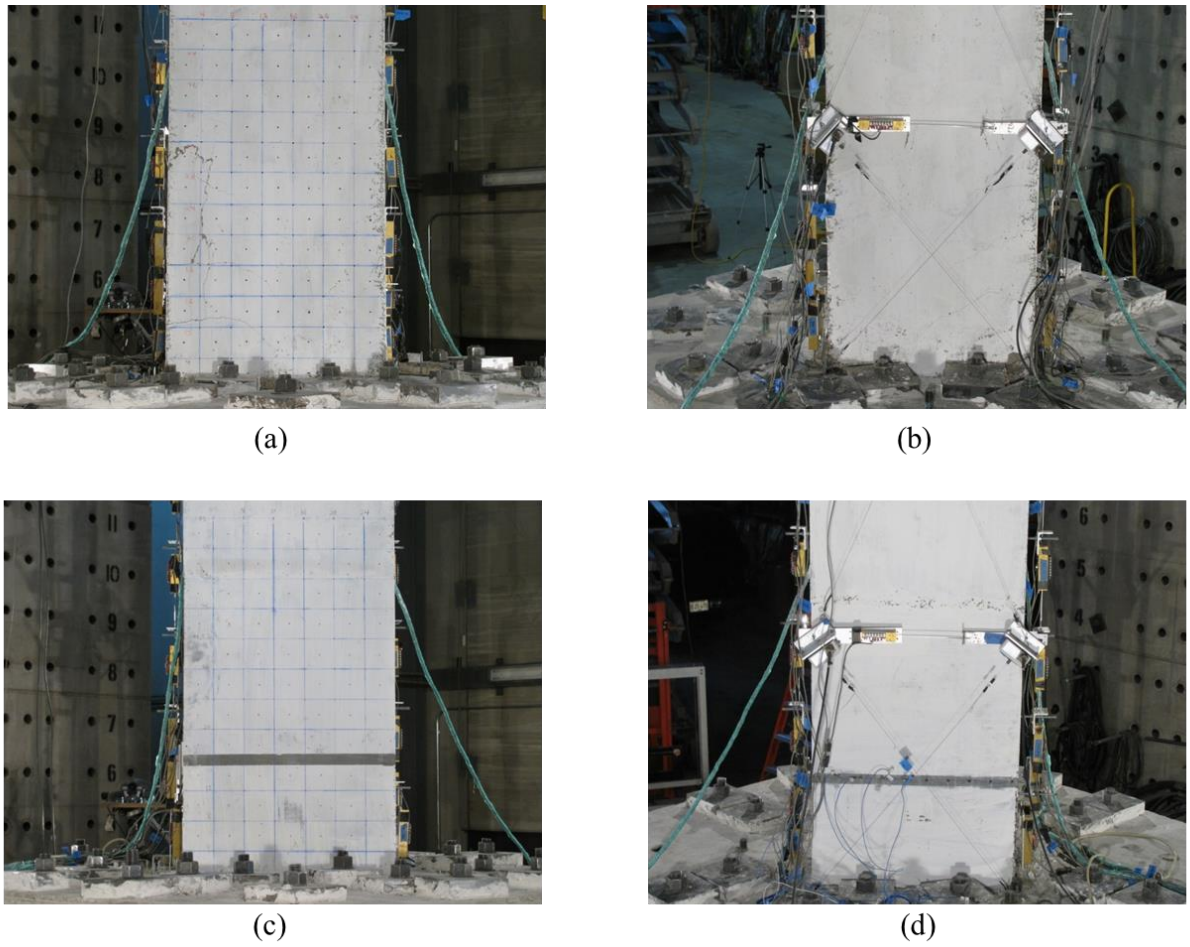

Figure 7.12 Photographs from columns RC3 and UHP-FRC at 1% drift level: (a) photo from RC3 at 1% drift level (Front side), (b) photo from RC3 at 1% drift level (Back side), (c) photo from UHP-FRC at 1% drift level (Front side), and (d) photo from UHP-FRC at 1% drift level (Back side).

7.2.1 Ultrasonic velocity tomography

Figure 7.13 shows an example of ultrasonic signals measured through the thickness of column RC1. All three signals were obtained along the same wave path but at different drift levels. As the drift level increases, the amplitude of the signals are dampened and the arrivals of P-wave are delayed. The delay in wave arrival for a consistent wave path indicates a reduction in P-wave velocity with increasing column drift and the distributed internal cracking damage that is associated with that. This result implies that the elastic modulus of concrete in the column decreases with increasing drift level.

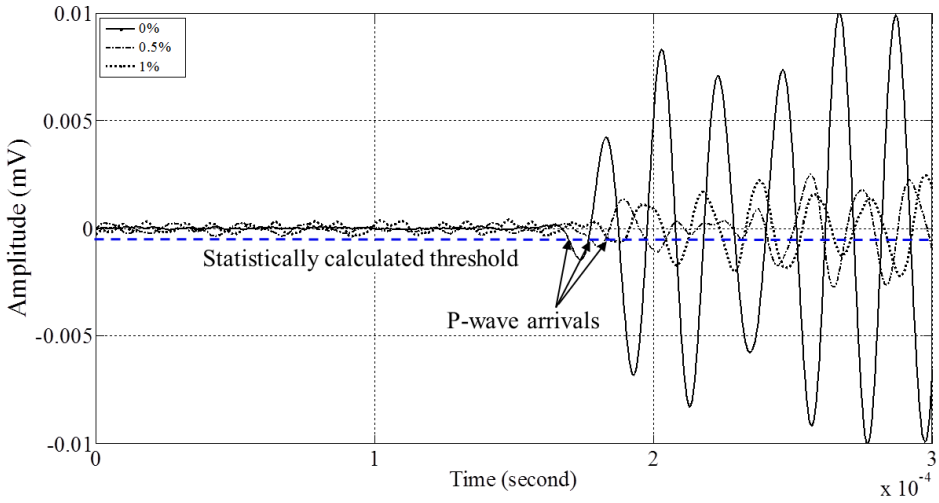

Figure 7.13 Example of through thickness ultrasonic time signals from column RC1 measured at drift levels indicated.

Ultrasonic cross-sectional P-wave tomograms were computed for each scan set. Figure 7.14 shows the overall normalized P-wave velocity distribution represented in the tomograms using the box plot format, where indicates the maximum and minimum (the top and bottom lines), the median (a line at a notch of the box), and the range of the first and third quartiles (the box) of data. As drift levels increase, P-wave velocity monotonically decreases. Normal concrete columns (RC1 and RC2) show more significant velocity drop, up to 25% reduction, than that in column UHP-FRC, which shows only a 10% reduction in velocity at 1% drift level. The variance of velocity values across the tomogram velocity distribution, which is represented by the height of the box in the plot, tends to increase with increasing drift levels. This increase in data variance likely represents increasing material non-uniformity caused by accruing internal damage. This behavior is especially evident in the data from column RC2 at 0.75% drift level.

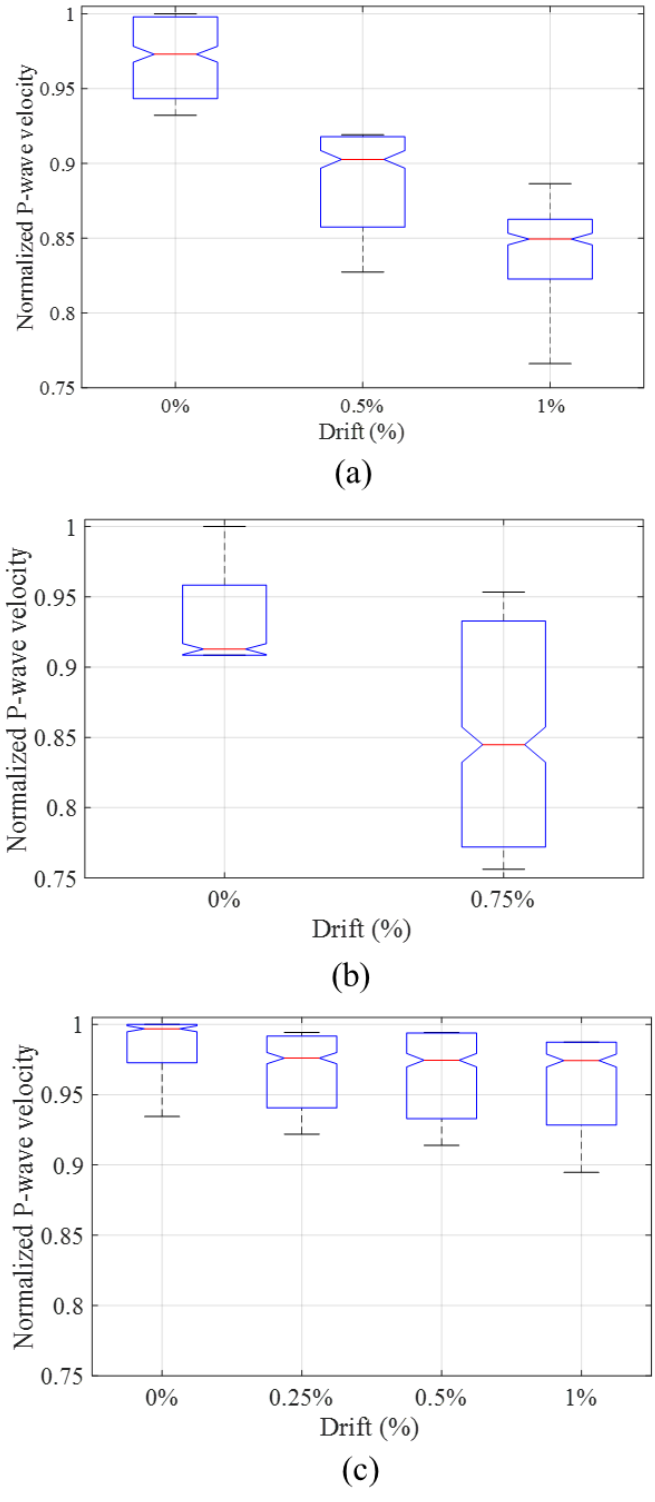

Figure 7.14 Normalized P-wave velocity distribution, expressed in box plot form, as a function of applied drift level: (a) RC1, (b) RC2, and (c) UHP-FRC.

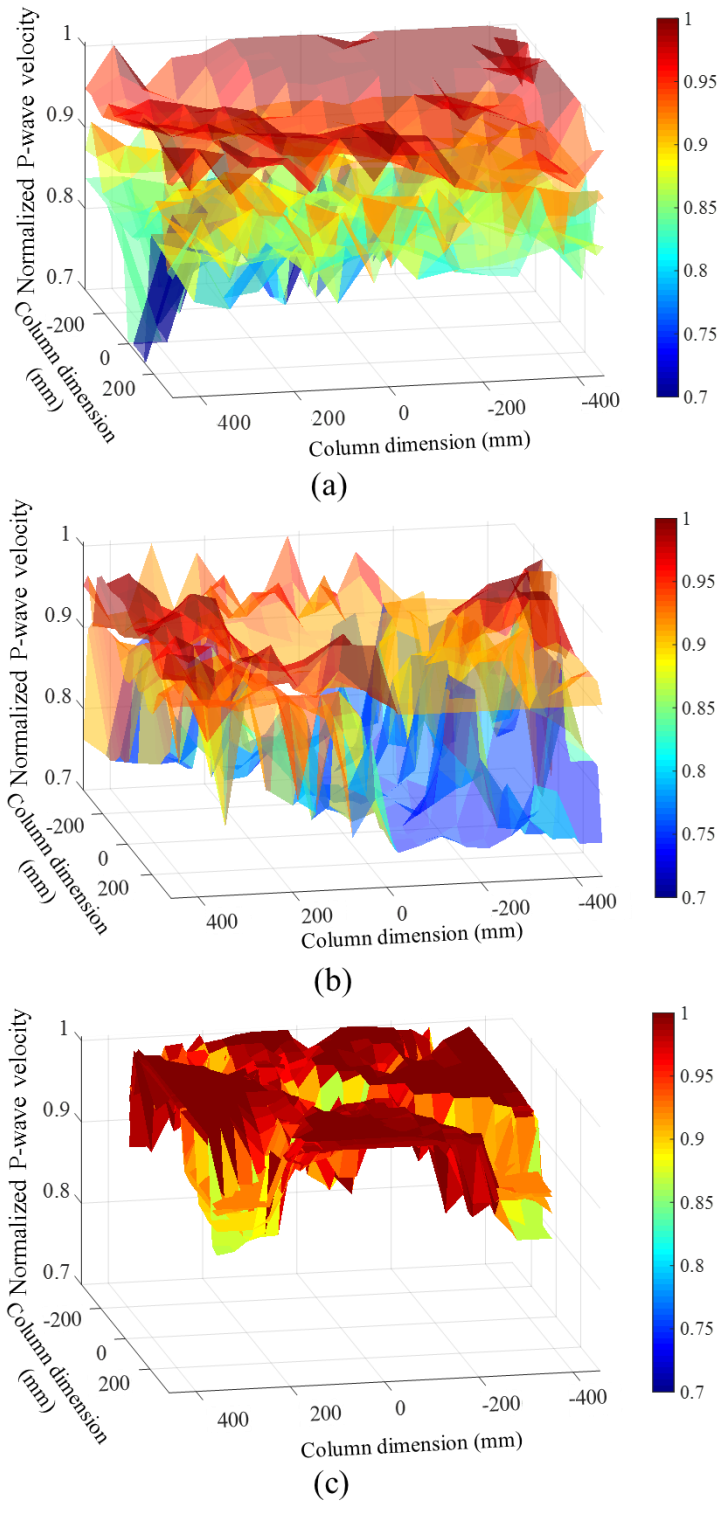

Figure 7.15 Stacked ultrasonic tomograms showing normalized P-wave velocity across test cross-section at different applied drift levels for columns: (a) RC1 (0%, 0.5%, 1% drift levels), (b) RC2 (0%, 0.75% drift levels), and (c) UHP-FRC (0%, 0.25%, 0.5%, 1% drift levels).

The constructed tomograms for each column at each tested drift level are stacked in a 3-D format and shown in Fig 7.15. The z-axis (color-scale) represents P-wave velocity, which is normalized by the maximum velocity of each tomogram at 0% drift cycle (before loading). Lower value of P-wave velocity represents possible degradation region over the seismic loading cycle. Tomograms from RC1 and RC2 show unique shape at each drift level while tomograms from UHP-FRC stacked in similar position due to minimal difference of P-wave velocity during the loading cycles. In the case of RC2, tomogram at 0.75% drift level shows broad range of velocity drop, which possibly represents severe material degradation due to bi-axial loading. Figure 7.16 represents comparison between tomogram from RC1 and photographs at 1% drift level. The tomogram in Fig 7.16a shows that right side (side-B) has relatively flat surface around 0.85 while left side (side-A) has significant velocity drop. These different behaviors are also found from photographs at each side of the column, where left side of the column only shows external cracking.

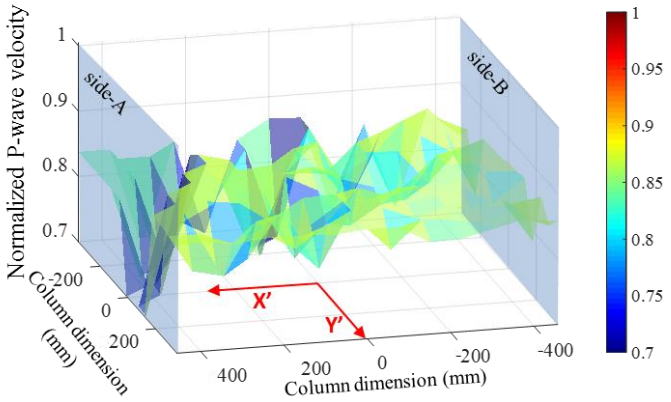

(a)

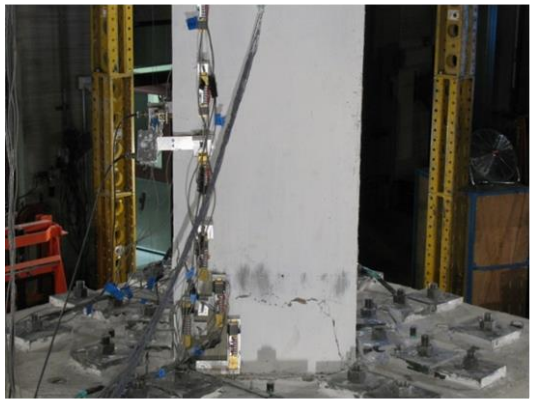

(b)

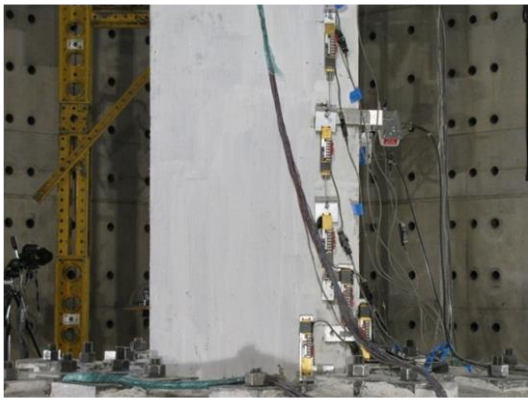

(c)

Figure 7.16 Comparison of cross-sectional normalized P-wave velocity tomogram and photographs of column RC1 at 1% applied drift level: (a) tomogram from RC1 at 1% drift level, (b) photo from RC1 at 1% drift level (side-A), and (c) photo from RC1 at 1% drift level (side-B).

7.2.2 Global compliance of the columns across drift levels

Global structural behavior of the columns is analyzed based on the stiffness slope and averaged P-wave velocity at each drift level. Figure 7.17 represents the graph of normalized stiffness slope and overall wave velocity from the cross-section. From the left of the graph to the right, drift levels grow and stiffness slope of the column decreases. The slope of fitting curves among normalized stiffness slope and averaged P-wave velocity indicate the rate of degradation over seismic loading. It is noted that UHP-FRC show significantly different behavior indicating much less degradation progression under seismic loading.

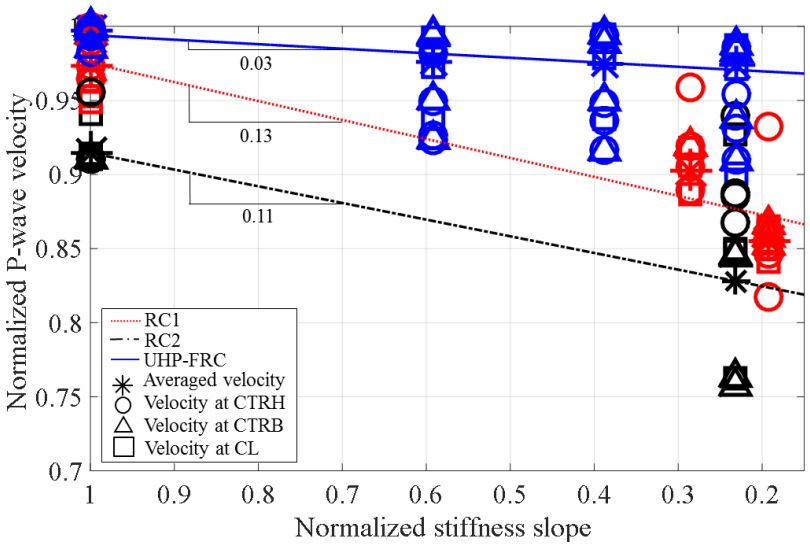

Figure 7.17 Global behavior of tested columns showing relation between normalized P-wave velocity and normalized stiffness slope.

7.2.3 Cross-sectional imaging at fixed drift levels

Residual strain from all drift levels and normalized P-wave velocity at the position of strain gauge is compared in Fig 7.18. UHP-FRC shows low range of normalized P-wave velocity distribution at the position of strain gauges. Due to the difference of loading protocol between RC1 and RC2, RC2 has much higher level of residual strain and corresponding normalized P-wave velocities from CTRB and CL gauges. From the tomogram of RC2 at 0.75%, the velocity distribution is irregular over the cross-section. Figure 7.19 represents direct comparison between normalized P-wave velocity and residual strains in RC2 at 0.75%. CTRB and CL gauge set show similar trends at each location, however; CTRH gauges do not follow the trend. This may be because ultrasonic waves are more disturbed by defects in perpendicular direction to the ray path and residual strains from CTRB (Y' direction) and CL (axial direction) sets possibly represent the displacement at the direction.

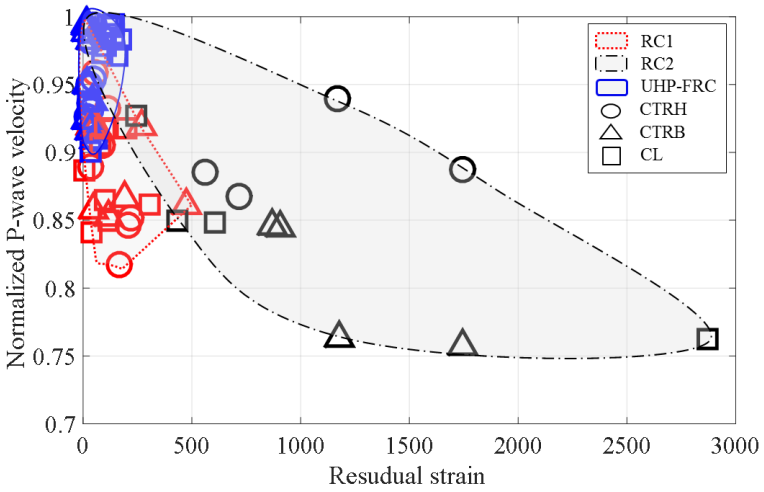

Figure 7.18 Local behavior of tested columns showing relation between normalized P-wave velocity and residual strain at specific strain gauge locations.

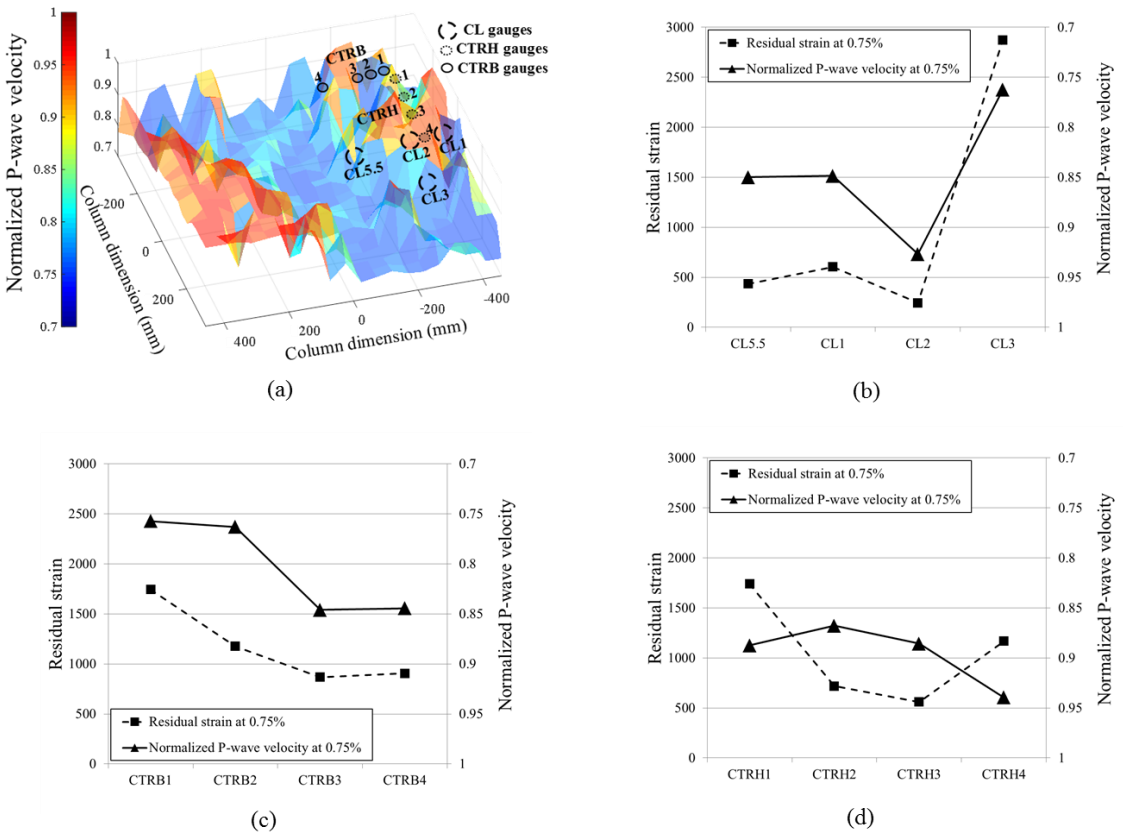

Figure 7.19 Local behavior of column RC2 at applied drift level of 0.75%, comparing computed P-wave velocity obtained from tomogram to stain values measured at locations of specific gauges indicated: (a) tomogram from RC2 at 0.75% drift level, (b) comparison between normalized P-wave velocity and CL gauges, (c) comparison between normalized P-wave velocity and CTRB gauges, and (d) comparison between normalized P-wave velocity and CTRH gauges.

CHAPTER 8 ATTENUATION TOMOGRAPHY

In this chapter, ultrasonic wave attenuation is investigated using the numerical simulation data set presented in Chapter 3 and the RC column tests described in Chapter 4. This study describes the development of a practical attenuation tomographic procedure and meaningful application to full-scale RC elements. This study introduces the concept of differential attenuation tomography at its great potential to detect internal damages from large-scale RC elements with enhanced capabilities with respect to velocity tomography.

8.1 Attenuation

Waves attenuate (lose energy) as they propagate through media. Attenuation is categorized as either intrinsic or extrinsic. Intrinsic attenuation represents internal friction or damping loss within the material, while extrinsic attenuation represents scattering and geometric (or beam) spreading (Kolsky 1963). Geometric spreading is the apparent loss of amplitude of the propagating waves owing to the wave energy being spread over increasing area as the wavefront travels from the source. In homogeneous media, the wave amplitude decreases as a function of wave travel distance owing to geometric spreading, where the nature of the decay rate depends on the shape of the wave field. Scattering is set up by heterogeneities within the medium. For wave propagation through the heterogeneous media, waves are reflected and refracted by interfaces between materials having different acoustic impedances, as described in Chapter 2. If the propagating medium includes many heterogeneities, the propagating wave is constantly being redirected and scattered in various directions.

Intrinsic attenuation is attributed to material hysteretic behavior and viscous loss of the materials (Kolsky 1963). Hysteresis is time-dependent behavior (i.e., lag between input and output), defining the output from present and past inputs. In a dynamic system where the input quickly changes, a hysteric relation between stress and strain causes the energy to be dissipated. In materials, the hysteretic behavior is mainly caused by internal material friction. In the case of viscous materials, irrecoverable deformation of a solid occurs, which dissipates the energy.

To quantify the amplitude decay of transmitted waves through the media, the attenuation coefficient, α, is used. The attenuation coefficient is defined in terms of amplitudes

$$\mathrm{A} = A_0 \left(\frac{1}{r}\right)^{\beta} e^{-\alpha r} \tag{8.1}$$

where r is the distance the waves travel, β is the geometric spreading factor, and A and A_0 are the wave amplitudes after travelling the distance r and the amplitude at the source (initial amplitude), respectively.

β represents the geometry of the wave field, having a value of 0.5 for cylindrical and 1 for spherical wavefronts, respectively. From equation (8.1), the attenuation coefficient α can be extracted

$$\alpha = \frac{1}{r}\left(-\ln\frac{A}{A_0} - \beta \ln r\right). \tag{8.2}$$

The attenuation coefficient is expressed in units of Neper (N_p) per length.

In tomographic reconstruction, the attenuation coefficient of a material can be reconstructed in the form of an image. Attenuation tomography has been investigated and applied to characterize concrete (Prada et al. 2000, Chai et al. 2011). Similar to velocity tomography, linear equations are constructed based on the distance traveled by rays, the logarithm of the amplitude ratio, and the geometric spreading factor. However, tomogram results from previous research efforts exhibit limited the number of measurements and pixels in the images, and furthermore the test specimens are restricted to small-sized concrete elements without rebar.

8.1.1 Finite element model analysis

Data from the numerical simulation were analyzed to interrogate the characteristics of wave attenuation through reinforced concrete. As shown in Fig 8.1, four different simulation models were created: plain concrete (C); concrete and steel (CS); concrete and defect (CD1); and concrete, steel, and defect (CSD1). The assigned material properties were the same as those presented in Chapter 3 (see Table 3.2). It should be noted that material damping is not considered in the numerical simulation.

Figure 8.2 shows the comparison between the simulated models—C and CSD1—and the corresponding stacked A-scan images. The stacked A-scan images are the obtained signal set from one receiver attached to the right side of cross-section while the input source moves along the surface (total 327 points). The P-wave front clearly arrives faster when the input source is close to the position of the receiver. From the "only concrete" case shown in Fig 8.2(c), the arrivals of the boundary reflection (yellow dashed lines) and surface waves (green dashed lines) are observed after P-wave arrivals. The amplitude analysis was performed within the first cycle (period) of the waves to avoid the effects of reflection from the side walls. In the case of CSD2 presented in Fig 8.2(d), the P-wave arrivals have a lower amplitude (i.e., darker color) at the beginning part (ray number 0 to 100) of the source compared to the only concrete case. This is because the rays are transmitted through the center defect and the amplitudes of the waves are scattered and absorbed and thus attenuated.

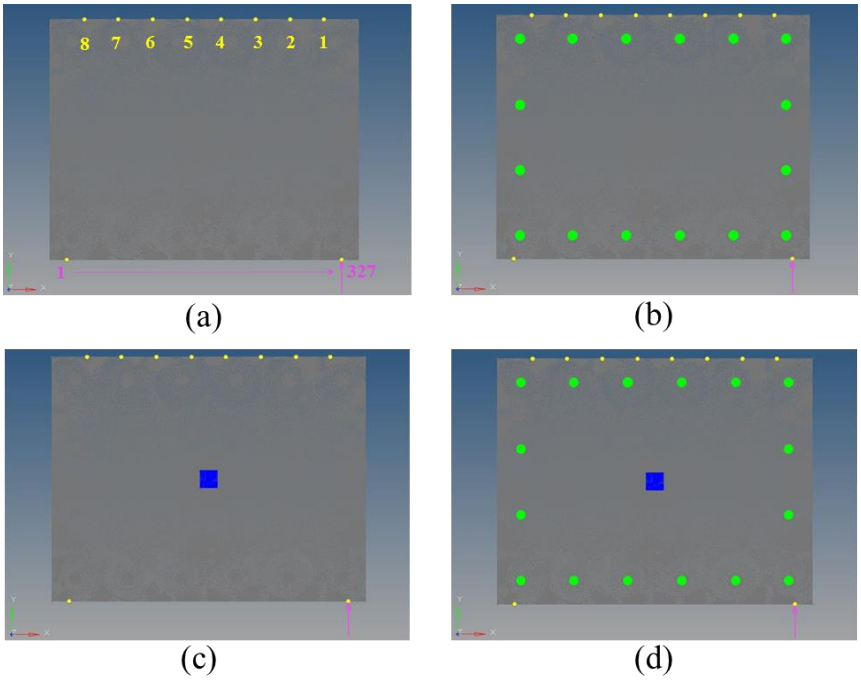

Figure 8.1 Finite element model cross-sections: (a) plain concrete, (b) concrete and steel, (c) concrete and defect case 1, and (d) concrete, steel and defect case 1. Input (pink arrow) and receiver (yellow points) positions are indicated.

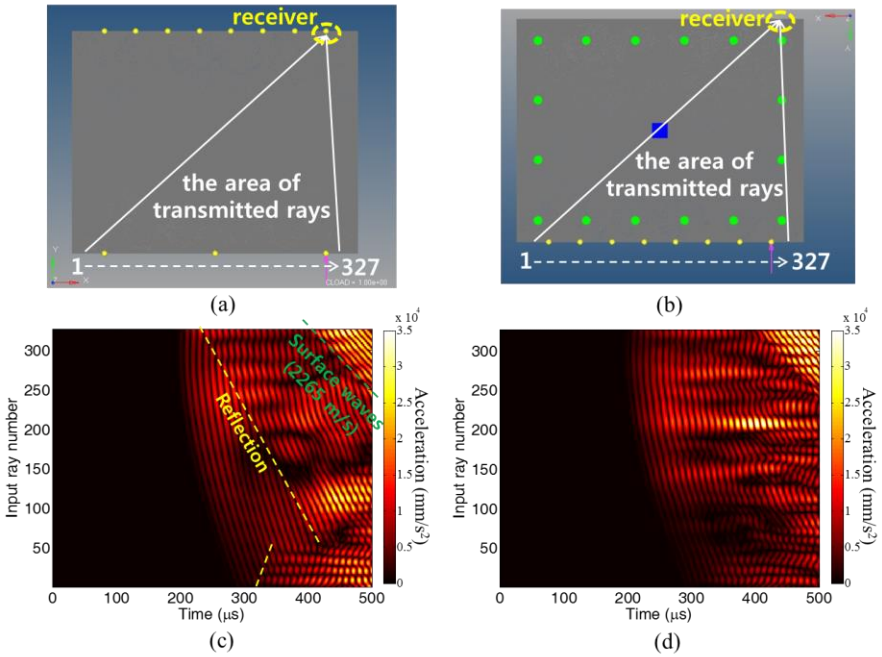

Figure 8.2 Finite element model cross-sections s showing the location of receiver 1 and ray coverage above and corresponding stacked A-scans below: (a) plain concrete model, (b) concrete, steel and defect case 1, (c) stacked A-scans from receiver 1, and (d) stacked A-scans from receiver 1.

Individual A-scan signals from three different cases are plotted in Fig 8.3. Each ray has the same path through simulation models C, CS, and CSD1. The arrival portion of the signals is enlarged in Fig 8.3(c), showing that the first cycles of the waves have different amplitudes. The amplitude of the waves through CSD1 (blue line) is clearly attenuated with delayed arrivals. In the case of CS, the amplitude of the waves is also damped, although the arrival of the waves is not significantly different from that of plain concrete. The obtained arrival times and peak amplitudes (absolute numbers of the first negative peak) of additional ray paths are presented in Table 8.1. The results reveal that the decay rate of the amplitude is much more sensitive than the delay time of the arrival; the maximum difference of obtained arrivals is 1μs while the amplitudes (acceleration) of the wave decay the maximum 138.7 mm/s^2.

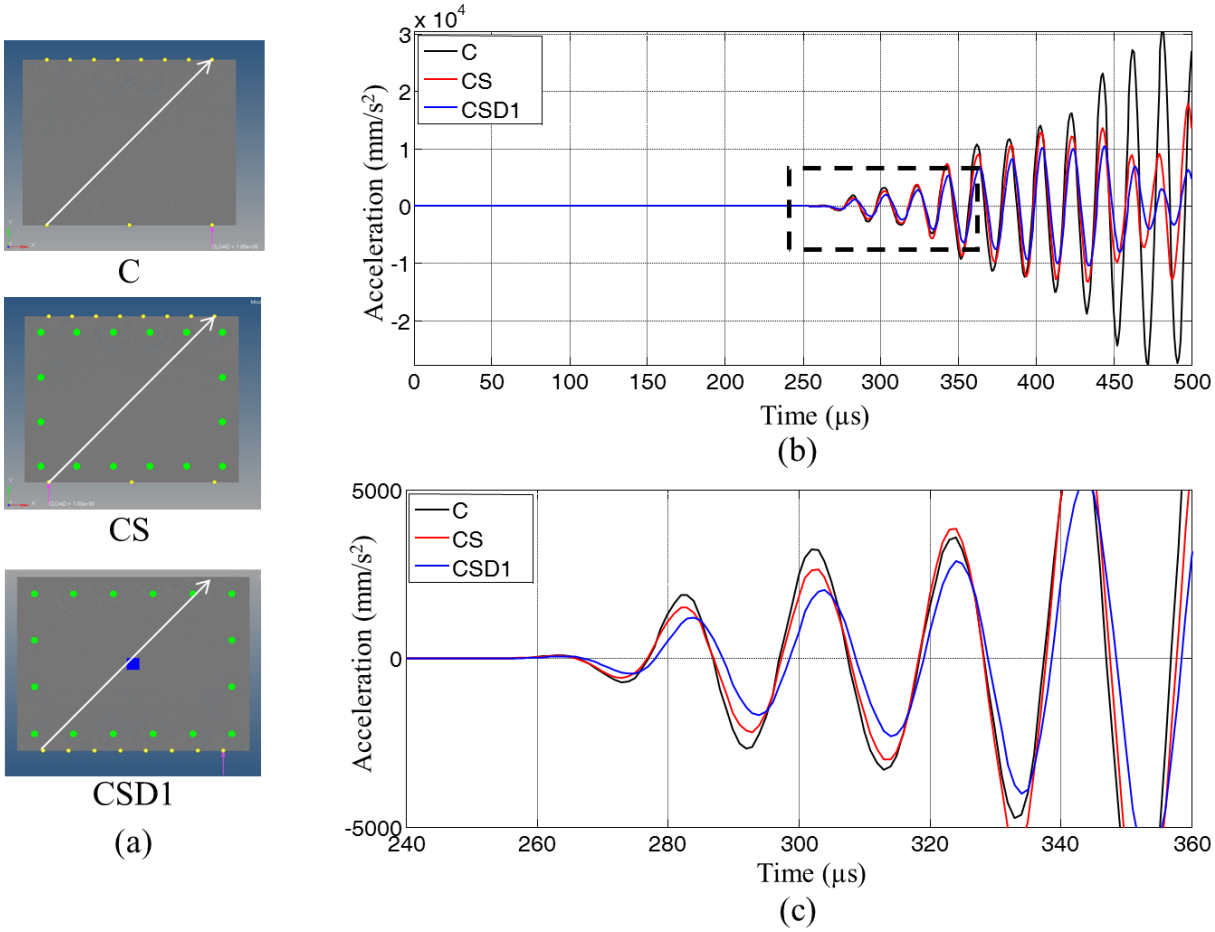

Figure 8.3 Comparison of FEM signal data: (a) model cross-sections showing ray path, (b) the obtained signals from the ray path defined in (a), and (c) the enlargement of dashed line box in (b).

Table 8.1 Comparison of arrival times and peak amplitudes for the defined rays.

Parameter	Model	Ray1 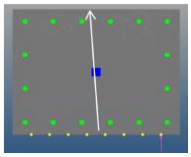	Ray2 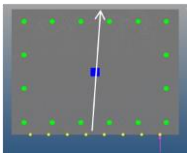	Ray3 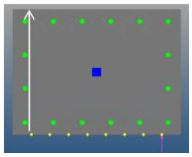	Ray4 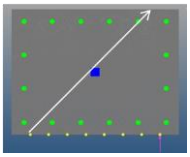
Arrival time (μs)	C	192	192	192	263
	CS	192	192	191	263
	CSD2	193	193	191	264
Amplitude (mm/s^2)	C	367.8	368.3	359	94.8
	CS	324.4	324.9	220.3	77.61
	CSD2	232.3	233.5	220.3	61.59

The attenuation of waves captured in a digitized signal can be characterized by either peak amplitude or the area under the signal (energy). In this study, the energy was obtained by the integral of the first half cycle of the waves, as shown in Fig 8.4(a), where the integration has a unit of mm/s. Figure 8.5 presents the energy of the waves from four different simulation models, while Fig 8.6 shows the first peak amplitude, indicated by the shaded box in Figure 8.4(b) from the same models. Although the two parameters show similar trends from each receiver set, the obtained energy is highly variable and unstable. This is because the integral of the area under the curve is affected by digitization error. Figure 8.4(b) shows the enlargement of the first half cycle of the signals for several input ray numbers in the only concrete case, where lower attenuation is expected for higher input ray numbers (closer to the receiver). However, the digitized first half cycles contain several discrete points (indicated by the dashed line box) where this expected trend is not seen as all lines have the same value. This causes disruption to the actual amplitude value and is caused by signal digitization.

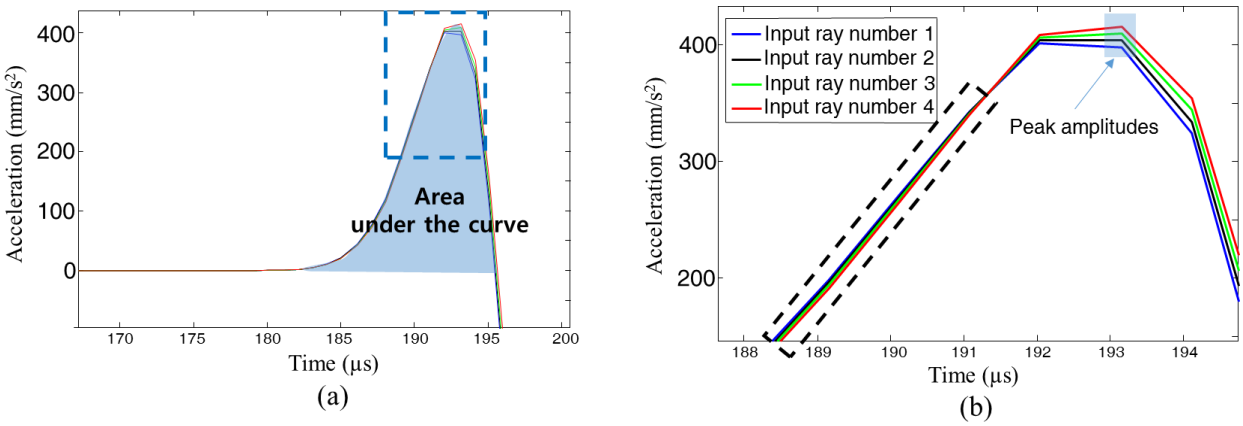

Figure 8.4 The calculation of signal energy from the digitized signal: (a) the defined area under the signal curve, and (b) enlargement of blue dashed line box in (a) presenting peak amplitudes and digitizing errors (dashed line box).

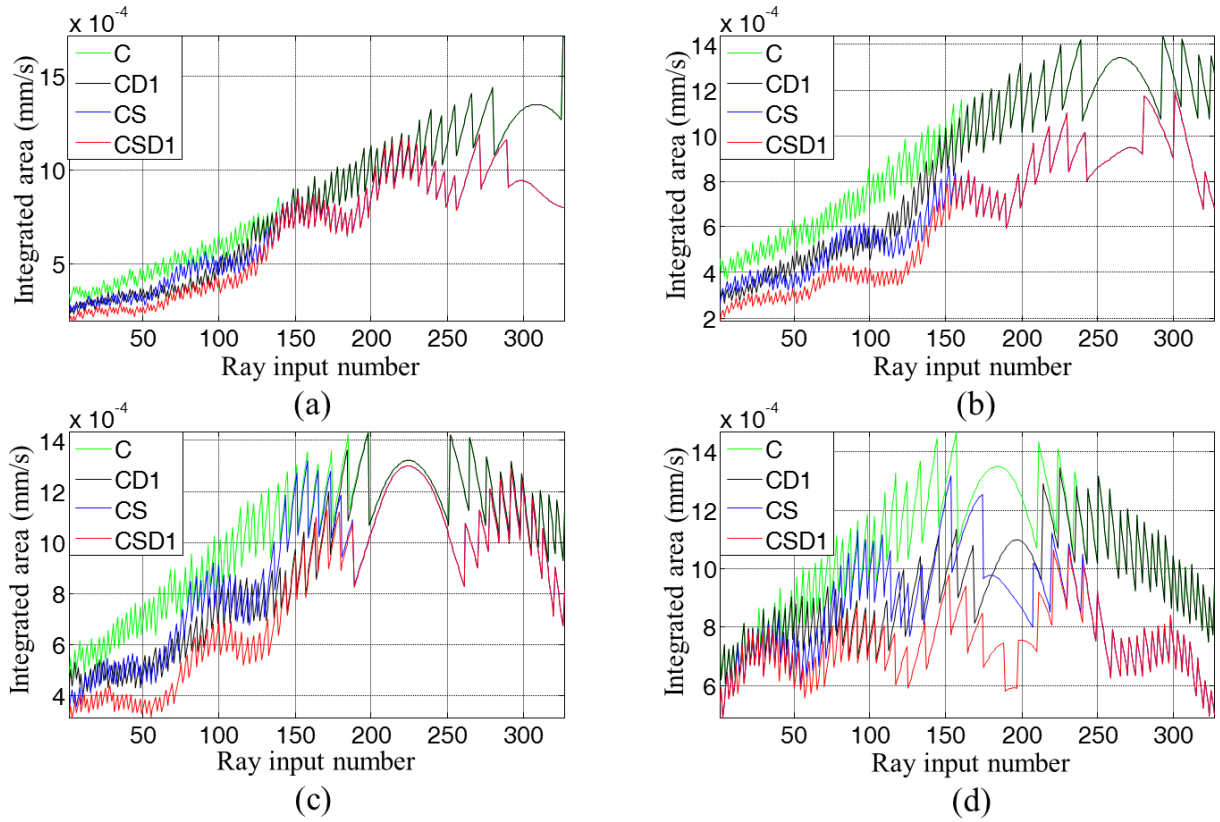

Figure 8.5 Computed signal energy across all rays (the integral area) for each model: (a) Receiver 1, (b) Receiver 2, (c) Receiver 3, and (d) Receiver 4 (see fig 8.1).

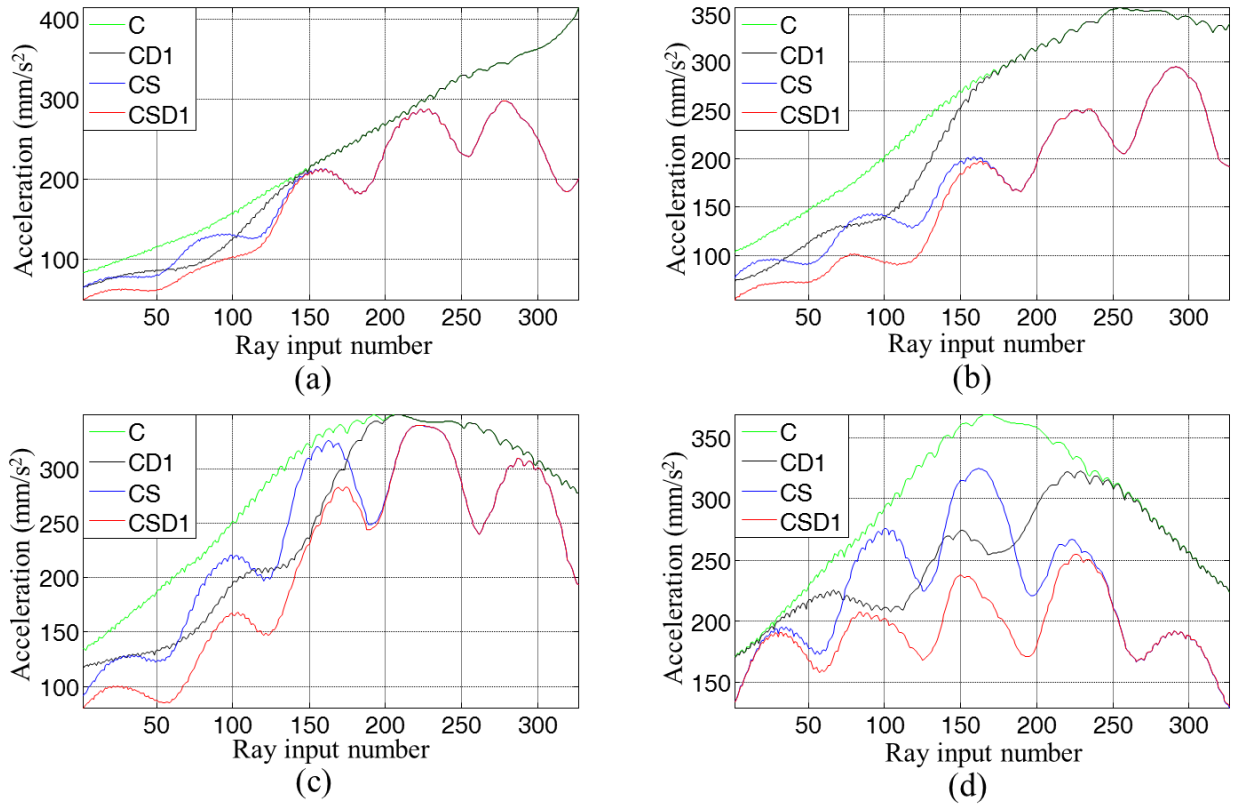

Figure 8.6 Computed signal amplitude across all rays for each model: (a) Receiver 1, (b) Receiver 2, (c) Receiver 3, and (d) Receiver 4.

The peak amplitudes are relatively stable and clearly show distinction in attenuation among the models, as seen in Fig 8.6. Comparison of the set of peak amplitudes from concrete only (green lines) and the CD1 (black line) models illustrate the attenuation effect caused by the center defect, showing that the air-void defect significantly attenuates the waves. The embedded rebar with regular spacing also appears to affect the amplitude of the waves. The set of the peak amplitudes from the CS case (blue lines) regularly fluctuate along the ray input number and the CSD1 case (red lines) shows the influence from both rebar and the defect. The analysis of the simulated data indicates that the amplitude of the waves appears to be influenced by the inclusion in the media, and furthermore the sensitivity of the amplitude is higher than that of the arrival time and signal energy.

8.1.2 Linear equations for attenuation tomography

Linear equations for attenuation tomography can be constructed from the measured attenuation along a ray travelling through the medium. Similar to velocity tomography, the linear equation system is

$$Amp_i = \sum_{j=1}^{M} r_{ij}\alpha_j \quad (\text{i} = 1\sim\text{N}) \tag{8.3}$$

where Amp_i is a function of the wave amplitudes and the geometric spreading factor, r_{ij} is the distance traveled by ray i in pixel j, α_j is the attenuation coefficient in pixel j, and N and M are the number of measurements and pixels, respectively. Unlike the arrival time set used in velocity tomography, the measurement, Amp_i has more complicated form

$$Amp_i = -\ln\frac{A_i}{A_0} - \beta \ln r_i \tag{8.4}$$

where A_i is the measured wave amplitude (peak amplitudes in this work) and r_i is the distance traveled by ray i. After constructing the linear equations, the algebraic reconstruction technique is applied to solve for the attenuation coefficient so that a attenuation tomogram, the spatial map of attenuation coefficient, is constructed.

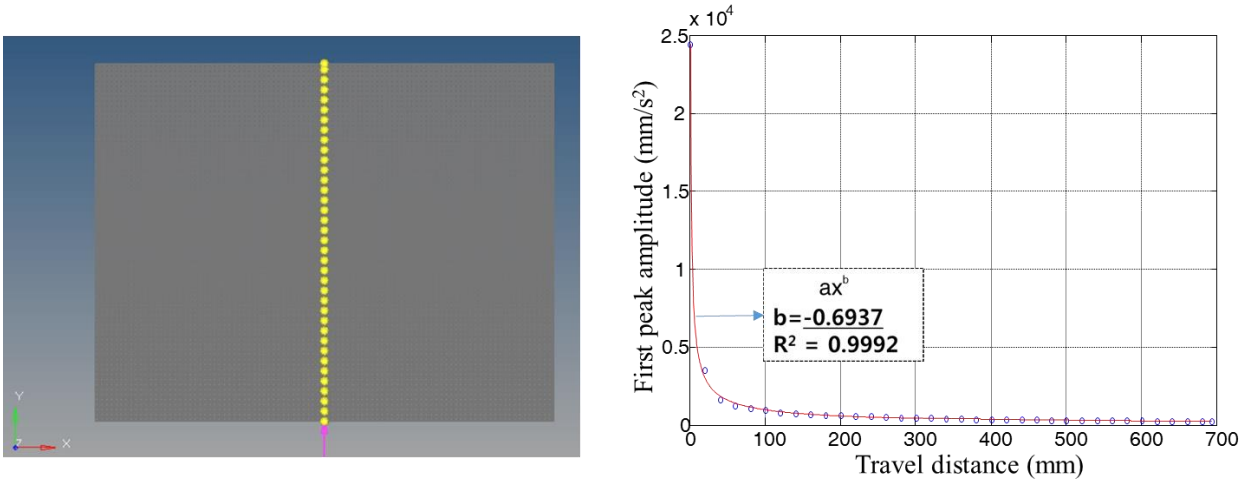

Figure 8.7 Illustration of the calculation of the geometric spreading factor: (a) plain concrete model showing input position (pink arrow) and output positions (yellow dots), (b) peak amplitudes from the output data (points) with best fit power curve (line, the inset presents the function of the power line).

Figure 8.7 shows the obtained decay rate of the peak amplitudes for the geometric spreading factor, β. The peak amplitudes of signals from the plain concrete model (Fig. 8.7a) are obtained and fitted into a power series function using Matlab. The single term power series model (see the inset in Fig. 8.7b) was applied to the peak amplitudes, initial amplitude, and distance traveled by the ray. The geometric spreading factor is obtained around 0.7 from the best fit curve and the coefficient of determination (R^2) is 0.9992. The attenuation coefficient from the simulated models is obtained based on Eqn (8.2) and presented in Fig 8.8. Although the attenuation coefficient is relatively stable from the data of the plain concrete model, the other

cases show higher attenuation when the input ray travels through heterogeneities within the cross-section. The attenuation coefficient from the CD1 model (red line) clearly presents the effect of the center defect, while the attenuation coefficient from the CS model (black line) shows a ripple due to the regularly positioned rebar. In the case of CSD1, both the rebar and the defect attenuate the waves, so that the obtained attenuation coefficient has both the effects of the defect and bar ripple.

Randomized Kaczmarz method was applied to the numerically simulated data to create attenuation tomograms. The reconstructed sectional images for each case are shown in Fig 8.9. While the plain concrete model has all pixel values under 0.55 N_p/cm, the other images show attenuated areas (red color): 1) the CS model indicates the location of the four centermost bars near the surface of applied input sources; 2) the CD1 model clearly indicates location of the defect in the center of the image; and, 3) the CSD1 model indicates both bar and defect. It is noted that the bars near the receivers are difficult to show in tomogram due to the limited ray coverage. The attenuation tomograms present all inclusions as red because the propagating waves are attenuated by both rebar and defect. It is noted that velocity tomography in Chapter 3 could not show the presence of the rebar from the CSD1 model.

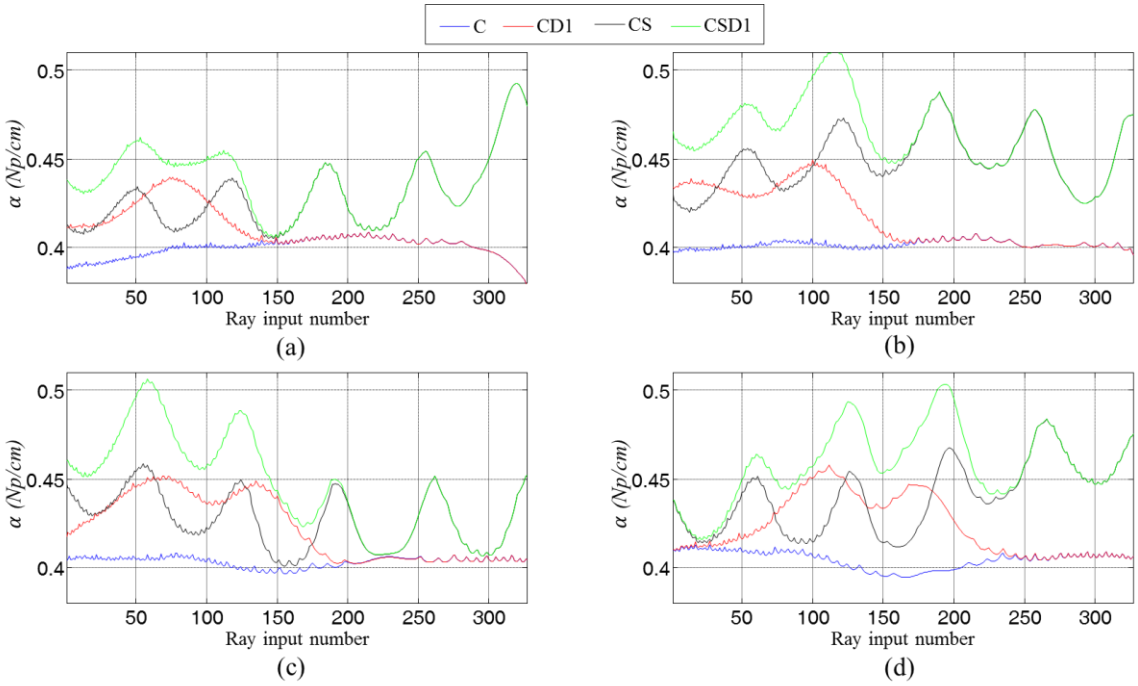

Figure 8.8 Computed attenuation coefficient across all rays for each model: (a) Receiver 1, (b) Receiver 2, (c) Receiver 3, and (d) Receiver 4.

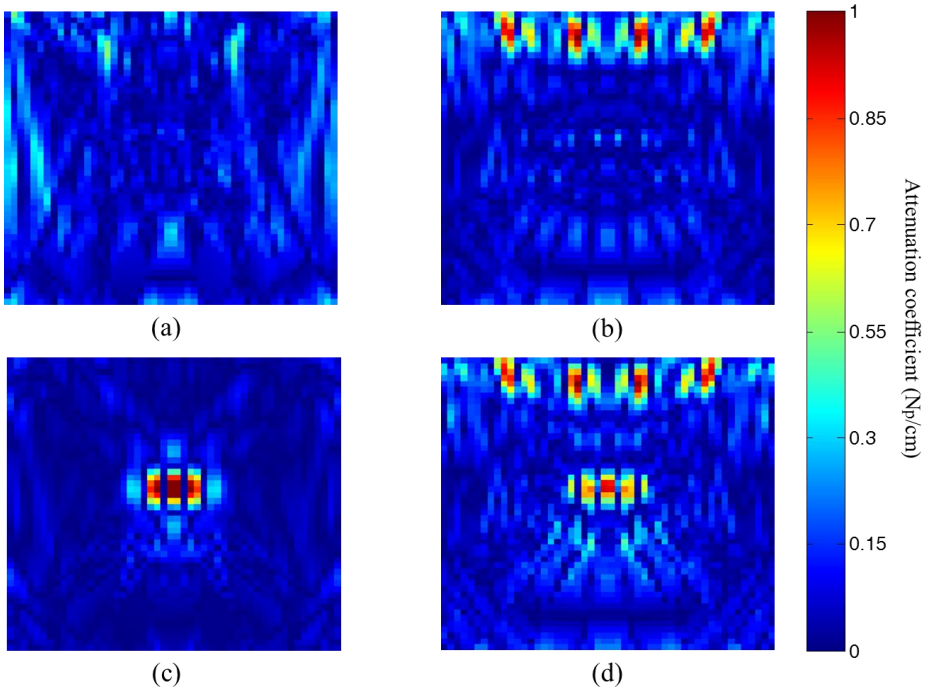

Figure 8.9 Constructed attenuation tomograms: (a) plain concrete, (b) concrete and steel, (c) concrete and defect case 1, and (d) concrete, steel and defect case 1.

From an experimental point of view, attenuation tomography presents several practical issues. The parameters A_0 and β are usually unknown and values must be assumed; he initial amplitude A_0 is sometimes defined as the measured amplitude at a reference position (Prada et al. 2000). In this case, the geometric spreading term must be redefined as a function of the travel distance between the reference and the measured positions—a less accurate approach. Furthermore, the amplitude radiation pattern of the transmitter and the response pattern of the receiver must also be considered, so equation (8.1) becomes

$$\mathrm{A} = A_0 \left(\frac{1}{r}\right)^{\beta} e^{-\alpha r} f_t(\theta) f_r(\theta) \tag{8.5}$$

where $f_t(\theta)$ is the beam radiation pattern of the transmitter and $f_r(\theta)$ is the response pattern of the receiver, where both are a function of angle, θ. The coupling condition of the sensors also affects the measurement, which needs to be considered in the attenuation tomographic procedure.

8.1.3 Differential attenuation tomography

Differential attenuation tomography can be applied to obviate the effects of the unknown parameters in Eqn. 9.5. The amplitude decays from simulation models CS and CSD1 are defined by

$$\mathrm{A}_{CS} = A_0 \left(\frac{1}{r}\right)^{\beta} e^{-\alpha_{CS} r} f_t(\theta) f_r(\theta) \tag{8.6}$$

$$A_{CSD1} = A_0 \left(\frac{1}{r}\right)^{\beta} e^{-\alpha_{CSD1} r} f_t(\theta) f_r(\theta) \tag{8.7}$$

where A_{CS} and A_{CSD1} are the first peak amplitudes of the waves and α_{CS} and α_{CSD1} are the attenuation coefficient of the waves for models CS and CSD1, respectively. The ratio of Eqns. 8.6 and 8.7 cancels the unknown parameters and becomes

$$\ln \frac{A_{CS}}{A_{CSD1}} = r(\alpha_{CSD1} - \alpha_{CS}) = r\Delta\alpha \tag{8.8}$$

where $\Delta\alpha$ is the difference between the attenuation coefficients of the waves between the two cases. In Eqn. 8.8, the differential attenuation coefficient represents the difference between CS and CSD1 models, which represents he defect positioned in the center of the cross-section. In the case of experimental application, Eqn. 8.8 assumes: 1) the same transmitter and receiver are applied; 2) the cross-sections have similar material properties so that the geometric spreading is mathematically equivalent; and, 3) the coupling condition of sensors is identical. Using Eqn. 8.8, the linear equations for differential attenuation tomography become

$$Amp'_i = \sum_{j=1}^{M} r_{ij} \Delta\alpha_j \ \ (\mathrm{i} = 1 \sim \mathrm{N}) \tag{8.9}$$

where $\Delta\alpha_j$ is the differential attenuation coefficient in pixel j, and Amp'_i is a newly defined function of amplitudes which is a natural logarithm of the peak amplitude ratio

$$Amp'_i = \ln \frac{A_{case1_i}}{A_{case2_i}} \tag{8.10}$$

where A_{case1_i} and A_{case2_i} are the wave amplitudes of ray i for each case. Therefore, Amp'_i is expressed in units of Neper (N_p).

Figures 8.10 and 11 show the computed differential attenuation coefficient obtained from the numerical simulations. The specific type of inclusion, steel bars or center defect, can be isolated by selecting the appropriate set of models in the ratios. For example, the logarithm ratio of amplitude between numerical models CS and CSD1 isolates the center defect. Fig 8.10 shows a differential attenuation data where the center defect is isolated, while Fig 8.11 shows that where the bars are isolated. Both the differential attenuation coefficients are highly sensitive to inclusions. Differential attenuation tomography was applied to the same numerical data, and the images were compared to differential velocity tomography computed from the same data set as shown in Fig 8.12. The color scale of the images is normalized by the maximum

pixel value of each image, where red colors represent maximum difference in attenuation coefficient profiles between two simulations in the ratio. The differential attenuation tomograms clearly indicate the position of center defect and bar inclusions; however, the size of the center defect is overestimated. The differential attenuation tomogram clearly indicates the existence of all bars near the surface where there wave sources are applied, in contrast to differential velocity tomography which does not. This is because the wave attenuation is more sensitive to the presence of heterogeneities compared with the wave arrival time delay.

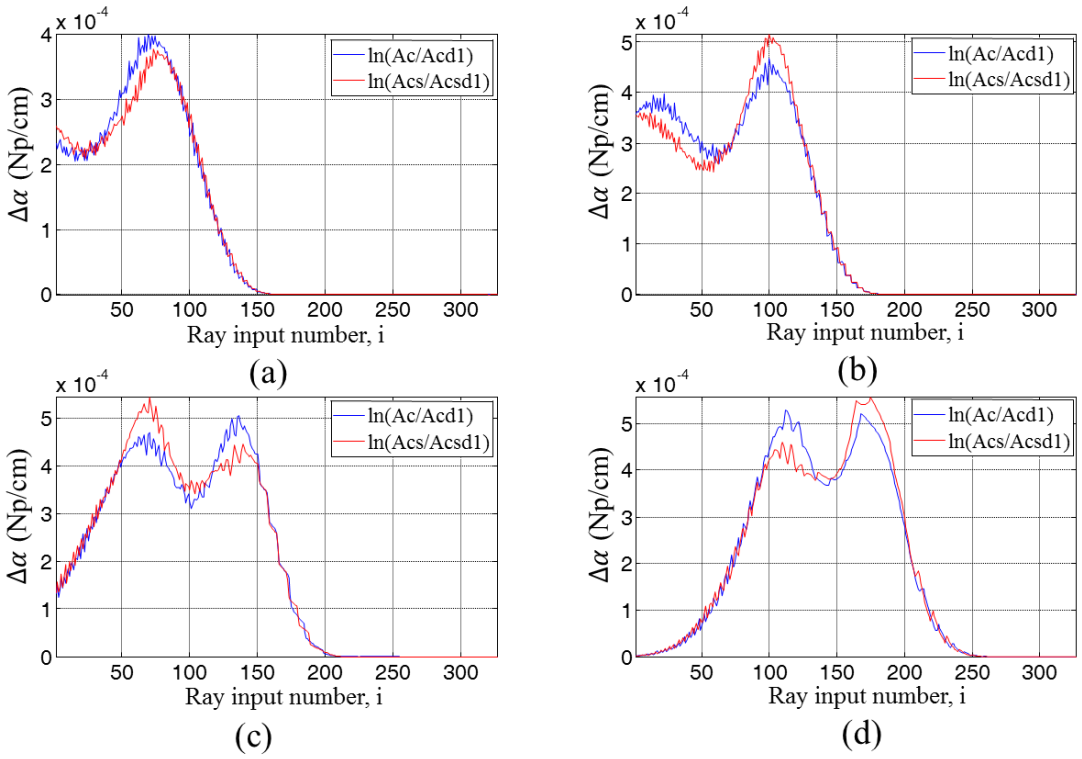

Figure 8.10 Computed differential attenuation coefficient across all rays for defect and defect-free cases: (a) Receiver 1, (b) Receiver 2, (c) Receiver 3, and (d) Receiver 4.

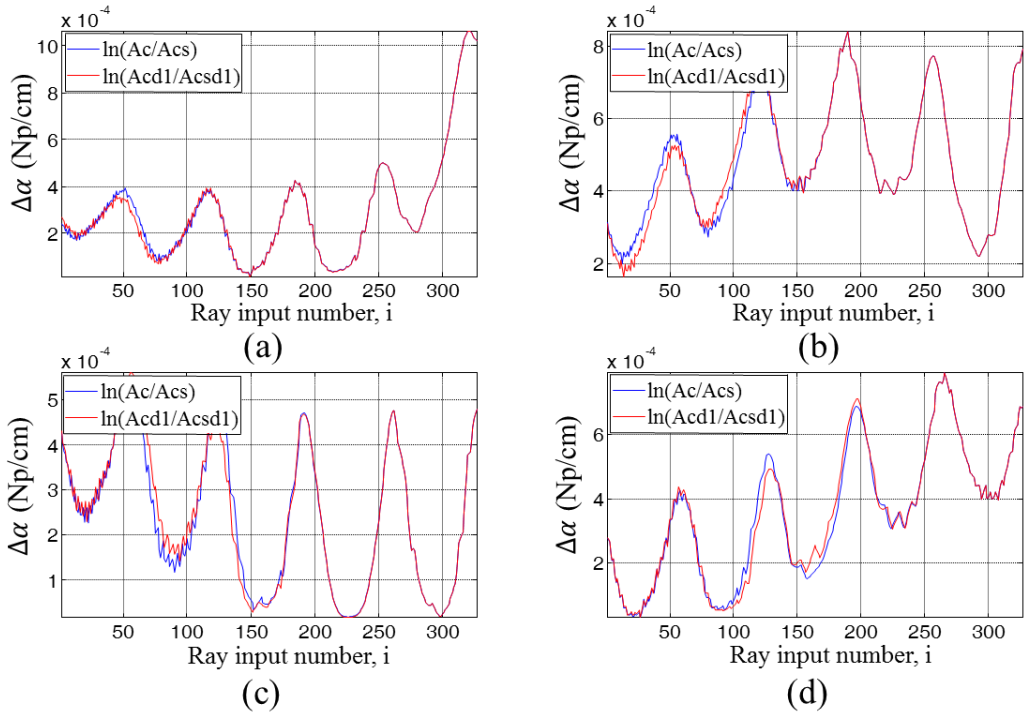

Figure 8.11 Computed differential attenuation coefficient across all rays for rebar and rebar-free cases: (a) Receiver 1, (b) Receiver 2, (c) Receiver 3, and (d) Receiver 4.

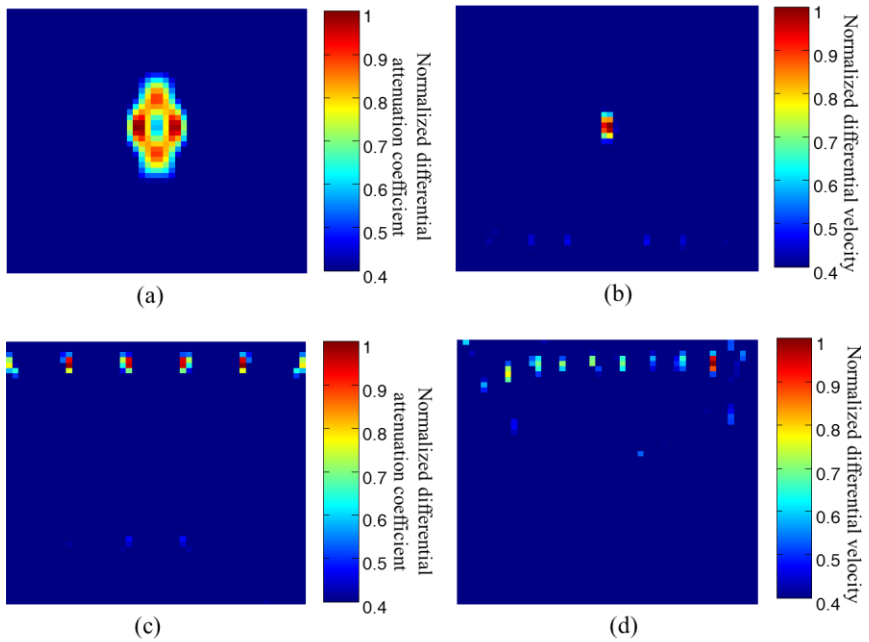

Figure 8.12 Computed normalized differential tomograms: (a) attenuation difference between CSD1 and CS, (b) velocity difference between CSD1 and CS, (c) attenuation difference between CS and C, (b) velocity difference between CS and C.

8.2 Application to full-scale RC column

Differential attenuation tomography was applied using experimental data collected from the full-scale RC column mock-up described in Chapter 4. The applied frequency of ultrasound was 50 kHz so the corresponding wavelength is larger than the maximum size of the aggregate assuming a P-wave velocity of 4000 m/s. Therefore, the attenuation from aggregate scattering can be reasonably ignored. Five column cross-sections that reasonably represent those in the numerical simulation, i.e. similar to CS, CSD1, and CSD2 models, were selected. Figure 8.13 illustrates the location of the selected cross-sections, numbered 1 to 5, and descriptions of each. The details of the data acquisition and testing set-up are presented in Chapter 4.

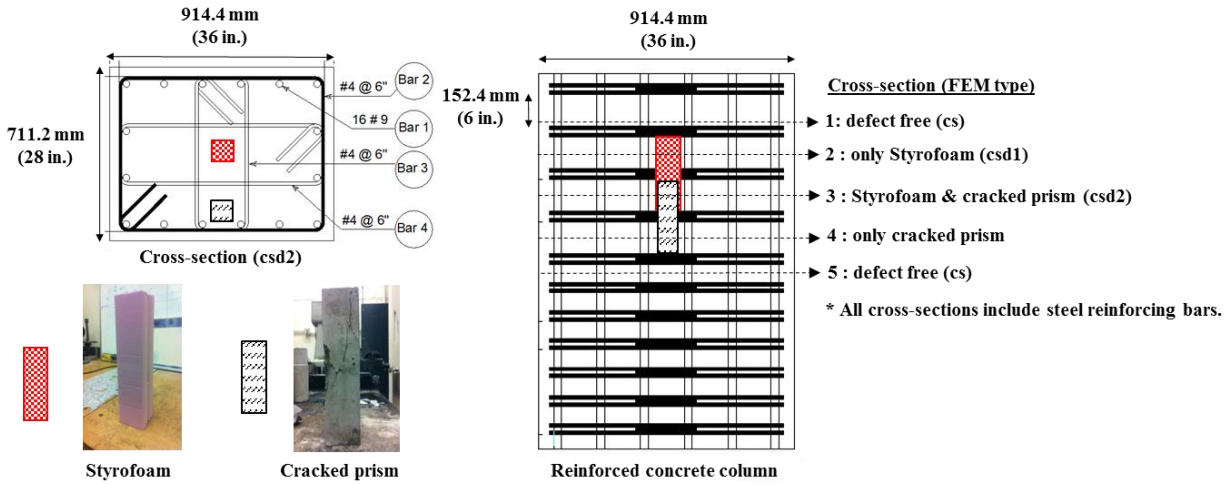

Figure 8.13 Five selected cross-sections for the concrete column sample including descriptions of the cross-sections.

8.2.1 Data analysis

The peak amplitudes of the first arrivals in the signal were obtained from experimental data, as illustrated in Fig 8.14. The defined arrivals by the noise-threshold were within the first half (negative) cycle of the signal (see Chapter 4). Then, the first half cycle of the signal was windowed and the maximum value was recorded as the peak amplitude. The set of the obtained peak amplitudes from each accelerometer (see Chapter 4) is presented in Fig 8.15, showing that the set of amplitude has a significantly different scale. The large gap of the amplitude scale is because the coupling condition between sensors and the concrete surface is different for each sensor, even though the applied accelerometers have the same nominal sensitivity. To construct the Amp'_i data set based on equation (9.10), the set of peak amplitudes from each receiver is normalized by the maximum value, which is from the shortest ray path.

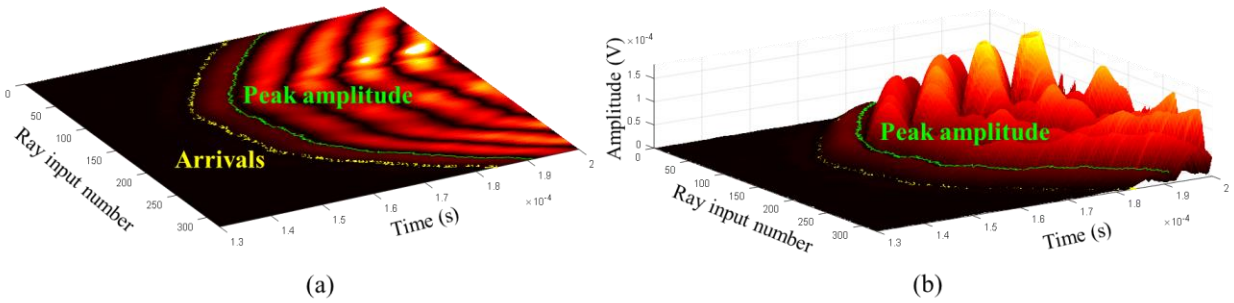

Figure 8.14 Illustration of peak amplitude picking process: (a) stacked A-scans with picked arrivals and peak amplitude, (b) 3-D visualization of the stacked A-scan.

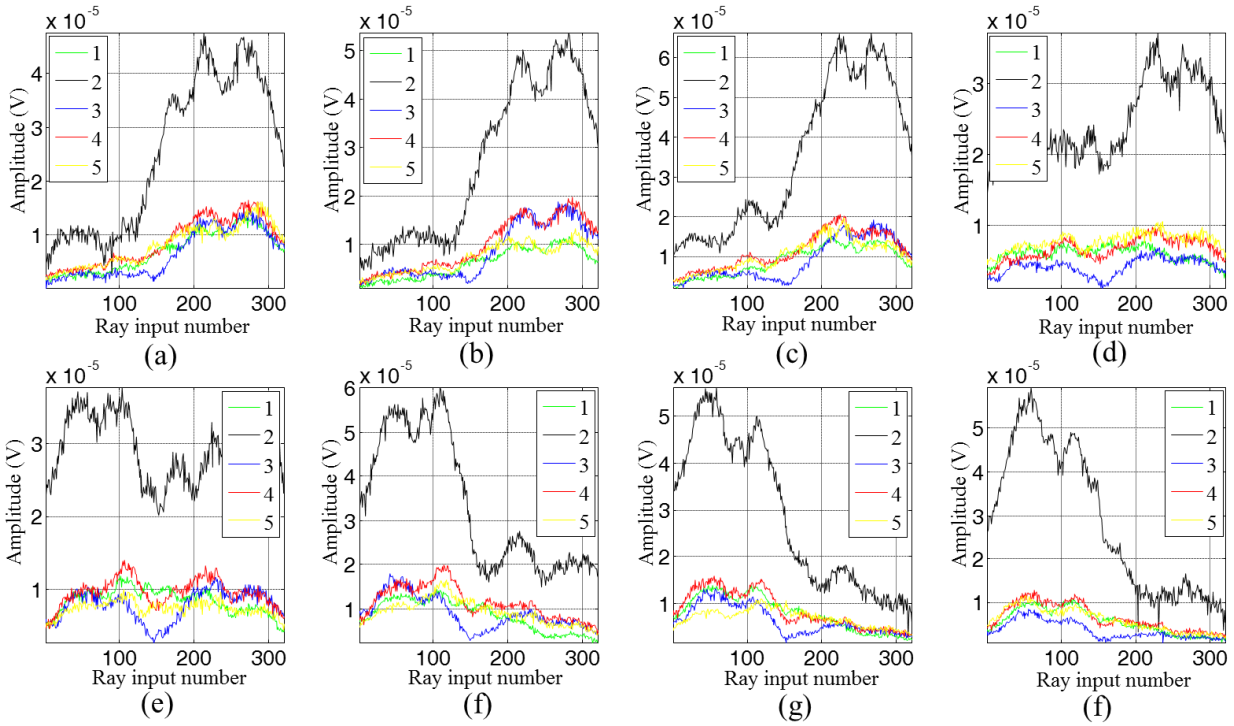

Figure 8.15 Computed peak amplitude across all rays from cross-sections 1 to 5: (a) Receiver 1, (b) Receiver 2, (c) Receiver 3, (d) Receiver 4, (e) Receiver 5, (f) Receiver 6, (g) Receiver 7, and (f) Receiver 8.

Figure 8.16 compares the normalized peak amplitudes between experimental data and the numerical simulation for equivalent cross-sections. The fluctuating trend of the peak amplitude along the input ray positions, especially for attenuations from rebars, matches well with the results of the simulation. The experimental data show attenuation effects owing to both the bar and the defects. Experimental data show higher attenuation along certain ray numbers, especially long ray paths or paths that traverse a defect. The reasons for this are likely because: 1) the intrinsic attenuation by concrete is not considered in numerical

simulation (no material damping); 2) concrete is highly heterogeneous and scatters the ultrasonic waves; and, 3) the embedded defects in the experiment show more attenuation due to the large mismatch of acoustic impedances. Amp'_i is calculated with respect to the cross-section without defects (section 1) and presented in Fig 8.17, showing the comparison between non-defect and defect sections. The ratio between cross-sections 3 and 1 is expected to have higher attenuation in the center due to the embedded defects while the comparison between cross-section 5 and 1 (both defect-free) should have a flat line. The Amp'_i function from the amplitude ratio 3 to 1 clearly indicates the presence of the defect embedded in the center of the cross-section, while the ratio 5 to 1 is not perfectly flat owing to possible misalignment of rebars from each section.

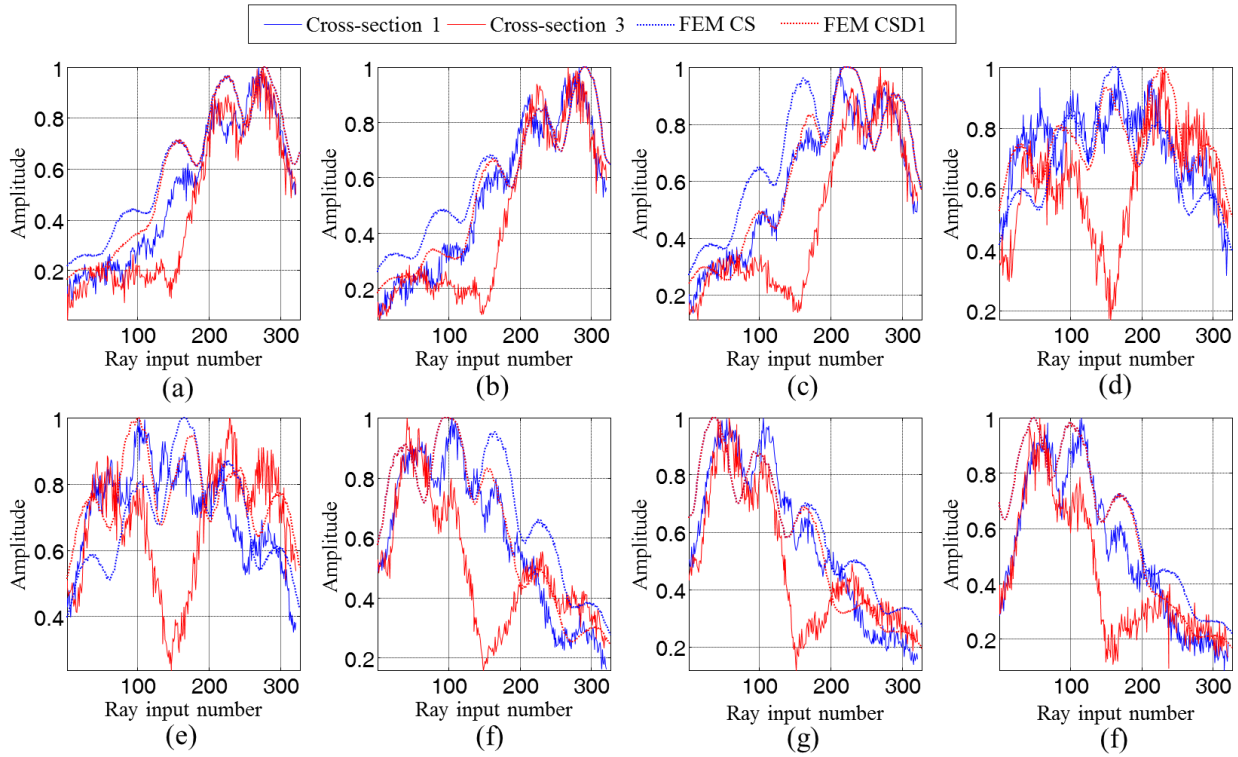

Figure 8.16 Comparison of normalized peak amplitude results among experimental and FEM simulation data for different paths through the concrete column: (a) Receiver 1, (b) Receiver 2, (c) Receiver 3, (d) Receiver 4, (e) Receiver 5, (f) Receiver 6, (g) Receiver 7, and (f) Receiver 8.

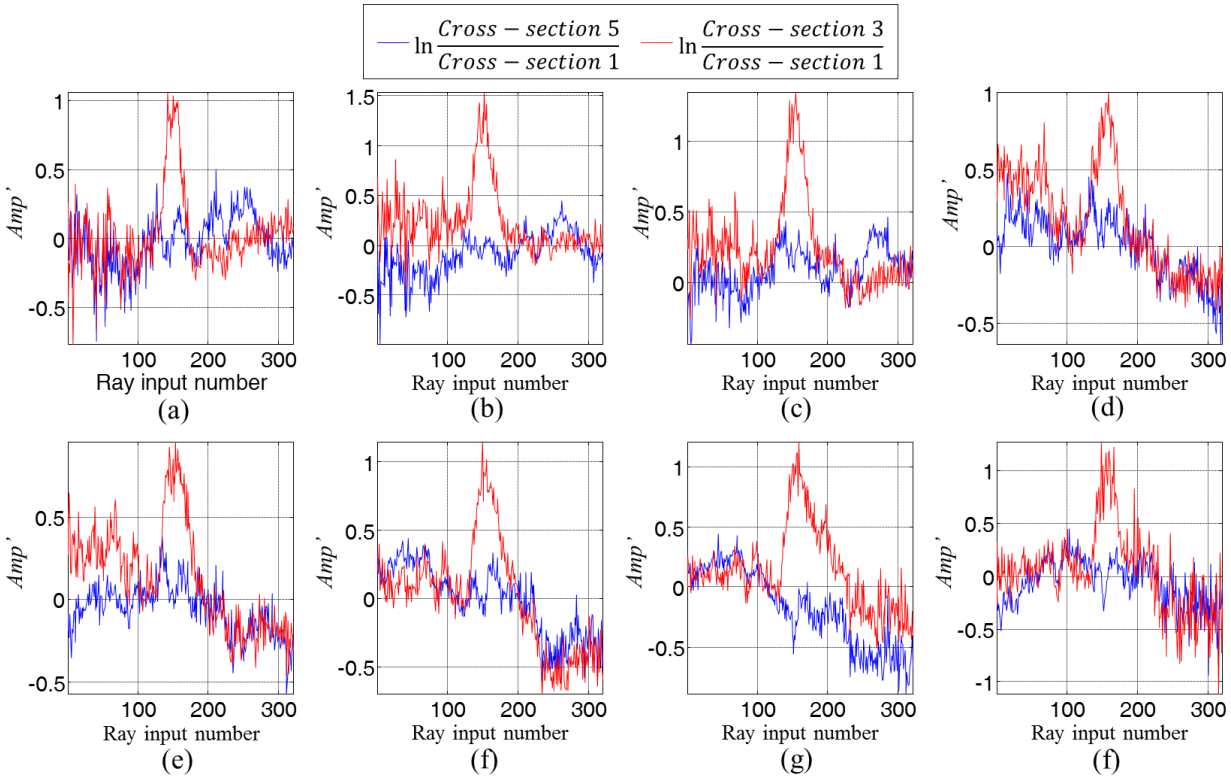

Figure 8.17 Comparison of the peak amplitude results among non-defect (blue) and defect (red) sections from: (a) Receiver 1, (b) Receiver 2, (c) Receiver 3, (d) Receiver 4, (e) Receiver 5, (f) Receiver 6, (g) Receiver 7, and (f) Receiver 8.

8.2.2 Differential attenuation tomography from experimental data

Differential attenuation tomograms were generated from the experimental data using the algebraic reconstruction technique (Randomized Kaczmarz method). Selected reconstructed images are presented in Fig 8.18. The differential tomogram from two defect-free sections shown in fig 8.18a presents no indication of defects but some differentials at rebar locations; it is likely because the locations of rebars in two cross-sections are not identical and the difference of the attenuation may occur. The other tomograms show high attenuation indications in the regions where we expect embedded defects. It is noted that the defect sizes are over-estimated in all images; however, the differential tomogram for cross-section 4 clearly shows the location of the cracked-prism without any artifacts. Differential tomography possibly minimizes artifacts caused by limited ray coverage because the ratio of two data set from different cross-sections but same test configuration compensates artifacts from each section. Furthermore, the normalized step focuses on higher attenuation among the other pixel values.

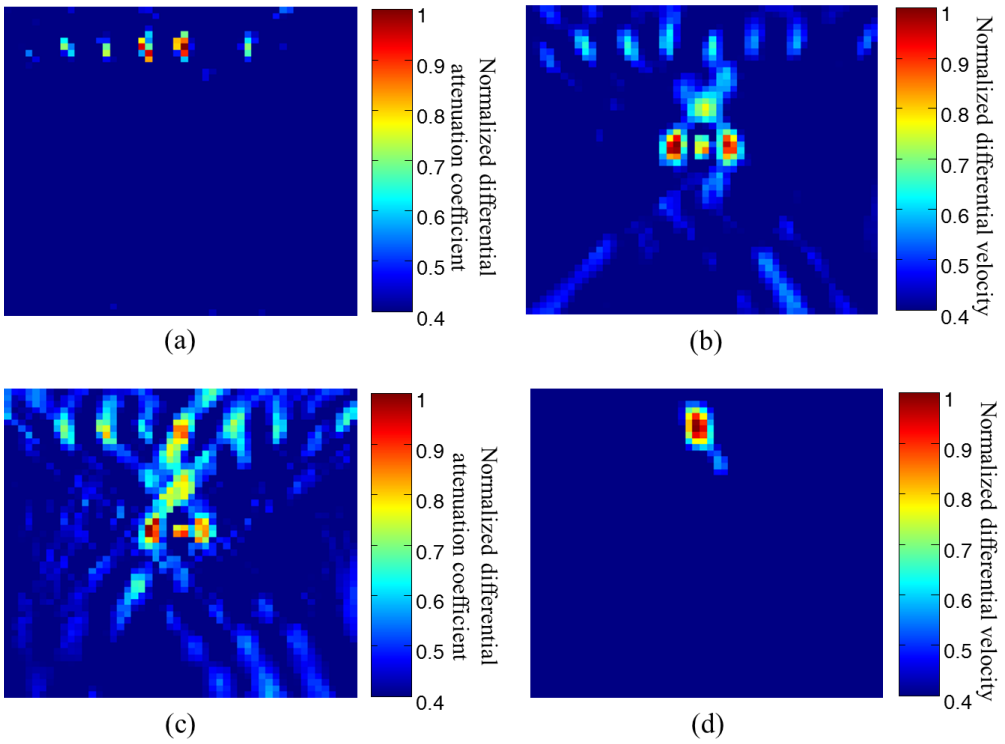

Figure 8.18 Differential tomograms using experimental data from the concrete column: (a) tomogram based on the attenuation differentials between sections 1 and 5, (b) tomogram based on the attenuation differentials between sections 1 and 2, (c) tomogram based on the attenuation differentials between section 1 and 3, and (d) tomogram based on the attenuation differentials between section 1 and 4.

CHAPTER 9 DIFFERENTIAL VELOCITY AND ATTENUATION TOMOGRAPHY APPLIED TO BEAM AND COLUMN CONNECTIONS SUBJECTED TO SEISMIC LOADING

In this chapter, the developed hybrid air-coupled ultrasonic testing system and ultrasonic velocity and attenuation tomographic schemes are applied to full-scale reinforced concrete (RC) and high performance fiber reinforced concrete (HP-FRC) moment frame components subjected to simulated earthquake loading. This study presents the first application of ultrasonic velocity and attenuation tomography for evaluating realistic degradation progress within full-scale structures under simulated earthquake loading. Developed images clearly show the differences in damage progression between HP-FRC and RC specimens at the beam and column connection. Both differential velocity and attenuation tomograms confirm that HP-FRC material distributes internal stress and delays degradation (cracking) rate as compared with conventional RC material, which concentrates the damage at the beam and column joint interface.

9.1 Application of velocity and attenuation tomography

The seismic response of two different full-scale moment frame components (beam and column connections) were investigated using velocity and attenuation tomography. One was composed of normal RC and the other of HP-FRC.

9.1.1 Description of full-scale RC slab-beam-column sub-assemblages

Table 9.1 shows information about the slab-beam-column sub-assemblages, and the tests carried out on them. HP-FRC is expected to increase tensile/shear resistance of the component as compared with conventional RC. Figure 9.1 shows the overall experimental testing configuration, which is housed at the Multi-Axial Sub-Assemblage Testing (MAST) Laboratory at the University of Minnesota. These tests are a part of a research project funded by Network for Earthquake Engineering Simulation (NEES) of the National Science Foundation (NSF). All data collected from these tests are freely available and can be accessed as described in Appendix B. The degradation progress within the plastic hinge region, the joint between the beam and column, was monitored by ultrasonic data collected using the automated scanning system described in Chapter 4. Figure 9.2 presents structural details about the plastic hinge connection area including locations of installed internal concrete strain gauges. The strain gauges were embedded in two different directions: X' (perpendicular to the applied cyclic loads) and Y' (parallel to the applied cyclic loads). In addition, external surface strains of the connection region were monitored using digital image correlation (DIC). It should be noted that HP-FRC connections are designed to have lower volumes of steel reinforcement compared with conventional RC connections because the HP-FRC material itself is expected to increase shear resistance of the element compared to normal concrete. In the HP-FRC structure, the spacing of transverse reinforcing bars in the column is increased, and the stirrups are removed at the

connection with the beam. The differences in reinforcing bar layout are illustrated in figure 9.3. Figure 9.4 describes the loading protocol applied to both specimens, indicating when ultrasonic scanning tests were performed during the loading process. The drift level is used to monitor the extent of deformation response of the element, and is defined as the ratio between the height of specimen and lateral displacement caused by the applied simulated seismic loading, normally expressed as percent. The cyclic loads were applied in the Y' direction for both specimens.

Table 9.1 Details of the test specimens.

Specimen	f'_c, ksi (MPa)	Loading protocol	Drift levels at which ultrasonic scans were performed)
RC connection	7.2 (49.5)	Symmetric Cyclic (ACI 374-05)	(0%, 0.5%)
HP-FRC connection	6.7 (46.0)	Symmetric Cyclic (ACI 374-05)	(0%, 0.5%, 1%)

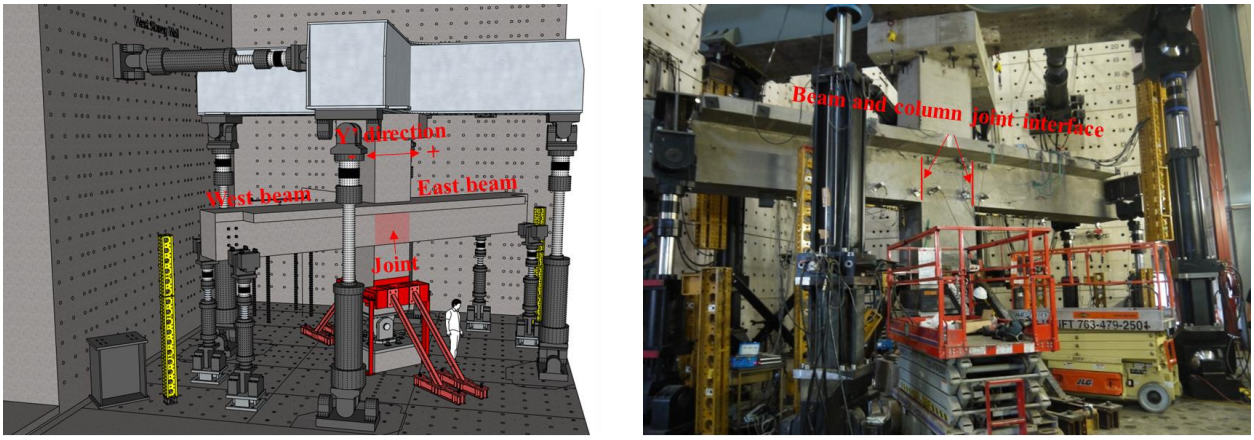

(a) (b)

Figure 9.1 Experimental set-up to test full-scale beam and column connections at the Multi-Axial Subassemblage Testing (MAST) laboratory: (a) illustration of test plan indicating the direction of the cyclic loading, (b) photograph of the experimental set-up.

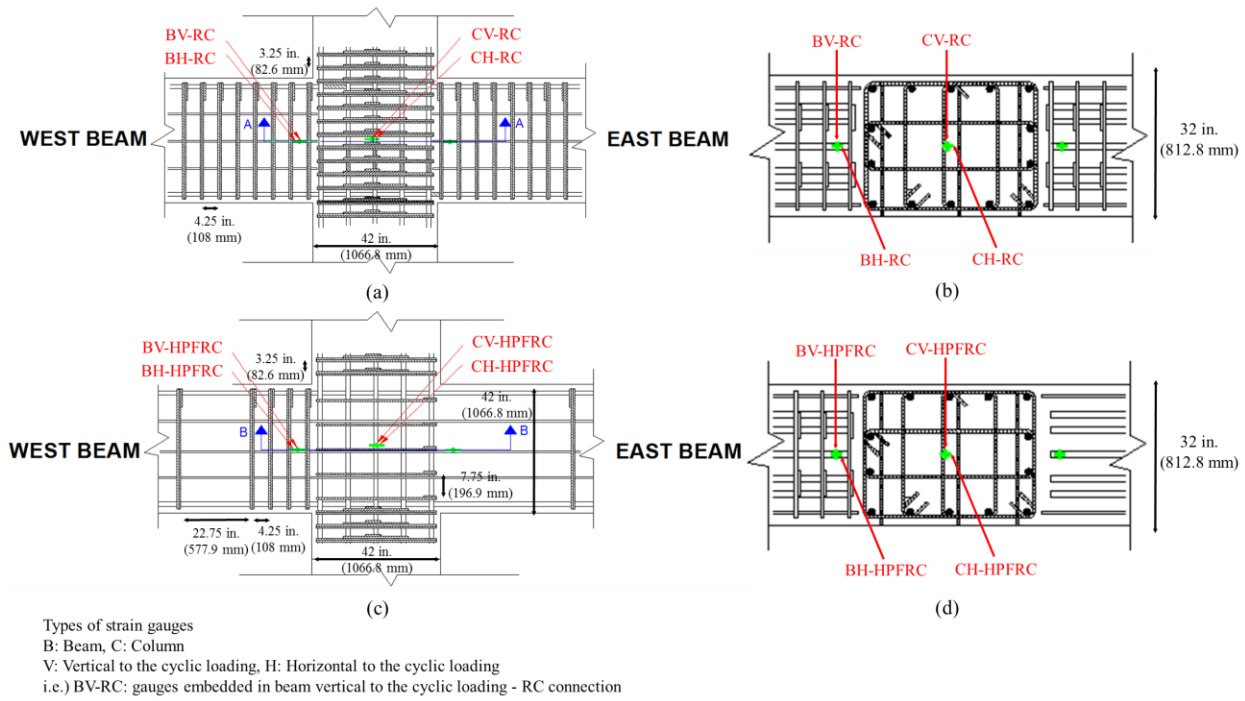

Figure 9.2 Detail of the beam and column connections indicating embedded strain gauges: (a) RC connection, (b) cross-section A-A presented in (a), (c) HP-FRC connection, and (d) cross-section B-B presented in (c).

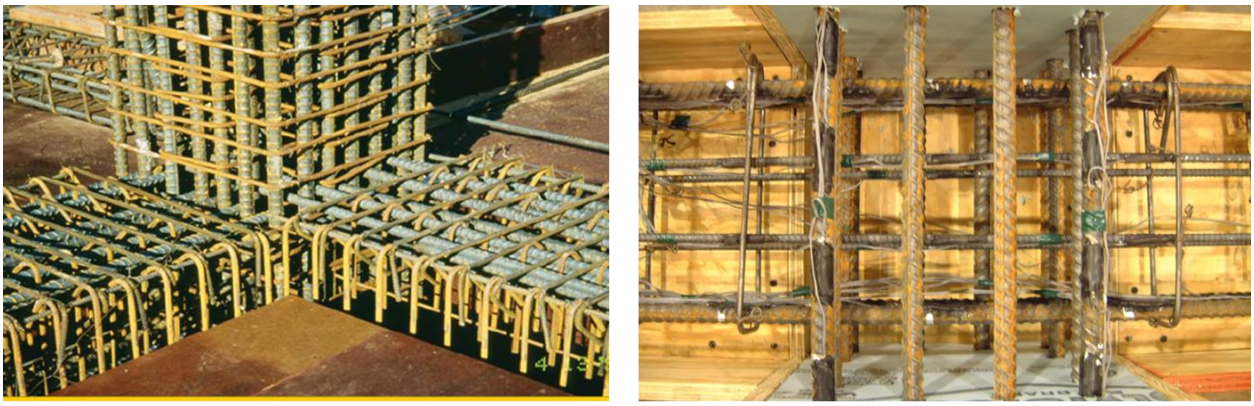

(a) (b)

Figure 9.3 Comparison of seismic RC structural design: (a) conventional RC in California and (b) an example of that for HP-FRC (Parra-Montesinos et al. 2005).

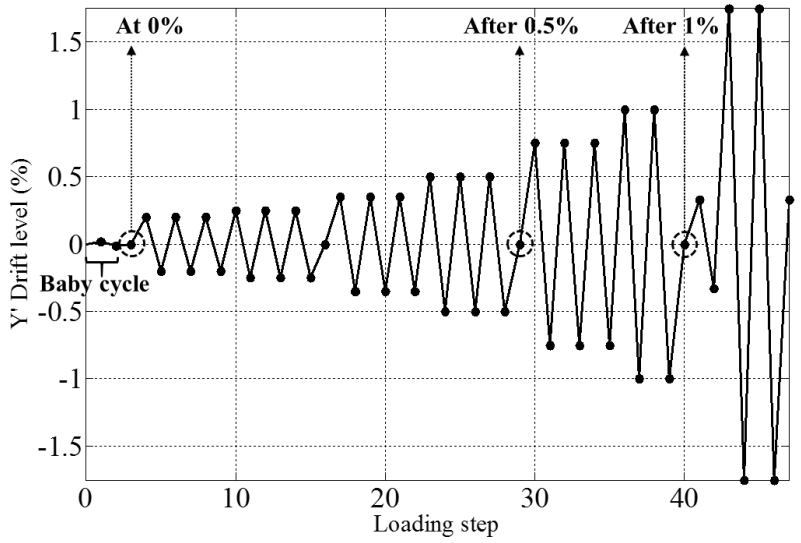

Figure 9.4 Applied loading protocol where dotted circles indicate instance of ultrasonic scanning tests expressed in terms of applied drift level.

9.1.2 Ultrasonic data measurement

Ultrasonic scanning tests were performed at the juncture of the "west" beam and the joint; the relative positions of the "west" and "east" beams are indicated in Figs. 9.1 and 9.2. Within the selected scanning zone, four horizontal and parallel cross-sections were scanned using the automated testing frame described in Chapter 4. Figure 9.5 shows the design of the HP-FRC connection, identifies the location of the four ultrasonic scanning lines (A to D), and indicates receiving sensor positions. The location of the scanning lines and sensor position are nominally identical for both RC and HP-FRC structures. Each scan line generates data that were used to reconstruct conventional and differential cross-sectional tomograms across sections A to D. The size of the scanned cross-section is 42 by 18 inches (1067 by 457 mm) as shown in figure 9.5b. Along each scan line, the ultrasonic sending transducer was moved in 0.1 in. (2.54 mm) increments along the scan line. On the opposite surface along the same cross-sectional plane, eight accelerometers (PCB 352c15) were attached onto the surface. The accelerometers were positioned along one single line with 1.5 in. (38.1 mm) to 3 in. (76.2 mm) spacing between sensors. Figures 9.5 and 9.6 provide detail about the hybrid air-coupled test configuration. The scanning tests were performed after a certain loading protocol was applied, where the sample was held constant at its neutral position (0% drift). After a round of ultrasonic data collection was completed, the test frame was removed so that the next round of loading could be applied. Figure 9.7 presents photos of the ultrasonic scanning set-up and measurements.

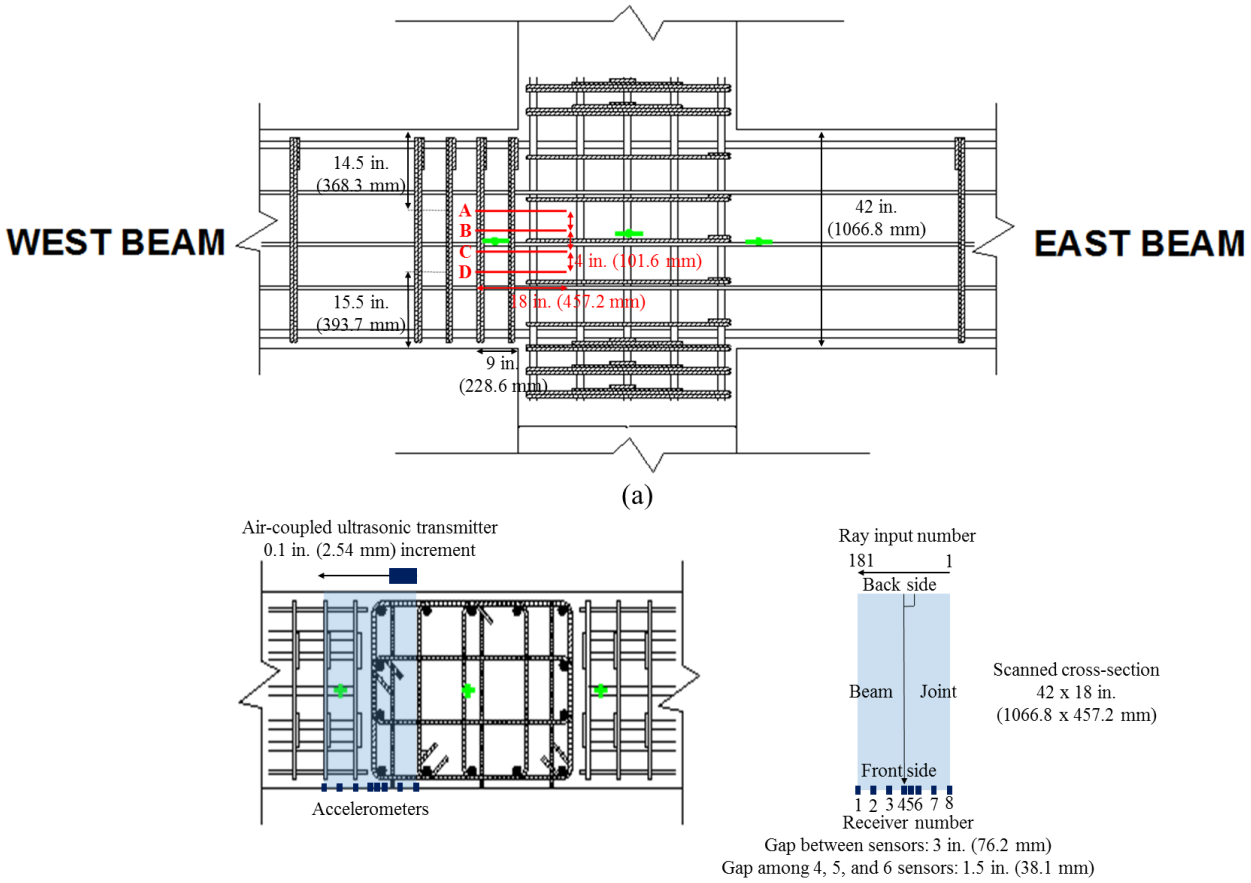

Figure 9.5 Detail of ultrasonic scanning tests: (a) grid lines (red lines) indicate e the four lines A through D where ultrasonic scanning tests were performed and (b) the shaded blue box indicates approximate scanned volume position and relative of moving transmitter and eight receivers. The cross-sections for ultrasonic scanning test are identical for both RC and HP-FRC structures.

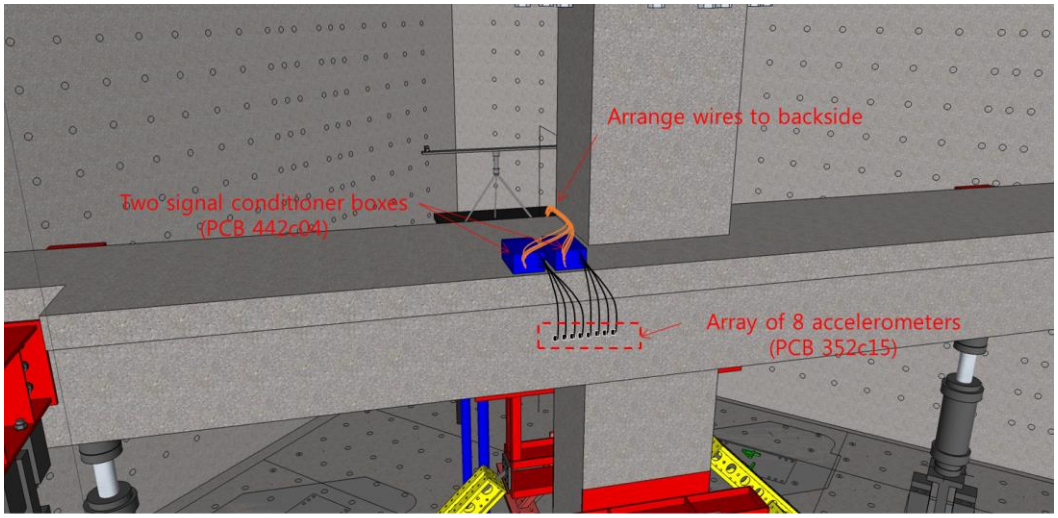

(a)

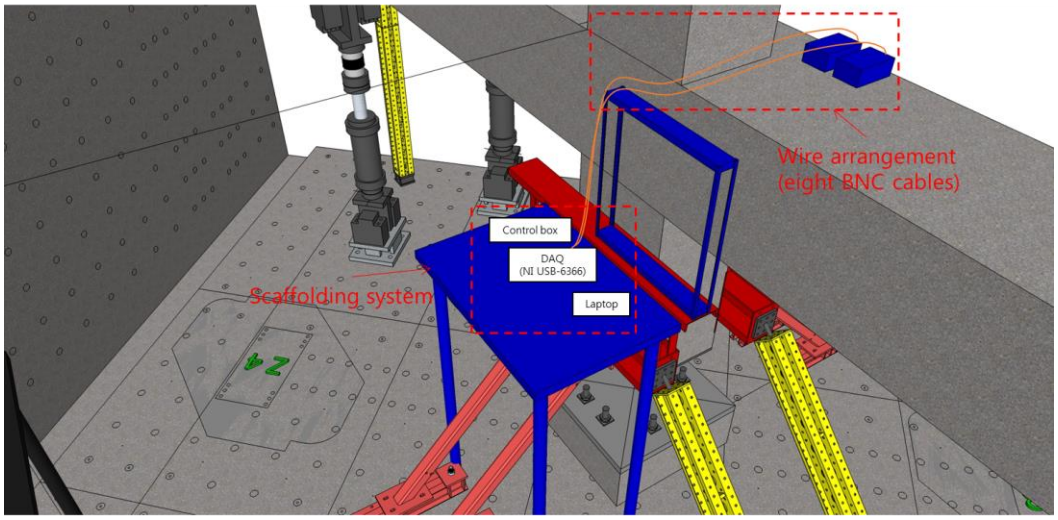

(b)

Figure 9.6 Schematic illustration of ultrasonic scanning test set-up: (a) the front side where receivers were attached and (b) the back side where robotic scanning frame was set up.

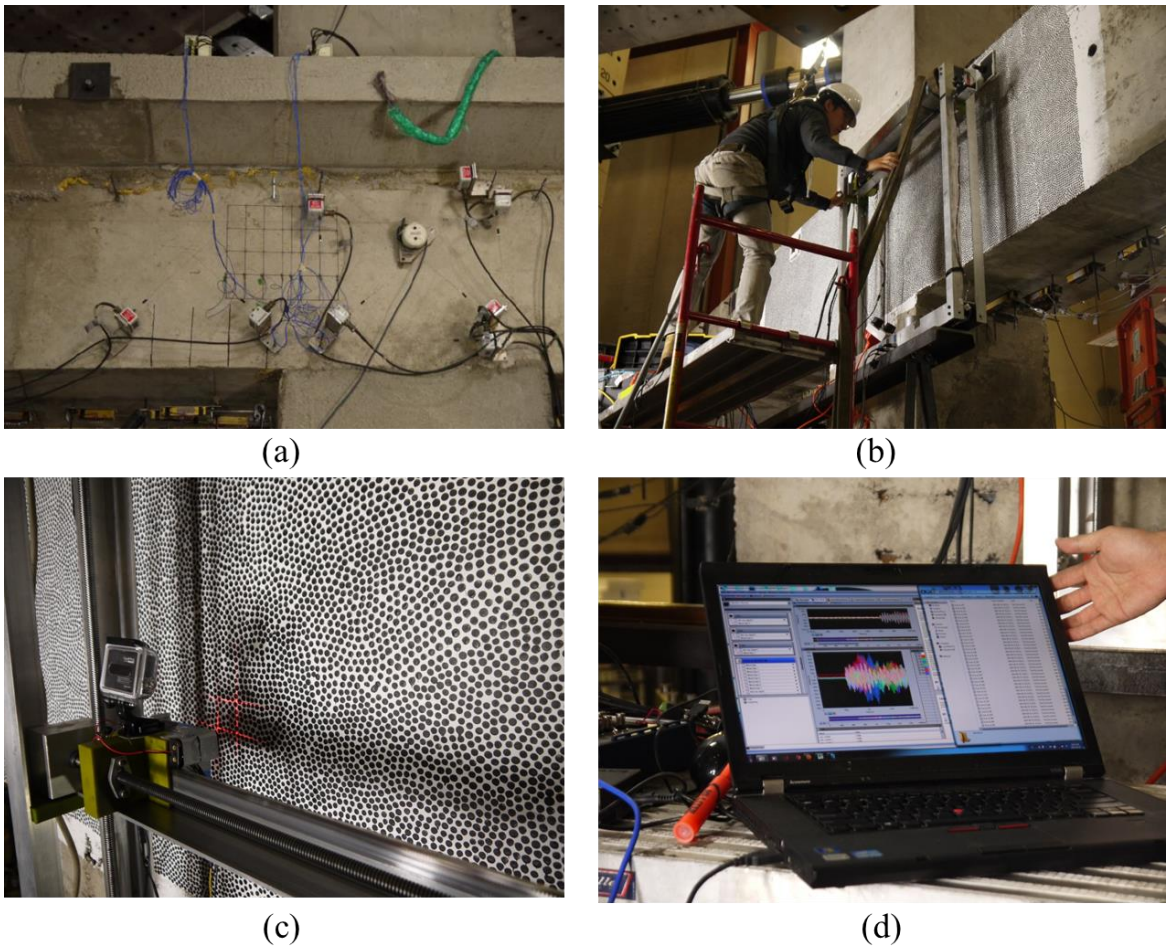

Figure 9.7 Example photographs from ultrasonic scanning tests: (a) attached receiving sensors on the surface of the connection, (b) robotic scanning frame set-up, (c) air-coupled ultrasonic scanning process, and (d) through-thickness ultrasonic signal data collection.

The ultrasonic waves were generated using the air-coupled transducer (SensComp 600) using a 16-cycle 50 kHz narrow band excitation signal. The measurement set-up included signal conditioners (PCB 442c04) for the accelerometer array and a data acquisition digitizer (NI USB-6366) with a 2MS/s sampling rate per channel. A total 1,448 through thickness time signals were obtained at each scanned cross section, thus a total of 5,792 signals from four cross-sections were obtained at each drift level. The air gap between the transmitting transducer and concrete surface was measured at every scanning position using the procedure described in Chapter 4.

The repeatability of the data obtained from the ultrasonic measurement configuration was evaluated by carrying out one repeated scan line data collection at the same cross-section (scan line B), specimen (HP-FRC), and drift level (1%). This test was done to understand the disrupting effects of experimental set-up error including variation of the transducer alignment and position and the coupling condition between the

accelerometers and the surface. After collecting data from cross-sections A to D for this sample and case, cross-section B was re-scanned. To do this. the array of receiving accelerometers was detached and re-attached onto the surface, and the automated scanning frame was removed and replaced to the sending position on the opposite side. Figure 9.8 shows an example set of time signals from the same ray path through the thickness of the cross-section. Because the scale of the amplitudes from each signal set is different due to irregular coupling condition, the signals are normalized by each maximum amplitude of the entire signal. The signals match very well at the beginning (coherent) part of the wave, both in terms of amplitude and phase, where the first arrival and peak amplitude of the wave are defined. Notable mismatch between the signals occurs later in the signal, after about 1000 μs of signal time. The small differences in the signals are likely caused by small variations in position, alignment and coupling of the sensors. Figures 9.9 and 9.10 present stacked A-scan images at the eight different receivers and all sending positions for the repeated scan measurement. Although the amplitudes of the signals vary slightly, especially at later portions of the time signal, the overall appearance of the images is very similar. The results demonstrate the excellent reproducibility of ultrasonic scanning test, especially for early portions of the signal.

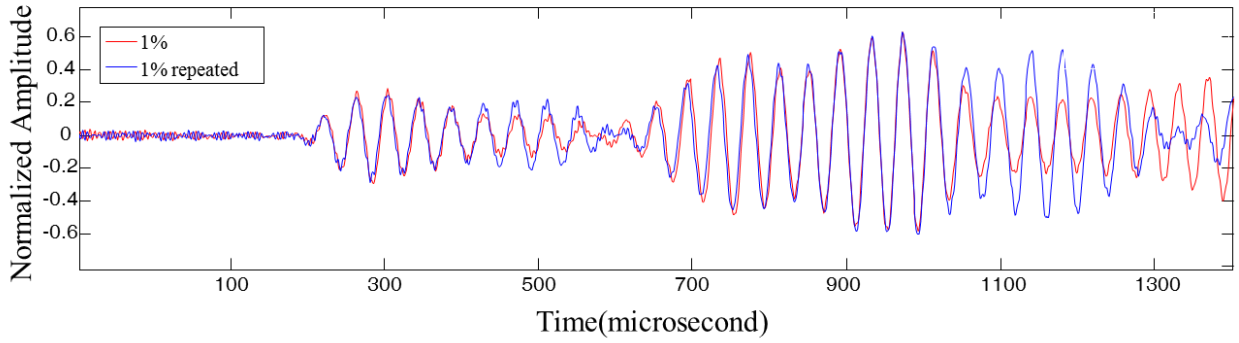

Figure 9.8 Example time signal data from repeated ultrasonic scans on the HP-FRC connection collected from the same position and drift level.

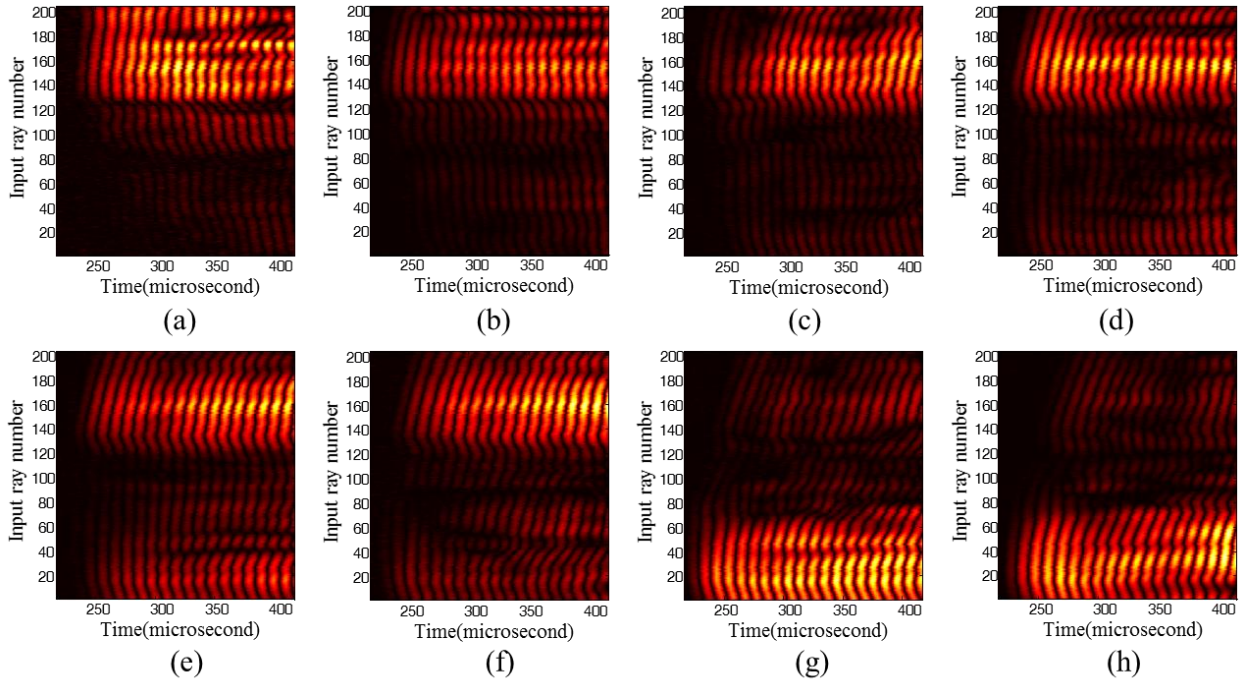

Figure 9.9 Stacked A-scan images measured by receiver positions (a) to (h) through section B of the HP-FRC connection at 1% drift level; trial 1. Brightness is related to time signal amplitude.

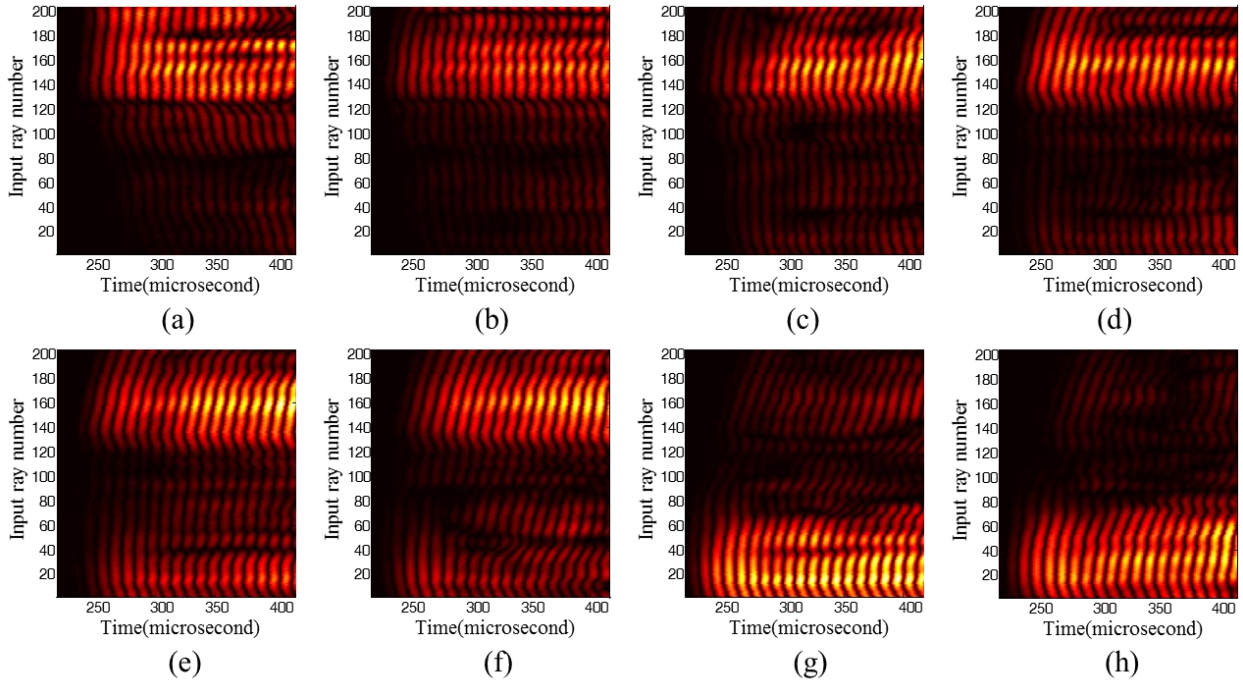

Figure 9.10 Stacked A-scan images from different receiver positions (a) to (h) through section B of the HP-FRC connection at 1% drift level; trial 2. Data are collected under the same conditions as those in Fig. 9.9. Brightness is related to time signal amplitude.

9.1.3 Development of differential ultrasonic tomography

The noise content in the measured ultrasonic signals were reduced using a digital low-pass filter applied through the Matlab platform. The assigned frequencies of the filter at the start of the pass band and the end of the stop band were 90 and 100 kHz, respectively. The arrivals of first wave arrival were defined by the noise-threshold method in the filtered signals (King 2012). Then, the first half cycle of the signal immediately after the defined arrival was windowed and the maximum value within the window was recorded as the peak amplitude.

The linear equations needed to construct differential velocity and attenuation tomograms were applied using P-wave arrival and peak amplitude data, respectively. The details of velocity and attenuation tomographic procedures are described in Chapters 3 and 8, respectively. The difference in P-wave arrivals, Δt_i between 0% and 0.5% drift levels was considered for differential velocity tomography, and the logarithm of the amplitude ratio, Amp'_i for attenuation tomography

$$Amp'_i = \ln \frac{A_{0\%_i}}{A_{0.5\%_i}} \tag{9.1}$$

where $A_{0\%_i}$ and $A_{0.5\%_i}$ are the peak amplitudes of the i-th ray at 0% and 0.5% drift levels, respectively. The ray travel distance matrix, $\mathbf{D_{ij}}$ was constructed based on the assigned j-th pixel of the i-th ray. For each cross-section, the number of measurements, N and assigned number of pixels, M are 1448 and 900 (30 by 30), respectively. The maximum computation time for completing a tomographic reconstruction of one cross-section was 95 seconds. The randomized Kaczmarz method was applied to the linear equations (Hansen and Saxild-Hansen 2012). All computation processes were performed using the Matlab platform.

9.2 Damage evaluation of RC beam and column connections

Photographs of the joint region were taken at each drift level. Figures 9.11 to 9. 13 show the surface of the joint connection zone at 0.5%, 1%, and 1.75% drift levels, respectively for both specimens. At the 0.5% drift level, the RC specimen shows tight surface cracks on the back side of the beam and column joint interface but none on the front side (Figs. 9.11a and 9.11b). The HP-FRC specimen does not reveal any visible cracks at the 0.5% drift level (Figs. 9.11c and 9.11d). As the drift level increases the width of the cracks in the RC specimen increases and appear on both front and back sides, and after 1.75% drift level the interface between beam and column joint completely separate (Fig 9.13b). In the case of HP-FRC, the first visible surface cracks were observed after 1.75% drift level, and those cracks appear mostly in the center of the column joint region (Fig 9.13d).

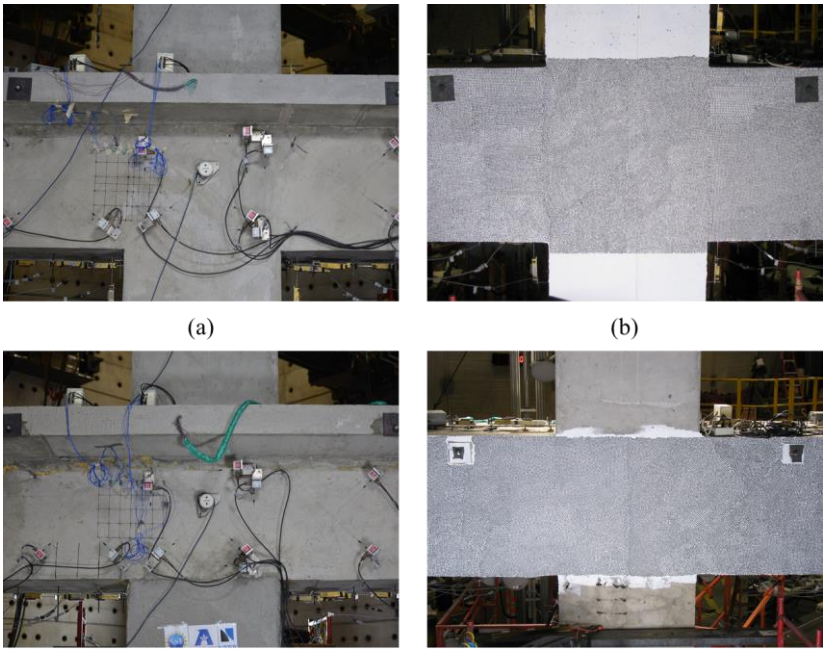

Figure 9.11 Photographs from the beam and column connections at 0.5% drift level: (a) the front side of RC connection, (b) the back side of RC connection, (c) the front side of HP-FRC connection, and (d) the back side of HP-FRC connection.

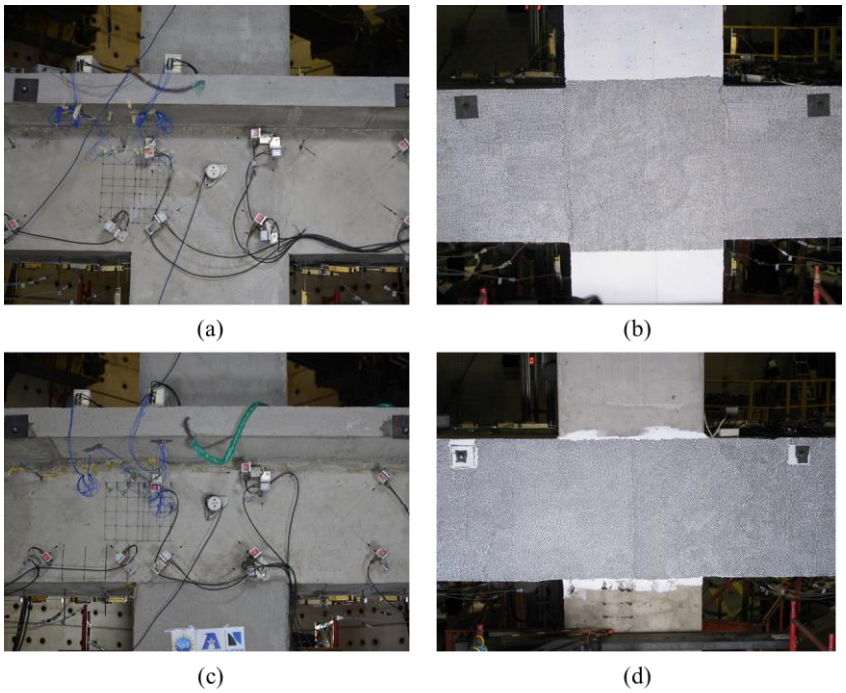

Figure 9.12 Photographs from the beam and column connections at 1% drift level: (a) the front side of RC connection, (b) the back side of RC connection, (c) the front side of HP-FRC connection, and (d) the back side of HP-FRC connection.

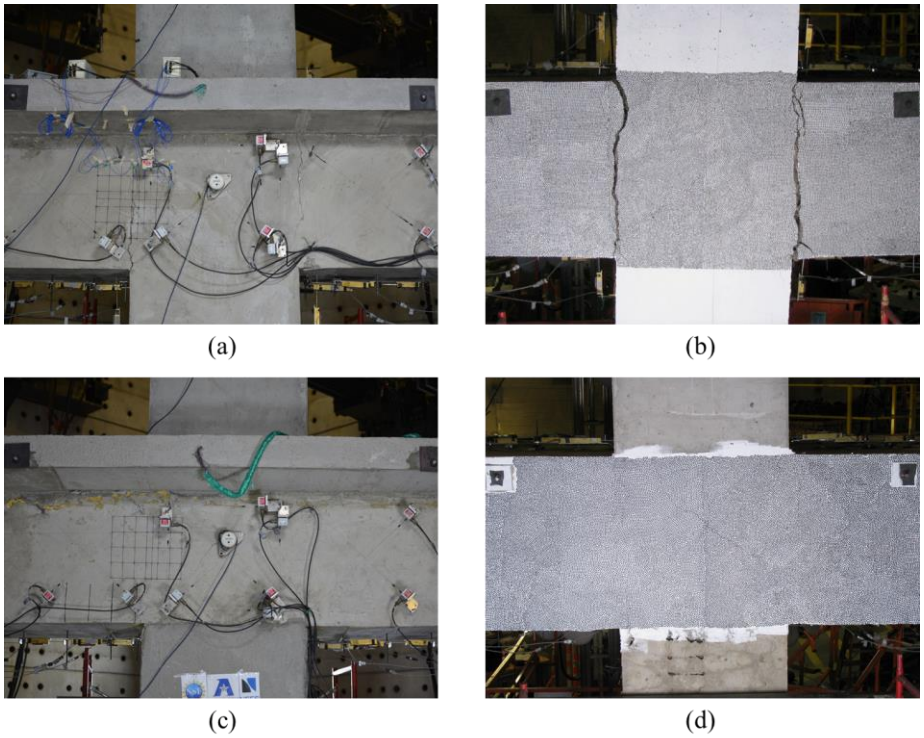

Figure 9.13 Photographs from the beam and column connections at 1.75% drift level: (a) the front side of RC connection, (b) the back side of RC connection, (c) the front side of HP-FRC connection, and (d) the back side of HP-FRC connection.

Figure 9.14 presents the results of digital image correlation imaging for both connection types at the 0.5% and 1% drift levels. The color scale of the image indicates the intensity of the surface strain in the horizontal direction (the same direction as the applied load). Overall, the magnitude of surface strain is much higher in RC than in HP-FRC at the same drift level. Furthermore, the strains in the RC connection are concentrated along the interface between the beam and column joint, while the strains in HP-FRC connection are distributed across the volume of the element. At the 1% drift level, the magnitude of the strain along the beam-column interface in the RC connection is higher than 0.003 (0.3%) strain, which is the conventionally accepted maximum strain limit for tensile concrete failure (Mindess et al. 2002, Metha and Monteiro 2005). These results correlate with the photographs (Fig 9.12b), showing cracks that form only at beam and column joint interface. In the case of HP-FRC, the maximum strain intensities are always under 0.002 (0.2%) at the 1% drift level.

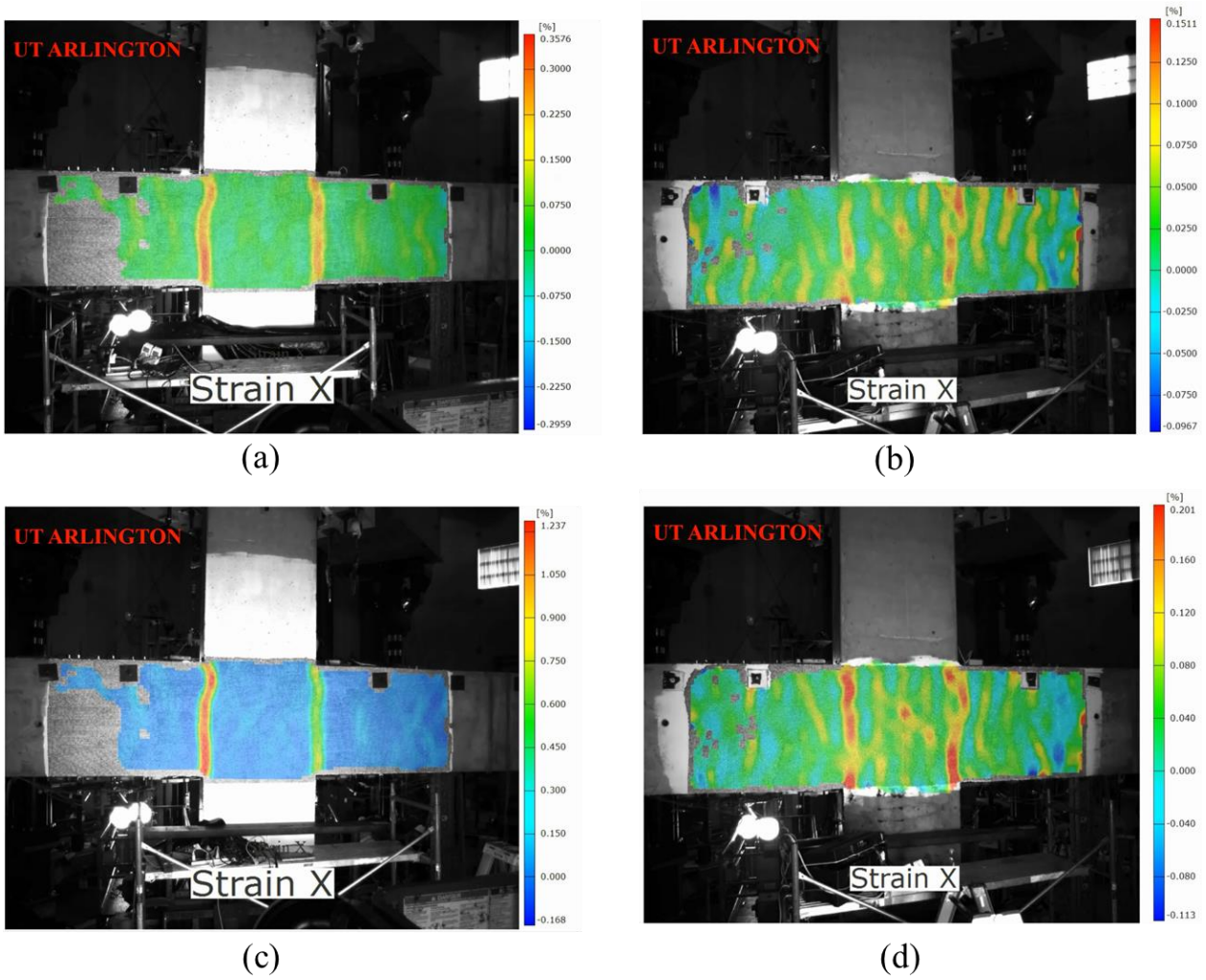

Figure 9.14 Digital image correlation images indicating the magnitude of surface strain in the direction of loading on the back side of the connection: (a) RC at 0.5% drift level, (b) HP-FRC connection at 0.5% drift level, (c) RC at 1% drift level, and (d) HP-FRC at 1% drift level; the color scale represents the magnitude of strain in the Y' direction with units of strain percentage.

To quantify the mechanical response of the structural elements under the applied loads, stiffness slope and concrete internal strain gauge data were monitored. The calculations of global stiffness slope and local internal residual strains are described in Chapter 7 (see Figs. 7.6 and 7.7). Figure 9.15 shows the sub-assemblages' drift owing to the applied force, and figure 9.16 presents the calculated stiffness slopes at each drift level. The stiffness slopes of the two specimens are essentially identical up to the 1 % drift level. At the 1.75% drift level, the RC specimen was observed to exhibit severe surface cracking the beam and column joint interface (Fig 9.13b) and also the stiffness slope of the RC specimen starts to become lower than that of the HP-FRC specimen.

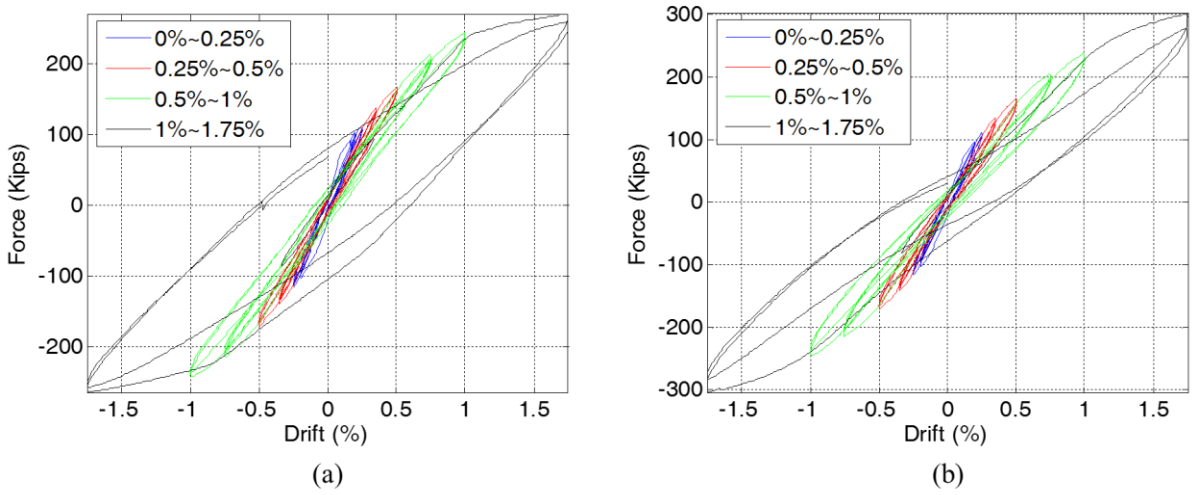

Figure 9.15 Mechanical behavior curves under cyclic loadings up to 1.75% drift level: (a) RC and (b) HP-FRC.

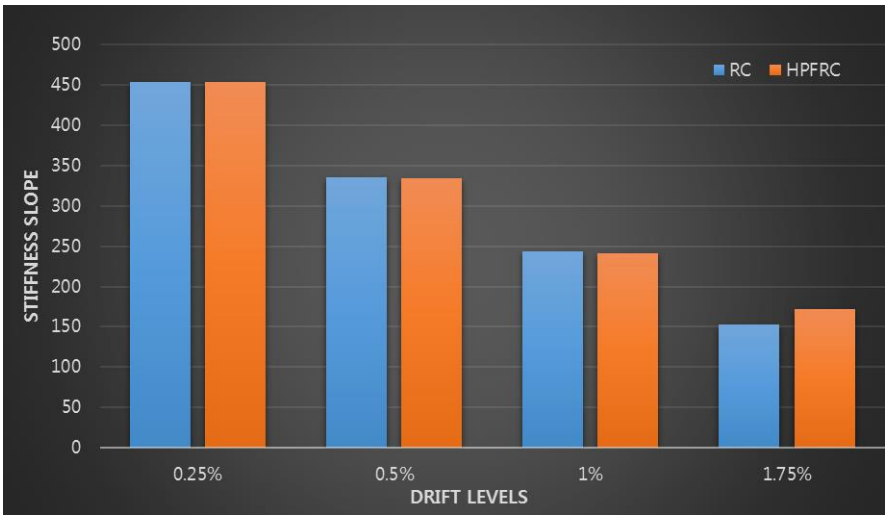

Figure 9.16 Stiffness slope as a function of applied drift level. Units of presented stiffness slope values are applied lateral force in the Y' direction in kN per percentage column drift in that direction.

The cumulative residual strains measured by embedded strain gauges are presented in Fig 9.17. Overall, the residual strains measured from the joint region show significantly higher magnitude than those from the beam region. It is expected that concrete within the joint experiences faster degradation than that in the beam. The strain gauges positioned in the Y' direction (the same direction to the loading cycle) in HP-FRC specimen exhibit higher residual strains compared to those in the X' direction, most likely because of the direction of the loading. However, some horizontally (Y' direction) embedded gauges show significantly higher strains than the vertically embedded (X' direction) gauges in the RC specimen, as seen in gauge RC_BV at 0.5% and RC_CV at 1% drift levels in Fig. 9.17. This is because of possible concrete damage

or confinement pressure from the densely placed reinforcing bars in the RC specimen. From the analysis of cumulative residual strains, RC specimens possibly contains higher level of internal cracking damages compared to HP-FRC specimens at 0.5% and 1% drift levels. The effect of confinement pressure shown in RC specimen can be significantly reduced from HP-FRC specimen because of less volume of embedded reinforcements.

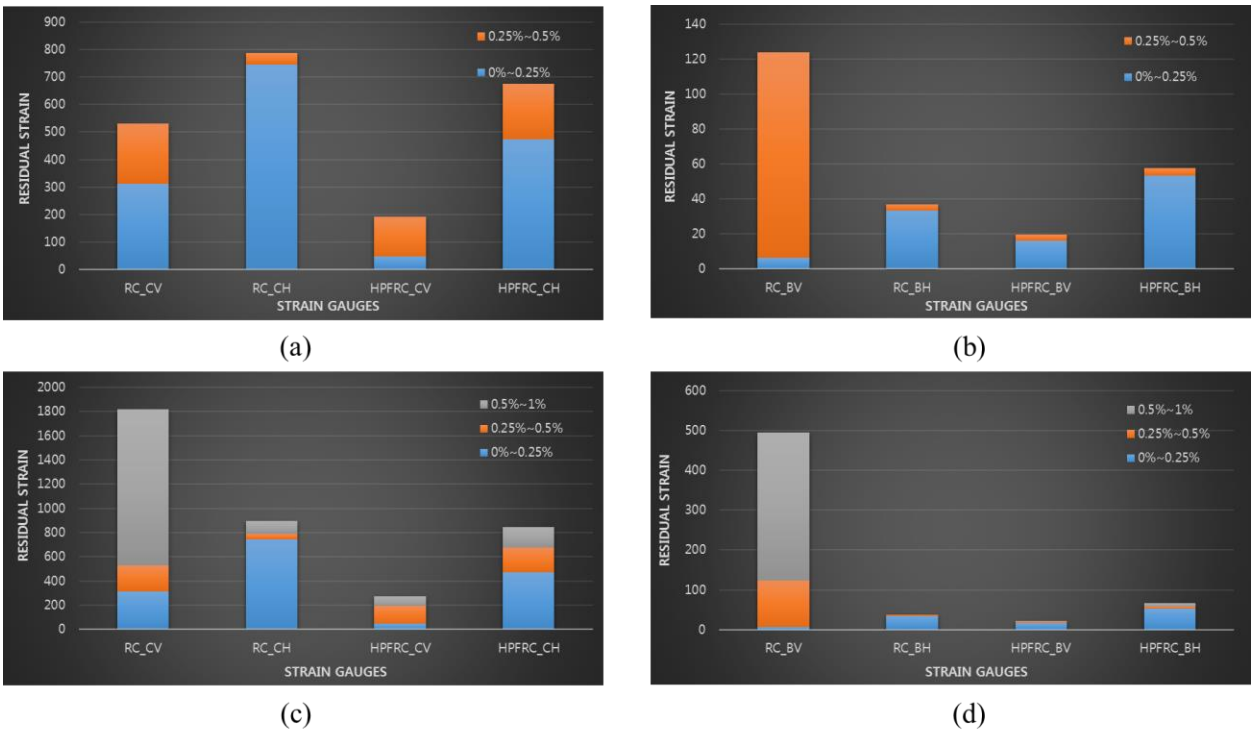

Figure 9.17 Residual strain (microstrain) from internal embedded strain gauges as a function of applied drift level: (a) gauges in column at 0.5% drift level, (b) gauges in beam at 0.5% drift level, (c) gauges in column at 1% drift level, and (d) gauges in beam at 1% drift level. Position of strain gauges shown in Fig. 9.2

9.2.1 Stacked A-scan representations

The ultrasonic signals received by one accelerometer (receiver number 4 shown in Fig 9.5) along all four scan lines are stacked to create an image and shown in Figs. 9.18 to 9.22 for the various cases. The signals are normalized by the maximum amplitude from each data set within an image, and the brighter colors in the image represent higher amplitude. Because the receiver was attached at the center of the scanned region (at beam and column joint interface), a parabolic shaped wave front is expected in the stacked A-scan images because of changing path lengths as the sending transducer moves. Figures 9.18 and 9.19 show the stacked A-scans at 0% and 0.5% drift levels, respectively, for the RC connection. The expected parabolic shaped wave fronts are observed at 0% drift level from all four scan lines. However, after a 0.5% drift level

has been achieved, the wave fronts show clear indentation in the wave front shape at location of the interface between the beam and column joint, and the patterns of the indented wave fronts are similar for all four cross-sections. The wave front indentation represents a region of local amplitude loss, likely indicating a location or path that contains material cracking degradation.

Figures 9.20, 9.21, and 9.22 show the stacked A-scans at 0%, 0.5% and 1% drift levels, respectively, for the HP-FRC connection. Similar to the RC connection, a parabolic shaped wave front is observed before loading. However, the shape of wave fronts in the images change after 0.5% drift level has been attained: scan line A shows indentation across a broad region near the beam and column joint interface, while scan lines B, C, and D indicate indentations of the wave fronts across the joint region. The stacked A-scan image from scan line A suggest that the damage near the interface between beam and column joint is more broadly distributed than those from RC connection. The stacked A-scan images from scan lines B, C, and D suggest that the material in the joint region is more damaged than that in the beam region. After the 1% drift level is achieved, deeper and broader wave front indentations were observed as compared to those at the 0.5% drift level, confirming that higher levels of internal cracking damage are seen with increasing draft level.

Stacked A-scan representations demonstrate that ultrasonic waves are highly sensitive to internal material degradation at the initial stage of seismic loading, which cannot be evaluated by external photographs and stiffness slope data. At the 0.5% drift level, only very thin external surface cracks were observed in RC connection sample, which are difficult to identify in the photo in Fig 9.11b. In the case of HP-FRC, no surface cracks were reported up to the 1% drift level, although the ultrasonic images show clear wave front indentations at certain locations within the cross section. Although the stiffness slope decreases as the drift level increases, this one value cannot assess the different patterns of damage within the two specimens. Because the mechanical performance from the stiffness slope is calculated based on the lateral displacement of the specimen under applied loading, the calculation is more affected by yielding of reinforcing bar than by concrete cracking.

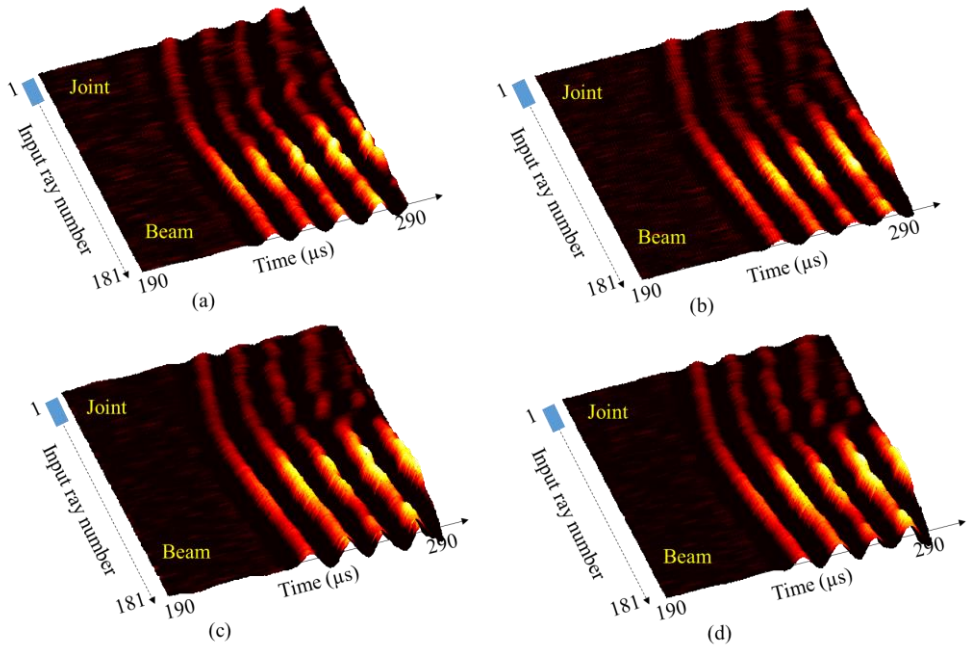

Figure 9.18 Stacked A-scan images from RC connection obtained by accelerometer 4 at 0% drift level: (a) cross-section A, (b) cross-section B, (c) cross section C, and (d) cross-section D; brightness is related to time signal relative amplitude. Cross-section locations shown in Fig. 9.5.

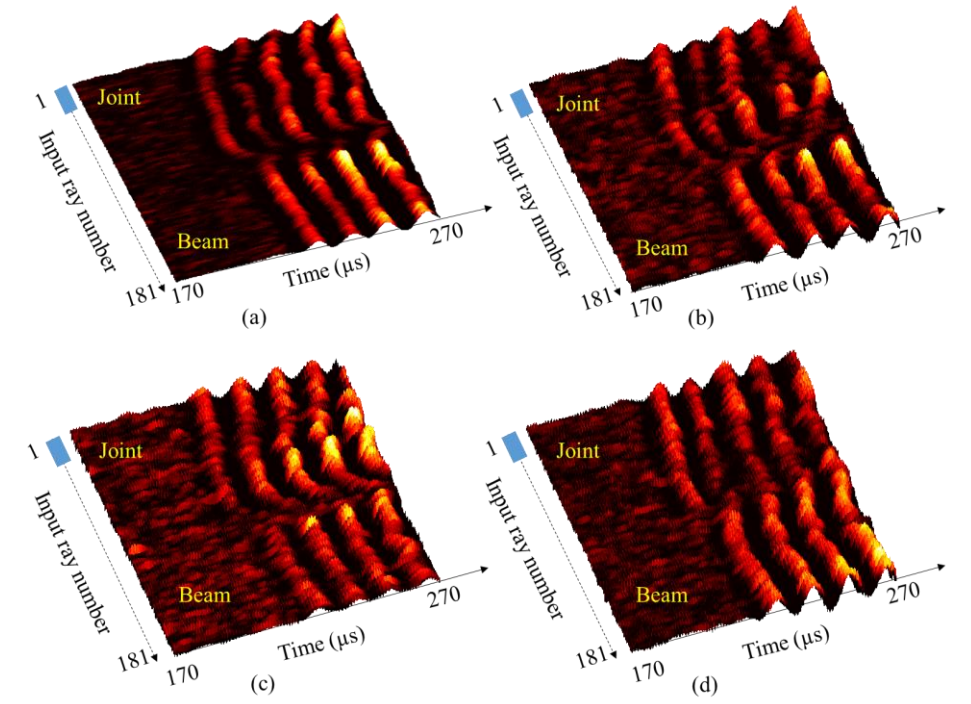

Figure 9.19 Stacked A-scan images from RC connection obtained by accelerometer 4 at 0.5% drift level: (a) cross-section A, (b) cross-section B, (c) cross section C, and (d) cross-section D; brightness is related to time signal relative amplitude. Cross-section locations shown in Fig. 9.5.

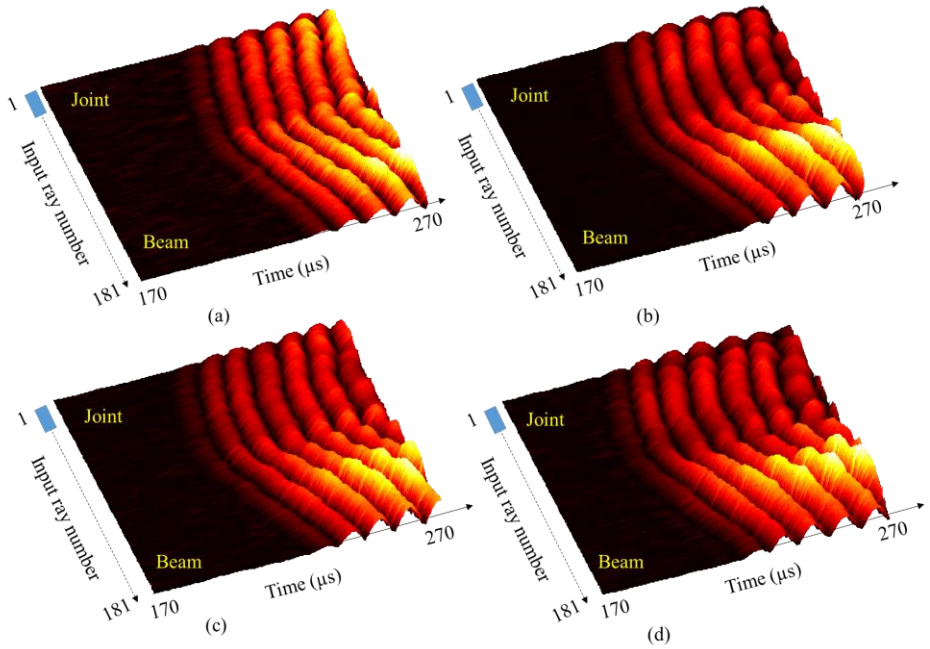

Figure 9.20 Stacked A-scan images from HP-FRC connection obtained by accelerometer 4 at 0% drift level: (a) cross-section A, (b) cross-section B, (c) cross section C, and (d) cross-section D; brightness is related to time signal relative amplitude. Cross-section locations shown in Fig. 9.5.

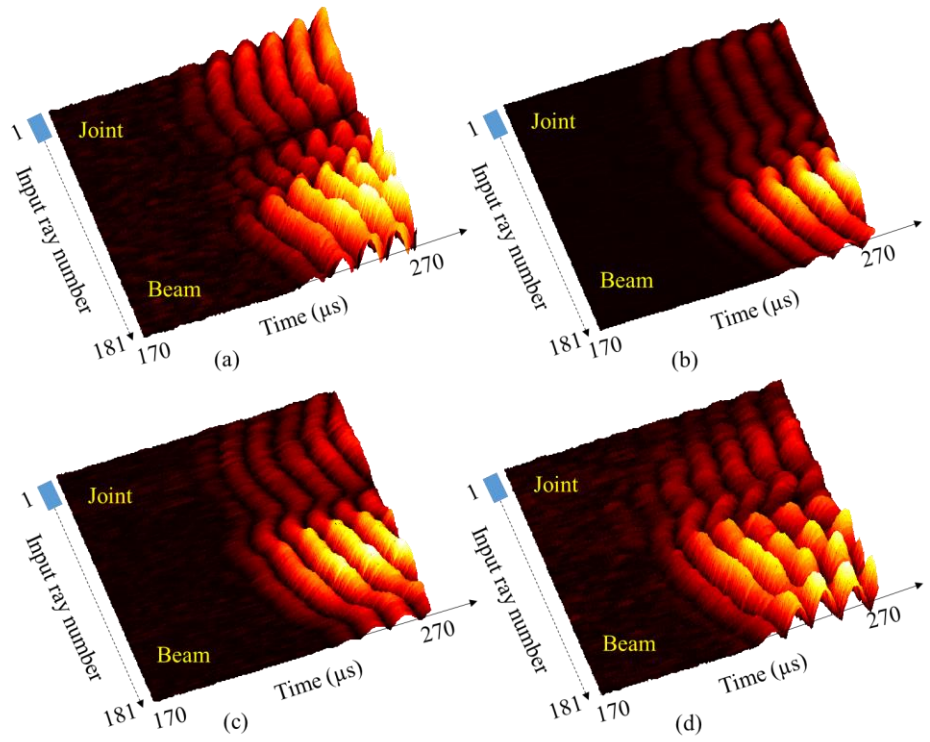

Figure 9.21 Stacked A-scan images from HP-FRC connection obtained by accelerometer 4 at 0.5% drift level: (a) cross-section A, (b) cross-section B, (c) cross section C, and (d) cross-section D; brightness is related to time signal relative amplitude. Cross-section locations shown in Fig. 9.5.

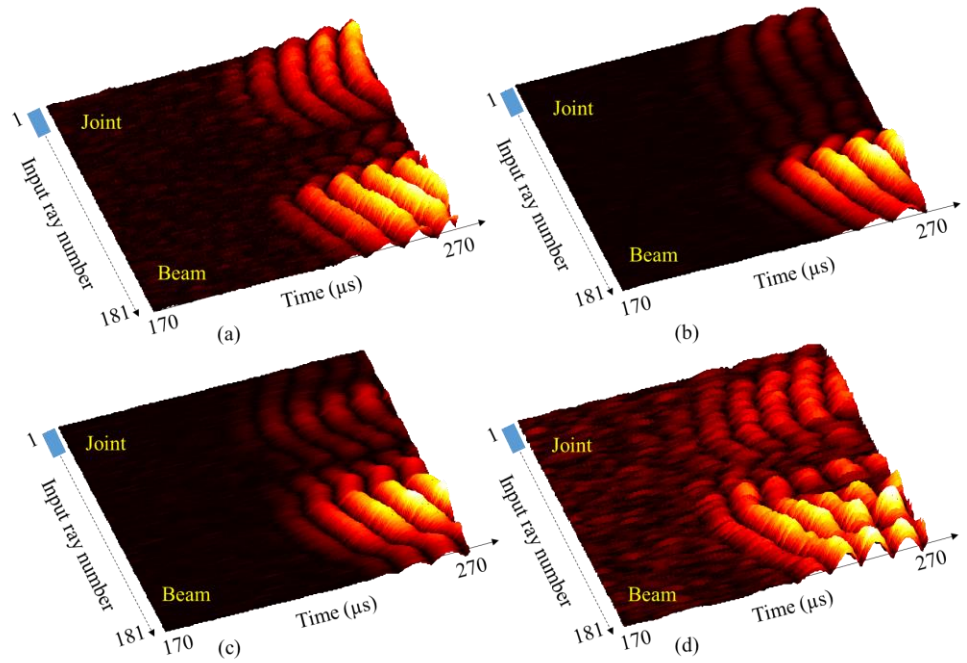

Figure 9.22 Stacked A-scan images from HP-FRC connection obtained by accelerometer 4 at 1% drift level: (a) cross-section A, (b) cross-section B, (c) cross section C, and (d) cross-section D; brightness is related to time signal relative amplitude. Cross-section locations shown in Fig. 9.5.

Figure 9.23 shows the overall normalized P-wave velocity data distribution from all measurements (5,792 signal data) represented as box plots. As drift levels increase, average P-wave velocity decreases. The RC specimen shows more significant velocity drop, up to 17%, as compared with HP-FRC, which shows less than 10% reduction in average velocity. The box plot data suggest that the RC connection experiences greater amounts of internal cracking damage, assuming that higher amounts of cracking result in lower measured P-wave velocity. The variance of velocity values (the height of the box in the plot) shows significant increase with increasing drift levels for the HP-FRC specimen. This increase in data variance likely represents increasing material non-uniformity caused by accruing, but distributed, internal damage. The collected velocity data indicate that the HP-FRC samples experience more distributed cracking damage compared to the RC specimen.

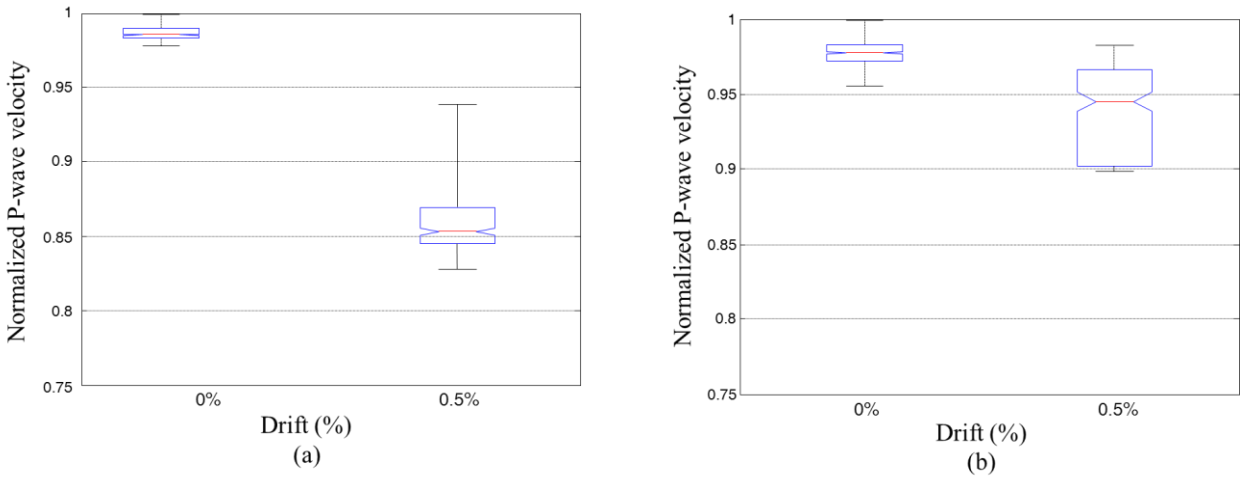

Figure 9.23 Normalized P-wave velocity distribution, expressed in box plot form, as a function of applied drift level: (a) RC and (b) HP-FRC.

9.2.2 Differential velocity and attenuation tomograms

Differential velocity and attenuation tomograms were generated following the procedure described in section 9.1.3. The details of differential velocity and attenuation tomography are described in Chapter 3 and Chapter 8, respectively. Each image represents a cross-sectional image that corresponds to each of the four scanning lines. As shown in Fig 9.5a, the four cross-sections span the interface of the connection, and are offset from each other with a vertical spacing of 4 inches. The interface between the column joint and beam regions is represented by a vertical line at the center of each image, meaning that half of the scan line runs over the beam region and the other half over the column joint region. Differential tomograms from each cross-section are presented in Figs. 9.24 to 9.27. The differentials represent the difference of either velocity or attenuation coefficients between the 0% and 0.5% drift levels at a given cross-section. The image values are normalized with respect to the maximum from each image, so that large differentials (red colors indicate more than 80% difference with respect to the image maximum value) are expected to indicate regions of cracking and material degradation within the cross-section.

Both the velocity and attenuation tomograms for the RC connection (Figs. 9.24 and 9.25) show higher differential values, indicated by warmer (red) colors, mostly clustered along the interface between the beam and column joint, especially at the back side of the specimen where the transmitting air-coupled transducer is located. The attenuation tomograms for the RC connection show differential patterns that are similar to those for the velocity tomograms, although the attenuation tomograms also show some more significant differentials close to the front side of the specimen, some of which are located nearby the beam column joint interface. The internal images indicate that the RC connection has damage that localizes at the interface

between the beam and column joint, that this damage initiates at the back side of the specimen, and that the damage pattern is consistent among the four cross-sections. These findings are supported by the sample photographs in Fig. 9.11a and b and also DIC image in Fig. 9.14a where it can be seen that surface cracks form first on the back side and are especially concentrated at the interface between beam and column joint.

The velocity and attenuation tomograms from the HP-FRC connection (Figs. 9.26 and 9.27) show different differential value patterns from those of the RC connection. In general, tomograms for the HP-FRC connection exhibit higher differential values that are spread out more broadly across the entire cross-section compared to those from the RC connection. The differential values are again more observed at the back side of the specimen but not concentrated at the interface between the beam and column joint as in the case of the RC specimen. Furthermore, the high differential values from HP-FRC cross-sectional images are concentrated more on the column joint side and thus suggest that the damage is well distributed through the cross-section rather than focused on the interface region.

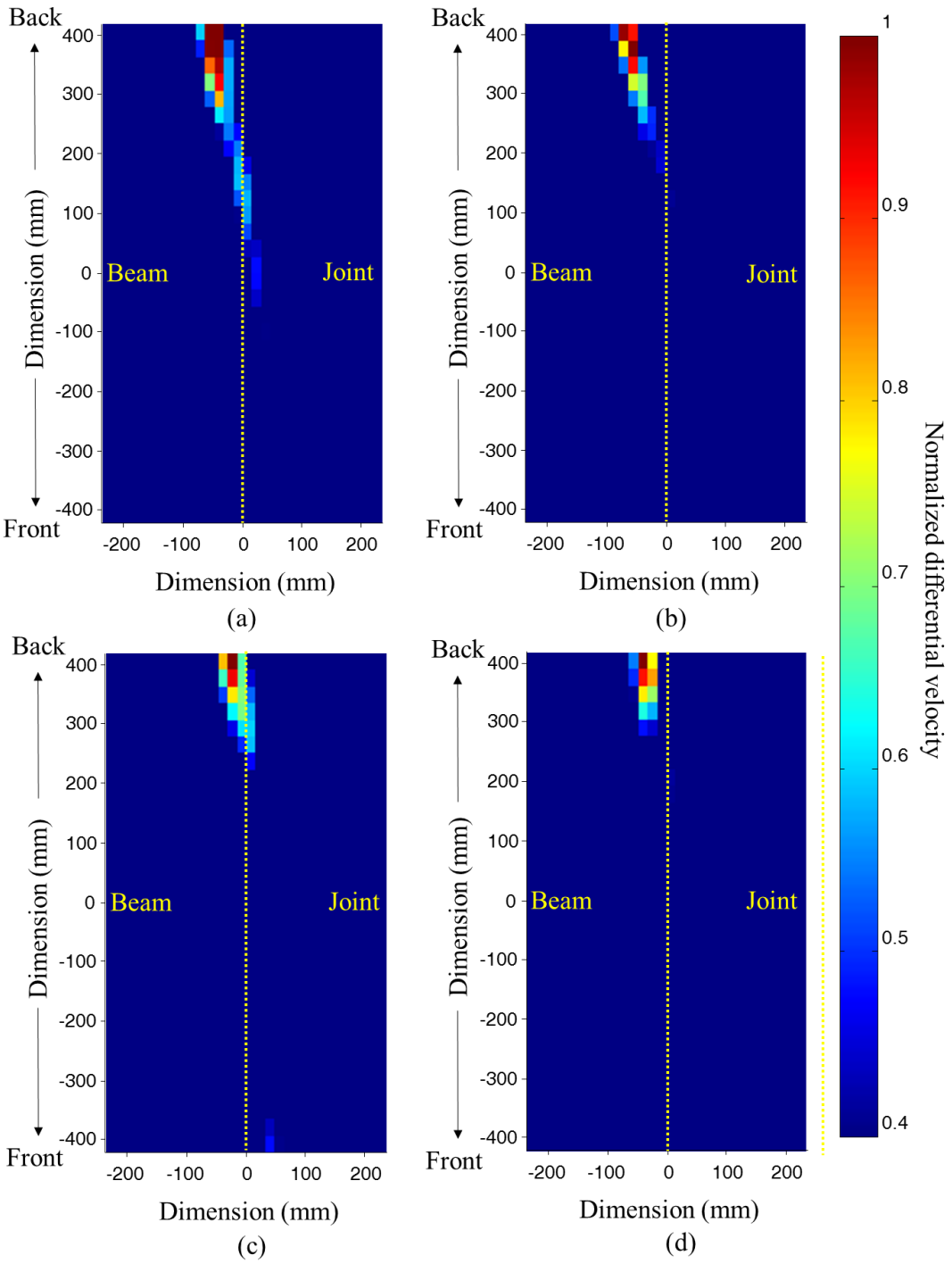

Figure 9.24 Differential velocity tomograms for RC connections computed from responses at 0% and 5% drift levels: (a) cross-section A, (b) cross-section B, (c) cross-section C, and (d) cross-section D. Yellow dotted line in each image represents the location of beam and column joint interface.

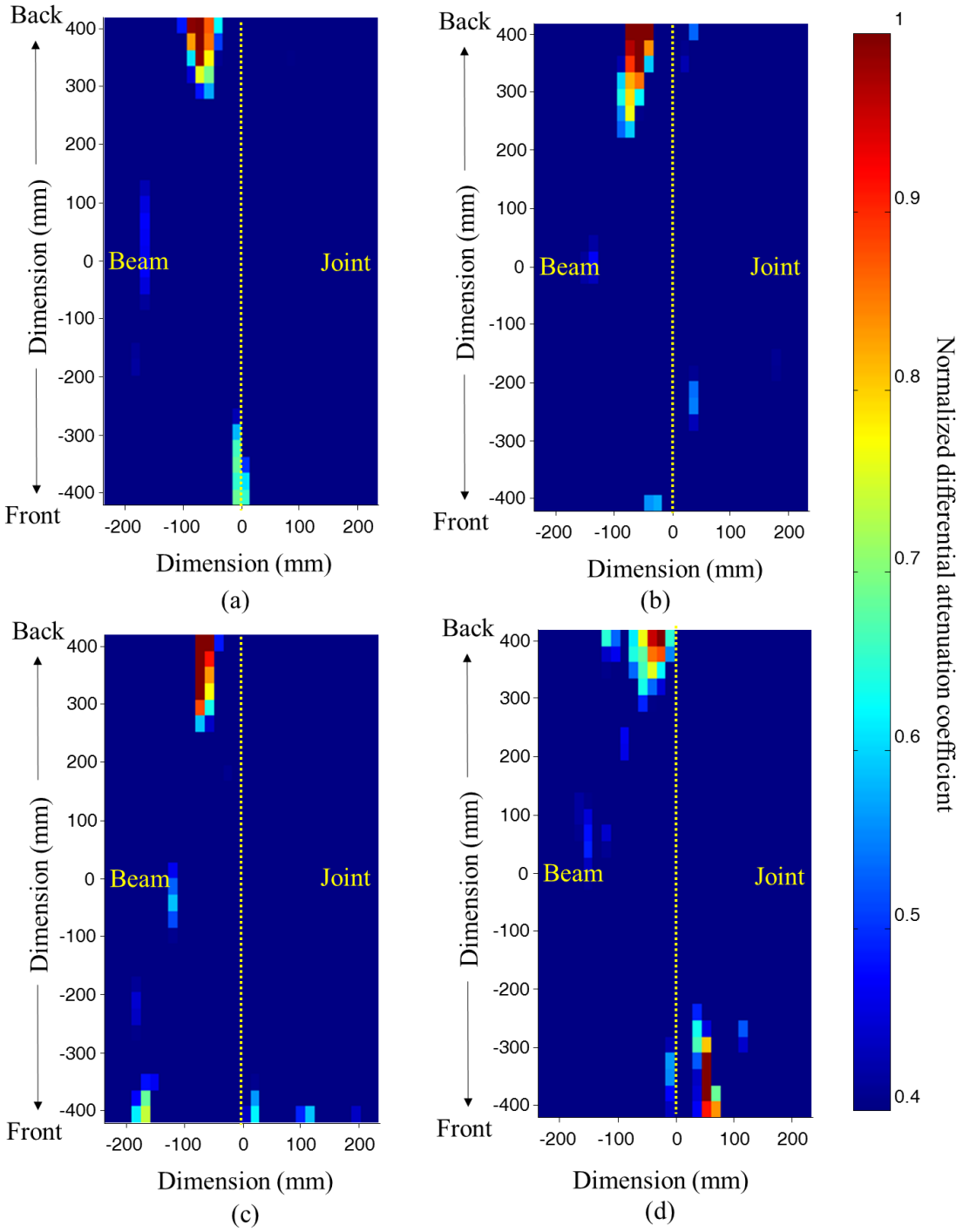

Figure 9.25 Differential attenuation tomograms for RC connections computed from responses at 0% and 5% drift levels: (a) cross-section A, (b) cross-section B, (c) cross-section C, and (d) cross-section D. Yellow dotted line in each image represents the location of beam and column joint interface.

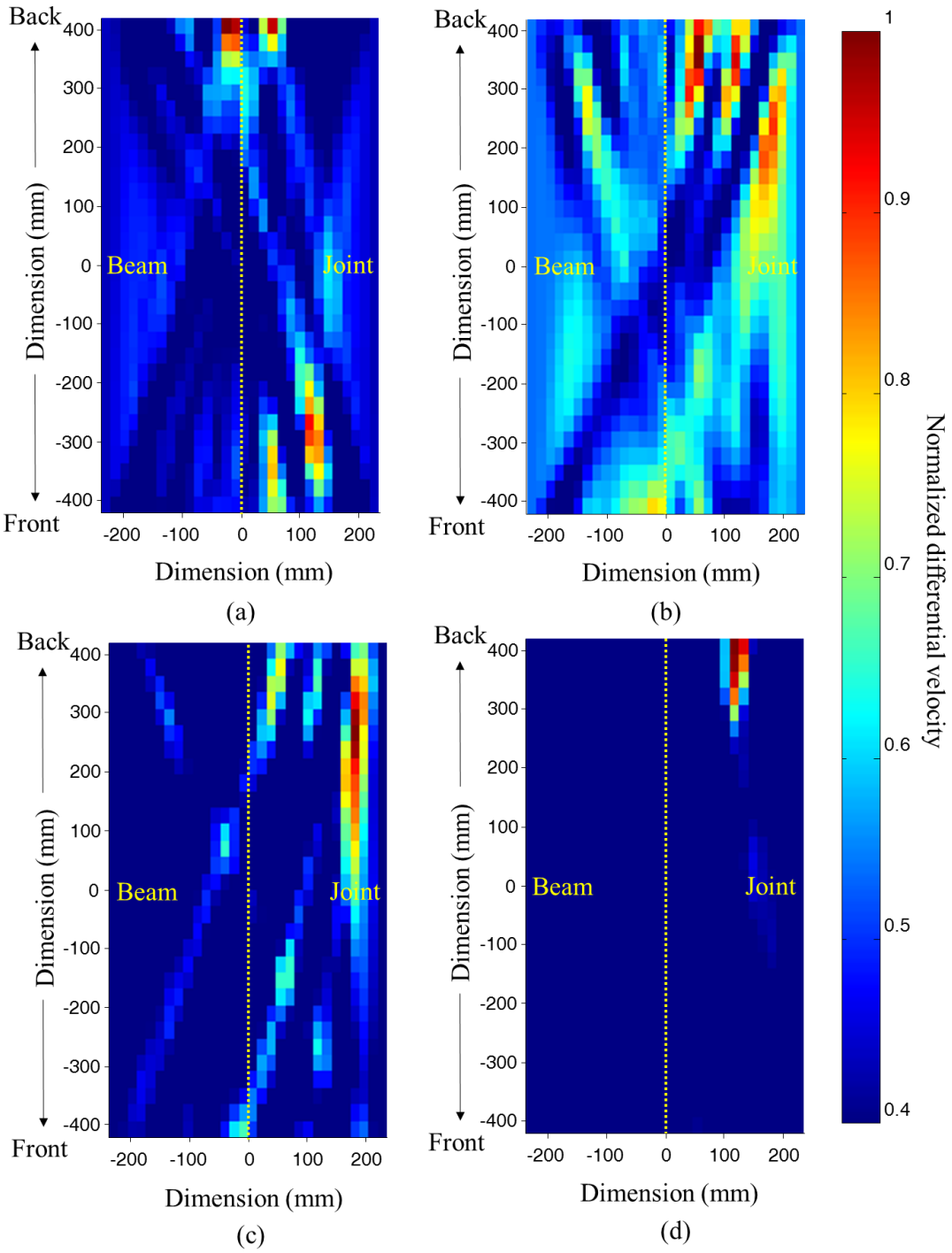

Figure 9.26 Differential velocity tomograms for HP-FRC connections computed from responses at 0% and 5% drift levels: (a) cross-section A, (b) cross-section B, (c) cross-section C, and (d) cross-section D. Yellow dotted line in each image represents the location of beam and column joint interface.

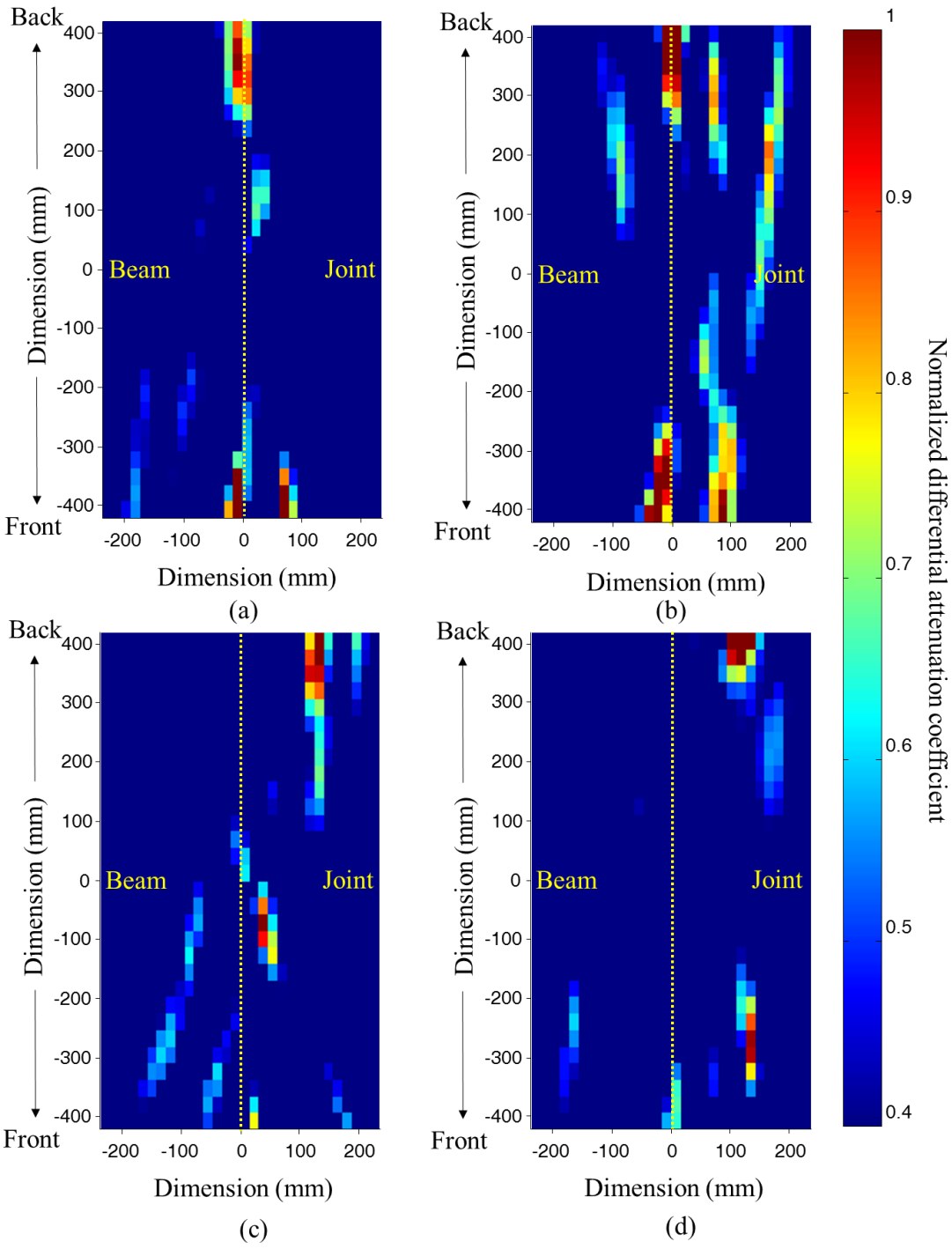

Figure 9.27 Differential attenuation tomograms for HP-FRC connections computed from responses at 0% and 5% drift levels: (a) cross-section A, (b) cross-section B, (c) cross-section C, and (d) cross-section D. Yellow dotted line in each image represents the location of beam and column joint interface.

CHAPTER 10 CONCLUSIONS

To address the national need for an effective ultrasonic system to inspect full-scale reinforced concrete structures, this dissertation presents new technology - a hybrid/air-coupled ultrasonic testing system - and new data processing and imaging capabilities - velocity and attenuation tomographic reconstruction. Here, work summaries are presented and conclusions are drawn based on the work presented in this dissertation.

10.1 Evaluation of velocity and attenuation tomographic algorithms

This work evaluates a range of existing tomographic algorithms using synthetically and numerically generated (finite element) data to simulate the wave propagation response of reinforced concrete column cross-sections. This study provides the development of practical tomographic procedures considering application to full-scale reinforced concrete elements. The study demonstrates the feasibility of using ultrasonic P-wave velocity and attenuation tomography for detecting internal defects from a limited set of ultrasonic data. The following conclusions are drawn:

• From the analysis of the tomographic algorithms using synthetically simulated data, Kaczmarz's method and Randomized Kaczmarz method show best performance for accuracy of image reconstruction compared to the seven other iterative solvers examined, exhibiting the lowest error: within ± 10 percent of known velocity for all pixels.

• Of the three signal time arrival picking algorithms evaluated using numerically simulated data, the noise-threshold method offers the most stable and reliable performance, superior to those of Akaike information criterion (AIC), Hinkley criterion (HIC) methods.

• Wave amplitude decay is a more sensitive wave propagation parameter to the presence of internal inclusions than arrival time delay. The first peak amplitude of the wave provides a reliable metric of wave attenuation, superior to the integrated area of the wave (energy) from digitized signal data.

• Reconstructed velocity and attenuation tomograms from numerically simulated data indicate the presence and location of internal inclusions from a limited set of data. The numerical results demonstrate that ultrasonic tomography has potential for deployment using experimental data, to obtain cross-sectional images from full-scale reinforced concrete elements.

• Differential attenuation tomography provides better distinction between damaged and non-damaged areas within a cross-section than raw attenuation tomography. The algorithm for differential tomography obviates the need for advanced knowledge of wave field parameters such as the geometric beam spreading angle.

10.2 Development of hybrid air-coupled ultrasonic scanning system

This work demonstrates, for the first time, application of ultrasonic tomography to full-scale steel reinforced concrete elements using air-coupled transducers. The experimental data, ultrasonic velocity tomograms and differential attenuation tomograms demonstrate the significant beneficial potential of ultrasonic tomography for condition assessment of civil infrastructure elements. Air-coupled transducers significantly improve practical application by providing high quality data while at the same time obviating physical coupling processes and enabling large amounts of data to be collected. The following conclusions are drawn:

• A contactless ultrasonic transducer attached to an automated robotic scanning system significantly increases the number of ultrasonic data that can be collected and enables high spatial position accuracy ($\pm$0.1mm). The developed system obtains 2,720 signals over 6 minutes while conventional contact UPV obtains 64 signals over 1 hour assuming a single 1m linear scan.

• The reconstructed ultrasonic velocity tomograms successfully detect embedded void defects within the reinforced concrete column, which exhibit as areas of lower P-wave velocity. Cracked regions and reinforcing bars within concrete were more difficult to identify, but in some cases the cracked region were also detected.

• The reconstructed differential attenuation tomograms successfully identify embedded defects without a priori knowledge of the geometric spreading parameter and initial amplitude. Cracked regions near steel reinforcement were successfully identified, and in some cases embedded bars were also detected.

10.3 Comparison of ultrasonic imaging methods

This experimental study compares transmitted through-thickness ultrasonic tomography develop as part of this effort to one-sided ultrasonic SAFT imaging using commercially available hardware and image processing packages. Both ultrasonic measurement systems can be applied to reinforced concrete structures without a priori knowledge of defect placement, steel bar positioning, and material properties. The following conclusions are drawn:

• The one-sided SAFT images clearly indicated significant volumetric reflectors (steel reinforcing bars, voids) within the test specimen. Because of shadowing effects, however, defects located below or behind densely spaced steel bars could not be detected. Cracked concrete regions did not provide significant reflection and were not detected in any instance in the SAFT images.

• Embedded steel bars were not observed in transmitted wave velocity tomograms, but were readily detected in one-sided SAFT images.

• Tomographic and SAFT image reconstructions each have distinct characteristics, advantages and disadvantages. Optimal application of each depends on the type of structure tested and the image target of interest. For example, velocity tomograms constructed from through-thickness data show superior performance for isolated critical concrete elements that contain high volumes of steel reinforcement. On the other hand, SAFT imaging techniques show superior performance for detecting volumetric inclusions like embedded bars or large voids.

10.4 Application of integrated visualization

This work integrates ultrasonic velocity tomography and 3-D computer vision techniques to evaluate a full-scale reinforced concrete column in a new way. Based on tomographic cross-sectional slice images, 3-D volumetric internal images are built up to obtain full stereoscopic analysis. An automated image-based 3-D reconstruction technique is applied to the same structure to visualize external condition. Both internal and exterior visualizations of the column are integrated into a single three-dimensional image. The approach is demonstrated on a reinforced concrete column sample that exhibits exterior geometric inconsistency with the original design and also includes controlled internal defects. The following conclusions are drawn:

• Image based 3-D reconstructions using computer vision techniques provide accurate information about surface conditions, such as surface color variations, numbers and other markings, and geometrical deviations from the original or intended design.

• Integrated internal/external visualization offers deeper understanding of the test sample as compared with the data provided by each method individually. Multi-perspective analysis of the integrated images in a single unified coordinate environment provides powerful holistic information of internal and external condition of the inspected structure.

10.5 Tomography applied to full-scale RC structural elements subjected to seismic loading

The hybrid air-coupled ultrasonic testing system is applied to full-scale RC structural elements subjected to simulated earthquake loading. The degradation progress within plastic hinge connection areas is monitored by ultrasonic velocity and attenuation tomography. The reconstructed internal images provide helpful information across complete cross-sections at a pixel resolution (minimum 15x15 mm), a capability

that has not been reported previously. This research demonstrates the stability and reliability of the hybrid air-coupled ultrasonic system and the application of ultrasonic tomography for monitoring realistic degradation progress within full-scale structures under simulated earthquake loading, and establishes tomography as an effective approach to evaluate structural condition of structures in situ.

10.5.1 Columns

Full-scale reinforced concrete (RC) and ultra-high-performance fiber-reinforced concrete (UHP-FRC) columns are subjected to simulated earthquake loads and imaged using ultrasonic velocity tomography before, during, and after the loads were applied. The following conclusions are drawn:

• The developed hybrid air-coupled ultrasonic scanning set-up can be applied at an off-site testing site, providing 550 total pieces of high quality ultrasonic data for each cross-sectional line scan from the full-scale RC column within 5 minutes (not considering the set-up time).

• Decreases in global P-wave velocity, as represented as the average values within cross-sectional ultrasonic tomograms, correlate well with global interior column damage caused by applied simulated seismic loads, as characterized by column stiffness slope.

• P-wave velocity obtained from pixels within the tomograms at fixed drift (damage) level reliably indicate relative material soundness across the cross-section, where local decreases in velocity correlate well with increases in internal residual strain reported by transversely and axially embedded strain gauges.

• The UHP-FRC column shows distinct performance under simulated seismic loading, both with regard to mechanical and ultrasonic testing behavior, as compared with conventional RC columns. UHP-FRC columns exhibit less residual internal strain and slower rates of decreasing P-wave velocity with applied drift level.

10.5.2 Beam and column connections

Full-scale reinforced concrete (RC) and high-performance fiber-reinforced concrete (HP-FRC) slab-beam-column sub-assemblages are subjected to simulated earthquake loads and imaged using ultrasonic velocity and attenuation tomography before, during, and after loads were applied. The following conclusions are drawn:

• The developed hybrid air-coupled ultrasonic scanning set-up can be applied at an off-site testing site, providing 1,448 total pieces of high quality ultrasonic for each cross-sectional line scan from full-scale RC beam-column connections within 10 minutes (not considering the set-up time).

• Differential tomograms enable monitoring internal degradation progress of the beam and column connections at early stages of loading and damage input (0.5% drift level), even where only very small surface cracks are visible. Mechanical response behaviors, indicated by the stiffness slope responses, were not able to capture this subtle damage.

• Different degradation patterns within the RC and HP-FRC beam and column connections can be clearly distinguished in the tomographic images. The RC connection exhibits concentrated damage immediately around the beam-column interface, while the HP-FRC connection exhibits more distributed cracking damage in the column.

• The HP-FRC connection subjected to simulated seismic loading shows distinct stress distribution behavior, both with regard to internal cross-sectional imaging (differential tomograms) and external surface visualization (digital image correlation), as compared with a conventional RC connection. The HP-FRC connection exhibits more distributed cracking damage, less surface strain, and slower rate of decreasing P-wave velocity with applied drift level.

10.6 Future work

This dissertation presented several significant steps towards meaningful application of ultrasonic technology to nondestructive evaluation of full-scale reinforced concrete structural elements. In order to achieve successful implementation of developed technique in the field, however, additional research and implementation work are needed.

10.6.1 Deployment of a configurable robotic scanning platform

The development and evaluation of a new hybrid ultrasonic scanning system are discussed in Chapter 4; however, further improvements to hardware will significantly increase the applicability of ultrasonic scanning tests for actual field tests on structures. Suggestions for improvements to the hardware in order to realize eventual application in the field are presented here:

• Although the use of air-coupled ultrasonic transmitters increases the amount of data that can be collected within a specific amount of time, the current reliance on contact-based sensing needs to be addressed in order to have higher volumes of data from the receiving side, thus improving the quality and accuracy of tomogram built up from those data. A suitable detecting sensor system should have minimal contact, or better yet contactless, interface with the tested material, and furthermore the obtained signals should exhibit signal to noise ratio no lower than 10 dB. To date, dry-point contact shear transducer arrays or laser Doppler

vibrometery (LDV) have shown promise in these regards and have potential to be implemented in an effective ultrasonic scanning system.

• In order to acquire large amounts of data with high accuracy in the field, an automated robotic scanning platform is essential. The access to civil infrastructure can be limited, and thus a manual surface testing approach cannot always be implemented on large-scale structures. Unmanned aerial vehicles (UAVs) offer great potential to serve as a platform for ultrasonic scanning in such cases (Ham et al. 2016). A suitable system should be able to carry and position an appropriate air-coupled ultrasonic sending and sensing system close by, within 15 cm, to the surface of the inspected structure.

10.6.2 Fusion with external imaging technologies

The integrated visualization scheme described in Chapter 6, demonstrates the benefits of combining tomographic reconstructions with images from external visualization techniques. The combination of internal and external visualizations has the great potential to provide a holistic and practical understanding of the inspected structure for practitioners. Furthermore, the 3-D reconstruction of test configuration in-situ minimizes possible alignment errors in repeated data acquisition. Possible applications of fused visualization procedure should be considered.

• Light Imaging, Detection, And Ranging (LIDAR) technology, which reconstructs the external position of an object in virtual 3-D space coordinates, is becoming an accepted tool in civil engineering (Wang et al. 2013). Although high precision laser scanners for the LIDAR are relatively high-priced compared to photo-based visualization, its application in the field provide benefits for rapid data measurement and high resolution imaging. The fusion of LIDAR images with internal tomograms shows promise

• External visualization techniques can also be used increase the repeatability of ultrasonic scanning tests in the field. For the purpose of structural health monitoring over an extended period of time, nondestructive point tests, such as ultrasound, require that the same test positions be analyzed at each testing time. 3-D reconstructions of the operating test configuration could serve to document sensor alignment and position and minimize errors between measurement sets.

10.6.3 Consideration of other ultrasonic analysis and imaging techniques

The tomographic reconstruction procedures discussed in Chapters 3 and 8 demonstrate the utility of velocity and attenuation tomography to full-scale RC cross-sections. Two different approaches from the same measurement set provide distinct imaging results and performance. However, other data processing and imaging approaches should also be considered. For example, the broad range of "data analytics" tools, such as qualitative data analysis (QDA) of combined tomography, would likely provide capability to extract more information and present those data in different and improved manners. The work reported here uses

the initial, coherent, portion of the ultrasonic wave pulse in the generation of the tomograms. However, the complete ultrasonic field, which includes the later arriving multiply reflected coherent pulse rays and also the incoherent component of the field, likely contains much important information about the internal damage condition and material properties of the sample. Considering these points, the following advanced ultrasonic analysis and imaging schemes should be investigated.

• Velocity and attenuation tomography show different internal characteristics within their respective reconstructed images: velocity tomograms show clear location of void-like defects without influence or disruption from reinforcing bars, while attenuation tomograms provide some information about reinforcing bars and damaged (cracked) regions. Combined imaging accompanying with qualitative data analysis likely provides all information from the applied cross-section.

• The later portions and incoherent content of ultrasonic signals likely provide a great amount of information, including multiple reflections by geometrical boundaries, other modes of wave propagation, and wave scattering behavior. Recently considered diffuse wave or non-linear wave analyses may provide additional, sensitive information about internal damage from the obtained data set, which could enable new types of imaging analysis, such as full-field waveform imaging and reverse time migration, to be carried out (Muller et al. 2012).

REFERENCES

ACI Committee 228. (2013). *Report on Nondestructive test methods for evaluation of concrete in structures.* Farmington Hills, MI.

ACI Committee 546. (2001). *Concrete repair guide.* Farmington Hills, MI.

Abraham, O., Piwakowski, B., Villain, G., & Durand, O. (2012). Non-contact, automated surface wave measurements for the mechanical characterization of concrete. *Construction and Building Materials, 37*, 904-915.

Aggelis, D. (2013). Wave propagation through engineering materials; assessment and monitoring of structures through non-destructive techniques. *Materials and Structures, 46*, 519-532.

Aghdasi, P., Palacios, G., Heid, A., & Chao, S.-H. (2015). Mechanical properties of a highly flowable ultra-high-performance fiber-reinforced concrete mixture considering large-size effects. *Seventh International RILEM Conference on High Performance Fiber Reinforced Cement Composites (HPFRCC7)* (pp. 193-200). RILEM Publications SARL.

ASCE. (2013). *Report Card for America's Infrastructure*. Retrieved September 2016, from www.infrastructurereportcard.org.

Bittner, J. (2015). *OpenSAFT software package*. Retrieved September 2016, from https://github.com/Jabittner/openSAFT

Carpinteri, A., Xu, J., Lacidogna, G., & Manuello, A. (2012). Reliable onset time determination and source location of acoustic emissions in concrete structures. *Cement and Concrete Composites*, *34*(4), 529-537.

Centrangolo, G., & Popovics, J.S. (2010). Inspection of concrete using air-coupled ultrasonic pulse velocity. *ACI Materials Journal*, *107*(2), 155-163.

Chai, H., Momoki, S., Kobayashi, Y., Aggelis, D., & Shiotani, T. (2011). Tomographic reconstruction for concrete using attenuation of ultrasound. *NDT&E International, 44*, 206-215.

Chekroun, M., Le Marrec, L., Abraham, O., Durand, O., & Villain, G. (2009). Analysis of coherent surface wave dispersion and attenuation for non-destructive testing of concrete. *Ultrasonics*, *49*(8), 743-751.

Chimenti. D.E. (2014). Review of air-coupled ultrasonic materials characterization. *Ultrasonics, 54*(7), 1804-1816.

Choi, H., & Popovics, J.S. (2015). NDE application of ultrasonic tomography to a full-scale concrete structure. *IEEE Transactions on Ultrasonics, Ferroelectrics, and Frequecy Control, 62*(6), 1076-1085.

Choi, H., Bittner, J., & Popovics, J.S. (2016). Comparison of ultrasonic imaging techniques for full-scale reinforced concrete. *Transportation Research Record: Journal of the Transportation Research Board*, in press.

Choi, H., Ham, Y., & Popovics, J.S. (2016). Integrated visualization for reinforced concrete using ultrasonic tomography and image-based 3-D reconstruction. *Construction and Building Materials, 123*, 384-393.

Choi, H., Song, H., Quang, N.V.T., Roesler, J.R., & Popovics, J.S. (2016). Contactless system for continuous monitoring of early-age concrete properties. *Concrete International*, 35-41.

Clayton, D., Smith, C., Ferraro, C., Nelson, J., Khazanovich, L., Hoegh, K., Chintakunta, S., Popovics, J.S., Choi, H., Ham, S. (2013). *Evaluation of Ultrasonic Techniques on Concrete Structures.* Oak Ridge, TN: Oak Ridge National Laboratory.

De La Haza, A., Samokrutov, A., & Samokrutov, P. (2013). Assessment of concrete structures using the Mira and Eyecon ultrasonic shear wave devices and the SAFT-C image reconstruction technique. *Construction and Building Materials, 38*, 1276-1291.

De Witte, A. (1959). Equivalence of Huygens' principle and Fermat's principle in ray geometry. *American Journal of Physics, 27*(5), 293-301.

Dutton, M., Take, W., & Hoult, N. (2014). Curvature monitoring of beams using digital image correlation. *Journal of Bridge Engineering, 19*(3). 1-13.

Furukawa, Y., & Ponce, J. (2008). Accurate, dense, and robust multiview stereopsis. *IEEE Transactions on Pattern Analysis and Machine Intelligence, 32*(8), 1362-1376.

Gabriels, P., Snieder, R., & Nolet, G. (1987). In situ measurements of shear wave velocity in sediments with higher-mode Rayleigh waves. *Geophysical Prospecting, 35*(2), 187-196.

Golparvar-Fard, M., Bohn, J., Teizer, J., Savarese, S., & Peña-Mora, F. (2011). Evaluation of image-based modeling and laser scanning accuracy for emerging automated performance monitoring techniques. *Automation in Construction, 20*(8), 1143-1155.

Guan, H., & Gordon, R. (1994). A projection access order for speedy convergence of ART: a multilevel scheme for computed tomography. *Physics in Medicine and Biology, 39*(11), 2005-2022.

Hall, K. (2011). *Air-coupled ultrasonic tomographic imaging of concrete elements, Ph.D Dissertation.* Urbana, IL: University of Illinois at Urbana-Champaign.

Ham, S., & Popovics, J. (2015). Application of micro-electro-mechanical sensors contactless NDT of concrete structures. *Sensors, 15*(4), 9078-9096.

Ham, Y., & Golparvar-Fard, M. (2013). An automated vision-based method for rapid 3D energy performance modeling of existing buildings using thermal and digital imagery. *Advanced Engineering Informatics, 27*(3), 395-409.

Ham, Y., & Golparvar-Fard, M. (2013). EPAR: Energy Performance Augmented Reality models for identification of building energy performance deviations between actual measurements and simulation results. *Energy and Buildings, 63*, 15-28.

Ham, Y., Han, K., Lin J., & Golparvar-Fard, M. (2016).Visual monitoring of civil intrastructure systems via camera-equipped unmanned aerial vehicles (UAVs): a review of related works. *Visualization in Engineering, 4*, 1-8.

Hansen, P., & Saxild-Hansen, M. (2012). AIR Tools — A MATLAB package of algebraic iterative reconstruction methods. *Journal of Computational and Applied Mathematics, 236*(8), 2167-2178.

Hartley, R., & Zisserman, A. (2004). *Multiple view geometry in Computer Vision.* Cambridge University Press.

Hassouna, M., & Farag, A. (2007). MultiStencils fast marching methods: A highly accurate solution to the Eikonal equation on cartesian domains. *IEEE Transactions on Pattern Analysis and Machine Intelligence, 29*(9), 1563-1574.

Herman, G. (2009). *Fundamentals of Computerized Tomography: Image Reconstruction from Projections.* New York: Springer.

Hoegh, K., & Khazanovich, L. (2011). Ultrasonic tomography for evaluation of concrete pavements. *Transportation Research Record: Journal of the Transportation Research Board*(2232), 85-94.

Horn, B. (1987). Closed-form solution of absolute orientation using unit quaternions. *Journal of the Optical Society, 4*(4), 629-642.

Hounsfield, G. (1973). Computericed transverse axial scanning tomography: part I, discription of the system. *British journal of Radiology, 46*, 1016-1022.

Hu, B., Kundu, T., Grill, W., Liu, B., & Toufigh, V. (2013). Embedded piezoelectric sensors for health monitoring of concrete structures. *ACI Materials Journal, 16*(4), 149-159.

Jackson, M.J., & Tweeton, D.R. (1994). *Geophysical tomography using wavefront migration and fuzzy constraints.* U.S. Bureau of Mines: Report of Investigations 9497.

Jahanshahi, M., & Masri, S. (2012). Adaptive vision-based crack detection using 3D scene reconstruction for condition assessment of structures. *Automation in Construction, 22*, 567-576.

Jones, R. (1955). A vibration method for measuring the thickness of concrete road slabs in situ. *Magazine of Concrete Research, 7*(20), 97-102.

Jones, R. (1962). Surface wave technique for measuring the elastic properties and thickness of roads: theoretical development. *British Journal of Applied Physics, 13*(21), 21-29.

Joulian, B., & Gubbins, D. (1977). Three-dimensional seismic ray tracing. *Journal of Geophysical Research, 43*, 95-113.

Kaczmarz, S. (1937). Angenäherte Auflösung von Systemen linearer Gleichungen. *Sciences Mathématiques, 35*, 355-357.

Kak, A., & Slaney, M. (1988). *Principles of computerized tomographic imaging.* IEEE press.

Kewalramani, M., & Gupta, R. (2006). Concrete compressive strength prediction using ultrasonic pulse velocity through artificial neural networks. *Automation in Construction, 15*(3), 374 - 379.

King, D. (2012). *Collapse dynamics of ultrasound contrast agent microbubbles, Ph.D. Dissertation.* Urbana, IL: University of Illinois at Urbana-Champaign.

Kolsky, H. (1963). *Stress Waves in Solids.* New York: Dover Publications.

Krautkramer, J., & Krautkramer, H. (1990). *Ultrasonic testing of materials.* New York: Springer-Verlag.

Landis, E., & Shah, S. (1995). Frequency-dependent stress wave attenuation in cement-based materials. *Journal of Engineering Mechanics, 121*(6), 737-743.

Langenberg, K., Marklein, R., & Mayer, K. (2012). *Ultrasonic Nondestructive Testing of Materials: Theoretical Foundations.* Boca Raton, FL: CRC Press.

Lee, K., Zhu, J., Shum, J., Zhang, Y., Muluk, S., Chandra, A., & Esjabdari, M. (2013). Surface curvature as a classifier of abdominal aortic aneurysms: A comparative analysis. *Annals of Biomedical Engineering, 41*(3), 562-576.

Long, R. (2010). *The improvement of ultrasonic apparatus for the routine inspection of concrete, Ph.D Dissertation.* London SW7 2BX: University of London.

Lu, L., Wang, C., & Zhang, B. (2007). Inversion of multimode Rayleigh waves in the presence of a low-velocity layer: numerical and laboratory study. *Geophysical Journal International, 168*(3), 1235-1246.

Maierhofer, C., Reinhardt, H., & Dobmann, G. (2010). *Non-destructive Testing Methods.* Boca Raton, FL: CRC Press.

Metha, P., & Monteiro, P. (2005). *Concrete: Microstructure, Properties, and Materials, 4th edition.* McGraw-Hill.

Mindess, S., Young, J., & Darwin, D. (2002). *Concrete, 2nd edition.* Prentice Hall.

Muller, S., Niederleithinger, E., & Bohlen, T. (2012). Reverse time migration: A seismic imaging technique applied to synthetic ultrasonic data international. *International Journal of Geophysics, 2012*, Article ID 128465, 1-7.

Naik, T., Malhotra, V., & Popovics, J. (2004). The ultrasonic pulse velocity method. In *Handbook on Nondestructive testing of Concrete.* Boca Raton, FL: CRC Press.

Natterer, F. (2001). *The Mathematics of Computerized Tomography.* Philadelphia: SIAM.

Nazarian, S., & Stokoe, K. (1986). *In-situ determination of elastic moduli of pavement systems by spectreal-Analysis-of-surface-waves method (Practical aspects).* Austin, TX: Research Report 368-1F, Center for Transportation Research, University of Texas at Austin.

Oh, T. (2012). *Defect characterization in concrete elements using vibration analysis and imaging, Ph.D. Dissertation.* Urbana, IL: University of Illinois at Urbana-Champaign.

Palacios, G. (2015). *Performance of full-scale ultra-high performance fiber-reinforced concrete column subjected to extreme earthquake-type loading and effect of surface preparation on the cohesion and friction factors of the AASHTO interface shear equation.* Arlington, TX: University of Texas at Alrington.

Parra-Montesinos, G., Peterfreund, S., & Chao, S.-H. (2005). Highly damage-tolerant beam-column joints through use of high-performance fiber-reinforced cement composites. *ACI Structural Journal, 102*(3), 487-495.

Popovics, S., Bilgutay, N., Karaoguz, M., & Akgul, T. (2000). High-frequency ultrasound technique for testing concrete. *ACI Materials Journal, 97*(1), 58-65.

Prada, J., Fratta, D., & Santamarina, J. (2000). Tomographic detection of low-velocity anomalies with limited data sets (velocity and attenuation). *Geotechnical Testing Journal, 23*(4), 472-486.

Pratt, D., & Sansalone, M. (1992). Impact-echo signal interpretation using artificial intelligence. *ACI Materials Journal, 89*(2), 178-187.

Schickert, M., Krause, M., & Mu, M. (2003). Ultrasonic imaging of concrete elements using reconstruction by synthetic aperture focusing technique. *Journal of Materials in Civil Engineering, 15*(3), 235-246.

Sethian, J., & Vladimirsky, A. (2000). Fast methods for the Eikonal and related Hamilton–Jacobi equations on unstructured meshes. *Proceedings of the National Academy of Sciences, 97*(11), 5699–5703.

Shepp, L., & Logan, B. (1974). The Fourier reconstruction of a head section. *IEEE Transactions on Nuclear Science, 21*, 21-43.

Shevaldykin, V., Samakrutov, A., & Kozlov, V. (2003). Ultrasonic low-frequency short pulse transducers with dry point contact. *International Symposium Non-Destructive Testing in Civil Engineering (NDT-CE), 66*, pp. 16-19. Berlin, Germany.

Shokouhi, P., Wostmann, J., Schneider, G., Milmann, B., Taffe, A., & Wiggenhauser, H. (2011). Nondestructive detection of delamination in concrete slabs: A multi-method investigation. *Transportation Research Record: Journal of the Transportation Research Board*(2251), 103-113.

Siciliano, B., & Khatib, O. (2008). *Handbook of Robotics.* Berlin Heidelberg: Springer-Verlag.

Snavely, N., Seitz, S., & Szeliski, R. (2008). Modeling the world from internet photo collections. *International Journal of Computer Vision, 80*(2), 189-210.

Torok, M., Golparvar-Fard, M., & Kochersberger, K. (2012). Image-based automated 3D crack detection for post-disaster building assessment. *Journal of Computing in Civil Engineering, 28*, 1-13.

Triggs, B., McLauchlan, P., Hartley, R., & Fitzgibbon, A. (1999). Bundle adjustment -- a modern synthesis. *ICCV '99 Proceedings of the International Workshop on Vision Algorithms: Theory and Practice* (pp. 153-177). London, UK: Springer-Verlag.

Tweeton, D.R., Jackson, M.J., & Roessler, K.S. (1992). *BOMCRATR: A curved ray tomographic computer program for geophysical application.* U.S. Bureau of Mines: Report of Investigations 9617.

Um, J., & Thurber, C. (1987). A fast algorithm for two-point seismic ray tracing. *Bulletin of the Seismological Society of America, 77*(3), 972-986.

Wang, C., Cho, Y., and Gai, M. (2013). As-Is 3D Thermal modeling for existing building envelopes using a hybrid LIDAR system. *Journal of Computing in Civil Engineering*, *27*(6), 645-656.

Wang, L., & Yuan, F. (2005). Damage identification in a composite plate using prestack reverse-time migration technique. *Structural Health Monitoring, 4*(3), 195-211.

Wu, C., Agarwal, S., Curless, B., & Seitz, S. (2011). Multicore bundle adjustment. *IEEE Conference on Computer Vision and Pattern Recognition (CVPR)*, (pp. 3057-3064).

Zhao, A., Zhang, M., & Ding, Z. (2006). Seismic travel time computation for transversely isotropic media. *Chinese Journal of Geophysics*, *49*(6), 1603-1612.

Zhu, J. (2005). *Non-Contact NDT of Concrete Structures Using Air-Coupled Sensors.* Urbana, IL: University of Illinois at Urbana-Champaign.

APPENDIX A: Tomographic inversion code and auto-picking algorithms

Tomographic inversion Matlab code

The code is based on the linear equations

$$Ax = b \tag{A.1}$$

where x represents pixel values of a tomographic image, A is the matrix of weight factors of the penetrating ray at pixel x, and b is the ray-sum measured from the experiment. The attached tomography codes technically construct A and b matrices and solve the linear equations using the iterative solver. The code contains one operation file (main.m), two function files (settingA.m and constructA.m) for constructing A matrix, and one function file (Backprojection.m) for iterative solver (Kaczmarz's method).

The operation file (main.m) is attached below.

```
clear all
clc

%% Setting A matrix

load('Position_transReceiv.mat')

% transmitter: Transmitter s position (x,y) in mm
% receiver: Receivers position (x,y) in mm

NofR = 1:8; % Total No. of Receivers
NofT = 1:327; % Total No. of Transmitters

% No. of Pixels in image (one axis, N = NofPixels^2)
NofPixels = 50;

[setting, Model] = settingA(NofR,NofT,transmitter,receiver,NofPixels);

%% Construct A matrix
R = 0.05; % Wavelength in m
[A, RayDistance, ElapsedTime_Amatrix] = constructA(R,Model,setting);

%% b matrix (arrival time)
load('arrivals.mat')
c = 0;
for i = NofT(1:327)
   for j = NofR(1:8)
      c = c + 1;
      b(c) = Arrivals_H(i,j);
   end
end
UPV = RayDistance./b;
b_avg = mean(UPV);
x_initialguess = (1/b_avg)*ones(1,length(Model))';
```

```
%% b matrix (attenuation)
load('Ampratio.mat')
c = 0;
for i = NofT(1:327)
   for j = NofR(1:8)
      c = c + 1;
      b(c) = dalpha(i,j);
   end
end

Amp_del = dalpha/DRd;
x_initialguess = mean(Amp_del(:))*ones(1,length(Model))';


%% Iteration Solver
%% Backprojection
maxit = 10000; % Matrix iteration
N = length(Model);

tic
[x_Backprojection1]= Backprojection1(A,b,RayDistance,N,maxit,x_initialguess);
ElapsedTime_Backprojection1 = toc

%% Results of iteration solver
% Number of iteration
Iter_Backprojection1 = size(x_Backprojection1,2);

% residual matrix
residual_Backprojection1 = A*x_Backprojection1-b'*ones(1,Iter_Backprojection1);

% check minimum residual
[m_rBackprojection1, i_rBackprojection1] = min(abs(mean(residual_Backprojection1(:,:))));

%% Plot Image
c =0;
xx = zeros(NofPixels);
for j = 1:NofPixels
   for i = 1:NofPixels
      c = c+1;
                  xx_Backprojection1(i,j) = x_Backprojection1(c,end);
       end
end
figure;
imshow(1./xx_Backprojection1,[min(1./xx_Backprojection1(:))
max(1./xx_Backprojection1(:))],'InitialMagnification','fit','XData',[-406 406],'YData',[-356 356]);
box off; axis off; axis image on
title('Backprojection')
colormap jet, axis image on.
```

The settingA.m is attached below.

```
function [setting, Model] = settingA(NofR,NofT,transmitter,receiver,NofPixels)

%% Setting 1
% Location of transmitter and receiver (x,y)
% Assign the order of rays
% Unit: m (data files are in unit of mm)

c = 0; countA = 0;
% Parallel pairs of source and receiver
for i = NofT(1:327)   % Assign No.
   for j = NofR(1:8) % Assign No.
      c = c + 1;
      setting(c,2) = transmitter(i,1)/1000; % Transmitter location in x
      setting(c,1) = transmitter(i,2)/1000; % Transmitter location in y
      setting(c,4) = receiver(j,1)/1000;    % Receiver location in x
      setting(c,3) = receiver(j,2)/1000;    % Receiver location in y
   end
end
% % Parallel pairs of source and receiver (if this exists)
% for i = NofT(322:322+240) % Assign No.
%     for j = NofR(9:16)    % Assign No.
%         c = c + 1;
%         setting(c,2) = transmitter(i,1)/1000; % Transmitter location in x
%         setting(c,1) = transmitter(i,2)/1000; % Transmitter location in y
%         setting(c,4) = receiver(j,1)/1000;    % Receiver location in x
%         setting(c,3) = receiver(j,2)/1000;    % Receiver location in y
%     end
% end
%% Settimg 2
% Set up model (size of cross-sectional image)

% NofPixels = 35; % No. of Pixels in image (one axis)
ModelMax_x = max(abs(transmitter(:,1))/1000);
ModelMax_y = max(abs(transmitter(:,2))/1000);

Model = zeros(NofPixels^2,2);

unit_x = ModelMax_x*2/NofPixels;
unit_y = ModelMax_y*2/NofPixels;
end_x = ModelMax_x-ModelMax_x/NofPixels;
end_y = ModelMax_y-ModelMax_y/NofPixels;

for i = 1:NofPixels
   Model((i-1)*NofPixels+1:i*NofPixels,:) = [-end_x:unit_x:end_x;
      (-end_y+(i-1)*unit_y)*ones(1,NofPixels)]';
end
```

The constructA.m is attached below.

```
function [A, RayDistance, ElapsedTime_Amatrix] = constructA(R,Model,setting)

%% Construct A matrix

tic
N = length(Model);
M = 1:size(setting,1);

A = zeros(length(M),N);
RayDistance = dist(setting(:,1:2),setting(:,3:4)); % in m

% figure;
% hold on;
% xlim([min(Model(:,1))-unit_x/2 max(Model(:,1))+unit_x/2]);
% ylim([min(Model(:,2))-unit_x/2 max(Model(:,2))+unit_x/2]);
% isDisp = 1;

for i = M
   Vector_TtoR = setting(i,1:2)-setting(i,3:4);
   Ratio_sum = 0;

%     plot(setting(i,[1 3]),setting(i,[2 4]))
%     hold on

   for j = 1:N
      Vector_TtoP = Model(j,1:2)-setting(i,1:2);
      d = norm(cross([Vector_TtoP 0],[Vector_TtoR 0]))/norm(Vector_TtoR);

      if d < R
         A(i,j) = (R-d)/R;
         Ratio_sum = Ratio_sum + A(i,j);
%            if isDisp
%               pause(isDisp)
%               plot(Model(j,1),Model(j,2),'x', 'Color', A(i,j).*[1,1,0])
%               hold on
%            end
      end
    end

   A(i,:) = A(i,:)*RayDistance(i)/Ratio_sum;
end
ElapsedTime_Amatrix = toc
```

The Backprojection.m is attached below.

```
function [x]= Backprojection(A,b,RayDistance,N,maxit,x_initialguess)

% Ax = b (DP = T)
x(:,1) = x_initialguess;

for k = 1:maxit;
   t = A*x(:,k);
   dt = b'-t;
   dp = zeros(N,1);
   for j = 1:N
      for i = 1:length(t)
         dp(j) = dp(j)+A(i,j)*dt(i)/RayDistance(i)^2;
      end
   end

   x(:,k+1) = x(:,k)+dp;

   if max(abs(dp)) < mean(x(:,k+1))/100
      break
   end
end
```

Arrival auto-picking algorithms

The noise-threshold method was provided by Dr. Daniel King (King 2012). The two function files are described here. The noisethresh.m is attached below.

```
% Noise Threshold
%
% SYNTAX
% [pos neg] = noisethresh(signal,xrange,stdevs)
%
% This function returns the positive and negative noise threshold values
% using a gaussian fit to histogram data.
%
% INPUTS
% signal = A matrix of length N x M, where N is the signal length and M is
% the number of realizations.
%
% xrange = A vector of the portion of the signal to analyze. Use : to
% analyze the entire signal.
%
% stdevs = The number of standard deviations from the mean from which the
% noise threshold is drawn.
%
% Orig: 11/19/10; Last update: 5/15/13, D. King

% Test signal: signal = random('norm',1,2,10000,20);

% signal = sigf5p0;

function [pos neg] = noisethresh(signal,xrange,stdevs)

% Subtract DC component from signal (Zero mean)
if length(xrange)==1
   signal_zero = zeros(size(signal,1),size(signal,2));
else
   signal_zero = zeros(length(xrange),size(signal,2));
end

for n=1:size(signal,2)
   signal_zero(:,n) = signal(xrange,n) - mean(signal(xrange,n));
end

% Combine all snapshots
signal_all = signal_zero(:);

% Fit gaussian curve
[mu0 sigma0] = normfit(signal_all);

% Choose thresholds
pos = mu0+stdevs*sigma0;
neg = mu0-stdevs*sigma0;

%%% Validation plot
```

```
nbars = 100;
[h0,x0] = hist(signal_all,nbars); % For error checking

gausfit0 = normpdf(x0,mu0,sigma0);
% figure;
% hold on
% bar(x0,h0/sum(h0))
% plot(x0,gausfit0/sum(gausfit0))

end
```

The threshold.m is attached below.

```
function [ta,ti] = threshold(time,sig,tol)

for ti = 1:length(sig)
   if sig(ti)>tol
      break
   end
end

ta = time(ti);

return
```

The Akaike information criterion (AIC) was provided by Dr. Thomas Schumacher. The code is attached below.

```
clear all
clc

%% step 1:
figure
plot(sig)

% you dont need to plot it versus time, just plot it versus indices (1,2,3.....LENGTH(SIGNAL))

%% step 2: set a pretrigger based on the signal to noise ratio
pretrigger=350 ; %(this is just an example)

%% Step 3: pick a window length from the signal "sig" where the p-wave arrives

win =201;
% length of the window on which we apply the AIC.(always add the one to center the window: win1= 200+1;win2= 150+1, etc.))

twin = pretrigger-(win-1)/2:pretrigger+(win-1)/2;
% time corresponds to the window (Centered on the pretrigger)
sigwin = sig(twin);
% take only the part of the signal that corresponds to the window

%% Step 4: compute AIC
AIC=zeros(1,length(win));
 for i = 1:win
% i cannot be 1 because log(var(constante))=-infity because var(constante)=0
    AIC(i) = i*log(var(sigwin(1:i)))+(win-i-1)*log(var(sigwin(1+i:win)));       % Maeda`s formula
    if (AIC(i)==-Inf)
% eliminate the values of AIC equal to -Inf
       AIC(i)=0;
     else
       AIC(i)=AIC(i);
     end
end
[min_AIC ind] = min(AIC);                    % pick the min (AIC)
ind = twin(1)-1+ind;
% find the index that corresponds to the minimum AIC

onset=time(ind);

hold on
plot([pretrigger pretrigger], [-0.05 0.05], 'c-o')
plot([ind ind], [-0.05 0.05], 'g-x')
```

The Hinkley criterion was coded by the author. The code is attached below.

```
%% Hinkley criterion
function [ta, ind] = Hinkley(t1,sig1)

for i=1:length(sig1)
   Si(i) = sum(sig1(1:i).^2);
end
N = length(sig1);
alpha = 50;
Sn = Si(end);
delta = Sn/(alpha*N);

for i=1:length(sig1)
   Hi(i) = Si(i)-i*delta;
end
[onset ind] = min(Hi);

ta = t1(ind);

% % Modify to pick first negative ver1
% preset = 100;
% sigmin = sig1(ind-preset:ind);
% [nx ind1] = min(sigmin);
% ta = t1(ind1+ind-(preset+1));

% % Modify to pick first negative ver2
% sigmin = sig1(1:ind);
% [nx ind1] = min(sigmin);
% ta = t1(ind1);

% Modify to pick first negative ver3
% sigtwin = sig1(1:ind+80);
% for i=1:length(sigtwin)
%     Sii(i) = sum(sigtwin(1:i).^2);
% end
% NN = length(sigtwin);
% Snn = Sii(end);
% deltaa = Snn/(alpha*NN);
%
% for i=1:length(sigtwin)
%     Hii(i) = Sii(i)-i*deltaa;
% end
% [onset ind1] = min(Hii);

% preset = 20;
% sigmin = sig1(ind-preset:ind1+preset);
% [nx ind2] = min(sigmin);
% ind3 = ind2+ind1-(preset+1);

end
```

APPENDIX B: NEEShub databases

The tests are a part of a research project funded by Network for Earthquake Engineering Simulation (NEES) of the National Science Foundation (NSF). All data including ultrasonic signals, test set-up detail, and strain gauges are available online (https://nees.org/). The project number is 927 and the digital object identifiers (DOI) of the data presented in this dissertation are listed, identified by test sample:

RC1: Alireza Nojavan, Arturo Schultz, Xuejian Liu, Sanputt Simasathien, Guillermo Palacios, Shih-Ho Chao, Curt Haselton, Hajin Choi, John Popovics (2014). "CI-1 RC Perimeter-Frame Column under Near Collapse Loading", Network for Earthquake Engineering Simulation (distributor), Dataset, DOI:10.4231/D3G44HQ9B

RC2: Alireza Nojavan, Arturo Schultz, Xuejian Liu, Sanputt Simasathien, Guillermo Palacios, Shih-Ho Chao, Curt Haselton, Hajin Choi, John Popovics (2014). "CI-7 RC Perimeter-Frame Column under Bi-Axial Loading Protocol", Network for Earthquake Engineering Simulation (distributor), Dataset, DOI:10.4231/D3BC3SX4Q

RC3: Alireza Nojavan, Arturo Schultz, Xuejian Liu, Sanputt Simasathien, Guillermo Palacios, Shih-Ho Chao, Curt Haselton, Hajin Choi, John Popovics (2014). "CII-2 RC Space-Frame Column under Symmetric Cyclic Loading (ACI 374)", Network for Earthquake Engineering Simulation (distributor), Dataset, DOI:10.4231/D3KW57J3S

UHP-FRC: Alireza Nojavan, Arturo Schultz, Xuejian Liu, Sanputt Simasathien, Guillermo Palacios, Shih-Ho Chao, Curt Haselton, Hajin Choi, John Popovics (2014). "CIII-2 UHPFRC Space-Frame Column under Symmetric Cyclic Loading (ACI 374)", Network for Earthquake Engineering Simulation (distributor), Dataset, DOI:10.4231/D36M3340C

RC connection: Young-Jae Choi, Shih-Ho Chao (2016). "SBC2-SYM-RC Slab-Beam-Column Subassemblage under Symmetric Cyclic Loading", Network for Earthquake Engineering Simulation (distributor), Dataset, DOI:10.5072/FK2ZC7XJ5K

HP-FRC connection: Young-Jae Choi, Shih-Ho Chao (2016). "SBC3-SYM-HPFRC Slab-Beam-Column Subassemblage under Symmetric Cyclic Loading", Network for Earthquake Engineering Simulation (distributor), Dataset, DOI:10.5072/FK2TM76Q9X.